Dominik Suckart, M.Sc.

Phenomenology and Modelling of Flame-Wall-Interactions in Spark-Ignition-Engines

DISSERTATION

zur Erlangung des akademischen Grades

Doktor der technischen Wissenschaften

eingereicht an der

Technischen Universität Graz

Betreuer

Univ.-Prof. Dipl.-Ing. Dr.techn. Helmut Eichlseder

Institut für Verbrennungskraftmaschinen und Thermodynamik

Zweitbetreuer

Prof. Dr.-Ing. Christian Hasse

Institut für Simulation reaktiver Thermo-Fluid Systeme, Technische Universität Darmstadt

Graz, April 2018

Eidesstattliche Erklärung
Affidavit

Ich erkläre an Eides statt, dass ich die vorliegende Arbeit selbstständig verfasst, andere als die angegebenen Quellen/Hilfsmittel nicht benutzt, und die den benutzten Quellen wörtlich und inhaltlich entnommenen Stellen als solche kenntlich gemacht habe. Das in TUGRAZonline hochgeladene Textdokument ist mit der vorliegenden Dissertation identisch.

I declare that I have authored this thesis independently, that I have not used other than the declared sources/resources, and that I have explicitly indicated all material which has been quoted either literally or by content from the sources used. The text document uploaded to TUGRAZonline is identical to the present doctoral dissertation.

München, am 05.04.2018   Dominik Suckart

Preface

The present thesis is the result of my work as a doctoral candidate within the BMW Group in Munich.

Primarily, I want to express my thanks to Professor Helmut Eichlseder for the supervision of this work and his support. He has given me the confidence and the necessary freedom to shape this work according to my own ideas, which has contributed greatly to my personal and professional development. Furthermore, I would like to thank Professor Christian Hasse for his role as co-supervisor of this thesis.

I am deeply indebted to Dr. Dirk Linse for his guidance throughout this work and his constant encouragement to question every last detail. It would have been almost impossible to complete this thesis without his advice and support. Our in-depth discussions significantly improved the quality of this work as well as my understanding of combustion theory and CFD modelling.

I also want to acknowledge the general support of AVL and their close collaboration regarding the implementation of the GFWI model. In particular, I would like to thank Dr. Peter Priesching and Dr. Jooyoung Hahn for providing the necessary framework in AVL FIRE™ as well as for their advice and work on the numerical issues which appeared during the implementation of the combustion model. I am indebted to Kurt Schierl for his assistance and help on all general issues concerning AVL FIRE™.

I also want to thank Dr. Eberhard Schutting for supporting the engine measurements as well as for the subsequent post-processing of the experimental data.

I would like to express my sincere gratitude to Ulrich Ernst, Josef Hösl, Jürgen Knupe and Claus Borack for giving me the opportunity to pursue my PhD within the powertrain development department at BMW M. Many thanks to my current and former colleagues at BMW M, who accompanied me during the time of this work. The numerous discussions and conversations around all topics of automotive engineering have broadened my horizon and made the daily routine during my PhD even more interesting.

Finally and most importantly, I want to thank my family - my parents, who fostered my aspirations and encouraged me in all my decisions and my wife Isabel for her boundless patience, incessant motivation, unconditional love and her ability to always make me smile.

Munich, April 2018   Dominik Suckart

Kurzfassung

Die Optimierung der Verbrennung in Kolbenmotoren erfordert neben einem tiefgehenden Verständnis der zugrundeliegenden Prozesse genaue und umfassende physikalische Modelle. Das derzeitige Wissen über die letzte Phase der Verbrennung, in welcher die Flamme mit den Brennraumwänden interagiert, ist diesbezüglich begrenzt. Die vorliegende Arbeit hat daher das Ziel, das Verständnis der Flamme-Wand-Interaktion sowie dessen Modellierung zu verbessern. Aufbauend auf einer umfangreichen Analyse der Flamme-Wand-Interaktion anhand der existierenden Literatur wird der Verlöschvorgang in einem direkteinspritzenden Ottomotor untersucht, um einen tieferen Einblick in die dabei ablaufenden physikalischen Prozesse zu erhalten. Unter Einbeziehung der Resultate wird im Anschluss das G-Gleichungs-Verbrennungsmodell um die Effekte der Flamme-Wand-Interaktion erweitert.

Zur Bestimmung der Charakteristika des Verlöschprozesses in einem Ottomotor wird eine hochauflösende Messung des Wandwärmestroms im Zylinderkopf mit umfangreichen numerischen Simulationen kombiniert. Es werden hierbei fünf verschiedene Betriebspunkte untersucht, um den Einfluss von Drehzahl, Last, Ladungsbewegung sowie Gemischzustand auf die charakteristischen Größen des Verlöschvorgangs, wie z.B. den Quenchabstand, zu bestimmen. Die zyklenbasierten Wandwärmeströme werden mithilfe einer Aufeinanderfolge von 3D-CFD, 3D-FE und 1D Simulationen analysiert. Die Resultate zeigen, dass der Verlöschvorgang einer vorgemischten Flamme in einem Ottomotor dem einer laminaren vorgemischten Flamme ähnelt. Der Quenchabstand ist daher durch den thermodynamischen Zustand im Brennraum bestimmt, welcher wiederum stark von der Motorlast abhängt. Auf Basis der Daten werden zwei Korrelationen zur Berechnung des Quenchabstands vorgeschlagen.

Anhand von klassischen Konzepten der Turbulenz- und Verbrennungsmodellierung wird auf Basis der G-Gleichung ein Level-Set Flamelet Modell für vorgemischte Verbrennung hergeleitet, welches das Verlöschen von Flamelets sowie wandnahe Turbulenz mit einbezieht. Zunächst wird der Verlöschvorgang laminarer Flammen mithilfe des Level-Set Ansatzes untersucht und eine konsistente Modellvorstellung abgeleitet. Diese wird durch Einführung der Wahrscheinlichkeit, verlöschte Flamelets vorzufinden, auf turbulente Flammen übertragen. Es wird gezeigt, dass der Anteil nicht verlöschter Flamelets zur Skalierung der turbulenten Brenngeschwindigkeit verwendet werden kann. Darauf aufbauend wird ein einheitliches G-Gleichungsmodell für verlöschte und nicht verlöschte Flammen hergeleitet. Die Modellierung der ungeschlossenen Terme des Modells erfolgt unter Einbeziehung der Auswirkungen von Flammenentwicklung und wandnaher Turbulenz. Die abschließende Anwendung des Modells zur Simulation der Verbrennung in einer turbulenten Kanalströmung sowie in Ottomotoren zeigt vielversprechende Ergebnisse und unterstreicht die Bedeutung der Flamme-Wand-Interaktion für Verbrennungsprozesse in geschlossenen Brennräumen.

Abstract

The optimization of combustion in reciprocating engines necessitates an in-depth understanding of the underlying processes as well as accurate and comprehensive physical models. In this respect, the current knowledge on the last stage of combustion in which the flame interacts with the combustion chamber walls is limited. Hence, the objective of this thesis is to improve the understanding of flame-wall interaction and its modelling. Using a comprehensive analysis of the existing literature on flame-wall interactions as a starting point, the quenching process in a direct-injection spark-ignition engine is investigated to gain insight into the underlying physical processes. Building on the results, the G-equation combustion model is subsequently extended to incorporate the effects of flame-wall interaction.

To reveal the characteristics of the quenching process in a spark-ignition engine, a highly-resolved measurement of the wall heat flux in the cylinder head is combined with extensive numerical simulations. Five different operating points are investigated to study the influence of speed, load, equivalence ratio and charge motion on the characteristic scales of flame-wall interactions such as the quenching distance. The cycle-resolved wall heat fluxes are analysed using a succession of 3D-CFD, 3D-FE and 1D simulations. The results reveal that the quenching process of a premixed flame in a spark-ignition engine is similar to the one of a laminar premixed flame. The quenching distance is thus determined by the in-cylinder thermodynamic state which is strongly influenced by the engine load. Based on the data, two correlations for calculating the quenching distance are proposed.

Following classic concepts of turbulence and combustion modelling, a level-set flamelet model for premixed combustion that takes flame quenching and near-wall turbulence into account is derived based on the G-equation. Using the level-set approach, the quenching process is studied for laminar flames and a consistent model concept is derived. The concept is transferred to turbulent flames by introducing the probability of finding quenched flamelets. It is shown that the fraction of unquenched flamelets can be used to scale the turbulent burning velocity. Based on the findings, a unified G-equation model for quenched and unquenched flames is derived. The modelling of the unclosed terms of the model is done by taking the effects of flame development and near-wall turbulence into account. The final application of the model for simulating combustion in a turbulent channel flow as well as in spark-ignition engines shows promising results and highlights the importance of flame-wall interactions for combustion processes in enclosed combustion chambers.

Contents

Nomenclature

Latin symbols

a	Model constant of the k-ζ-f turbulence model	–
a_1	Proportionality factor for estimating l_t (table 5.1)	–
a_2	Constant (table 5.1)	–
a_4	Model constant of the GFWI model (table 5.1)	–
A	Cross section area	m^2
A_0	Cross section area perpendicular to the direction of flame propagation	m^2
A_j, B_j	Coefficients of the Fourier analysis	K
A_T	Total flame front surface area	m^2
$A_{T,R}$	Reactive flame front surface area	m^2
A_r	Frequency or pre-exponential factor of reaction r	$1/s$
b_1, b_3	Proportionality factors for estimating the turbulent burning velocity in the corrugated flamelets and thin reaction zones regime, respectively (table 5.1)	–
b_2	Proportionality factor for estimating the turbulent flame brush thickness	–
B	Integration constant	–
c	Progress variable	–
$c_\mu, c_{\varepsilon 1}, c_{\varepsilon 2}$	Model constants of the k-ε and k-ζ-f turbulence model (table 2.1)	–
c'_μ	Model parameter of the GFWI model (table 5.1)	–
$c_1, c_2, c_\tau, c_L, c_\eta$	Model constants of the k-ζ-f turbulence model (table 2.1)	–
c_p	Specific isobaric heat capacity	$J//(kg\ K)$
$c_{p,\alpha}$	Specific isobaric heat capacity of species α	$J//(kg\ K)$
c_s, c_χ	Constants for modelling the scalar dissipation rate (table 5.1)	–
c_t	Model parameter of the GFWI model (table 5.1)	–
C	Steady-state heat flux	W/m^2
D	Thermal diffusivity	m^2/s
D_t	Turbulent diffusivity	m^2/s
D_w	Thermal diffusivity of the wall material	m^2/s
D_α	Binary diffusion coefficient of species α	m^2/s
D_Σ	Destruction term	$1/(m\ s)$
Da	Damköhler number	–
E	Energy spectrum of turbulence	m^3/s^2
E_r	Activation energy of reaction r	J/mol
f	Quantity	variable
f	Elliptic function (k-ζ-f model)	–
f_k	Instantaneous realisation of the variable f	variable
f_μ	Damping function for ν_t	–
G	G-scalar	m
G_0	G-scalar zero level-set	m

Nomenclature

h	Specific enthalpy	J/kg
h^+	Channel half width in wall units	$-$
h_α	Specific enthalpy of species α	J/kg
$h_{f,\alpha}^0$	Standard enthalpy of formation of species α	J/kg
ΔH	Lower heating value	J/kg
$\mathbf{I}$	Unit tensor	$\left[I_{ij}\right] = -$
I_0	Stretch factor	$-$
$\mathbf{j}_\alpha$	Diffusive flux vector of species α	$[j_{\alpha,i}] = J/(m^2 s)$
k	Turbulent kinetic energy	m^2/s^2
k_r	Reaction rate coefficient of reaction r	$1/s$
k_{br}	Backward reaction rate coefficient of reaction r	$1/s$
k_{fr}	Forward reaction rate coefficient of reaction r	$1/s$
Ka	Karlovitz number	$-$
Ka_δ	Karlovitz number based on the reaction zone thickness	$-$
$\overline{\mathcal{K}\sigma}$	Curvature term appearing in the G-variance equation	$-$
l^+	Viscous length scale	m
l^*	Length scale	m
l^*	Expansion factor to model flame development	$-$
l_δ	Reaction zone thickness	m
l_ϵ	Oxidation layer thickness	m
l_F	Laminar flame thickness	m
l_m	Mixing length scale	m
l_n	Eddy size	m
ℓ	Integral length scale used within the k-ζ-f model	m
ℓ_t	Integral length scale	m
$\ell_{F,t}$	Turbulent flame brush thickness	m
l_t	Integral length scale according to Bray [27]	m
$l_{F,t}$	Turbulent flame brush thickness based on the variance of G	m
$l_{F,t,alg}$	Algebraic turbulent flame brush thickness based on the variance of G	m
$\mathcal{L}$	Markstein length	m
L_H	Enthalpy loss parameter	$-$
Le	Lewis number	$-$
Le_α	Lewis number of species α	$-$
$\dot{m}$	Mass flow	kg/s
M	Number of single-step reactions of a reaction mechanism	$-$
M	Mean molar mass	kg/mol
M	Burning velocity ratio	$-$
M_α	Mean molar mass of species α	kg/mol
M_{ex}	Burning velocity ratio at the extinction limit	$-$
M_α	Chemical symbol for species α	
$\mathbf{n}$	Unit vector normal to the flame front	$[n_i] = -$
$\mathbf{n}_{rot}$	Unit vector specifying the rotation direction	$[n_i] = -$
n	Engine speed	$1/s$
n	Polytropic coefficient	$-$
N	Number of species of a reaction mechanism	$-$
N_P	Number of stochastic particles	$-$
p	Pressure	N/m^2

Pe	Peclet number	–
Pr	Prandtl number	–
Pr_t	Turbulent Prandtl number	–
$\mathbf{q}$	Heat flux vector	$[q_i] = J/(m^2 s)$
Q	Unquenched factor	–
$Q_{\alpha=0}$	Upper limit of the unquenched factor Q	–
Q_{skewed}	Unquenched factor Q for a skewed distribution of quenched flamelets	–
Q_{sym}	Unquenched factor Q for a symmetric distribution of quenched flamelets (lower limit)	–
Q_Σ	Unquenched factor based on flame surface densities	–
$\dot{Q}_F$	Laminar flame power	W/m^2
$\dot{Q}_W$	Wall heat flux	W/m^2
$\dot{Q}$	Heat source term	W/m^3
r_K	Spark kernel radius	m
R	Specific gas constant	$J/(kg\ K)$
$\mathcal{R}$	Universal gas constant	$J/(mol\ K)$
Re_t	Turbulent Reynolds number	–
Re_τ	Reynolds number based on the friction velocity u_τ	–
s_L^0	Laminar burning velocity of a planar unstretched flame	m/s
s_L	Generalised laminar burning velocity (incl. e.g., wall heat loss or flame strain)	m/s
s_n	Normal diffusion velocity	m/s
$\bar{s}_P$	Mean piston speed	m/s
s_r	Reaction velocity	m/s
s_T^0	Turbulent burning velocity of a planar unstretched flame	m/s
s_T	Generalised turbulent burning velocity (incl. e.g., flame quenching)	m/s
$s_{T,k}$	Turbulent burning velocity of the spark kernel	m/s
$\mathbf{S}$	Strain rate tensor	$[S_{ij}] = 1/s$
S	Strain rate	$1/s$
Sc	Schmidt number	–
Sc_α	Schmidt number of species α	–
Sc_t	Turbulent Schmidt number	–
$Sc_{t,\Sigma}$	Turbulent Schmidt number of Σ	–
$Sc_{t,k}, Sc_{t,\varepsilon}, Sc_{t,\zeta}$	Turbulent Schmidt number of k, ε and ζ (table 2.1)	–
t	Time	s
t_c	Chemical time scale	s
t_η	Kolmogorov time scale	s
t_F	Chemical time scale of a laminar flame	s
T	Temperature	K
T_0	Inner layer temperature	K
T_c	Core temperature of the burned gases	K
$T_{ref,0}$	Reference temperature of the inner layer formulation	K
$T_{ref,B}$	Reference temperature of the formulation by Boust	K
T_F	Flame temperature	K
T_G	Gas temperature	K
u	Velocity	m/s
u^*	Velocity scale	m/s
u_τ	Friction velocity	m/s

Nomenclature

$\mathbf{v}$	Vector of velocity	$[v_i] = m/s$
v'	Fluctuation velocity	m/s
v_η	Kolmogorov velocity scale	m/s
v_i	Component of the velocity vector	m/s
v'_n	Turnover velocity of eddies of size l_n	m/s
V	Volume	m^3
$\dot{w}_r$	Reaction rate of reaction r	$mol/(m^3 s)$
$\mathbf{x}$	3D spatial coordinate	$[x_i] = m$
$\mathbf{x}_c$	3D spatial coordinate with $\mathbf{x}_{rot}$ as coordinate center	$[x_i] = m$
$\mathbf{x}_f$	Instantaneous flame front position	$[x_i] = m$
$\mathbf{x}_{rot}$	Coordinates of the rotation center	$[x_i] = m$
x	1D spatial coordinate normal to the flame front	m
x_Q	Mean distance between the position of the mean flame front and the beginning of the quenching zone along the propagation direction of the flame front	m
x_W	Mean distance between the position of the mean flame front and the wall along the propagation direction of the flame front	m
y	Wall distance	m
Y	Mass fraction	$-$
Y_F	Fuel mass fraction	$-$
Y_P	Product mass fraction	$-$
Y_0	Species mass fraction of fuel or oxygen representative for the reaction zone	$-$
Y_α	Mass fraction of species α	$-$
Y_{EGR}	Residual gas mass fraction	$-$
Ze	Zeldovich number	$-$

Greek symbols

α	Probability of finding fresh gases	$-$
α	Conditional probability of finding quenched flamelets	$-$
α	Exponential factor (temperature) for estimating the laminar burning velocity	$-$
α	Crank angle	$^\circ CA$
$\alpha_{\partial Q}$	Crank angle in the instant when the wall heat flux attains its highest gradient	$^\circ CA$
β	Probability of finding burned gases	$-$
β	Conditional probability of finding unquenched flamelets	$-$
β	Exponential factor (pressure) for estimating the laminar burning velocity	$-$
β	Reduced activation energy	$-$
β_r	Temperature exponent (Arrhenius law)	$-$
χ	Wave number	$1/m$
$\widetilde{\chi}$	Scalar dissipation rate	m^2/s
δ	Proportionality factor for estimating l_δ	$-$
δ_F	Laminar flame thickness based on the temperature profile	m
ϵ	Oxidation layer thickness	$-$
ε	Dissipation rate	m^2/s^3
η	Kolmogorov length scale	m
γ	Probability of finding burning gases	$-$

γ	Conditional probability of finding flamelets in the transient stage of quenching	–
κ	von-Kármán constant	–
κ	Curvature	$1/m$
κ_m, κ_t	Surface strain contributions	$1/s$
λ	Thermal conductivity	$W/(m\,K)$
λ, μ	Set of curvilinear coordinates	–
μ	Dynamic viscosity	$kg/(m\,s)$
μ_t	Dynamic turbulent/eddy viscosity	$kg/(m\,s)$
ν	Kinematic viscosity	m^2/s
ν_t	Kinematic turbulent/eddy viscosity	m^2/s
ω	Angular frequency	$1/s$
$\widetilde{\omega}$	Kinematic restoration	m^2/s
$\dot{\omega}_\alpha$	Chemical source term of species α	$kg/(m^3 s)$
$\dot{\omega}_{max}$	Heat release maximum	$J/(m^3 s)$
π	Heat loss parameter	–
ϕ	Equivalence ratio	–
φ	Normalised wall heat flux	–
ψ	Set of reactive scalars	variable
ψ	Time derivative of the wall heat flux	$W/(m^2 s)$
ρ	Density	kg/m^3
σ_y	Flamelet crossing angle	–
$\overline{\sigma}$	Total flame surface area ratio	–
$\overline{\sigma}_R$	Reactive flame surface area ratio	–
$\overline{\sigma}_t$	Turbulent contribution to the total flame surface area ratio	–
σ	Norm of the G-scalar gradient	–
Σ	Flame surface density	$1/m$
Σ'	Local instantaneous or fine-grained surface to volume ratio	$1/m$
Σ_R	Reactive flame surface density	$1/m$
$\boldsymbol{\tau}$	Viscous stress tensor	$\left[\tau_{ij}\right] = N/m^2$
$\boldsymbol{\tau}_t$	Reynolds stress tensor	$\left[\tau_{t,ij}\right] = N/m^2$
τ	Integral time scale	s
θ	Angle between the propagation direction of the flame front and the wall	–
υ	Turbulent fluctuation velocity normal to the wall	m/s
$\upsilon'_{\alpha r}$	Forward stoichiometric coefficient of reaction r	–
$\upsilon'_{\alpha r}$	Backward stoichiometric coefficient of reaction r	–
ζ	Velocity scales ratio	–

Subscripts

alg	algebraic
b	burned (quantity evaluated in the burned gases)
ini	initial
max	maximum
min	minimum
Q	Quenching (quantity evaluated in the instant of flame quenching)
ref	reference
t	turbulent

Nomenclature

T	Threshold
u	unburned (quantity evaluated in the unburned gases)
W	Wall (quantity evaluated at the wall)

Superscripts

+	wall unit (quantity normalised in wall units)
0	reference conditions (quantity evaluated for specific reference conditions, e.g., a planar flame)

Abbreviations

BML	Bray-Moss-Libby
CA	Crank Angle
CFD	Computational Fluid Dynamics
CFM	Coherent Flame Model
DNS	Direct Numerical Simulation
EBU	Eddy-BreakUp
ECFM-3Z	Extended Coherent Flame Model - 3 Zones
ECU	Engine Control Unit
FE	Finite Element
GFWI	*G*-equation Flame-Wall Interaction
HOQ	Head-On Quenching
HRR	Heat Release Rate
IC	Internal Combustion
IHC	Intermediate HydroCarbon
ILF	Inner Layer Formulation
IMP	Indicated Mean Pressure
LES	Large-Eddy Simulation
MFB	Mass Fraction Burned
MON	Motor Octane Number
MP	Measuring Point
OP	Operating Point
PDF	Probability Density Function
PFI	Port Fuel Injection
PIV	Particle Image Velocimetry
PTV	Particle Tracking Velocimetry
RANS	Reynolds-Averaged Navier-Stokes
RMS	Root-Mean Squared
RON	Research Octane Number
SI	Spark-Ignition
SWQ	Side-Wall Quenching
TDC	Top Dead Center
URANS	Unsteady Reynolds-Averaged Navier-Stokes

1 Introduction

The development of modern internal combustion engines faces several key challenges such as strict emission regulations or further efficiency improvements in addition to meeting the customer demand and the targets regarding development cost and time. As a result of these objectives, complex questions and conflicts arise which have to be appropriately resolved during the design process. In the past, this process was almost exclusively driven by experiments. Due to the exponential increase in computational power, Computational Fluid Dynamics (CFD) took over this leading role, particularly in early development stages. Numerical simulation is now a fast and inexpensive method to study and optimize the design of an engine in a coherent way without having to manufacture costly prototypes. Moreover, additional insight into physical phenomena, which are not or hardly accessible by experiments, can be obtained by simulation contributing to the understanding of the physics within a combustion engine.

To simulate the combustion process in a modern spark-ignition (SI) engine, the physics of chemistry, thermodynamics, fluid mechanics and turbulence as well as their microscopic interaction have to be appropriately reproduced. Although each of these processes is largely understood on its own, their prediction via Direct Numerical Simulation (DNS) is not yet feasible for large-scale industrial applications such as spark-ignition engines and it is questionable if this will ever be a viable option. Reynolds-Averaged Navier-Stokes (RANS) methods are thus expected to remain the backbone of industrial CFD simulations due to their efficiency. The RANS approach only resolves the flow on a macroscopic level and thus requires physical sub-models to describe the microscopic interaction of turbulence and combustion on a macroscopic scale. The vast majority of flows in engineering applications such as IC engines is bounded by walls rendering the treatment of the wall a key factor determining the overall accuracy of the simulation. While an abundant literature on non-reacting flows can be found, few literature on reactive wall-bounded flows is available. Almost all combustion models lack a profound physical description of the flame-wall interaction process and use intuitive approaches to overcome their basic flaws near the wall. Consequently, the predictive capabilities of combustion models are still limited.

The scope of this problem is enhanced by the fact that every SI engine is subjected to flame-wall interactions. The interaction of a premixed flame with the combustion chamber walls substantially influences the wall heat losses, engine-out emissions and the combustion efficiency. Despite its significance, little is known to date on its nature and experimental data is scarce. The main objectives of this thesis are thus to clarify the phenomenology of flame-wall interactions in SI engines and to subsequently develop a comprehensive combustion modelling approach on this basis.

As a starting point, a coherent picture of premixed flame-wall interactions is established based on the available literature. Laminar and turbulent flame-wall interactions as well as

near-wall turbulence are discussed separately to discern the individual contributions of wall heat loss, chemical reactions and turbulence. Based on this a priori analysis, it is suggested that the interaction of a premixed flame with the walls of a SI engine is similar to the one observed for laminar premixed flames.

To prove or disprove this hypothesis, an extensive analysis of flame-wall interactions in a modern direct-injection SI engine is carried out. For this purpose, a highly-resolved measurement of the wall heat flux at the combustion chamber walls is combined with a comprehensive simulative workflow. Several operating points are examined to study the influence of speed, load, equivalence ratio and charge motion on the quenching process. The simulative workflow consists of several 3D-CFD, 3D-FE and 1D simulations in order to accurately predict the flow state as well as the laminar flame properties near the combustion chamber walls. Using this information, the cycle-resolved wall heat fluxes are analysed and the characteristics of the quenching process such as quenching distances are determined. The results are examined in detail and provide new insights into the physics of the quenching process in a SI engine.

Finally, a modelling approach that accounts for the previously identified main effects of flame-wall interactions, flame quenching and near-wall turbulence, is proposed. The aim is to correctly describe the near-wall behaviour of turbulent premixed flames based on a comprehensive theoretical approach. For this purpose, the framework of the G-equation combustion model, which has proven to successfully predict combustion processes in SI engines, is used. A virtue of the G-equation, which is also exploited in this work, is that standard modelling techniques of non-reacting turbulent flows can be applied. Following classic combustion modelling guidelines, a laminar quenched flame and a kinematic equation describing its behaviour is derived. The approach is transferred to turbulent flames by determining the probability of finding quenched flamelets within a turbulent flame brush and its impact on the turbulent burning velocity. The G-equation combustion model is subsequently extended to also describe partially or fully quenched turbulent flames. The impact of near-wall turbulence and flame development on the turbulent burning velocity as well as on the model closures is discussed and appropriate relations are provided. The presented approaches can also be applied to other combustion models, in particular to those that are based on the turbulent burning velocity. The resulting G-equation Flame-Wall Interaction (GFWI) model is subsequently analysed in an a priori fashion and tested against DNS data. Furthermore, it is applied to simulate combustion in SI engines and the impact of flame-wall interaction on the combustion process is studied. Finally, the experimental and simulative results are combined to draw a comprehensive phenomenological picture of flame-wall interactions in SI engines.

This work is divided into seven chapters. In chapter 2, the fundamentals of reactive flows, turbulence and premixed flames are briefly introduced. After presenting the governing equations for chemically reacting flows, the phenomenon of turbulence and its characteristic scales is discussed and the conservation equations are given in their reynolds-averaged form. The closure of the RANS equations is shortly addressed before the fundamentals of premixed combustion are discussed. Particular emphasis is laid on the description of the physics of laminar and turbulent premixed flames. The chapter is concluded by a short overview of the common modelling approaches for turbulent premixed flames.

A detailed analysis of flame-wall interactions based on the available literature is given in chapter 3. At first, laminar flame-wall interactions are examined in detail by focussing on the chemical reactions and the characteristics of the quenching process such as the wall heat flux. The basics of wall-bounded turbulent flows are introduced and turbulent flame-wall interactions are discussed on this basis. Finally, an a priori analysis of flame-wall interactions in SI engines as well as a brief literature review on flame-wall interaction models is presented.

Chapter 4 is devoted to the analysis of flame-wall interactions by a combined experimental and simulative approach. First, the experimental setup and procedure is presented before the measured wall heat fluxes are analysed on a phenomenological basis. The evaluation of the quenching process and the required simulative workflow are described thereafter. Finally, the results of the combined analysis are discussed in detail.

In Chapter 5, the modelling approach is presented. First, the original G-equation model is introduced before the modelling of flame quenching is discussed in detail. Based on the results, a consistent level-set approach for turbulent quenched and unquenched flames is introduced and complemented by modelling closures that take near-wall turbulence and flame development into account. The most important modelling assumptions of the GFWI model are reviewed and the model performance is analysed using a turbulent channel flow and a simple SI engine test case.

The application of the GFWI model to simulate combustion in a direct-injection SI engine is shown in chapter 6. The combustion simulation results are analysed and a summary of the phenomenology of flame-wall interactions in SI engines is provided.

Finally, the main findings of this thesis and possible areas for future work are summarized in chapter 7.

2 Fundamentals of reactive flows, turbulence and premixed flames

The vast majority of flows and combustion processes encountered in engineering problems are turbulent due to their ability to mix transported quantities much more effectively than molecular diffusion processes. However, turbulence is one of the most complex phenomenons encountered in classical physics due to its seemingly erratic and chaotical behaviour. As a consequence, many approaches describing turbulence based on different assumptions have been developed. For this reason, modelling requires an in-depth knowledge of the underlying concepts as well as the related equations. A comprehensive introduction in turbulent flows is out of the scope of this work and can be found in relevant textbooks, e.g., Pope [154]. This chapter is dedicated to introduce the physics of turbulent reactive flows in the context of the Reynolds-Averaged Navier Stokes (RANS) equations with a focus on turbulent premixed flames.

For this purpose, the instantaneous conservation equations for reacting flows are introduced in combination with the necessary constitutive and state relations in section 2.1. Section 2.2 contains a brief introduction to the nature of turbulence and its characteristic scales as well as a presentation of the Reynolds-Averaged Navier Stokes equations. Moreover, classical turbulence closures based on the turbulent-viscosity and gradient-diffusion hypotheses are shown. This chapter is concluded with an introduction to premixed combustion in section 2.3. Special emphasis is laid on the physics of laminar as well as turbulent premixed flames and the related physical concepts. Finally, the most important models for turbulent premixed combustion modelling are presented.

2.1 Governing Equations

The governing equations for turbulent reacting flows are commonly expressed by transport equations for continuity, momentum, species mass fractions and energy as well as constitutive relations for atomistic processes (e.g., diffusion, equation of state). Various forms of these equations, especially of the energy equation, can be found in literature. For a detailed discussion, the reader is referred to the books of Williams [212] and Poinsot and Veynante [150]. The following part focuses on the relations commonly used for turbulent combustion modelling and simulation.

2.1.1 Conservation equations

The instantaneous governing equations of a compressible flow are given by the transport equations for density, momentum, species mass fractions and enthalpy. In their conservative form, these equations read

$$\frac{\partial \rho}{\partial t} + \nabla \cdot (\rho \mathbf{v}) = 0 \tag{2.1}$$

$$\frac{\partial \rho \mathbf{v}}{\partial t} + \nabla \cdot (\rho \mathbf{v} \mathbf{v}) + \nabla p - \nabla \cdot \boldsymbol{\tau} = 0 \tag{2.2}$$

$$\frac{\partial \rho h}{\partial t} + \nabla \cdot (\rho \mathbf{v} h) - \frac{\partial p}{\partial t} - \mathbf{v} \cdot \nabla p + \nabla \cdot \mathbf{q} - \boldsymbol{\tau} : \nabla \mathbf{v} - \dot{Q} = 0 \tag{2.3}$$

$$\frac{\partial \rho Y_\alpha}{\partial t} + \nabla \cdot (\rho \mathbf{v} Y_\alpha) + \nabla \cdot \mathbf{j}_\alpha - \dot{\omega}_\alpha = 0 \tag{2.4}$$

when volume forces are neglected. In the above equations, ρ denotes the density, $\mathbf{v}$ the velocity vector, p the pressure, $\boldsymbol{\tau}$ the viscous stress tensor, h the enthalpy, $\mathbf{q}$ the heat flux vector, $\dot{Q}$ a heat source term, Y_α the mass fraction of species α, $\mathbf{j}_\alpha$ its diffusive flux vector and $\dot{\omega}_\alpha$ its source term. The equations (2.1)-(2.4) are solved for $(\rho, \rho \mathbf{v}, \rho h, \rho \mathbf{Y})$.

As already indicated, there are several different possibilities to formulate the energy equation (Eq. (2.3)). A comprehensive overview can be found in the textbook by Poinsot and Veynante [150]. In the present work, the transport equation for the enthalpy h is utilized. Therein, h is the sum of the specific enthalpy h_α of each species α defined by

$$h_\alpha = h^0_{f,\alpha} + \int_{T_{ref}}^{T} c_{p,\alpha} dT. \tag{2.5}$$

In this equation, $h^0_{f,\alpha}$ denotes the standard enthalpy of formation at a specific reference temperature T_{ref} (usually 298.15K) and $c_{p,\alpha}$ the specific heat capacity at constant pressure. Hence, h can be written as

$$h = \sum_{i=1}^{N} h_\alpha Y_\alpha = \int_{T_{ref}}^{T} c_p dT + \sum_{\alpha=1}^{N} h^0_{f,\alpha} Y_\alpha \quad \text{where} \quad c_p = \sum_{i=1}^{N} c_{p,\alpha} Y_\alpha \tag{2.6}$$

is the specific heat capacity at constant pressure of the mixture. Since h is composed of the sensible and chemical enthalpy, there is no source term due to reaction in the energy equation (Eq. (2.3)).

2.1.2 Constitutive and state equations, transport properties

To complete this set of equations, constitutive and state equations as well as relations for the transport properties are required. These relations introduce atomistic processes and relate them to the continuous quantities $(\rho, \mathbf{v}, h, \mathbf{Y})$. Commonly, turbulent reacting flows are treated as a Newtonian fluid and as an ideal gas. Hence, the thermal equation of state relating the density ρ, the pressure p and the temperature T is given by

$$p = \rho R T \tag{2.7}$$

where R is the gas constant. It can be calculated for a given composition by utilizing the mean molar mass M of the mixture or the molar masses M_α in combination with the species mass fractions Y_α:

$$R = \frac{\mathcal{R}}{M} = \mathcal{R} \sum_{\alpha=1}^{N} \frac{Y_\alpha}{M_\alpha}. \qquad (2.8)$$

The universal gas constant is represented by $\mathcal{R}$. Using Stokes' hypothesis, the constitutive relation for the viscous stress tensor $\boldsymbol{\tau}$ of a Newtonian fluid is defined by

$$\boldsymbol{\tau} = \mu \left[(\nabla \mathbf{v}) + (\nabla \mathbf{v})^T \right] - \frac{2}{3} \mu \left(\nabla \cdot \mathbf{v} \right) \mathbf{I}. \qquad (2.9)$$

Here, $\mathbf{I}$ denotes the unit tensor and μ the dynamic viscosity of the mixture.

In addition to these relations, the transport processes defining the flux vectors $\mathbf{j}_\alpha$ and $\mathbf{q}$ have to be appropriately determined. According to Hirschfelder et al. [91], the heat flux vector $\mathbf{q}$ consists of three individual contributions from different modes of heat transfer. These are heat conduction, heat diffusion by species diffusion and thermal diffusion (Dufour effect). The latter is negligible for almost any combustion process (Gerlinger [76]). Using the Fourier's law for heat conduction, the heat flux vector $\mathbf{q}$ reads

$$\mathbf{q} = -\lambda \nabla T + \sum_{i=1} h_\alpha \, \mathbf{j}_\alpha \qquad (2.10)$$

where λ represents the thermal conductivity. Similar to the heat flux vector $\mathbf{q}$, the diffusive flux vector $\mathbf{j}_\alpha$ can also be decomposed in different parts, namely diffusion by concentration gradients (Fickian diffusion), thermal diffusion (Soret effect) and pressure diffusion. The latter does have a negligible role compared to the former ones, since the spatial pressure gradients are usually small. The Soret-effect becomes important for light species or large temperature gradients (e.g., for laminar hydrogen-air flames) and is negligible for turbulent flames (cf. Gerlinger [76]). As a result, the diffusive flux can commonly be modelled by the binary flux approximation (Peters [142]):

$$\mathbf{j}_\alpha = -\rho D_\alpha \nabla Y_\alpha = -\frac{\mu}{Sc_\alpha} \nabla Y_\alpha \qquad \text{with} \qquad Sc_\alpha = \frac{\nu}{D_\alpha}. \qquad (2.11)$$

Therein, D_α denotes the binary diffusion coefficient of species α with respect to an abundant species like N_2. The Schmidt number Sc_α compares the momentum and molecular diffusion of species α. However, this approximation violates the mass conservation in a multicomponent system for unequal diffusion coefficients D_α. For simplicity, it is thus assumed that all mass diffusivities D_α are equal and proportional to the thermal diffusivity $D = \lambda/\rho c_p$ yielding constant Lewis numbers,

$$Le_\alpha = \frac{\lambda}{\rho c_p D_\alpha} = \frac{D}{D_\alpha}. \qquad (2.12)$$

These relations can be used to simplify the heat flux vector $\mathbf{q}$. By spatially differentiating the definition of the enthalpy h and inserting the result in Eq. (2.10), one arrives at

$$\mathbf{q} = -\frac{\mu}{Pr} \nabla h + \sum_{\alpha=1} h_\alpha \left(\frac{\mu}{Pr} - \frac{\mu}{Sc_\alpha} \right) \nabla Y_\alpha \qquad (2.13)$$

where the Prandtl number
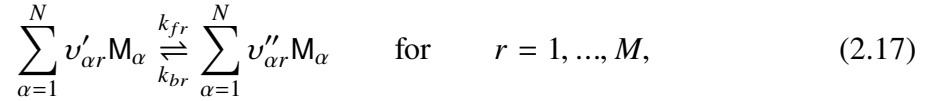
$$Pr = \frac{\mu c_p}{\lambda} \qquad (2.14)$$

was introduced (Gerlinger [76]). A common assumption for turbulent flows is a unity Lewis number, i.e., $Le_\alpha = Sc_\alpha/Pr = 1$. Hence, Eq. (2.13) can be further simplified and the relations for the diffusive and heat flux read

$$\mathbf{j}_\alpha = -\frac{\mu}{Sc_\alpha}\nabla Y_\alpha \,, \qquad (2.15)$$

$$\mathbf{q} = -\frac{\mu}{Pr}\nabla h \,. \qquad (2.16)$$

A more detailed discussion of transport processes can be found in Bird et al. [20] and Hirschfelder et al. [91].

The last remaining term which has to be suitably determined is the chemical source term. The chemistry is commonly described by a collection of elementary reactions comprising multiple transition states and intermediate species. Due to the complexity and nonlinearity of combustion, considerable effort was put into the research and development of suitable reaction mechanisms (Westbrook et al. [209]). For example, reaction mechanisms which accurately describe the behaviour of long-chain hydrocarbons can consist of several hundred species and thousands of reactions (cf. Cai et al. [32]). The general notation of a reaction mechanism comprising M (single step) reactions and N species reads

$$\sum_{\alpha=1}^{N} \upsilon'_{\alpha r}\mathsf{M}_\alpha \underset{k_{br}}{\overset{k_{fr}}{\rightleftharpoons}} \sum_{\alpha=1}^{N} \upsilon''_{\alpha r}\mathsf{M}_\alpha \qquad \text{for} \qquad r = 1, ..., M, \qquad (2.17)$$

where M_α is the chemical symbol for species α and $\upsilon'_{\alpha r}$ and $\upsilon''_{\alpha r}$ are the stoichiometric coefficients of reaction r in forward and backward direction, respectively. Correspondingly, k_{fr} and k_{br} are the reaction rate coefficients of the forward respectively backward reaction. For each reaction, a reaction rate $\dot{w}_r$ can be defined

$$\dot{w}_r = k_{fr}\prod_{\beta=1}^{N}\left(\frac{\rho Y_\beta}{M_\beta}\right)^{\upsilon'_{\beta r}} - k_{br}\prod_{\beta=1}^{N}\left(\frac{\rho Y_\beta}{M_\beta}\right)^{\upsilon''_{\beta r}} \qquad (2.18)$$

The reaction rate coefficients k_{fr} and k_{br} comprise statistical information about the rate of collisions, the fraction of collisions resulting in a reaction and a factor taking the shape of the molecules into account. They are commonly modelled by the empirical Arrhenius equation

$$k_r(T) = A_r T^{\beta_r}\exp\left(-\frac{E_r}{\mathcal{R}T}\right) \qquad (2.19)$$

where A_r is a frequency factor, β_r the temperature exponent and E_r the activation energy. The main challenge of chemical kinetics lies in providing these values as well as determining the most important reactions and species to keep the reaction mechanism as lean as possible (Warnatz et al. [203]). The reaction rate $\dot{\omega}_\alpha$ of each species α can then be determined by addition of all relevant reaction rates $\dot{w}_r$

$$\dot{\omega}_\alpha = M_\alpha \sum_{r=1}^{M}\left(\upsilon''_{\alpha r} - \upsilon'_{\alpha r}\right)\dot{w}_r \,. \qquad (2.20)$$

2.2 Turbulence

Turbulence is a three-dimensional and unsteady phenomenon where the fluid velocity varies seemingly chaotic in space and time. A common feature of all turbulent flows is the existence of a multitude of eddies of different sizes. These eddies enhance diffusion and mixing processes which are essential for a large range of applications including internal combustion engines. For a comprehensive introduction and discussion of turbulent flows and its manifold aspects, the reader is referred to the textbook of Pope [154]. The following discussion focuses on homogeneous, isotropic turbulence. In general, turbulence in near-wall flows is anisotropic. This circumstance plays an important role during flame-wall interactions and is discussed separately in chapter 3.

2.2.1 Scales of turbulent motion

Flows become turbulent when the convective forces are large compared to the viscous forces. In this case, small disturbances (e.g., the roughness of a wall) can lead to a transition from a laminar to a turbulent flow. Unstable eddies are formed which continuously break-up and induce smaller eddies. This process continues until the kinetic energy of the eddies is finally dissipated at the turbulent dissipation rate ε due to the viscous forces. The idea of a steady transfer of kinetic energy from large to small scales until its viscous dissipation was first proposed by Kolmogorov [103] and is called the eddy cascade hypothesis.
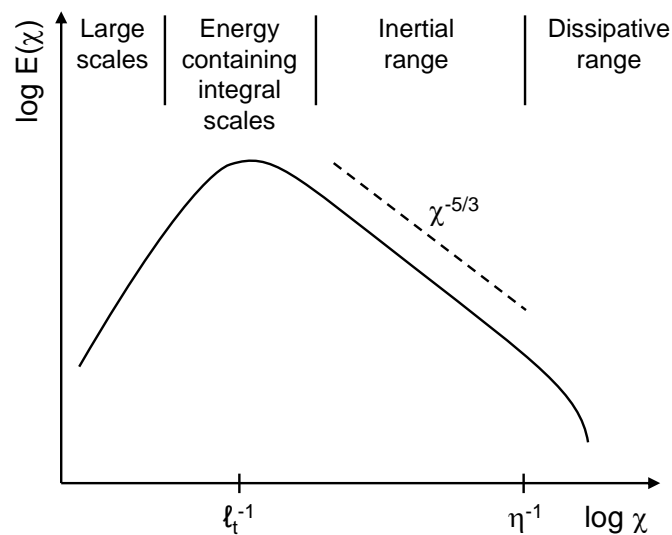

Figure 2.1: Energy spectrum of homogeneous, isotropic turbulence (adapted from Peters [142]).

The resulting energy spectrum $E(\chi)$ of homogeneous, isotropic turbulence is shown in Fig. 2.1. Small eddies are associated to large spatial wave numbers χ and vice versa. The turbulent kinetic energy k of eddy motion defined by the trace of the Reynolds stress tensor

can be related to the energy spectrum as follows

$$k = \frac{1}{2}\overline{\mathbf{v}' \cdot \mathbf{v}'} = \int_0^\infty E(\chi)d\chi, \tag{2.21}$$

where $\mathbf{v}'$ is the fluctuation of the velocity. The eddy motion in a turbulent flow can be characterized by distinctive length scales and turnover times. Based upon the similarity analysis by Kolmogorov [103], the turbulent energy spectrum is usually subdivided in four different ranges. The first range depends on the boundary conditions of the flow and is thus not universal. It comprises the largest eddies which are of the size of the mean flow scales.

The second range contains the integral scale eddies which comprise most of the energy of the turbulent flow. Moreover, the production of turbulence by mean velocity gradients also peaks in this region. There are various definitions and approximations of the integral length scale, however, all are proportional to

$$\ell_t = \frac{k^{3/2}}{\varepsilon}. \tag{2.22}$$

Bray [27] defined the turbulent length scale as

$$l_t = a_1 \frac{v'^3}{\varepsilon} \qquad \text{with} \qquad a_1 = 0.37. \tag{2.23}$$

Another definition originates from the law of the wall in combination with k-ε-turbulence models. By assuming a local balance between the production and dissipation of turbulent kinetic energy in the logarithmic law region, the mixing length l_m is related to k and ε by

$$l_m = \kappa y = c_\mu^{3/4} \frac{k^{3/2}}{\varepsilon} \qquad \text{with} \qquad c_\mu = 0.09. \tag{2.24}$$

Here, $\kappa \approx 0.41$ denotes the von-Kármán constant and y the wall distance. The expressions l_t and l_m for the integral length scale differ in magnitude by around 20% (Ewald [66]). An important quantity for combustion modelling is the turnover velocity of integral size eddies v' defined as

$$v' = \sqrt{\frac{2}{3}k}, \tag{2.25}$$

often referred to as turbulence intensity denoted by either u' or v'. The turnover time of the energy containing eddies is called the integral time scale and is defined as

$$\tau = \frac{k}{\varepsilon}. \tag{2.26}$$

The third range, called inertial range, is characterized by a steady energy transfer towards the smaller scales. Therein, production and dissipation of turbulence is negligible. Using dimensional analysis, it can be shown that the energy spectrum obeys the scaling law

$$E(\chi) \sim \varepsilon^{2/3}\chi^{-5/3}. \tag{2.27}$$

Furthermore, the turbulent turnover velocity v'_n of eddies of size l_n within the inertial subrange is given by

$$v'_n \approx (\varepsilon l_n)^{1/3} = v \left(\frac{l_n}{l_t} \right)^{1/3}. \tag{2.28}$$

Similar approximations can be found for the length and time scales (cf. Pope [154]).

In the fourth range, called dissipative range, the kinetic energy is eventually dissipated to thermal energy by viscous forces. The characteristic length scale η, called Kolmogorov length scale, can be defined based upon a dimensional analysis as

$$\eta = \left(\frac{\nu^3}{\varepsilon} \right)^{1/4}. \tag{2.29}$$

It is considered to be the smallest spatial scale of turbulence. The corresponding turnover velocity v_η and time t_η are defined as

$$v_\eta = (\nu \varepsilon)^{1/4} \qquad \text{and} \qquad t_\eta = \sqrt{\frac{\nu}{\varepsilon}}. \tag{2.30}$$

Using the turbulent Reynolds number,

$$Re_t = \frac{v' \ell_t}{\nu}, \tag{2.31}$$

the ratio between the Kolmogorov and the integral scales can be determined (Pope [154]),

$$\frac{\eta}{\ell_t} \sim Re_t^{-3/4} \qquad , \qquad \frac{v_\eta}{v'} \sim Re_t^{-1/4} \qquad , \qquad \frac{t_\eta}{\tau} \sim Re_t^{-1/2}. \tag{2.32}$$

As the Reynolds number of turbulent flows is usually large, turbulence exhibits a vast range of time and length scales. To solve equations (2.1)-(2.4), all these scales have to be resolved. DNS therefore requires sufficiently fine computational meshes and small time steps. As a consequence, it is only feasible for simple geometries and moderate Reynolds numbers and less suited for engineering problems at high Reynolds numbers.

The computational effort can be drastically reduced by solving the Reynolds-Averaged Navier-Stokes equations which describe the flow on integral time and length scales. The unsteady turbulent motions are not resolved and its effects have to be completely modelled leading to a high modelling complexity and effort. A trade-off between the computational effort of DNS and the modelling complexity of RANS methods are large-eddy simulations (LES). LES methods resolve the large-scale, energy-carrying motions, whereas the small scales still have to be modelled. Despite the emergence of new methods, it is expected that the RANS approach will remain prevalent in the industry (Drake et al. [53], Pope [155]).

2.2.2 Reynolds-Averaged Navier-Stokes Equations

In order to derive the Reynolds-Averaged Navier-Stokes equations, an averaging scheme has to be introduced which separates the unresolved small scale from the resolved large scale motions. Any quantity f can be split into its average $\overline{f}$ and its fluctuation f', such that

$$f = \overline{f} + f' \qquad \text{with} \qquad \overline{f'} = 0. \tag{2.33}$$

This approach is called Reynolds decomposition and is attributed to Reynolds [161]. The average $\overline{f}$ can either be calculated by time-averaging for statistically stationary flows or by ensemble averaging for unsteady flows. The ensemble average is calculated by averaging the individual measurements f_k, $k = 1, 2, ..., n$ of a quantity f over n realisations of the turbulent flow,

$$\overline{f}(\mathbf{x}, t) = \frac{1}{n} \sum_{k=1}^{n} f_k(\mathbf{x}, t). \tag{2.34}$$

For flows exhibiting large density variations, e.g., due to combustion, the density-weighted or Favre average

$$\widetilde{f} = \frac{\overline{\rho f}}{\overline{\rho}} \tag{2.35}$$

is preferred as unclosed correlations related to density fluctuations such as $\overline{\rho' u'}$ can be avoided resulting in a substantial simplification of the averaged equations. Correspondingly, each quantity f is split into $\widetilde{f}$ and f'',

$$f = \widetilde{f} + f'' \qquad \text{whereby} \qquad \widetilde{f''} = 0. \tag{2.36}$$

However, the comparability of Favre-averaged simulations with experiments commonly providing Reynolds-averaged results can be problematic (Poinsot and Veynante [150]). The application of density-weighted ensemble averaging to the governing equations (2.1)-(2.4) yields the Reynolds-Averaged Navier Stokes equations for reactive flows:

$$\frac{\partial \overline{\rho}}{\partial t} + \nabla \cdot (\overline{\rho} \widetilde{\mathbf{v}}) = 0 \tag{2.37}$$

$$\frac{\partial \overline{\rho} \widetilde{\mathbf{v}}}{\partial t} + \nabla \cdot (\overline{\rho} \widetilde{\mathbf{v}} \widetilde{\mathbf{v}}) + \nabla \overline{p} - \nabla \cdot \overline{\boldsymbol{\tau}} + \nabla \cdot \left(\overline{\rho \widetilde{\mathbf{v}'' \mathbf{v}''}} \right) = 0 \tag{2.38}$$

$$\frac{\partial \overline{\rho} \widetilde{h}}{\partial t} + \nabla \cdot \left(\overline{\rho} \widetilde{\mathbf{v}} \widetilde{h} \right) - \frac{\partial \overline{p}}{\partial t} - \widetilde{\mathbf{v}} \cdot \nabla \overline{p} - \nabla \cdot \left(\frac{\mu}{Pr} \nabla \widetilde{h} \right) + \nabla \cdot \left(\overline{\rho \widetilde{\mathbf{v}'' h''}} \right) - \overline{\boldsymbol{\tau} : \nabla \mathbf{v}} - \overline{\dot{Q}} = 0 \tag{2.39}$$

$$\frac{\partial \overline{\rho} \widetilde{Y}_\alpha}{\partial t} + \nabla \cdot \left(\overline{\rho} \widetilde{\mathbf{v}} \widetilde{Y}_\alpha \right) + \nabla \cdot \left(\overline{\rho \widetilde{\mathbf{v}'' Y_\alpha''}} \right) - \nabla \cdot \left(\frac{\mu}{Sc_\alpha} \nabla \widetilde{Y}_\alpha \right) - \overline{\dot{\omega}}_\alpha = 0 \tag{2.40}$$

The enthalpy equation (Eq. (2.39)) has already been simplified by neglecting the pressure-velocity correlation $\overline{\mathbf{v}'' \cdot \nabla p'} \approx 0$ as done in most RANS codes (Poinsot and Veynante [150]). Furthermore, the averaged enthalpy and species fluxes have been approximated as $\overline{\mu/Pr \nabla h} = \mu/Pr \nabla \widetilde{h}$ and $\overline{\mu/Sc_\alpha \nabla Y_\alpha} = \mu/Sc_\alpha \nabla \widetilde{Y}_\alpha$, respectively (Gerlinger [76]). The averaged equation of state (Eq. (2.7)) reads

$$\overline{p} = \overline{\rho} \widetilde{R} \widetilde{T}, \tag{2.41}$$

where $\widetilde{R}$ is calculated using Eq. (2.8) and replacing Y_α with $\widetilde{Y}_\alpha$.

The system of equations (2.37)-(2.40) contains unclosed second-moment terms which have to be modelled. The Reynolds stress tensor $\overline{\rho \widetilde{\mathbf{v}'' \mathbf{v}''}}$ appearing in the averaged momentum equation (Eq. (2.38)) represents the classic closure problem of RANS methods addressed by turbulence models. It causes an additional convective momentum transfer due to turbulent fluctuations. In a similar manner, the turbulent transport terms $\overline{\rho \widetilde{\mathbf{v}'' h''}}$ and $\overline{\rho \widetilde{\mathbf{v}'' Y_\alpha''}}$ enhance

the convective enthalpy and species transport, respectively. The most important modelling strategies for the turbulent transport terms as well as the Reynolds stress tensor are discussed in the following section.

The remaining unclosed terms are the mean chemical reaction rates $\bar{\dot{\omega}}_\alpha$. They pose a major challenge to modelling since they cannot be simply stated as a function of mean values. The main reason for this is the exponential character of the Arrhenius law (Eq. (2.19)) causing considerably enhanced fluctuations of the chemical source term when subjected to temperature fluctuations (Gerlinger [76]). Providing an appropriate closure for $\bar{\dot{\omega}}_\alpha$ is the objective of combustion modelling. The most important modelling strategies for premixed combustion are introduced in section 2.3.3.

2.2.3 Turbulence modelling

The closure of the unclosed Reynolds stresses $\widetilde{\rho \mathbf{v}'' \mathbf{v}''}$ as well as the turbulent fluxes $\overline{\rho \mathbf{v}'' h''}$ and $\overline{\rho \mathbf{v}'' Y_\alpha''}$ received considerable attention in turbulence research. In the following, a short overview of common modelling strategies is given.

Turbulence models

In the context of RANS methods, the most important approaches are turbulent-viscosity and Reynolds-stress models. The former models introduce a turbulent viscosity related to turbulence quantities like k or ε to provide an algebraic relation for the Reynolds stresses in analogy to the viscous stress tensor (Eq. (2.9)). The latter explicitly solve transport equations for each component $\widetilde{v_i'' v_j''}$, $i = 1, 2, 3$, $j = 1, 2, 3$ of the Reynolds stress tensor. For complex flows, Reynolds-stress models are usually superior to turbulent-viscosity models, however, they are computationally more demanding and contain third-moment correlations which require additional modelling (Pope [154]). Hence, turbulent-viscosity models are the de-facto standard in most commercial CFD codes and presented in the following. An in-depth description and discussion of turbulence modelling can be found in the textbook by Pope [154].

All turbulent-viscosity models utilize the so-called turbulent-viscosity hypothesis

$$\boldsymbol{\tau}_t = -\overline{\rho \widetilde{\mathbf{v}'' \mathbf{v}''}} = \mu_t \left[(\nabla \widetilde{\mathbf{v}}) + (\nabla \widetilde{\mathbf{v}})^T - \frac{2}{3} (\nabla \cdot \widetilde{\mathbf{v}}) \, \mathbf{I} \right] - \frac{2}{3} \overline{\rho} k \mathbf{I} \qquad (2.42)$$

which was first proposed by Boussinesq. The basic idea is that all turbulent transport processes can be modelled in analogy to molecular transport processes. The turbulent or eddy viscosity μ_t is solely a property of the flow field in contrast to μ, which is determined by the state of the gas mixture. In general, the kinematic eddy viscosity ν_t is generally specified by a product of an appropriate velocity u^* and length scale l^*,

$$\nu_t = \frac{\mu_t}{\overline{\rho}} = u^* \times l^*. \qquad (2.43)$$

The determination of these scales and thereby of the kinematic turbulent viscosity ν_t is the main task of turbulent-viscosity models. The models can be classified according to the

number of additional transport equations which have to be solved. Zero-equation, such as the mixing length model by Prandtl [160], and one-equation closures usually require the specification of a turbulent length scale which restricts their applicability to complex flows. As a consequence, two-equation models are prevailing due to the fact that no such flow-dependent relations are necessary (Pope [154]). The most prominent two-equation model is the k-ε-model, which is incorporated in most commercial CFD codes. The original model was first proposed by Jones and Launder [98] and specifies the turbulent viscosity by

$$v_t = u^* l^* = c_\mu \frac{k^2}{\varepsilon} \qquad \text{with} \qquad u^* = k^{1/2} \qquad \text{and} \qquad l^* = \frac{k^{3/2}}{\varepsilon}. \qquad (2.44)$$

The transport equations for k and ε read

$$\frac{\partial \overline{\rho} k}{\partial t} + \nabla \cdot (\overline{\rho} \widetilde{v} k) = \nabla \cdot \left[\left(\mu + \frac{\mu_t}{Sc_{t,k}} \right) \nabla k \right] + \tau_t : \nabla \widetilde{v} - \overline{\rho} \varepsilon \qquad (2.45)$$

and

$$\frac{\partial \overline{\rho} \varepsilon}{\partial t} + \nabla \cdot (\overline{\rho} \widetilde{v} \varepsilon) = \nabla \cdot \left[\left(\mu + \frac{\mu_t}{Sc_{t,\varepsilon}} \right) \nabla \varepsilon \right] + \frac{c_{\varepsilon_1} \tau_t : \nabla \widetilde{v} - c_{\varepsilon_2} \overline{\rho} \varepsilon}{\tau}. \qquad (2.46)$$

where $\tau = k/\varepsilon$ is the turbulent time scale defined according to Eq. (2.26). The standard modeling constants can be found in Table 2.1. Various other two-equation models have been proposed and most of them also use k as one of the two variables. A well-known example is the k-ω-model, which was developed by Wilcox and others (cf. Wilcox [211]).

A drawback of the standard k-ε model is the fact that it fails to accurately reproduce the turbulent viscosity near a solid wall. As a consequence, it requires the definition of a damping function f_μ,

$$v_t = f_\mu c_\mu \frac{k^2}{\varepsilon}. \qquad (2.47)$$

For example, Rodi and Mansour [165] proposed the empirical correlation

$$f_\mu = 1 - \exp(-0.0002 y^+ - 0.00065 y^{2+}) \qquad (2.48)$$

based on DNS data. However, the damping function merely compensates the incorrect physics of the base model and is devoid of a physical justification (Pope [154]).

To circumvent these problems, Durbin [57] proposed an elliptic-relaxation model solving an additional transport equation for $\overline{v^2}$, where v can be interpreted as a turbulent fluctuation velocity normal to the wall. The k-ε-$\overline{v^2}$ was applied successfully to a number of complex flows (e.g., Durbin [58]), however, it is computationally sensitive to the near-wall grid. A robust version of the model, called the k-ζ-f-model, was proposed by Hanjalić et al. [85], which solves a transport equation for the velocity scales ratio $\zeta = \overline{v^2}/k$ rather than $\overline{v^2}$. In this case, the turbulent viscosity is given by

$$v_t = c_\mu \zeta k \tau \overset{\tau = k/\varepsilon}{=} c_\mu \zeta \frac{k^2}{\varepsilon}. \qquad (2.49)$$

In addition to the transport equations for k (Eq. (2.45)) and ε (Eq. (2.46)), a balance equation for ζ is solved

$$\frac{\partial \overline{\rho} \zeta}{\partial t} + \nabla \cdot (\overline{\rho} \widetilde{\mathbf{v}} \zeta) = \nabla \cdot \left[\left(\mu + \frac{\mu_t}{Sc_{t,\zeta}} \right) \nabla \zeta \right] + \overline{\rho} f - \frac{\zeta}{k} \boldsymbol{\tau}_t : \nabla \widetilde{\mathbf{v}} \tag{2.50}$$

where f is given by the elliptic differential equation

$$\ell^2 \nabla^2 f - f = \frac{1}{\tau} \left(c_1 + c_2 \frac{\boldsymbol{\tau}_t : \nabla \widetilde{\mathbf{v}}}{\varepsilon} \right) \left(\zeta - \frac{2}{3} \right) \tag{2.51}$$

The model can be completed by specifying the appropriate turbulent length and time scales. As a lower bound, the Kolmogorov scales are chosen whereas the integral scales constitute the upper bound. Combined with Durbin's realizability constraints [59], these scales read

$$\ell = c_L \max \left[\min \left(\frac{k^{3/2}}{\varepsilon}, \frac{k^{1/2}}{\sqrt{6} c_\mu |\boldsymbol{S}| \zeta} \right), c_\eta \left(\frac{\nu^3}{\varepsilon} \right)^{1/4} \right] \tag{2.52}$$

$$\tau = \max \left[\min \left(\frac{k}{\varepsilon}, \frac{a}{\sqrt{6} c_\mu |\boldsymbol{S}| \zeta} \right), c_\tau \left(\frac{\nu}{\varepsilon} \right)^{1/2} \right] \tag{2.53}$$

where $|\boldsymbol{S}| = |(\nabla \mathbf{v} + \nabla \mathbf{v}^T)/2|$ is the Frobenius norm of the strain rate tensor $\boldsymbol{S}$ and a a constant satisfying $a \leq 1$ (recommended $a = 0.6$). The k-ζ-f-model can be seen as a three-equation model. A similar model was proposed by Laurence et al. [109]. The modelling constants as proposed by Hanjalić et al. [85] can be found in Table 2.1.

Table 2.1: Modelling constants of the k-ε and k-ζ-f turbulence model.

	c_μ	c_{ε_1}	c_{ε_2}	c_1	c_2	$Sc_{t,k}$	$Sc_{t,\varepsilon}$	$Sc_{t,\zeta}$	c_τ	c_L	c_η
k-ε	0.09	1.44	1.92	-	-	1.0	1.3	-	-	-	-
k-ζ-f	0.22	$1.4(1 + 0.012/\zeta)$	1.9	0.4	0.65	1.0	1.3	1.2	6.0	0.36	85

In order to conclude this section, a few limitations shall be remarked. As noted by Gerlinger [76] and Poinsot and Veynante [150], most of the turbulence models are developed for non-reacting, constant-density flows questioning of their validity within reacting flows. Moreover, the parameters given in Table 2.1 are calibrated based on canonic turbulent flows such as a plane channel flow or a round impinging jet. Their applicability to unsteady in-cylinder or bluff body flows without modification of the parameters is questionable. Nevertheless, RANS models are able to predict a variety of flows with reasonable results and a relatively low computational effort.

Turbulent scalar fluxes

The turbulent scalar fluxes $\widetilde{\overline{\rho} \mathbf{v}'' h''}$ and $\widetilde{\overline{\rho} \mathbf{v}'' Y_\alpha''}$ are commonly closed in a similar way as the Reynolds stresses by assuming an analogy between turbulent and molecular transport

processes. The application of the gradient-diffusion hypothesis yields

$$\overline{\rho \widetilde{\mathbf{v}'' h''}} = -\frac{\mu_t}{Pr_t} \nabla \widetilde{h} \tag{2.54}$$

and

$$\overline{\rho \widetilde{\mathbf{v}'' Y_\alpha''}} = -\frac{\mu_t}{Sc_t} \nabla \widetilde{Y}_\alpha. \tag{2.55}$$

The values for the turbulent Schmidt number Sc_t and the turbulent Prandtl number Pr_t may vary between 0.25-1.0 and 0.5-1.0, respectively. Commonly, they are assumed to be equal and chosen between 0.7-1.0 (Gerlinger [76]). The gradient-diffusion hypothesis is widely adopted despite some known issues.

The assumption that the scalar flux vector aligns with the gradient of the mean scalar can be violated, even in simple configurations (cf. Tavoularis and Corrsin [185]). Analogous to Reynolds-stress models, a transport equation for each individual component $\overline{\rho \widetilde{\mathbf{v}'_i h''}}$ respectively $\overline{\rho \widetilde{\mathbf{v}'_i Y_\alpha''}}$ can be derived in order to improve the prediction of the scalar fluxes. However, additional modelling is required and the solution of these equations is computationally expensive, especially for numerous species. For this reason, algebraic models for a tensorial turbulent diffusivity have been proposed as an alternative (e.g., Abe et al. [3], Philips et al. [145]).

Reactive scalars may even exhibit counter-gradient diffusion (Poinsot and Veynante [150]). The phenomenon is encountered in premixed flames (cf. Libby et al. [110]) and constitutes a classic problem of turbulent premixed combustion modelling (cf. Veynante et al. [196], Rutland and Cant [167]).

2.3 Premixed Combustion

Combustion processes can be subdivided depending on the flow conditions and the mixing state of the reactants. The characteristic feature of premixed combustion is that fuel and oxidizer are mixed on a molecular level before the combustion process is initiated. After ignition, the combustion proceeds in the form of a propagating flame front. During non-premixed combustion, on the other hand, mixing and combustion occurs simultaneously. In any case, the combustion process can be influenced by the flow field which is either laminar or turbulent. Turbulent combustion is a two-way coupling process between chemistry and turbulence. The on-going reactions influence the flow by large density and viscosity changes inducing flow acceleration and an increased dampening of turbulent fluctuations. The chemistry, which comprises a large number of reactions with different time scales, is in turn affected by the turbulent scales in the inertial range. Theoretically, all these scales interact with each other. However, as discussed by Peters [136], the chemical reactions usually occur in thin layers smaller than the Kolmogorov scale. Hence, the scales of combustion and turbulence are decoupled. This scale separation is a key feature of many practical combustion applications and used in almost all turbulent combustion models either explicitly or implicitly. The concept that chemical reactions occur in thin reactive layers which are embedded in an otherwise non-reacting turbulent flow field is also called the flamelet hypothesis. Concerning

turbulent premixed combustion, flamelets can be seen as an ensemble of laminar premixed flames.

Based on this discussion, this chapter shortly presents the fundamentals of premixed laminar and turbulent flame propagation as well as the most common modelling approaches.

2.3.1 Laminar premixed flames

Before studying turbulent premixed flames, it is necessary to understand the physics of laminar flame propagation due to the fact that almost any premixed combustion model is based upon the flamelet hypothesis. In the following, the inner structure and characteristic scales of one-dimensional laminar flames are discussed to provide a description of the physical processes within a flame. This section is concluded by a short introduction in the mechanisms of flame extinction as they are helpful to understand certain aspects of flame-wall interactions.

Physics of laminar premixed flames

The structure of a premixed flame is determined by the underlying chemical kinetics as well as by the thermodynamic properties and the transport characteristics of the mixture. In general, laminar flames are described by the Navier-Stokes equations for reactive flows (Eq. (2.1))-(Eq. (2.4)). For complex chemistry and multicomponent transport, this system of equations can only be solved by numerical methods. For this purpose, specialized computer programs, such as Cantera or Chemkin, are readily available which usually compute a one-dimensional, steady and planar laminar flame. A comprehensive overview concerning the simulation of laminar flames was given by Smooke [178].

Analytical solutions can only be obtained by simplifying the chemistry as well as the transport processes. The theoretical study of laminar flames employing asymptotic analysis proved to be extremely useful to understand the basic controlling mechanisms of a flame. The starting point is a planar, steady and one-dimensional flame. In this case, the mass flow rate through the flame is constant and yields sensible definitions of the laminar burning velocities $s_{L,u}^0$ and $s_{L,b}^0$ with respect to the unburned and burned gas, respectively,

$$(\rho u) = \text{const.} = (\rho s_L^0) = \rho_u s_{L,u}^0 = \rho_b s_{L,b}^0. \tag{2.56}$$

The expression (ρs_L^0) is usually referred to as mass burning rate. For convenience, the laminar burning velocity will be denoted with respect to the unburned gas in the following, i.e., $s_L^0 \equiv s_{L,u}^0$.

The first asymptotic analysis was conducted by Zeldovich and Frank-Kamenetzki [217] using an irreversible one-step reaction. A more elaborate analysis of the laminar flame structure of methane-air flames was conducted by Peters and Williams [144] using a four-step reaction mechanism. The resulting schematic structure of the flame is shown in Fig. 2.2 and exhibits three characteristic regions, namely the preheat zone, the inner layer and the oxidation layer. The coordinate normal to the flame front x is normalized by the laminar flame thickness l_F. The preheat zone, which is also found by a one-step asymptotic analysis, is chemically inert and characterized by a balance between convection and diffusion. Its
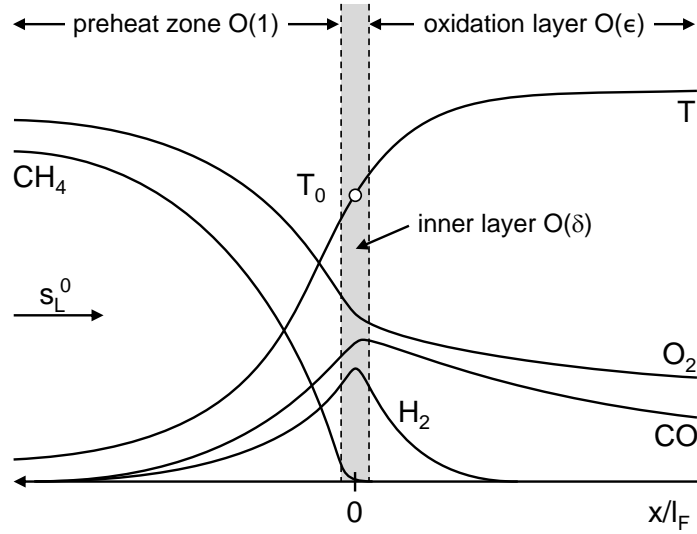
Figure 2.2: Schematic illustration of the inner structure of a laminar premixed flame obtained by a four-step kinetic mechanism (adapted from Peters [140]).

thickness of $O(1)$ is therefore mainly determined by molecular transport processes. Thermal energy is conveyed from the inner layer to the preheat zone leading to the flame propagation towards the unburned mixture. The primary heat release occurs in the inner layer of size $O(\delta)$, where a balance between reaction and diffusion exists. The fuel is completely consumed and the intermediate species CO and H_2 are formed. A characteristic feature of the inner layer is the inner layer temperature T_0, which corresponds to the cross-over temperature between chain-branching and chain-terminating reactions (cf. Peters [140]). Combustion can only proceed as long as the inner layer remains intact. An enhanced transport of thermal energy or radicals out of the inner layer may lead to flame extinction. The inner layer is followed by the oxidation layer of size $O(\epsilon)$, in which the major intermediate species are oxidized to CO_2 and H_2O. A similar structure is found for all hydrocarbons (cf. Pitsch et al. [147], Seshadri et al. [176]).

Each of these regions is defined by a characteristic length scale. The overall size of the flame structure, the laminar flame thickness l_F, can be approximated by the size of the preheat zone commonly defined by

$$l_F = \frac{D}{s_L^0} = \frac{\left(\lambda/c_p\right)_{T_{ref}}}{\rho_u s_L^0} \tag{2.57}$$

with an appropriate reference temperature T_{ref}. If not indicated otherwise, the inner layer temperature T_0 is chosen as the reference temperature throughout this thesis. It can be estimated by evaluating the temperature within the flame at the position of the maximum heat release (Ewald [66]). The laminar flame thickness can alternatively be approximated by the temperature profile of the flame

$$\delta_F = \frac{T_b - T_u}{(\partial T/\partial x)|_{max}}. \tag{2.58}$$

According to Poinsot and Veynante [150], this definition yields a larger flame thickness and can be related to l_F by

$$\frac{\delta_F}{l_F} = 2 \left(\frac{T_b}{T_{ref}}\right)^{0.7}. \tag{2.59}$$

The second characteristic length scale is the size of the inner layer l_δ which can be related to the laminar flame thickness by

$$l_\delta = \delta l_F \tag{2.60}$$

where δ varies between 0.1 and 0.03 for stoichiometric methane-air flames at 1atm and 30atm, respectively (Peters [137]). The size of the oxidation layer l_ϵ is typically three times larger than l_δ. Using the definitions of s_L^0 and l_F, the characteristic flame time scale t_F as well as thermal diffusivity D can be calculated by

$$t_F = l_F/s_L^0 \qquad \text{and} \qquad D = s_L^0 l_F. \tag{2.61}$$

According to Peters [139], the flame time t_F is comparable to the chemical time scale t_c of the flame. An approximation of the diffusivity D for hydrocarbon flames was given by Smooke and Giovangigli [179],

$$\frac{D}{\rho_u} = \left(\frac{\lambda}{c_p}\right) = 2.58 \times 10^{-5} \frac{kg}{m\,s} \left(\frac{T_{ref}}{298K}\right)^{0.7}. \tag{2.62}$$

It can be used in combination with the laminar flame velocity s_L^0 to estimate the laminar flame thickness l_F.

For multidimensional laminar or turbulent flames, additional notions have to be introduced. A laminar flame in a three-dimensional, non-uniform flow field is subject to strain and curvature effects changing the laminar burning velocity. In the limit of small curvature and strain, the burning velocity becomes (Peters [142])

$$s_L = s_L^0 - s_L^0 \mathcal{L}\kappa - \mathcal{L}S \tag{2.63}$$

where $\kappa = \nabla \cdot \mathbf{n}$ is the flame curvature, $S = -\mathbf{n} \cdot \nabla\mathbf{v} \cdot \mathbf{n}$ is the strain rate and $\mathcal{L}$ the Markstein length. Here, $\mathbf{n}$ is the unit vector normal to the flame front pointing towards the unburned gases. Depending on the local values of strain and curvature, a laminar flame can either be accelerated or decelerated. If the Lewis number of the flame is smaller than unity, this phenomenon can ultimately lead to thermo-diffusive instabilities (Poinsot and Veynante [150]).

Extinction mechanisms of laminar premixed flames

For the subsequent discussion of flame-wall interactions in chapter 3, it is useful to shortly introduce and discuss the main extinction mechanisms of laminar flames. In view of the flame structure shown in Fig. 2.2, it was noted by Peters [139] that a sufficient amount of fuel should exceed the inner layer temperature T_0 in order to enable a flame propagation without the addition of heat from the outside. A lower limit for flame propagation is thus given by

$$T_b = T_0. \tag{2.64}$$

This criterion was successfully used to explain the lean flammability limits of methane-air flames (Peters [139, 140]). The extinction of a flame by flame stretch or heat losses can be explained in a similar way. If stretch is acting on a flame, the burning velocity (Eq. (2.63)) and thereby the local heat release may reduce up to a point where the temperature of the reaction zone falls below a critical value and the flame extinguishes. Heat losses, in turn, reduce the amount of thermal energy which is available to preheat the fresh gases. It can thus be noted that flame extinction is closely connected to the ability of the flame to exceed a critical temperature level. Based on the previous discussion, it can be suggested that this critical temperature is close to the inner layer temperature T_0.

An indicator for the temperature sensitivity of a laminar flame is the Zeldovich number Ze. According to Peters [139, 140], it can be interpreted as a dimensionless activation energy measuring the sensitivity of the burning velocity to fluctuations of the temperature T_b. He stated furthermore that the Zeldovich number increases when the pressure rises and the mixture becomes leaner. The higher the Zeldovich number, the more sensitive the flame becomes towards the effects of heat losses and stretch. In case of (volumetric) heat losses, for example, a correlation for the burning velocity ratio $M = s_L/s_L^0$ can be derived by asymptotic analysis (Peters [139], Chao and Law [38]). For a one-step reaction, this approach yields

$$M^2 \ln M^2 = -\pi Ze \qquad (2.65)$$

where π is a non-dimensional heat loss parameter (cf. Peters [139]). If the product πZe increases, the burning velocity ratio M decreases up to a critical point $(\pi Ze)_{\text{crit}}$ where no solution for M can be found. The non-dimensional burning velocity at $(\pi Ze)_{\text{crit}}$ is $M_{ex} \approx 0.61$ for one-step kinetics and $M_{ex} \approx 0.64$ for four-step kinetics (Peters [139]). For higher Zeldovich numbers, $(\pi Ze)_{\text{crit}}$ is already attained for smaller heat losses π.

Real laminar flames can be subjected to both, flame stretch and heat losses. In this case, it can be expected that the critical heat loss is considerably lowered by flame stretch and vice-versa. This suggestion is backed by experiments of Egolfopoulos et al. [62].

2.3.2 Turbulent premixed flames

A premixed flame is strongly affected by the wide range of flow motions present in a turbulent flow leading to a wrinkling and convolution of the flame surface. In the following, the main physical processes of turbulent premixed flame propagation are presented and different combustion regimes are introduced. Furthermore, the concept of the turbulent burning velocity is introduced and the limiting cases are discussed.

Regimes of turbulent premixed combustion

A qualitative understanding of the physics of turbulent combustion can be provided by using various non-dimensional classification numbers comparing the turbulent to the chemical length and time scales. In general, a turbulent flow is characterized by the turbulent Reynolds number Re_t which corresponds to the ratio of inertial to viscous forces. By assuming that

the Schmidt number $Sc = \nu/D$ is equal to unity, it is given by

$$Re_t = \frac{v'l_t}{\nu} \overset{\text{Eq. (2.61)}}{=} \frac{v'l_t}{s_L^0 l_F}. \tag{2.66}$$

The turbulent Damköhler number is defined as the ratio of the integral turbulent and the chemical time scales

$$Da = \frac{\tau}{t_c} = \frac{s_L l_t}{v'l_f}. \tag{2.67}$$

In the limit of high Damköhler numbers, the chemical time scale is considerably shorter than the turbulent one meaning that the inner flame structure is not strongly affected by turbulence. The premixed flame is wrinkled and strained by turbulence and can locally be described as a flamelet. Slow chemical reactions, on the other hand, result in low Damköhler numbers ($Da \ll 1$). In this case, products and reactants are mixed by the turbulent flow field before reaction. In most practical situations, a medium to high Damköhler number is encountered (Veynante and Vervisch [197]).

The second important classification number, the Karlovitz number Ka, is obtained by comparing the chemical to the Kolmogorov time scale

$$Ka = \frac{t_c}{t_\eta} = \frac{l_f}{\eta} \frac{v_\eta}{s_L^0} = \left(\frac{l_F}{\eta}\right)^2 = \left(\frac{v_\eta}{s_L^0}\right)^2. \tag{2.68}$$

In the case of $Sc = 1$, the Karlovitz number also compares the laminar flame and Kolmogorov length scale as well as the corresponding velocity scales. If the Karlovitz number is larger than unity, the smallest eddies are able to penetrate the inner flame structure. The reaction zone may not necessarily be affected, since it is considerably thinner than the laminar flame thickness. To evaluate the effect of turbulence on the reaction zone, a second Karlovitz number, Ka_δ, may be introduced comparing the thickness of the reaction zone to the Kolmogorov length scale

$$Ka_\delta = \left(\frac{l_\delta}{\eta}\right)^2 = \delta^2 Ka. \tag{2.69}$$

It shall be noted that additional length scales can be introduced. For a more detailed discussion, the reader is referred to publications by Peters [136, 141, 142].

Combustion diagrams which classify different regimes of turbulent premixed combustion in terms of these classification numbers have been proposed by Borghi [23], Abdel-Gayed and Bradley [2], Poinsot et al. [151], Peters [136], only to name a few. As pointed out by Veynante and Vervisch [197], such analyses are only qualitative and should thus be utilized with great care. Fig. 2.3 shows the diagram suggested by Peters [141]. Four main regimes can be distinguished:

- $Re_t < 1$. Laminar flames.

- $Re_t > 1$, $Ka < 1$. Flamelet regime. The Karlovitz number is smaller than unity and the laminar flame thickness is smaller than the smallest eddies. Therefore, turbulence does not affect the inner flame structure and the flame front remains thin. Two subdivisions can be made based upon the velocity ratio v'/s_L^0.
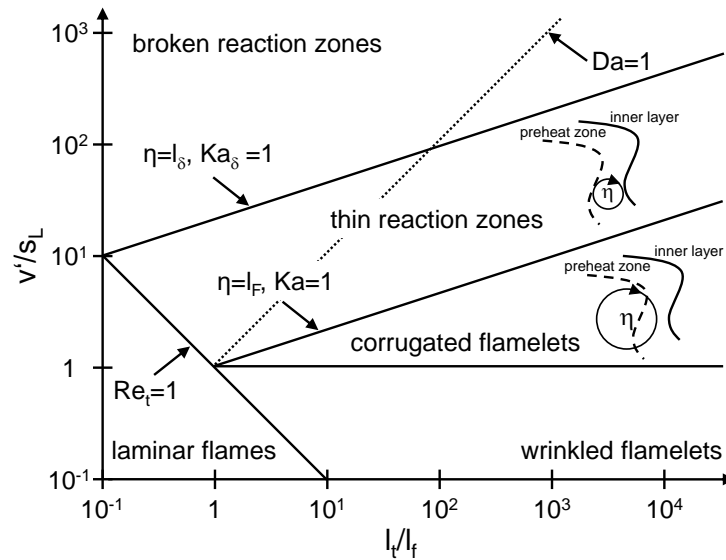
Figure 2.3: Regime diagram for turbulent premixed combustion according to Peters [142].

- $v' < s_L^0$. Wrinkled flamelets. The turnover velocity v' of the largest eddies is too small to compete with the advancement of the flame front. The laminar flame front propagation is predominant while the interaction between turbulence and combustion is limited.

- $v' > s_L^0$. Corrugated flamelets. The large scale turbulent eddies are able to wrinkle the flame front leading to pockets and an increase in flame front surface. Thus the flame structure remains laminar and the interaction between turbulence and combustion is purely kinematic.

- $Re_t > 1, Ka > 1, Ka_\delta < 1$ Thin reaction zones regime. The smallest eddies of size η are able to enter and thicken the preheat zone. The reaction zone is not affected and remains thin as well as close to a laminar reaction zone.

- $Re_t > 1, Ka_\delta > 1$. Broken reaction zones. The preheat and reaction zones are strongly affected by turbulence as the smallest eddies are of the order of the inner layer thickness l_δ or even smaller. In this case, no laminar flame structure can be identified.

It was shown by Wirth [214] and Linse et al. [112] that combustion in a SI engine occurs in the corrugated flamelets and thin reaction zones regime depending on the level of charge motion. Thus, a comprehensive premixed combustion model has to account for the dominating physical processes in both regimes.

Turbulent burning velocity

The turbulent burning velocity can be defined in analogy to the laminar burning velocity (Eq. (2.56)). However, it mainly depends on the characteristics of the turbulent flow field rather than on the thermodynamic state of the mixture. According to Damköhler [47], the turbulent

burning velocity s_T^0 can be defined as the velocity of the mean turbulent flame front normal to itself and the turbulent flow field. He stated that the mass flow through a duct containing a stationary turbulent flame is constant. In this case, continuity requires that the mass flow through the mean flame front with the cross section A and velocity s_T^0 has to be equal to the mass flow through the instantaneous flame front with surface area A_T and velocity s_L^0,

$$\dot{m} = \rho_u s_L^0 A_T = \overline{\rho}_u s_T^0 A. \tag{2.70}$$

For constant unburned density, the burning velocity ratio is proportional to the surface ratio

$$\frac{s_T^0}{s_L^0} = \frac{A_T}{A} = 1 + \overline{\sigma}_t, \tag{2.71}$$

where $\overline{\sigma}_t$ is the turbulent contribution to the flame surface area ratio defined as $\overline{\sigma}_t = (s_T^0 - s_L^0)/s_L^0$. Damköhler [47] has also been the first to derive theoretical expressions for the turbulent burning velocity s_T^0. He distinguished between two different limits of turbulent premixed combustion, namely the limit of large scale and small scale turbulence. As discussed by Peters [141, 142], these limits are related to the corrugated flamelets and thin reaction zone regime, respectively.

In the limit of large scale turbulence (associated to the corrugated flamelets regime), Damköhler assumed that the interaction between the turbulent flow field and the flame front is purely kinematic. The enhancement of the flame surface area and thereby the turbulent burning velocity is thus proportional to

$$A_T/A = s_T^0 \sim v'/s_L^0. \tag{2.72}$$

Experimental data for fully developed turbulent flames by Abdel-Gayed and Bradley [1] suggests that the turbulent burning velocity can be approximated by

$$s_T^0 - s_L^0 = s_L^0 \overline{\sigma}_t = b_1 v' \qquad \text{with} \qquad b_1 = 2.0, \tag{2.73}$$

in the limit of large-scale turbulence limit and $v' \gg s_L^0$.

This linear relationship can no longer be observed in the limit of small scale turbulence being associated to the thin reaction zones regime. In this case, Damköhler postulated that turbulent eddies modify the transport processes between the reaction zone and the unburned gases. Based on the scaling relationship for laminar flames,

$$s_L^0 \sim (D/t_c)^{1/2}, \tag{2.74}$$

he proposed a relation for turbulent flames by replacing the laminar D with the turbulent diffusivity D_t

$$s_T^0 \sim (D_t/t_c)^{1/2}. \tag{2.75}$$

This equation implies that the chemical time scale t_c remains unaffected by turbulence. Combining these two scaling relationships yields

$$\frac{s_T^0}{s_L^0} \sim \left(\frac{D_t}{D}\right)^{1/2} \qquad \Rightarrow \qquad \frac{s_T^0 - s_L^0}{s_L^0} = \overline{\sigma}_t = b_3 \left(\frac{D_t}{D}\right)^{1/2}. \tag{2.76}$$

Damköhler suggested that b_3 should equal unity. Wenzel [207] determined b_3 by DNS simulations and found that $b_3 = 1.02$. Since this result essentially confirms Damköhlers assumption, the constant b_3 is set to unity in the following, $b_3 = 1.0$.

These limits will be used in chapter 5 to derive a unified correlation for the turbulent burning velocity in the corrugated flamelets and thin reaction zones regime that also accounts for the effects of near-wall turbulence and flame development.

2.3.3 Turbulent premixed combustion modelling

Turbulent combustion modelling has received considerable interest over many decades resulting in a variety of approaches, paradigms and modelling strategies, which are often closely related (Peters and Bray [143], Vervisch et al. [194], Vervisch and Veynante [195]). For a comprehensive overview and introduction, the reader is referred to Poinsot and Veynante [150], Echekki and Chen [61], Peters [142], Veynante and Vervisch [197] and Bilger et al. [19]. In the following, a brief general overview of turbulent premixed combustion models, their basic ideas and characteristics is given. Special emphasis is laid on flamelet models due to their significance for the simulation of combustion in SI engines.

General overview

The main objective of combustion modelling is to provide a physical description of the interaction between flames and turbulence and thereby an accurate estimate of the mean reaction rates $\bar{\dot{\omega}}_\alpha$ based on the the mean flow quantities. As indicated in section 2.2.2, the average reaction rates cannot be expressed as a function of the mean values due to the nonlinear nature of the reaction rate coefficients. Depending on their physical concept, three different approaches for the modelling of turbulent premixed combustion can be distinguished (cf. Herrmann [89]):

- Turbulence or mixing controlled models

- Transported Probabilty Density Function models

- Flamelet models

Turbulence or mixing controlled models like the Eddy-Breakup (EBU) model by Spalding [181] or the Magnussen model [117] are based on the premise that chemistry is infinitely fast. In this case, the mean reaction rate is only governed by the turbulent mixing process and can thus be assumed to be inversely proportional to the turbulent time scale $\tau^{-1} = \varepsilon/k$. EBU-type models have been widely adopted in CFD codes due to their simplicity and low computational cost. However, there are several drawbacks limiting their applicability to engineering problems. The disadvantages are the lack of sensitivity to chemistry, the tendency to overestimate the flame propagation close to walls and the need to tune the model constants for each individual problem (Cant [34]).

Transported PDF models for turbulent combustion modelling were initially developed by Pope [152]. The basic element is a complete one-point description of the statistic properties

of the turbulent flow field given by the joint probability density function $P(\mathbf{v}, \psi; \mathbf{x}, t)$ of velocity $\mathbf{v}$ and a set of reactive scalars ψ. In order to determine the evolution of P, a joint pdf transport equation can be derived in which the effects of convection, reaction, body forces and mean pressure gradient appear in closed form (Pope [152]). Herein lies the major advantage of transported PDF models. However, some terms, in particular the molecular mixing term, still have to be modelled (Haworth [88]). This is complicated by the fact that the one-point probability density function P does not incorporate the required informations about the mixing time and length scales (Poinsot and Veynante [150]). Transported PDF methods can be used in combination with arbitrary chemistry and are commonly solved by Monte-Carlo methods which represent the flow by a number N_p of stochastic particles (Pope [152]). Since the statistical error scales with $1/\sqrt{N_p}$ (Peters [142]), a large number of particles has to be introduced leading to a high computational effort.

Flamelet models are based on the concept of scale separation, introduced in the beginning of section 2.3. All chemical reactions are assumed to occur within thin layers. These reactive-diffusive layers are subject to the motions of the turbulent flow field but retain their laminar inner structure. Hence, the chemistry is decoupled from the turbulent flow field. The flame surface is defined as a geometrical entity separating fresh and burned gases. In this context, the turbulent flame brush can be viewed as an ensemble of flamelets. If the statistical distribution of the instantaneous flame front locations is known, profiles of the reactive scalars obtained by the flamelet equations can be reattached to the turbulent flow field (Peters [142]). The major challenge of the flamelet concept is therefore the determination of the probability of finding an instantaneous flame front at a given position $\mathbf{x}$ and time t. An in-depth discussion of this topic can be found in the textbook by Peters [142]. The most important flamelet models are introduced in the following.

Flamelet models

Flamelet models for premixed combustion are either based on the progress variable c or the scalar G. The most important models employing the progress variable are the Bray-Moss-Libby (BML) model and the Coherent Flame Model (CFM). Both are briefly summarized in this section. The G-equation model is presented in chapter 5. Nevertheless, some of its key features are discussed below.

Bray-Moss-Libby model

The BML model was first proposed by Bray and Moss in 1977 [28] and has been continuously improved over time (cf. papers by Bray, Moss and Libby and later by Bray, Champion and Libby). It introduces the progress variable c which can be defined either as a normalized temperature or a normalized product mass fraction

$$c = \frac{T - T_u}{T_b - T_u} \qquad \text{respectively} \qquad c = \frac{Y_P}{Y_{P,b}}. \qquad (2.77)$$

The key concept of the BML model is the presumed pdf for the progress variable c,

$$P(c; \mathbf{x}, t) = \underbrace{\alpha(\mathbf{x}, t)\delta(c)}_{\text{fresh gases}} + \underbrace{\beta(\mathbf{x}, t)\delta(1 - c)}_{\text{burned gases}} + \underbrace{\gamma(\mathbf{x}, t)f(c, \mathbf{x})}_{\text{burning gases}} \qquad (2.78)$$

where δ is the Dirac δ-function and α, β as well as γ are the probability of finding fresh, fully burned and burning gases at location $\mathbf{x}$. The normalization of this probability density function yields

$$\alpha(\mathbf{x}, t) + \beta(\mathbf{x}, t) + \gamma(\mathbf{x}, t) = 1. \tag{2.79}$$

In combination with a physical analysis, this statistical approach has been successfully used to investigate and explain specific features of turbulent premixed combustion such as counter-gradient diffusion (Poinsot and Veynante [150]).

In order to model the flame propagation, a Favre-averaged transport equation of the mean progress variable $\widetilde{c}$ can be defined as

$$\frac{\partial \overline{\rho}\,\widetilde{c}}{\partial t} + \nabla \cdot \left(\overline{\rho}\,\widetilde{\mathbf{v}}\,\widetilde{c} \right) = -\nabla \cdot \left(\overline{\rho}\,\widetilde{\mathbf{v''}c''} \right) + \overline{\dot{\omega}}_c. \tag{2.80}$$

The turbulent transport term $\widetilde{\mathbf{v''}c''}$ and the mean chemical source term $\overline{\dot{\omega}}_c$ are unclosed and require modelling. As shown in section 2.2.3, the scalar turbulent flux can simply be closed by a gradient assumption. However, $\widetilde{c}$ is a reacting scalar and counter-gradient diffusion effects have to be accounted for. For this reason, more elaborate modelling closures have been developed (cf. Veynante et al. [196]). There are several different closures of the mean reaction rate within the BML framework such as the scalar dissipation rate or flame crossing frequency formulation. An overview is provided in the textbook by Poinsot and Veynante [150]. One of the most important closure employs the flame surface density Σ,

$$\overline{\dot{\omega}}_c = (\rho_u \langle s_L \rangle_S)\,\Sigma = \left(\rho_u s_L^0 I_0 \right) \Sigma, \tag{2.81}$$

where $\langle s_L \rangle_S$ is the surface-averaged flamelet consumption speed commonly modelled by multiplying s_L^0 with the stretch factor I_0 (cf. Meneveau and Poinsot [122]). The flame surface density can either be defined by an algebraic expression or by solving a balance equation for Σ. The latter is more common and shortly introduced in the following.

Coherent Flame Models

A balance equation for Σ was first proposed by Marble and Broadwell [121]. Extensive research on this subject lead to a variety of different versions (e.g., Pope [153], Candel and Poinsot [33], Trouvé and Poinsot [192]). In general, the closed transport equation for Σ can be written as

$$\frac{\partial \Sigma}{\partial t} + \nabla \cdot (\widetilde{\mathbf{v}}\Sigma) = \nabla \cdot \left(\frac{\nu_t}{Sc_{t,\Sigma}} \nabla \Sigma \right) + \kappa_m \Sigma + \kappa_t \Sigma - D_\Sigma \tag{2.82}$$

where $Sc_{t,\Sigma}$ is the turbulent Schmidt number of the surface, κ_m and κ_t are surface strain contributions and D_Σ is a destruction term (Poinsot and Veynante [150]). The terms $\kappa_m \Sigma$ and $\kappa_t \Sigma$ can be interpreted as production terms since κ_m and κ_t are always positive. The destruction term D_Σ is always proportional to Σ^2. A comprehensive overview of different modelling closures can be found in Poinsot and Veynante [150] and Veynante and Vervisch [197]. Coherent flame models are implemented in many commercial CFD codes and have been successfully applied to a number of different applications including SI engines (e.g., Colin et al. [42], Duclos et al. [55]).

G-equation model

The *G*-equation model was originally proposed by Williams [212] and considerably extended by Peters [138, 141, 142]. The basic idea is to define the location of the flame front by an iso-scalar surface of the non-reacting level set scalar *G* which separates burned and unburned gases. Knowing the location of the flame front, the mean chemical composition of the flow can be calculated by assigning the corresponding ensemble average of laminar flamelets to each point of the flow field based on the local probability of finding flamelets. The *G*-equation model approach is introduced in detail in chapter 5. At this point, some key features are discussed in comparison to the previously introduced flamelet models. A major advantage of the *G*-equation model is that the scalar *G* is a non-reacting quantity. For this reason, no chemical source term has to be closed and counter-gradient diffusion is avoided. As a consequence, classic turbulence closures based on the eddy cascade hypothesis can be applied (Peters [142]). Moreover, it has been rigorously derived to accurately model the physics of the different flamelet regimes and is able to incorporate detailed chemical kinetics by combining it with the one-dimensional flamelet equations (Peters [141, 142]). The *G*-equation model has been successfully applied to premixed (e.g., Ewald [66], Linse [111]) or partially premixed combustion (e.g., Dahms [46]). The major drawback of the *G*-equation is that the scalar *G* has no physical meaning outside the flame front surface. For this reason, a numerical reinitialization technique has to be applied which prevents feedback of the unphysical *G*-field outside the flame front surface. This is accompanied by an additional computational effort (Peters [142]).

3 Flame-wall interaction: a literature-based analysis

Every premixed combustion taking place in an enclosure, e.g., in SI engines, is subjected to flame-wall interactions. Although flame quenching can also occur for non-premixed flames (cf. Dabireau et al. [45], De Lataillade et al. [51], Wang and Trouvé [202]), the majority of research was conducted for premixed flames. Flame quenching in SI engines has already been observed in the late 1950's by Daniel [48]. After ignition, the flame propagates from the spark plug towards the relatively cold walls of the combustion chamber where it is eventually quenched. According to Liu et al. [115], approximately two thirds of the cylinder charge are burned in a decelerating flame near the wall. Hence, flame-wall interactions significantly influence the combustion efficiency. Their relevance is further emphasized by the high wall heat fluxes during quenching, which can easily exceed 1 MW/m^2 (cf. Gruber et al. [81], Labuda et al. [105]). This impacts the ageing of the wall material and can lead to material failure and the destruction of the combustion device in the worst case. Despite the significance of flame-wall interactions, little is known about its nature in practical applications and only very few modelling attempts have been made. The aim of this chapter is therefore to derive a comprehensive phenomenological description and abstraction of the flame-wall interaction process. This chapter thus provides the basis for the experimental evaluation of flame-wall interactions in a direct-injection SI engine (chapter 4) as well as the for the modelling of the phenomenon within the context of the *G*-equation (chapter 5).

The presence of the wall significantly affects the turbulent flow as well as the combustion reactions. Basically, premixed flame-wall interaction is a three-way coupling process between flame, wall and turbulence as shown in Fig. 3.1 (Poinsot and Veynante [150]):

- Flame - Turbulence: The interaction between a premixed flame and turbulence has already been addressed in chapter 2. A turbulent flow wrinkles and stretches a laminar flame thereby modifying its propagation velocity and inner structure. The flame in turn influences the flow by altering the viscosity and density in the burned gases leading to flow acceleration and enhanced dissipation of turbulence. The description of these processes is commonly the scope of combustion modelling.

- Walls - Turbulence: The no-slip condition at the wall restricts the fluid motion and induces the generation of a boundary layer with distinct features. The wall-normal fluctuation velocity as well as the turbulent length scales decrease towards the wall and coherent flow patterns may appear affecting the propagation of a flame. Turbulence, in turn, modifies and enhances the mean wall friction and the mean wall heat flux.

- Flame - Walls: When a premixed flame comes close to a wall, the temperature of the

gases at the wall increases and a wall heat flux is induced. As a consequence, the wall itself is heated and the flame is quenched once the heat losses exceed a critical level.
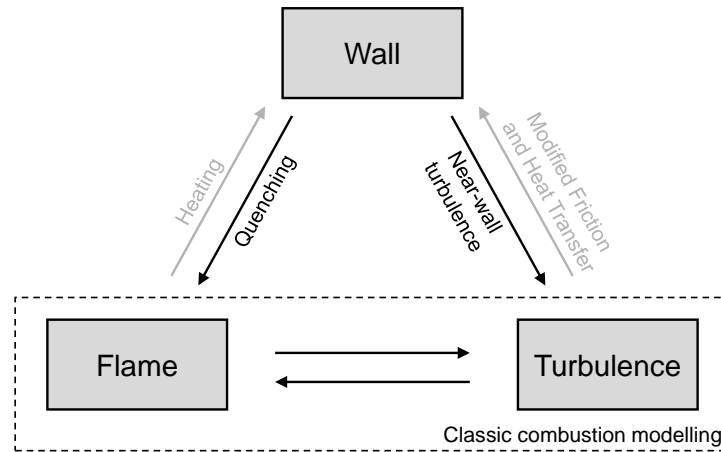

Figure 3.1: Overview of the interaction between walls, flames and turbulence from a combustion modelling perspective (adapted from Poinsot and Veynante [150]). The effects influencing the flame propagation are highlighted.

The effects described above cannot be strictly separated from each other due to their interaction. However, the study of individual aspects such as laminar flame-wall interaction is necessary to derive a comprehensive picture of flame-wall interactions in general. In this work, the focus lies on the aspect of quenching (wall - flame) and near-wall turbulence (wall - turbulence) since these are the main influences on the near-wall flame propagation (Fig. 3.1). This section is thus organized as follows: The simplest case, the interaction between a laminar premixed flame and a wall, is examined first and some key concepts for describing flame-wall interactions such as the Peclet number are introduced. Having discussed the basic process of flame extinction at a cold wall, the effect of turbulence is discussed. In this context, near-wall turbulence plays a decisive role. It is therefore shortly discussed before the studies on turbulent flame-wall interactions are reviewed on this basis. Based on the insights of the literature study, a short a priori analysis of flame-wall interactions in SI engines is conducted. This chapter is concluded by a summary of the most important flame-wall interaction models.

3.1 Laminar flame-wall interaction

In general, the interaction between a laminar premixed flame and a cold wall is a two-way coupling process and constitutes the simplest case of flame-wall interactions. Despite the absence of a flow motion influencing flame propagation, many aspects of the quenching process can already be highlighted and explained. Laminar flame-wall interactions can be divided in three characteristic configurations (Poinsot and Veynante [150], Dreizler and Böhm [54]):

- Head-on quenching (HOQ): HOQ is characterized by a flame front which is parallel to the wall and propagates towards it. Once it reaches a certain distance from the wall, the quenching distance y_Q, the flame is completely extinguished. HOQ is a one-dimensional problem which is intrinsically transient.

- Side-wall quenching (SWQ): During SWQ, the flame front propagates parallel to the wall. Outside the influence zone of the wall, the flame front is perpendicular to the wall surface. In contrast to HOQ, sidewall quenching is a two-dimensional problem which can be treated stationary.

- Tube quenching: Tube quenching occurs when a flame propagates through tubes with small diameters and is especially important for safety technology like flame arresters. A famous example are safe mine lamps (Davy [50] and Stephenson [204]). Referring to combustion in spark ignition engines, tube quenching is of minor importance since the dimensions of the combustion chamber are normally to large to induce total quenching. Thus it is not considered further.

In the following, the head-on quenching of a laminar premixed flame is examined. For this purpose, the general phenomenology is shortly discussed before important aspects such as the wall heat flux or the chemical reactions during quenching are detailed. Moreover, key concepts such as the Peclet number are also introduced in this context. On this basis, side-wall quenching is examined briefly before the main findings of this section are shortly summarized.

3.1.1 Head-on quenching

The HOQ configuration was investigated numerous times by analytical (e.g., Ferguson and Keck [71], Wichman and Bruneaux [210]), simulative (e.g., Westbrook et al. [208], Kiehne et al. [101], Popp and Baum [157, 158], Hasse et al. [87]) and experimental means (e.g., Vosen et al. [201], Huang et al. [92], Ezekoye et al. [69], Sotton et al. [180]).

A typical head-on quenching configuration is depicted in Fig. 3.2a, in which schematic temperature profiles of a laminar flame propagating towards a cold wall are shown. Initially, the flame propagates freely (t_1), before it encounters the wall and the wall heat losses start to increase (t_2). Once the wall heat losses become too high, the flame is extinguished (t_3) as the underlying reactions can no longer be sustained. After quenching, the isotherms move away from the wall due to the wall heat flux (t_4).

This thermal notion of flame quenching at cold walls is widely accepted (cf. Hasse et al. [87], Boust et al. [26], Poinsot and Veynante [150]). As shown in Fig. 3.2b, the moment of quenching exhibits several distinct features: the wall heat flux reaches its peak $\dot{Q}_{W,Q}$ whereas the flame-wall distance attains its minimal value, the quenching distance y_Q (Hasse et al. [87]). By dividing these values with the laminar flame power $\dot{Q}_F$ and the laminar flame thickness l_F, respectively, two characteristic figures of the quenching process can be defined, namely the normalized wall heat flux

$$\varphi_Q = \frac{\dot{Q}_{W,Q}}{\dot{Q}_F} = \frac{\dot{Q}_{W,Q}}{\rho_u s_L^0 c_P \left(T_b - T_u\right)} = \frac{\dot{Q}_{W,Q}}{\rho_u s_L^0 Y_F \Delta H} \tag{3.1}$$

(a) Schematic temperature profiles.

(b) Schematic wall heat flux and flame-wall distance (temperature iso-level) profiles.
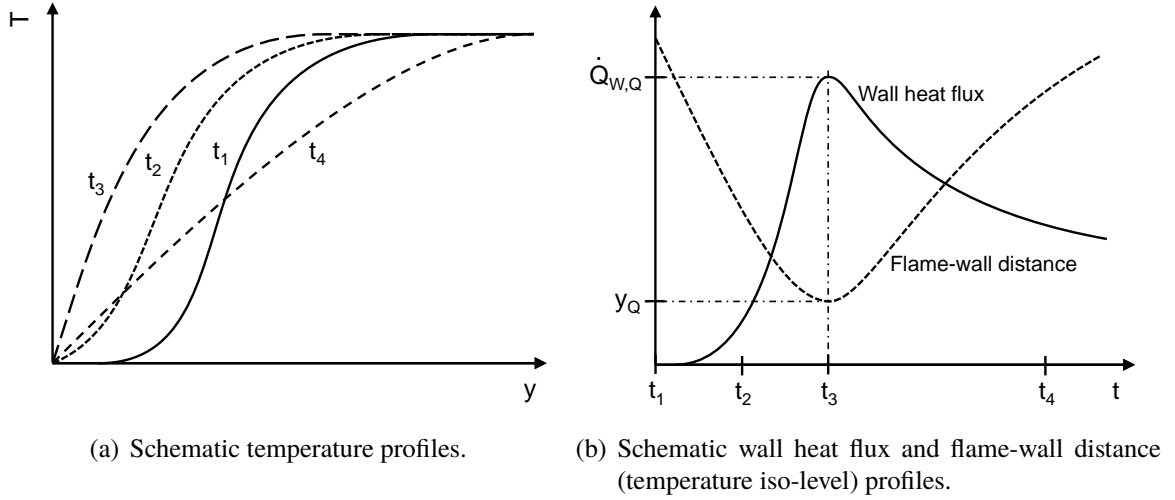
Figure 3.2: Head-on quenching of a laminar premixed flame.

and the Peclet number

$$Pe_Q = \frac{y_Q}{l_F} = \frac{y_Q \rho_u s_L^0}{\left(\lambda/c_p \right)_{T_{ref}}} \ . \tag{3.2}$$

The reference temperature T_{ref} is usually chosen as $T_{ref} = T_u$. The present definition of Pe_Q has been widely adopted (e.g., Poinsot et al. [149], Vosen et al. [201]), however, some authors (e.g., Hasse et al. [87], Popp and Baum [157]) utilize the flame thickness δ_F defined in Eq. (2.58).

The importance of these quantities is highlighted by the fact that the wall heat flux and the quenching distance are inversely correlated (Vosen et al. [201], Huang et al. [92]), i.e., $\varphi_Q \sim 1/Pe_Q$ (cf. Poinsot and Veynante [150]). This circumstance can be utilized to estimate quenching distance based on a measurement of the wall heat flux (cf. Boust et al. [26]). This topic is further addressed in chapter 4. Typical scales of HOQ are $\varphi_Q \approx 1/3$ and $Pe_Q \approx 3$. In dimensional terms, common magnitudes are $\dot{Q}_{W,Q} \sim O(1MW/m^2)$, $y_Q \sim O(100\mu m)$. The duration of flame-wall interactions is of order $O(100\mu s)$ (Popp and Baum [157], Sotton et al. [180], Labuda et al. [105]). For ambient conditions, this equals around 2-3 flame times t_F (Vosen et al. [201]). However, the dimensional values are strongly influenced by the initial and boundary conditions as well as by the fuel involved. Therefore it is sensible to conduct a more detailed analysis of the quenching phenomenon based on the normalized values.

Normalized wall heat flux and Peclet number

As already indicated, the wall heat flux during flame quenching is one of the most significant features of laminar flame-wall interactions. On the one hand, it is relatively simple to access in experiments and on the other hand, its normalized value φ_Q can be used to correlate and characterize the quenching process of various hydrocarbon-air flames (cf. Vosen et al. [201], Huang et al. [92]). For these reasons, many studies were carried out to clarify the influence

of fuel type, equivalence ratio, pressure and wall temperature on the normalized wall heat flux φ_Q.
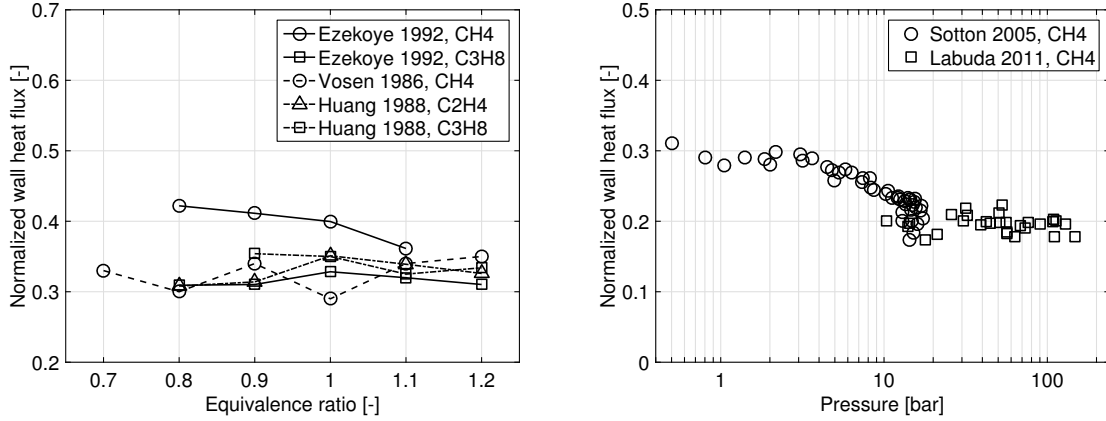
(a) Effect of fuels and influence of equivalence ratio ϕ (data taken from Vosen et al. [201], Huang et al. [92], Ezekoye et al. [69]).

(b) Influence of pressure p (stoichiometric CH_4-air flame; data taken from Sotton et al. [180], Labuda et al. [105]).

Figure 3.3: Effect of fuels, equivalence ratio and pressure on the normalized wall heat flux φ_Q.

The effect of different fuels and varying equivalence ratios is shown in Fig. 3.3a. Despite the different mixture conditions, the normalized wall heat flux φ_Q remains within a certain range of values. This underlines the thermal notion of flame quenching: once a certain threshold of the flame power $\dot{Q}_F$ is conveyed to the wall as heat losses, the flame quenches as further reactions cannot be sustained due to an insufficient temperature level. The underlying chemical reactions only have a minor importance. At this point, it shall be remarked that the behaviour of H_2 differs from the one of hydrocarbons. For hydrogen flames, the normalized wall heat flux ($\phi_Q \approx 0.13$) decreases and the normalized quenching distance ($Pe_Q \approx 1.7$ based upon δ_F) increases (cf. Table 3.1). However, in dimensional terms, the quenching of a premixed hydrogen flame with a wall results in very high wall heat fluxes combined with short interaction times indicating an intense and much faster interaction compared to hydrocarbon flames (Dabireau et al. [45]). For further details on this topic, the reader is referred to Owston et al. [133] and Gruber et al. [81].

When varying the pressure, a slight decrease of φ_Q towards higher pressures can be observed (Fig. 3.3b). This trend is also evident in the simulation results of Hasse et al. [87]. Recalling the effects of volumetric heat loss on a laminar flame (section 2.3.1), a possible explanation for this behaviour is the sensitivity of the flame towards heat losses. For rising pressures, the Zeldovich number Ze increases and the flame is already extinguished by smaller volumetric heat losses π (cf. Peters [139]). An analogous behaviour can also be expected for flame quenching at cold walls. The variation of unburned temperature has not yet been explicitly studied in literature, however, an indication for its influence can again be found by comparing the publications of Sotton et al. [180] and Labuda et al. [105]. In these studies, the unburned temperature ranged between $290-300K$ in the former and $800-900K$

in the latter. Albeit this difference, the normalized wall heat flux φ_Q possesses the same magnitude in the overlapping pressure region.
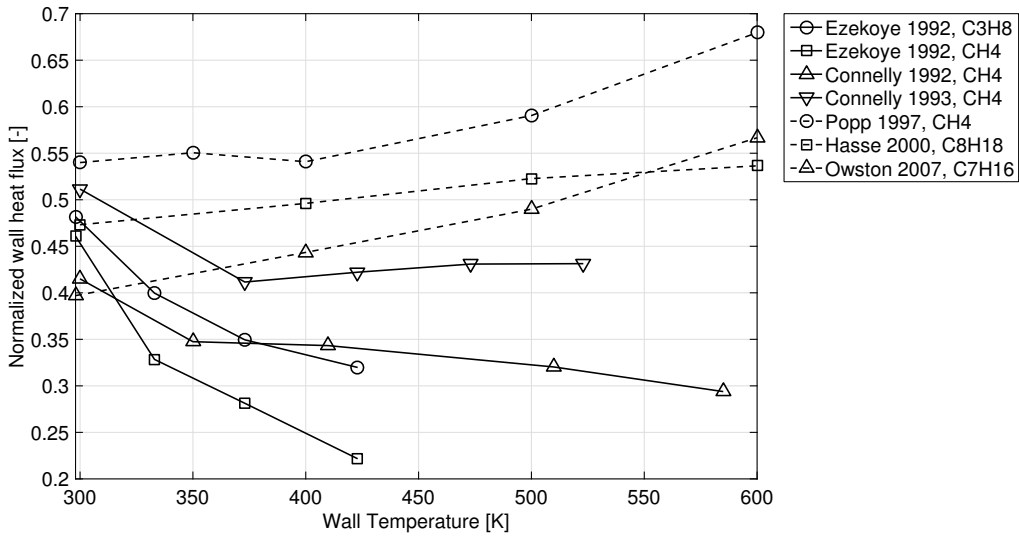

Figure 3.4: Influence of the wall temperature on the normalized wall heat flux φ_Q: comparison of experimentally (data taken from Connelly et al. [43, 44], Ezekoye et al. [69]) and numerically (data taken from Popp and Baum [157], Hasse et al. [87], Owston et al. [132]) obtained wall heat fluxes φ_Q during HOQ.

The variation of wall temperature was extensively studied in literature (cf. Ezekoye et al. [69], Connelly et al. [43, 44], Popp and Baum [157, 158], Hasse et al. [87], Owston et al. [132]). A compilation is shown in Fig. 3.4. The trend of experimentally and numerically obtained values is contrary. Numerical studies show an increasing trend independent of the considered chemistry (i.e., simplified vs. detailed chemistry), whereas experimental studies exhibit a slightly decreasing trend. The reasons for this discrepancy are surface reactions (Popp and Baum [158]), measurement inaccuracies and the inherent three-dimensional nature of experiments which does not allow an exact reproduction of a strictly one-dimensional simulation. For example, a non-uniform flame propagation and heat losses other than to the wall are inevitable in reality. The rising wall heat flux with increasing wall temperature can be attributed to an increased heat release rate in the vicinity of the wall during quenching (cf. Owston et al. [132, 133], Gruber et al. [81]) which results from an increased radical level near the wall. This behaviour becomes more and more distinctive for increasing wall temperatures.

Regarding the normalized wall heat flux φ_Q, it can be concluded that it ranges around 0.3 for a wide variety of different fuels and thermodynamic conditions. The question which arises at this point is whether the same is valid for the second important parameter characterising flame-wall interactions, the normalized quenching distance Pe_Q. However, in contrast to the normalized wall heat flux, less data has been published to date. Table 3.1 sums up the quenching Peclet numbers found in literature. Note that there are several definitions of the

Table 3.1: Head-on Quenching Peclet numbers Pe_Q found in literature. Annotations: '-' indicates that no data was published; 'generic' indicates the use of a generic single-step chemistry.

Author(s)	Ref.	Meth.	Pe_Q	Fuel	flame length	flame pos.
Westbrook et al.	[208]	DNS	3.5	CH_4, CH_4O	$l_F, T_{ref} = T_b$	$1500K$
Vosen et al.	[201]	exp.	$3.0 - 3.2$	CH_4	$l_F, T_{ref} = T_u$	-
Huang et al.	[92]	exp.	3.0	CH_4, C_2H_4, C_3H_8	$l_F, T_{ref} = T_u$	-
Poinsot et al.	[149]	DNS	$3.0 - 4.4$	generic	$l_F, T_{ref} = T_u$	$\frac{T-T_u}{T_b-T_u} = 0.9$
Wichman et al.	[210]	theor.	$2 - 4$	generic	-	-
Bruneaux et al.	[30]	DNS	$3.3 - 3.68$	generic	$l_F, T_{ref} = -$	-
Popp et al.	[157]	DNS	$0.34 - 0.37$	CH_4	δ_F	$\dot{\omega}_{max}$
Hasse et al.	[87]	DNS	$0.37 - 0.42$	C_8H_{18}	δ_F	$1500K$
Enomoto	[64]	exp.	$4 - 7$	CH_4	$l_F, T_{ref} = -$	optical
Bellenoue et al.	[17]	exp.	$3.8 - 4.7$	CH_4	$l_F, T_{ref} = T_u$	optical
Dabireau et al.	[45]	DNS	1.7	H_2	δ_F	$\dot{\omega}_{max}$
Desoutter et al.	[52]	DNS	3.46	generic	$l_F, T_{ref} = T_u$	-
Boust et al.	[26]	exp.	2.6	CH_4	$l_F, T_{ref} = -$	optical
Gruber et al.	[81]	DNS	1.4	H_2	δ_F	-
Chauvy et al.	[39]	DNS	$0.33 - 0.38$	C_8H_{18}	δ_F	$1500K$
Mann	[119]	exp.	0.37	CH_4	δ_F	$\dot{\omega}_{max}$
Lai et al.	[106]	DNS	$2.75 - 3.09$	generic	$l_F, T_{ref} = T_u$	$\frac{T-T_u}{T_b-T_u} = 0.9$

flame position and flame length. The use of δ_F rather than l_F commonly leads to smaller values for Pe_Q. The different definitons of the flame length can be related via Eq. (2.59). For stoichiometric methane-air flames at atmospheric conditions, for example, the ratio δ_F/l_F equals 8 (Dreizler and Böhm [54]). Using this factor, the Peclet numbers for these conditions reported by Popp and Baum [157] and Mann [119] can be converted to $Pe_Q \approx 3$. Hasse et al. [87] stated that if the quenching distances they calculated for iso-octane are normalized with l_F ($T_{ref} = T_u$), Peclet numbers larger than 3 are obtained. Analogously, this also applies to the results of Chauvy et al. [39]. It can thus be concluded that the Peclet number Pe_Q for HOQ at low pressures is almost constant and ranges around 3.5 for hydrocarbon fuels. This behaviour is plausible, since the wall heat flux φ_Q and Pe_Q are inversely correlated.

Chemical aspects

For a deeper understanding of flame-wall interactions, the investigation of the on-going chemical reactions is indispensable. Most studies on this issue used a simulative approach since the chemical state near the wall is very difficult to observe experimentally. Only recently, progress in laser diagnostics enabled some insights (cf. Dreizler and Böhm [54], Mann [119], Mann et al. [120]). One of the first calculations of HOQ using detailed chemistry was conducted by Westbrook et al. [208]. More recent results for methane-air (Popp and Baum [157, 158]), propane-air (Kiehne et al. [101], Popp and Baum [157]), hydrogen-oxygen (Dabireau et al. [45], Owston et al. [133]), n-heptane-air (Owston et al. [132]) and iso-octane-air (Hasse et al. [87], Chauvy et al. [39]) mixtures basically confirmed and extended the findings of Westbrook. In general, three phases can be distinguished during laminar flame-wall interaction at sufficiently low wall temperatures:

1. Initial phase. During the initial phase, the flame and its structure is equal to the undisturbed laminar planar flame. The flame starts to feel the presence of the wall at a wall distance of about two flame thicknesses (Popp and Baum [157]) or $Pe \approx 10$ (Poinsot et al. [149], Dabireau et al. [45]). Even after entering the so-called influence zone, the flame retains its inner structure as detailed in section 2.3.1 (cf. Popp and Baum [157]).

2. Transient phase and quenching. In this rapidly proceeding phase, the wall heat losses increase strongly. As a result, the reaction rate of radical-fuel reactions, which are the main pathway for radical consumption in a freely propagating laminar flame, decays since these reactions typically have a high activation energy. The radicals are then consumed by recombination reactions with small activation energies (Westbrook et al. [208]). This further decreases the rate of radical-fuel and chain-branching reactions and the flame cannot propagate further due to an insufficient amount of radicals. In this moment, the flame reaches its minimum distance to the wall and is quenched. An exemplary species distribution in the moment of quenching is shown in Fig. 3.5. As a result of the depleted radical pool near the wall, stable intermediate species as well as fuel and oxidizer peak at the wall whereas the highest concentration of radical species is found in some distance from the wall (Westbrook et al. [208], Popp and Baum [157], Hasse et al. [87]).

3. Post-flame oxidation. In this final stage, the unconsumed fuel and intermediate species diffuse towards the hot burned gas where they are subsequently oxidized due to a sufficiently high radical level. This process is further detailed in section 5.2.1. The rate of oxidation strongly depends on the type of fuel used. Short hydrocarbons decay significantly faster than long hydrocarbons which offer more pathways for the formation of IHCs (Kiehne et al. [101], Hasse et al. [87]).
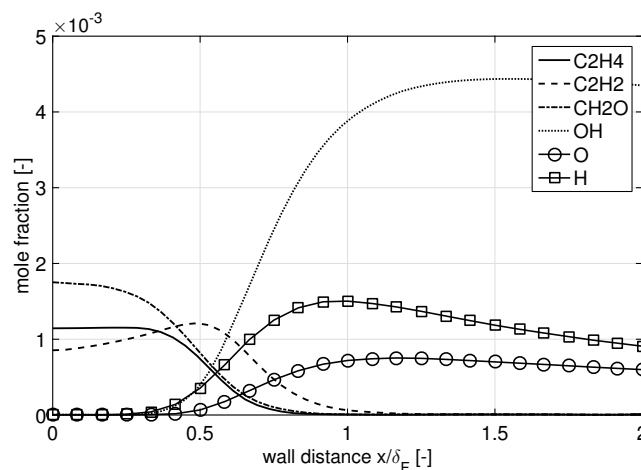

Figure 3.5: Species mole fractions at the quenching instant during HOQ of C_8H_{18} at $T_W = 400K$ (data taken from Hasse et al. [87]).

It shall be remarked that the radical level near the wall substantially increases for high wall temperatures ($T_W \gg 400K$) and that in this case, surface reactions as well as catalytic effects of the wall material have to be considered (cf. Vlachos et al. [198], Popp and Baum [157, 158], Egolfopoulus et al. [62], Owston et al. [132, 133]). Compared to inert walls, the computed wall heat fluxes are lower and the quenching distances are slightly higher. The effect of quenching due to radical recombination at surfaces is often referred to as radical or kinetic quenching and plays a major role in micro- or meso-scale combustion devices (cf. Bai et al. [16], Zhang et al. [218]). Below $T_W \leq 400K$, surface reactions can be completely neglected (Popp and Baum [157]).

3.1.2 Side-wall quenching

Side-wall quenching is the second limiting case of laminar flame-wall interactions. In contrast to HOQ, the flame propagates parallel to the wall and not perpendicular towards it. As a consequence, SWQ is intrinsically two-dimensional as heat conduction occurs parallel as well as perpendicular to the wall. SWQ has been examined less extensively as HOQ in theoretical (von Kármán and Millan [200], Makhviladze and Melikhov [118]), simulative (Blint and Bechtel [22], Carrier et al. [35], Ezekoye and Greif [68], Andrae et al. [13, 14]) and experimental studies (Potter and Berlad [159], Clendening et al. [40], Blint and Bechtel [22], Saffman [168], Fairchild et al. [70], Lu et al. [116], Bellenoue et al. [17], Enomoto [65], Boust et al. [26]).
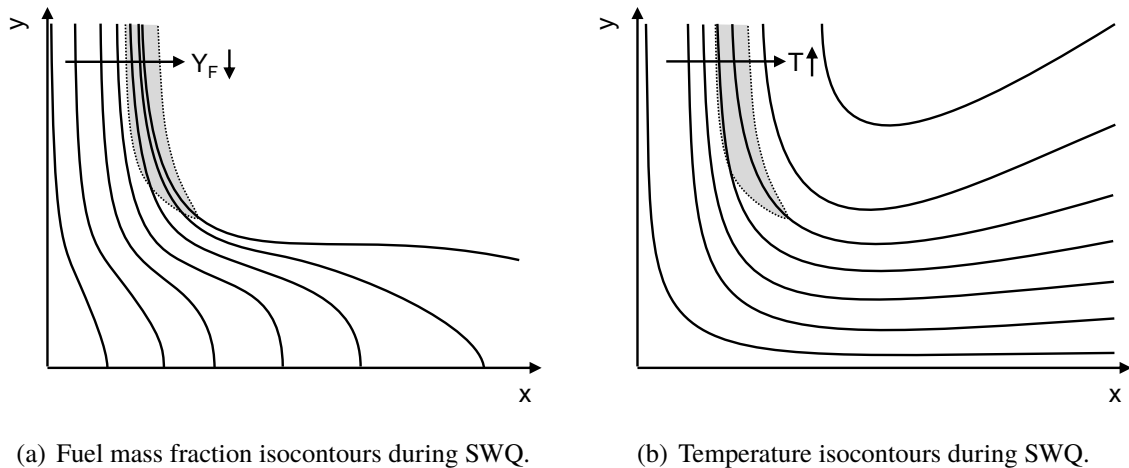

(a) Fuel mass fraction isocontours during SWQ.   (b) Temperature isocontours during SWQ.

Figure 3.6: Schematic fuel mass fraction and temperature isocontours during SWQ with an indicated luminous zone, the flame propagates from right to left (abstracted from von Kármán and Millan [200], Makhviladze and Melikhov [118], Carrier et al. [35]).

A typical SWQ configuration is schematically shown in Fig. 3.6. Based on the existing studies of SWQ, it can be concluded that the mechanism of quenching during SWQ is similar to the one during HOQ. The nearer the flame is to the wall, the more pronounced are the wall heat losses until a reaction can no longer be sustained due to the low temperature level. The

reaction halts as the radicals are depleted by recombination reactions near the wall (Andrae et al. [13]). With only few radicals left, the fuel can no longer be consumed . Subsequent to quenching, the isotherms move away from the wall behind the flame due to the wall heat flux. The unconsumed fuel diffuses away from the wall towards the burned gases, where post-oxidation may occur (Carrier et al. [35], Andrae et al. [14]).

The chemical aspects of HOQ and SWQ are quite similar and the question arises if the global aspects, the wall heat flux φ_Q and the Peclet number Pe_Q are comparable, too. Unfortunately, data on SWQ is scarce and contradictory to some extent. Using the same methodology as Vosen et al. [201], Huang et al. [92] and Ezekoye et al. [69], Lu et al. [116] stated that the normalized wall heat flux during SWQ is similar to HOQ and ranges between $\varphi_Q \approx 0.3 - 0.4$ for a wide variety of fuels and equivalence ratios. A numerical study by Ezekoye et al. [68] concluded that the maximum wall heat fluxes during SWQ and HOQ differ by less than 10%, which seems to confirm these results. However, more recent studies suggest a different conclusion.

Table 3.2: Side-wall Quenching Peclet numbers Pe_Q found in literature. Annotations: '-' indicates that no data was published; 'generic' indicates the use of a generic single-step chemistry.

Author(s)	Ref.	Meth.	Pe_Q	Fuel	flame length	flame pos.
Karman et al.	[200]	exp.	$5.9 - 6.66$	CH_4, C_2H_4, C_3H_8	$l_F, T_{ref} = -$	-
Bellenoue et al.	[17]	exp.	$5.6 - 8.5$	CH_4	$l_F, T_{ref} = T_u$	optical
Poinsot et al.	[149]	DNS	7	generic	$l_F, T_{ref} = T_u$	$\frac{T-T_u}{T_b-T_u} = 0.9$
Enomoto	[65]	exp.	$6.3 - 6.8$	CH_4	$l_F, T_{ref} = -$	optical
Boust et al.	[26]	exp.	4.5	CH_4	$l_F, T_{ref} = -$	optical

In this context, it is helpful to take a look at the quenching distances and utilize the inverse correlation between φ_Q and Pe_Q. As it can be seen in Table 3.2, the normalized quenching distances for SWQ ($Pe_Q \approx 7$) are larger compared to the ones during HOQ (Table 3.1) by a factor of about $2 - 3$. This is confirmed by the measurements of Bellenoue et al. [17] and Boust et al. [26] as well as by the numerical results of Poinsot et al. [149]. Consequently, φ_Q has to be smaller in the SWQ case. Assuming that $\varphi_{Q,HOQ} \approx 0.3$ and $Pe_{Q,SWQ}/Pe_{Q,HOQ} \approx 2$ yields $\varphi_Q \approx 0.15$ which is in good agreement to Poinsot et al. [149] and Poinsot and Veynante [150] who claim $\varphi_{Q,SWQ} \approx 0.16$. Hence, the typical scales of SWQ at low pressures can be estimated as $\varphi_Q \approx 0.15$ and $Pe_Q \approx 7$.

3.1.3 Conclusion

In this section, laminar flame-wall interactions were studied highlighting the effects of the wall on a premixed flame. In general, laminar flame quenching can be characterized by the normalized wall heat flux φ_Q and the normalized quenching distance Pe_Q. It was shown that these parameters remain almost constant for wall temperatures below 600K for a wide variety of fuels (except H_2), equivalence ratios, pressure and temperature levels. The typical scales at low pressures are given by:

- Head-on Quenching: $Pe_Q \approx 3.5$, $\varphi_Q \approx 0.3$

- Side-wall Quenching: $Pe_Q \approx 7$, $\varphi_Q \approx 0.15$

At engine-like conditions, the wall heat flux during HOQ is expected to decrease to $\varphi_Q \approx 0.2$. The fact that the normalized wall heat flux φ_Q remains almost constant indicates that quenching at wall temperatures below $600K$ is mainly influenced by heat losses, i.e., thermally controlled. Several numerical studies (e.g., Westbrook et al. [208], Popp and Baum [157, 158]) further clarified the thermal notion of laminar premixed flame quenching by examining the chemical reactions during the process. The heat loss leads to a promotion of radical recombination reactions depleting the radical pool needed for sustaining the radical-fuel and chain-branching reactions. Ultimately, fuel and stable intermediate species can no longer be consumed and the flame comes to a halt. After the rapidly proceeding extinction process, the remaining fuel reacts in a post-flame oxidation process. For wall temperatures $T_W \gg 400K$, surface reactions and catalytic effects become more and more important and quenching can become kinetically determined rather than thermally controlled.

Finally, it has to be remarked that in a strict sense, these conclusions are only valid for planar premixed flames and clean walls. In reality, flames may be stretched. In this case, the flame can be extinguished by smaller heat losses (cf. section 2.3.1) resulting in higher quenching distances (Benkhaldoun et al. [18], Egolfopoulos et al. [62], Enomoto [65]). However, flame stretch is expected to tend to zero during HOQ (Foucher et al. [73], Sotton et al. [180]) and there are studies indicating that it is a second order parameter in general (Boust et al. [26], Tayebi et al. [186]). In addition to flame stretch, the walls of the combustion chamber can be soiled. This may result in a completely different interaction between flame and wall. For example, if a liquid fuel film covers the wall, the flame is ultimately extinguished by reaching the rich flammability limit at a flame-film distance of $Pe_Q \approx 20$ (Desoutter et al. [52]).

3.2 Near-wall turbulence

Near-wall turbulence plays a decisive role for turbulent flame-wall interactions and a basic understanding of the effects of the wall on turbulent flows is essential. In most practical flows, the flow region is bounded by one or more solid surfaces and a boundary layer develops due to the no-slip condition at the wall. A comprehensive review of this topic can be found in the textbooks by Pope [154], Davidson [49] and Schlichting [172]. The focus of the present section lies on a short discussion of the characteristics of a turbulent boundary layer in a channel flow and of a turbulent, shear-free boundary layer. The difference between the two is that the former is governed by a mean flow whereas the latter is not. They can thus be interpreted as opposing limiting cases for turbulent boundary layer flows, which play a decisive role in the study of turbulent flame-wall interactions.

3.2.1 Fully developed turbulent channel flow

The fully developed turbulent channel flow is one of the basic canonical configurations of turbulence research. It bears strong similarities to turbulent boundary layer flows over flat planes. For example, the famous log-law is valid in both cases (Pope [154]). Turbulent

boundary layers driven by mean shear are governed by viscous effects and can be described using the viscous scales, namely the friction velocity u_τ and the viscous length scale $l^+ = \nu/u_\tau$. Using these scales, major statistical values of the boundary layer can be described almost independently of Reynolds number (Pope [154], Davidson [49]). Most prominently, the mean streamwise velocity $u^+ = \bar{v}_1/u_\tau$ can be described dependent on the normalized wall distance

$$y^+ = \frac{y}{l^+} = \frac{u_\tau y}{\nu}. \tag{3.3}$$

This was first done by von Kármán [199] and leads to the law of the wall for the viscous sublayer ($u^+ = y^+$) and for the logarithmic layer ($u^+ = 1/\kappa \ln y^+ + B$). It is interesting to note that the vast majority of near-wall treatments in turbulence modelling is based on these viscous near-wall scales.

In order to understand the near-wall behaviour of a turbulent flame, the flow motions perturbing the flame front have to be examined. In typical boundary layers over flat planes, the most vigorous turbulence activity occurs in the vicinity of the wall (Fig. 3.8a), typically around $y^+ \approx 20$ (Pope [154]). Turbulence production and dissipation, the turbulent kinetic energy and anisotropy all peak within this region. The flow motions in this region can best be illustrated by the concept of coherent motions, which describes the internal structure of the boundary layer by using quasi-periodic, repeating patterns. The coherent motions are responsible for the transfer of momentum, vorticity and turbulence as well as for generating Reynolds stresses and turbulence (Adrian et al. [6]). The prime example is the horseshoe or hairpin vortex (Fig. 3.7) introduced by Theodorsen [189] in 1952. A profound investigation of the structures found in turbulent boundary layers of flat planes was conducted by Robinson [163, 164]. His findings, which were later complemented and confirmed by Adrian et al. [5, 6], are summarized in Fig. 3.7.
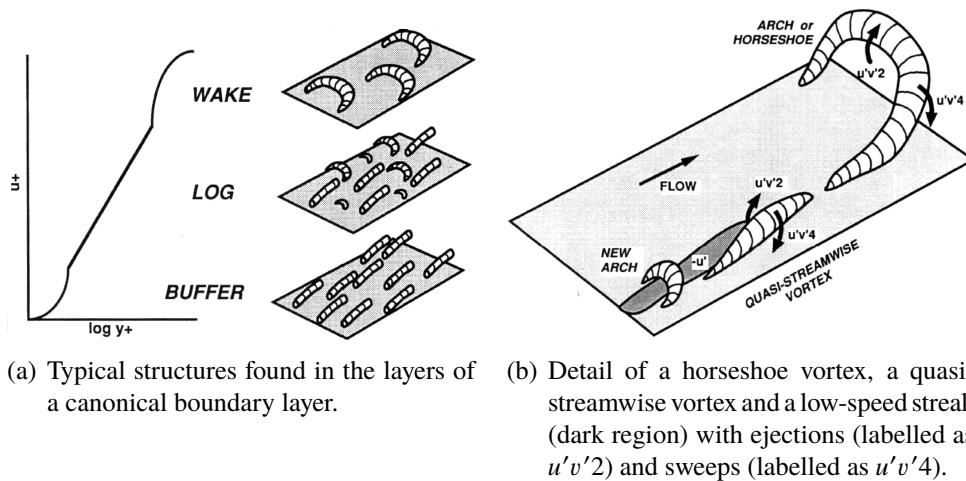

(a) Typical structures found in the layers of a canonical boundary layer.

(b) Detail of a horseshoe vortex, a quasi-streamwise vortex and a low-speed streak (dark region) with ejections (labelled as $u'v'2$) and sweeps (labelled as $u'v'4$).

Figure 3.7: Summary of coherent structures found in direct numerical simulations of a canonical boundary layer (taken from Robinson [164]).

Starting from the wall, coherent motions are first encountered in the buffer layer ($5 < y^+ < 30$) being the most important zone for the production and dissipation of turbulence. It

predominantly contains so-called stream-wise vortices which cause a fluid transfer away and towards the wall due to their rotation. Slow fluid is ejected from the wall (ejection) whereas faster fluid is propelled towards the wall (sweep) resulting in low-speed or high-speed streaks (Fig. 3.7b). As a consequence, the streamwise Reynolds stress $\overline{v_1' v_1'}$ strongly fluctuates near the wall. The mean spanwise spacing between the unsteady, elongated regions of high and low fluid velocity is approximately 100 viscous lengths l^+ (Robinson [163], Pope [154]). In the logarithmic layer, hairpin vortices, which may extend into the wake, are commonly found (Adrian et al. [5]). Their motion also induces ejections, sweeps and streaks as shown in Fig. 3.7b. Slow fluid is ejected between their legs whereas fast fluid is transferred towards the wall on their outer side.
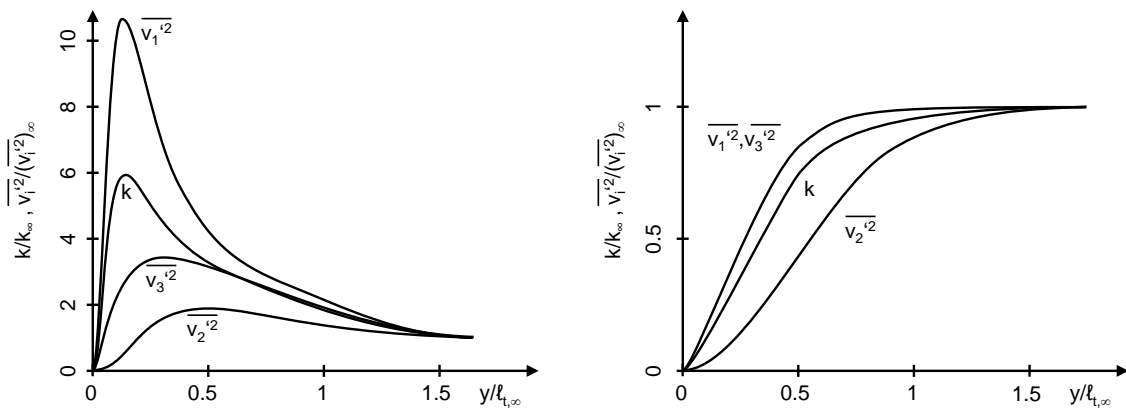
(a) Turbulent channel flow at $Re_\tau = 180$ (data from Moser et al. [125]).

(b) Shear-free boundary layer (abstracted from Perot et al. [135]).

Figure 3.8: Schematic Reynolds stresses of two different turbulent boundary layers. All values are normalized to the conditions in the middle of the channel (turbulent channel flow) or far away from the wall (shear-free boundary layer) indicated by '∞'.

3.2.2 Shear-free turbulent boundary layer

Without a mean flow driving the production of turbulence near the wall, the characteristics of the boundary layer change completely. A shear-free turbulent boundary layer is inherently unsteady as turbulence decays in time due to viscous dissipation. It can be encountered in separating and reattaching flows, for example (Perot and Moin [135]). It was examined in experimental (e.g., Uzkan and Reynolds [193], Thomas and Hancock [190], Hunt and Graham [93]) and simulative studies (e.g., Biringen and Reynolds [21], Perot and Moin [135]).

Fig. 3.8b schematically shows the Reynolds stresses in a shear-free turbulent boundary layer. As there is no mean production of turbulence, the tangential Reynolds stresses and the turbulent kinetic energy exhibit no peak near the wall as it is the case in a turbulent channel flow (Fig. 3.8a). Although energy is transferred form the wall-normal to the the

wall-tangential fluctuations, it is dissipated too quickly to have a decisive impact on the wall-tangential fluctuations (Perot and Moin [135]). The coherent motions found in this type of boundary layer are splats and anti-splats. A splat is a local stagnation point flow in a region where fluid impinges on the wall at a normal angle and is subsequently diverted into a wall-parallel direction. This constitutes an energy transfer from the wall-normal velocity to the wall-tangential velocity components (blocking effect of the wall). Due to continuity, the splat has a counterpart, namely the anti-splat describing regions ejecting fluid. However, anti-splates contain lesser energy than splats due to the viscous dissipation near the wall (Perot and Moin [135]).

3.2.3 Conclusion

The presence of the wall significantly affects a turbulent flow by the generation of a turbulent boundary layer, whose characteristics strongly depend on the outer flow. Two different limiting cases, a turbulent channel flow and a shear-free turbulent boundary layer, have been discussed. They are remarkably different, although the only difference is the presence of mean shear. In a turbulent channel flow, the mean shear, which is induced by an outer velocity and the no-slip condition at the wall, leads to a production of turbulence. As a consequence, the Reynolds stresses as well as the turbulent kinetic energy peak in the vicinity of the wall despite the enhanced dissipation. In a shear-free boundary layer, this mechanism is absent and all Reynolds stresses as well as the turbulent kinetic energy decay towards the wall without exhibiting a peak. The coherent motions are different, too. In a turbulent channel flow, elongated streamwise and hairpin vortices can be found whereas a shear-free turbulent boundary layer is governed by stagnation-point flows, the so-called splats. These aspects have a decisive impact on the near-wall flame propagation and are vital for discussing and understanding turbulent flame-wall interactions, which will be the topic of the following section.

3.3 Turbulent flame-wall interaction

Having discussed the fundamentals of turbulent flames (section 2.3.2), laminar flame-wall interactions (section 3.1) and near-wall turbulence (section 3.2), the literature concerning turbulent flame-wall interactions can be critically reviewed. The main focus is thereby laid on the question how near-wall turbulence influences the flame propagation and thereby the wall heat flux and the flame-wall distance during quenching. The aim of this section is to establish a comprehensive phenomenological picture of turbulent flame-wall interactions. For this purpose, the literature is classified by the type of boundary layer flow.

3.3.1 Flame-wall interaction in turbulent shear-free boundary layers

Shear-free turbulent boundary layers have been used by Poinsot et al. [149] and Lai and Chakraborty [106] to study the behaviour of a statistically one-dimensional turbulent flame in a head-on quenching situation. In these studies, the authors conducted DNS simulations

using a generic one-step chemistry. Although the insights into the chemistry are thus limited, the influence of turbulence on the flame-wall interaction process can be evaluated. A time sequence of a turbulent flame interacting with the wall is shown in Fig. 3.9.
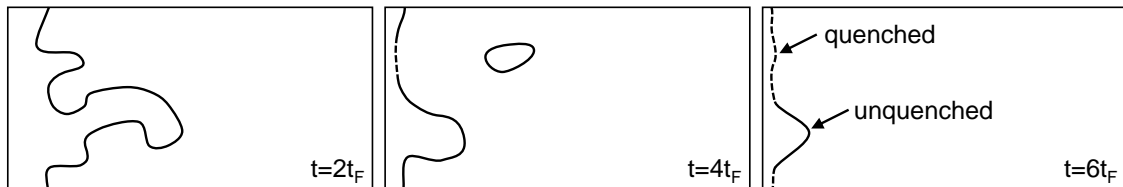

Figure 3.9: Schematic flame contours of a statistically one-dimensional turbulent flame during HOQ (abstracted from Lai et al. [106]).

In case of a shear-free turbulent boundary layer, the decrease of the turbulent fluctuations towards the wall causes a reduction of flame wrinkling as well as of the turbulent flame brush thickness. As a consequence, the parts of the flame which are in the immediate vicinity of the wall become laminar again and most flamelets are quenched almost unstretched (Poinsot et al. [149]). The convexly shaped leading flamelets are the first to interact with the wall (Fig. 3.9 at $t = 4t_F$). They encounter the wall at normal angles corresponding to a HOQ situation. For flames with $Le \geq 1.0$, the quenching distance in these cases was found to be equal to the laminar value, irrespective of turbulence intensity (Poinsot et al. [149], Lai and Chakraborty [106]). The Peclet numbers range from $Pe_Q = 2.83$ (Lai and Chakraborty [106]) to $Pe_Q \approx 3.5$ (Poinsot et al. [149]) for flames with $Le = 1.0$. Similarly, the wall heat flux during quenching remains within the bounds of laminar flame-wall interaction. However, if the Lewis number is smaller than unity, smaller quenching distances and higher wall heat fluxes are observed. In these cases, the convex shape of the flamelets cause an accumulation of reactants and a slower heat diffusion resulting in an increased heat release rate and burned temperature. For flames with $Le = 0.8$, the quenching distance consequently decreases by a factor of 1.5-2 whereas the wall heat flux increases correspondingly. This effect is more pronounced for higher turbulence intensities due to an enhanced wrinkling of the flame surface (Lai et al. [106]). Most hydrocarbon flames commonly have a Lewis number close to unity and it can thus be expected that the mentioned Lewis number effects are weak. At later stages of the interaction process, some of the trailing flamelets propagate parallel to the wall (Fig. 3.9 at $t = 6t_F$). They are quenched at $Pe_Q \approx 7$, similar to SWQ (cf. Poinsot et al. [149]).

These results suggest that in a shear-free turbulent boundary layer, the turbulent flow motions near the wall are too weak to substantially influence the local thermo-diffusive processes leading to quenching. However, turbulence decisively influences the overall shape and wrinkling of the turbulent flame prior to flame quenching. As a consequence, the turbulent flame-wall interaction process is governed by the kinematics of the turbulent flame brush causing the leading flamelets to quench earlier than the trailing ones. The local quenching process, however, remains laminar.

3.3.2 Flame-wall interaction in turbulent boundary layers with mean shear

Boundary layers similar to the previously discussed turbulent channel flow have often been used in experimental (e.g., Richard and Escudié [162], Tayebi et al. [186–188]) and simulative (e.g., Bruneaux et al. [29–31], Alshaalan and Rutland [11, 12], Gruber [79], Gruber et al. [80, 81]) studies of turbulent flame-wall interaction.

In contrast to shear-free boundary layers, the degree of wrinkling of the flame surface increases towards the wall (Richard and Escudié [162], Gruber et al. [81]). This can be attributed to the enhanced turbulent fluctuations near the wall. Moreover, the turbulent length and time scales decrease towards the wall, whereas the chemical time scale increases. Ultimately, the smallest eddies are able to penetrate into the preheat zone inducing a combustion regime change to the thin reaction zones regime (cf. Gruber et al. [81]). The flame, in turn, weakens the turbulent flow motions such as the streamwise vortices due to viscosity and density changes (Alshaalan et al. [12], Gruber et al. [81]).

The structure of the turbulent flame and the locations of quenching are closely connected to the large-scale, coherent near-wall structures inducing ejections and sweeps (Bruneaux et al. [30], Alshaalan and Rutland [12], Gruber et al. [81]). If slow fluid is ejected from the wall, the wall heat flux decreases in these regions (Alshaalan and Rutland [12], Gruber et al. [81]) and finger-like structures of unburned mixture may appear in the burned gases (Richard and Escudié [162], Bruneaux et al. [30]). During a sweep event on the other hand, the flame is pushed towards the wall by the high fluid velocity which increases the wall heat flux and ultimately leads to the quenching of the flame. The spatial and temporal patterns of these events are correlated with the spatial and temporal scalings of the near-wall coherent motions encountered in the quenching zone (Gruber et al. [81]). The spanwise spacing between the locations of the maximum wall heat flux observed by Gruber et al. [81] was approximately 100 wall units. This is in excellent agreement with the spacing between the counter-rotating, stream-wise vortices (cf. section 3.2) highlighting the kinematic nature of turbulent flame-wall interactions. Since the flame is pushed against the wall, the maximum local wall heat fluxes are higher than the laminar value. The factor between them ranges from 1.25 (Alshaalan and Rutland [12]) and 1.5 (Gruber et al. [81]) to 2 (Bruneaux et al. [30]). The inverse correlation between the wall heat flux and the quenching distance is still valid in turbulent conditions (Alshaalan and Rutland [12]). Consequently, the quenching distance decreases. For example, Bruneaux et al. [30] reported a minimum Peclet number of $Pe_Q \approx 2 - 2.3$ compared to $3.3 - 3.68$ for the laminar case.

By analysing the studies of Gruber et al. [80, 81], it can be suggested that the quenching process itself appears to be the same for turbulent and laminar flames. In both cases, recombination reactions lead to a decrease of the radical level near the wall. As a consequence, the fuel (in their case H_2) can no longer be consumed and the flame is quenched. However, the studies of Gruber et al. [80, 81] are the only ones of turbulent flame-wall interactions to date employing detailed chemistry and a complete picture can only be obtained by further work on this topic.

3.3.3 Conclusion

The phenomenology of turbulent flame-wall interactions is strongly connected to the structure of turbulence encountered near the wall. In a shear-free turbulent boundary layer, for instance, the individual flamelets become laminar in the vicinity of the wall. As a consequence, the wall heat flux and the quenching distance are comparable to the values for laminar flames. However, turbulence controls the initial wrinkling of the flame causing some parts of the flame brush to quench earlier than other ones. In a boundary layer dominated by shear on the other hand, the near-wall region is characterized by a vigorous turbulent activity influencing the near-wall flame propagation and quenching process. The wrinkling of the flame is enhanced near the wall and local quenching is initiated by the coherent motions prevailing in the quenching zone. The quenching distance may decrease by a factor up to 2. However, the flame is still quenched by the thermal effect of the wall as in the laminar case.

In this context, Pitsch [146] speculated that turbulent flame-wall interactions are substantially influenced by the Reynolds number of the flow. The quenching distance can be expressed in terms of wall units as $y_Q^+ = y_Q/l^+ = Pe_Q/Pr\, u_\tau/s_L^0$ (Poinsot et al. [149], Bruneaux et al. [31]). The laminar flame velocity and the quenching Peclet number can be assumed to be independent of Re_t at first order (Pitsch [146]). By increasing the Reynolds number, u_τ increases and the quenching distance can be located outside of the buffer region where the stream-wise vortices are typically found ($y^+ > 50$). Instead, the flame is subjected to different coherent structures, e.g., hairpin vortices, altering the periodicity of local quenching events. This underlines that turbulent flame-wall interactions are decisively influenced by the kinematic nature of near-wall turbulence. Although the effects of wall heat losses are still important for the quenching of individual flamelets, turbulent flame quenching is dominated by the kinematic effects of turbulence, which have to be correctly described by a combustion model.

In addition to the spatial and temporal patterns of turbulent flame quenching, near-wall turbulence also influences the combustion regime during quenching. Near the wall, the turbulent length scale l_t can be expressed in terms of the mixing length $l_m = \kappa y$. Inserting the quenching distance $y_Q = Pe_Q l_F$ leads to $l_t \approx l_F$. The Reynolds number is then proportional to $Re_t \sim v'/s_L^0$. Using the relations (2.32), the Kolmogorov length scale η can be expressed as $\eta \sim (v'/s_L^0)^{-3/4} l_F$. Consequently, the Karlovitz number is proportional to $Ka \sim (v'/s_L^0)^{3/2}$ at first order. Hence, the combustion regime during quenching mainly depends on the ratio of the laminar flame velocity to the fluctuation velocity. In a shear free turbulent boundary layer, the ratio v'/s_L^0 tends to zero. As a result, a laminar flame is encountered near the wall. In turbulent boundary layers with mean shear, the ratio v'/s_L^0 may exceed 1. In this case, the Karlovitz number becomes larger than unity indicating combustion in the thin reaction zones regime. In this case, the transport processes in the preheat zone are altered and the local quenching process may deviate from the one of a laminar flame.

These aspects emphasize that turbulent flame-wall interactions cannot be discussed independently from near-wall turbulence. In other words, if turbulence in the vicinity of the quenching distance can be characterized, a statement concerning the phenomenology of flame-wall interactions can be made. Such an a priori analysis is conducted for SI engines in the next section.

3.4 A priori analysis of flame-wall interactions in SI engines

Although the free-stream turbulence characteristics in the combustion chamber of an internal combustion engine are rather well-known (e.g., Heywood [90]), insights into the boundary layer structure are very limited as the experimental and simulative expenditure is very high. The experimental work of Alharbi et al. [7] and Jainski et al. [95] as well as the DNS simulations of Schmitt et al. [173, 174] can be used to shed some light on this issue.

Alharbi et al. and Jainski et al. measured the flow field in the vicinity of the cylinder head of a direct-injected SI engine using highly resolved, high-speed PIV and PTV (particle tracking velocimetry). The data reported by Alharbi et al. [7] shows that there is no peak of the fluctuation velocity v' in the vicinity of the combustion chamber wall at any given moment in the cycle despite the tumble flow in the cylinder. As shown in a follow-up study by Jainski et al. [95], the classic scaling arguments of turbulent boundary layers with mean shear do not apply to the boundary layers encountered in SI engines. Moreover, the physical thickness of the viscous sublayer was found to be only weakly influenced by engine speed and greater than $400\mu m$, which is larger than the order of the quenching distance ($< 100\mu m$) at elevated pressures. Hence, the boundary layer in a SI engine is expected to differ strongly from a canonical turbulent boundary layer over a flat surface. This conclusion is supported by the results of the DNS simulation of a simplified engine geometry conducted by Schmitt et al. [173, 174]. Again, neither the wall-normal velocity fluctuation nor the wall-tangential velocity fluctuations exhibit a peak near the wall at any point of the cycle. Instead, the profiles are strongly reminiscent of the ones encountered in a shear-free boundary layer.

The emerging picture can be complemented from a phenomenological point of view. The geometry and flow configuration of a combustion chamber is vastly different from any canonical configuration (e.g., pipe or channel flow). Moreover, the flow is highly transient: during the intake stroke, a tumble and/or swirl motion develops which is rapidly deformed during compression. The motion of the cylinder charge subsequently converts into turbulence whereby the swirl motion is partially and the tumble motion is almost completely dissipated (Merker [123]). Without a mean flow motion, the mean shear vanishes resulting in a more and more shear-free turbulent boundary layer. Turbulence in SI engines is thus predominantly created in shear layers caused by the charge motion (particularly tumble) as well as by the intake and squish flow in contrast to the canonical wall-bounded flows where turbulence is mainly generated in the buffer layer near the wall.

It can thus be expected that local flame quenching in SI engines is influenced little by turbulence as the flame is not subjected to velocity fluctuations which may push flamelets towards the wall lowering the quenching distance. Therefore, the quenching distance y_Q as well as Pe_Q and φ_Q are expected to be similar to laminar values. This statement also implies that the near-wall flame propagation is laminar. There is some evidence supporting this conclusion (e.g., Foucher et al. [75]), however, it has yet to be proven thus motivating the measurement and analysis of wall heat fluxes in a SI engine detailed in chapter 4.

3.5 A brief review of flame-wall interaction models

Although flame-wall interactions occur in almost any practical combustion system, little effort has been made on including this phenomenon in a combustion model due to the complexity of the task. The need to account for wall effects at least in some minimal way can already be explained by investigating turbulent mixing rate controlled combustion models, like the well-known EBU model. The burning rate is inversely proportional to the turbulent time scale $\tau = k/\varepsilon$, which tends to zero for $y \to 0$. This leads to an unrealistic acceleration of the flame near the wall as pointed out by many researchers, e.g., Weller et al. [205]. Even CFM models may exhibit similar problems by over-predicting the production of flame surface density near the wall (Nishiwaki [127], Poinsot et al. [149]). In general, each combustion model incorporating the turbulent time scale τ has to be reviewed critically against this background.

Ad-hoc solutions and simple models such as setting the reaction rate to zero in the vicinity of the walls, the subtraction of the incombustible mass (Nishiwaki [127]), the modification of the laminar burning velocity near the wall (Jennings [96]) or the introduction of empirical scaling functions fitted to a specific application (Abu-Orf and Cant [4], Alshaalan et al. [11]) are inadequate since they lack a profound physical description of the quenching process. A comprehensive flame-wall interaction model has to include at least the effects of wall heat loss / flame quenching and near-wall turbulence (Bruneaux et al. [31], Alshaalan et al. [11], Poinsot and Veynante [150]).

The first model that complies with these criteria in a minimal way is the FIST model (Flame Interacting with Surface and Turbulence) developed by Poinsot et al. [149] based on 2D-DNS data. It can be seen as a 'law-of-the-wall' model for specifying the flame surface density Σ in the first computational cell adjacent to the wall. For this purpose, the transport equation for the flame surface density was modified by using the phenomenological insights of the 2D-DNS simulations. However, as stated by Bruneaux et al. [31], the approach of Poinsot et al. [149] is only of limited suitability to study flame-wall interactions due to the decaying turbulence. To isolate the effects of the wall on the turbulent flame, Bruneaux et al. [29–31] conducted 3D-DNS simulations in which the flow is statistically stationary due to the assumption of a constant density and viscosity. The statistically averaged results of 30 simulations were subsequently used to model the main features of flame-wall interaction. The effect of quenching was accounted for by distinguishing between a reactive Σ_R and a total flame surface density Σ and using Σ_R instead of Σ to close the mean reaction rate $\overline{\dot{\omega}}_c$ (Eq. (2.81)). Both quantities are related by the so-called unquenched factor $Q_\Sigma = \langle s_L \rangle_S / s_L^0 = \Sigma_R / \Sigma$. It was modelled as $Q_\Sigma = \exp(-\text{const.} \times \overline{L}_H)$ using the enthalpy loss parameter L_H (cf. Williams [212], Wichman and Bruneaux [210]) which equals 0 for adiabatic flames and increases once the flame becomes non-adiabatic. The individual terms of the transport equation for Σ were modelled using the DNS data. Near-wall turbulence was accounted for by utilizing classic concepts of near-wall turbulence such as the Van Driest damping or the mixing length. The model was tested against DNS data and successfully used in piston engine calculations (e.g., Angelberger et al. [15], Duclos et al. [55]).

The most recent approaches to model flame-wall interactions trace back to Lai and Chakraborty. Similar to Bruneaux et al. [31], they also utilized the DNS data from their

simulations (Lai and Chakraborty [106]) to develop near-wall closures for the transport equations of the scalar dissipation rate (Lai and Chakraborty [107]) and the progress variable variance (Lai and Chakraborty [108]). On the same basis, Sellman et al. [175] derived near-wall closures for the flame surface density approach. All these models account for quenching as well as Lewis number effects. However, the models were only tested a priori against DNS data. Their predictive capabilities, especially in combination with RANS or LES turbulence modelling, have yet to be proven.

A comprehensive theoretical approach for modelling flame-wall interactions is still missing and appropriate models for flame-front tracking methods such as the *G*-equation model have yet to be developed. In this context, the behaviour of the turbulent burning velocity near the wall is of particular interest. A profound investigation of this topic is provided in chapter 5.

4 Experimental and simulative analysis of flame-wall interactions in a spark-ignition engine

The nature of flame-wall interactions in SI engines along with its characteristic scales is still largely unknown. The reason for this is the difficult experimental observability, which traces back to the small length and time scales of the quenching process (cf. chapter 3). Moreover, measurements within the combustion chamber of a SI engine are complicated by a restricted access, vibrations, thermal and mechanical stresses as well as by inherent cyclic fluctuations. For these reasons, a robust experimental method to estimate a characteristic quantity of flame-wall interactions is required. In this context, the wall heat flux is particularly interesting and has often been used since it is relatively easy accessible and allows an estimation of the quenching distance (cf. chapter 3). Methodologies for the highly-resolved measurements of wall heat fluxes in SI engines have already been developed and applied numerous times (e.g., Alkidas [8, 9], Wimmer et al. [213]). However, to the best of the author's knowledge, no study has yet been published that examines flame-wall interactions in SI engines on this basis. In this chapter, this issue is addressed by the following main steps:

1. Measurement and analysis of the wall heat flux traces at five different operating points in order to determine the quenching wall heat flux $\dot{Q}_{W,Q}$ and to provide a data basis for studying its dependency on engine speed, load, charge motion and equivalence ratio.

2. Estimation of flame properties such as s_L^0, l_F or T_0, which are required for analysing the quenching wall heat flux, using a combination of 3D-CFD, 3D-FE and 1D simulations.

3. Evaluation of the flame-wall interaction process based upon the quenching distances y_Q, normalized wall heat fluxes φ_Q and Peclet numbers Pe_Q.

Hence, this chapter is structured as follows: after shortly introducing the experimental layout and method, the wall heat fluxes are analysed. The focus is thereby laid on the analysis of single cycles as well as on the determination of the wall heat flux during quenching $\dot{Q}_{W,Q}$. Subsequently, a methodology is developed to estimate the quenching distance y_Q as well as φ_Q and Pe_Q based on a succession of 1D, 3D-CFD as well as 3D-FE simulations. Using this information, the scales of the flame-wall interaction process in a SI engine are analysed and compared to the values found in literature. This chapter is concluded by summarizing the main findings and their implications towards modelling.

4.1 Experimental setup and procedure

4.1.1 Engine test bench and measuring technology

The engine used in the experimental investigations was a series production three-cylinder BMW B38 engine which was modified to run only on cylinder 1. The rocker arms of cylinder 2 and 3 were removed so that the corresponding valves remained in a closed position. The pistons were retained in order to maintain a proper mass balance. The engine is equipped with a fourth generation Valvetronic allowing a seamless adjustment of valve lift and timing. Further technical details are presented in Table 4.1.

Table 4.1: B38 engine specifications.

Engine type	Gasoline engine 4-stroke
Cylinders/Valves per cylinder	1/4
Compression ratio	11.0
Displacement volume	$499.6 cm^3$
Bore x Stroke	82mm x 94.6mm
Connecting rod length	148.2mm
Injection system	Solenoid valve fuel injection
Combustion process	Direct injection, homogeneous charge combustion

Since the turbocharger had to be removed, the engine was charged by an external compressor. Exhaust pressure was influenced by a dedicated throttle valve. The ECU was used to control spark, valve and injection timing as well as valve lift and equivalence ratio. All other parameters like coolant temperature or intake manifold pressure were controlled by the test bed automation system. A complete overview of the test bench and the periphery is given in Fig. 4.1.

The wall heat fluxes were estimated by using the surface temperature method which was developed around 1930 by Eichelberg [63] and Salzmann [169]. It has already been used numerous times to estimate wall heat fluxes in internal combustion engines, e.g., Alkidas et al. [8, 9], Gilaber et al. [77], Harigaya et al. [86], Wendland [206], Wimmer et al. [213], Chang et al. [36]. It proved robust enough to withstand the harsh environment while providing a sufficient accuracy and low response times. For the present investigation, eight coaxial K-type surface thermocouples by the company Medtherm were installed in the cylinder head of the engine. According to the manufacturer, the thin plating of less than $2\mu m$ yields a time constant of around $1\mu s$. The thermocouples were mounted in aluminium sleeves, which is the same material as the cylinder head to minimize the impact on the heat conduction in the cylinder head. The assembly was calibrated by using a dynamic test rig described in a paper of Wimmer et al. [213]. With this approach, manufacturing tolerances can be accounted for and the error due to heat conduction between the sleeve and the thermocouple can be minimized. The assembled thermocouples were installed flush to the cylinder head wall thereby retaining the original geometry of the engine. The measuring locations can be seen in Fig. 4.2a. The sensors were connected with drilled copper cables to an analogue amplifier and subsequently
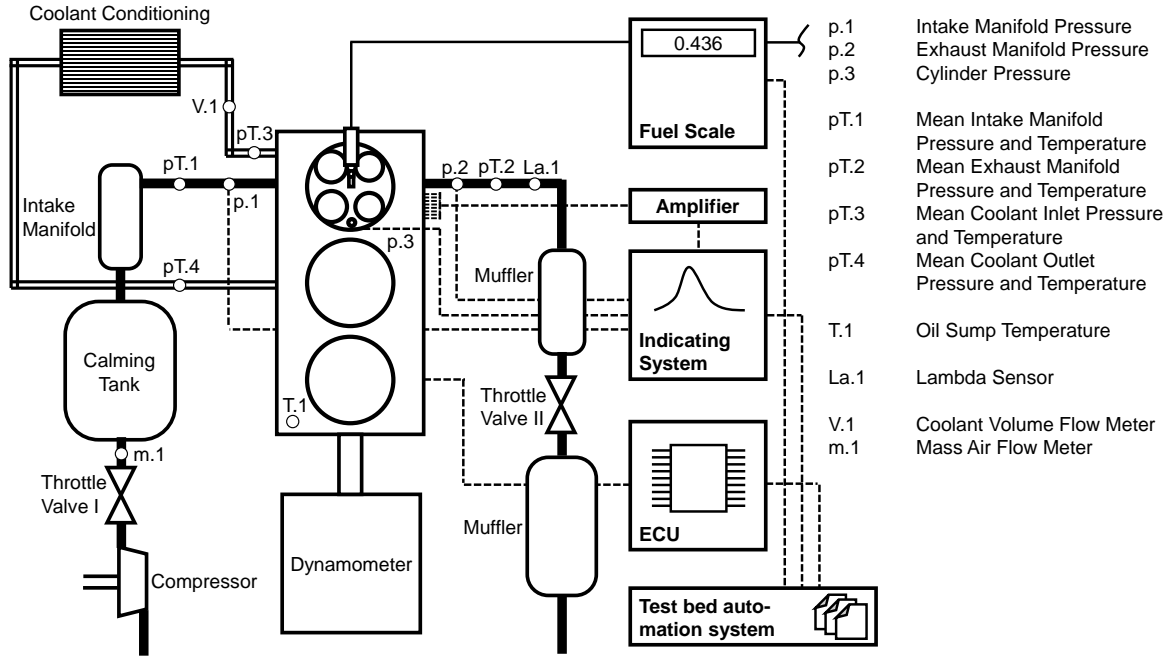
Figure 4.1: Overview of engine test bench and important measuring points.

to the indication system. The sampling interval was $0.5°CA$, which equals to a sampling frequency of 24 kHz and 48 kHz at 2000rpm respectively 4000rpm. Flame-wall interactions are expected to take around $O(150\mu s) - O(1ms)$ at elevated pressures [105, 180]. Therefore, the time resolution is sufficient. For a periodic working cycle, the wall heat flux can be calculated based on the (analytical) solution $T_W(x, t)$ of the one-dimensional heat conduction for infinite planes. Differentiation of $T_W(x, t)$ yields an expression for the transient wall heat flux at the surface ($x = 0$):

$$\dot{q}_W = -\lambda_W \frac{\partial T_W}{\partial x} = C + \lambda_W \sum_{j=1}^{\infty} \sqrt{\frac{j\omega}{2D_w}} \left[\left(A_j + B_j\right) \cos\left(j\omega t\right) + \left(-A_j + B_j\right) \sin\left(j\omega t\right) \right] \quad (4.1)$$

The constants A_j and B_j can be identified by a Fourier analysis of the measured temperature signal. The parameter C represents the steady state heat flux and D_w is the thermal diffusivity of the wall material. Using the gas temperature $T_G(t)$ from a 1D simulation, C can be estimated by requesting $\dot{q}_W = 0$ when $T_W(t) = T_G(t)$. For further details, the reader is referred to the paper of Wimmer et al. [213].

To account for a possible pollution of the surface of the thermocouple, a well-defined reference point was frequently measured. Soot correction was done by numerically solving the one-dimensional heat conduction equation for an assumed deposit layer. Its thickness was iteratively adjusted by comparing the resulting wall heat flux on the layer surface to the reference wall heat flux recorded with clean thermocouples. An example for this procedure is shown in Fig. 4.2b. The delay of the wall heat flux due to a polluted surface can be almost completely corrected, yet a small difference in the absolute amplitude remains.

Further quantities (cf. Fig. 4.1) were measured which provided the necessary data for
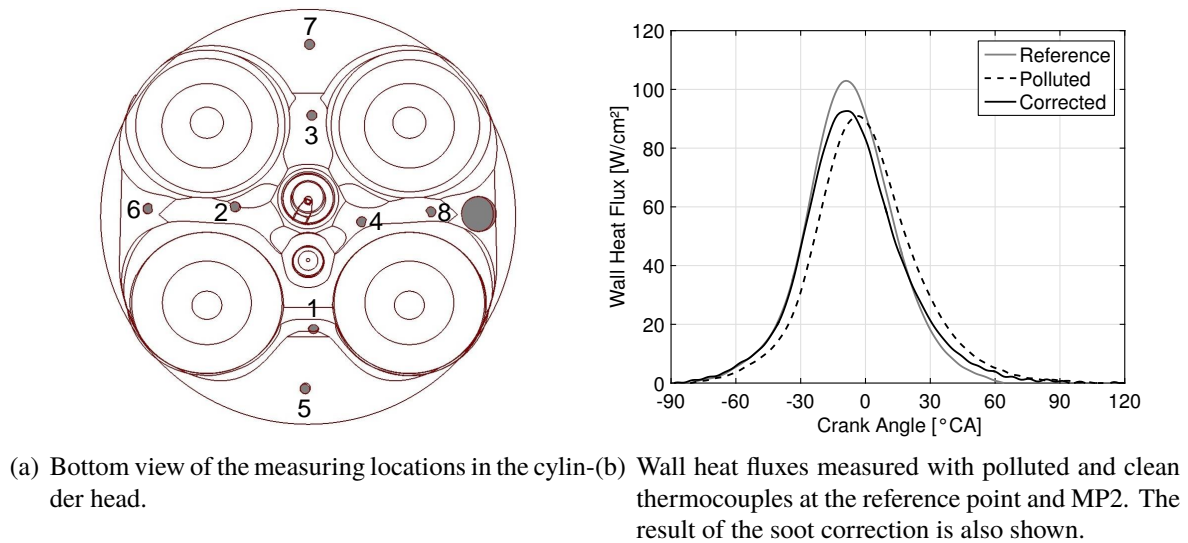
(a) Bottom view of the measuring locations in the cylin-
der head.

(b) Wall heat fluxes measured with polluted and clean thermocouples at the reference point and MP2. The result of the soot correction is also shown.

Figure 4.2: Measuring locations in the cylinder head and soot correction.

the validation of the simulations as well as for the analysis of the gas exchange process. The intake and exhaust pressures ($p.1$ and $p.2$) were recorded using piezo-resistive sensors, whereas the in-cylinder pressure ($p.3$) was measured by an piezo-electric sensor. Their output was captured by the indication system. All remaining quantities were recorded by the engine test bed automation system. Thereby, the pressures were captured by utilizing conventional (piezo-resistive) absolute pressure sensors. All temperatures were recorded by type K, NiCr-Ni thermocouples. The coolant flow was determined by a turbine flow meter and the fuel consumption was estimated using a gravimetric fuel scale.

4.1.2 Experimental procedure and operating points

All experiments were conducted following the same procedure. First, the operating point was set according to the pre-defined conditions (Table 4.2). The measurement started after thermal equilibrium was attained. Except for the signals recorded with the indication system, all quantities were measured and averaged over 60 seconds. In order to achieve a meaningful statistical statement, the indication system was set to capture 1000 consecutive cycles. After completing a small series of measurements, the pre-defined reference point was measured in order to provide the necessary data for the soot correction.

The engine was operated at five different operating points (Table 4.2) in order to investigate the influence of speed, load, charge motion and equivalence ratio on the quenching process. Hence, a wide range of different mixture conditions (e.g., pressure, equivalence ratio) can be covered which is decisive for a thorough analysis of flame-wall interactions. Table 4.2 provides an overview of all operating points and their respective operating parameters. The fuel used for all experiments was gasoline with an addition of 10% ethanol. Moreover, the mean exhaust pressure of all operating points was equal to the ambient pressure. OP1 and OP2 are full load points at different engine speeds whereas OP3 and OP4 are part load

Table 4.2: Investigated operating points and their respective operating parameters.

Operating point	Speed	Load	IMP	Φ	Intake pressure	50%MFB
OP1	2000rpm	full load	20bar	1.0	1.5bar	19°CA
OP2	4000rpm	full load	20bar	1.1	1.5bar	12°CA
OP3	2000rpm	part load	3bar	1.0	0.9bar	8°CA
OP4	2000rpm	part load	3bar	1.0	0.4bar	8°CA
OP5	2000rpm	full load	15bar	0.7	1.5bar	19°CA
RP	2000rpm	no load	0bar	0	1.5bar	–

points differing in the manner of throttling. At OP3, the intake valve lifts are asymmetrically reduced resulting in a swirling charge motion due to the different valve lifts (cf. Fig. 4.3). At OP4, in contrast, the cylinder charge is controlled by a conventional throttle valve while retaining the highest possible (symmetrical) valve lift. As a consequence, the charge motion is dominated by a tumble motion, which also prevails at OP1, OP2 and OP5 (cf. Fig. 4.3). The operating conditions of OP5 are similar to OP1 apart from the injected fuel mass, which was reduced to study flame-wall interactions for lean mixtures.
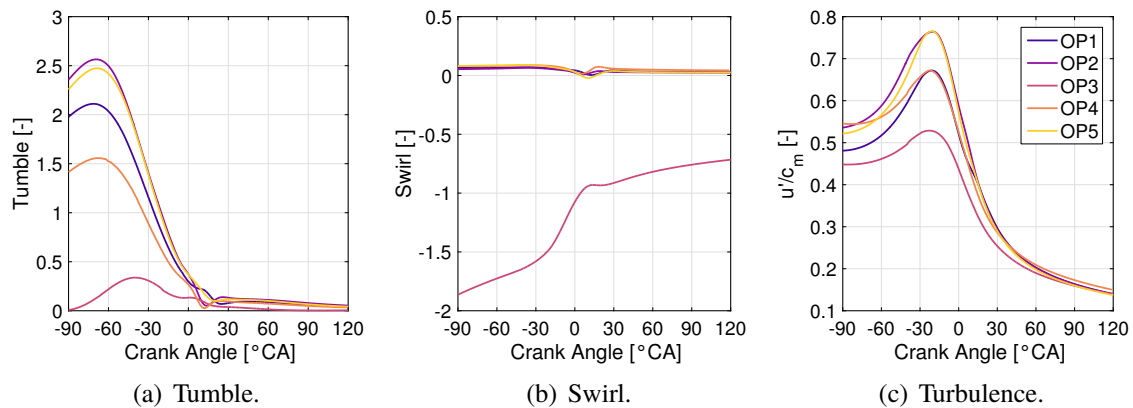

(a) Tumble. (b) Swirl. (c) Turbulence.

Figure 4.3: Charge motion calculated with 3D-CFD simulations. The definition of the tumble and swirl number is given in appendix A.

Note that the measuring points 1 and 7 at operating point 2 are excluded in the following as there were considerable deposits (1) or signal disturbances (7).

4.2 Analysis and phenomenology of wall heat fluxes in spark ignition engines

The wall heat flux in SI engines has often been investigated with respect to the ensemble-averaged wall heat fluxes. However, it was already remarked by Alkidas [9] that single cycle heat flux can exhibit significantly different characteristics than their corresponding average.

As a consequence, the investigation of flame-wall interactions requires the analysis of single cycles. In this section, the differences between ensemble-averaged and single cycle wall heat flux traces are shortly highlighted. The main focus lies on the analysis of single cycles as well as on the wall heat fluxes during quenching.

4.2.1 Analysis of ensemble-averaged wall heat fluxes

The ensemble-averaged wall heat fluxes at all measuring positions during motored and fired operation at OP1 are shown in Fig. 4.4. In motored conditions, the temporal behaviour of the wall heat flux at each location is strongly similar due to the homogeneous temperature level in the combustion chamber. Nonetheless, there are spatial differences which can be attributed to the local charge motion. The wall heat fluxes are not symmetrical to TDC due to the decaying charge motion (cf. Fig. 4.3).
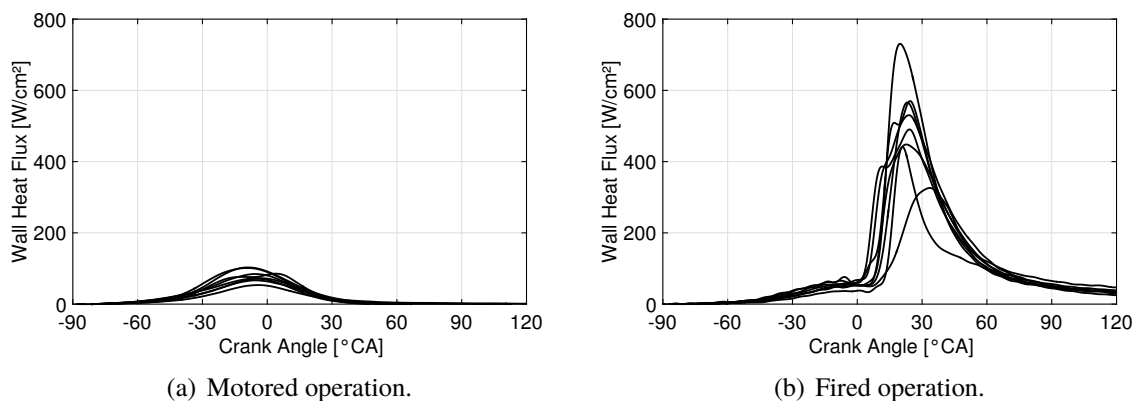

| (a) Motored operation. | (b) Fired operation. |

Figure 4.4: Mean wall heat fluxes during motored and fired operation at operating point 1.

In fired operating conditions, the wall heat fluxes again start rise simultaneously towards TDC before sharply increasing in a successive manner due to the arrival of the flame. The arrival of the flame leads to a rapid increase in the local temperature explaining the high absolute level of the wall heat flux and its spatial differences. After the completion of combustion, the temperature distribution in the combustion chamber becomes homogeneous again. Additionally, the charge motion quickly dissipates due to the enhanced viscosity of the fluid leading to equal wall heat fluxes levels during the expansion.

Similar observations can be made for the wall heat fluxes at the remaining operating points. About 80% of the total heat is transferred during the high pressure part (Fig. 4.5a) due to the high temperature during combustion. As the flame starts to spread from the spark plug, the measuring points close to it are exposed longer to high gas temperatures than the ones located far away from it. In addition, the wall heat flux is enhanced by the local charge motion, which is higher for an earlier flame arrival due to the decay of turbulence. As a result, around 40% more heat is transferred at the inner measuring points (1-4) compared to the outer ones (5-8) (Fig. 4.5b). At OP3, the swirling motion promotes the heat transfer in the outer regions of the cylinder head decreasing the difference to 20%. The relative importance of combustion
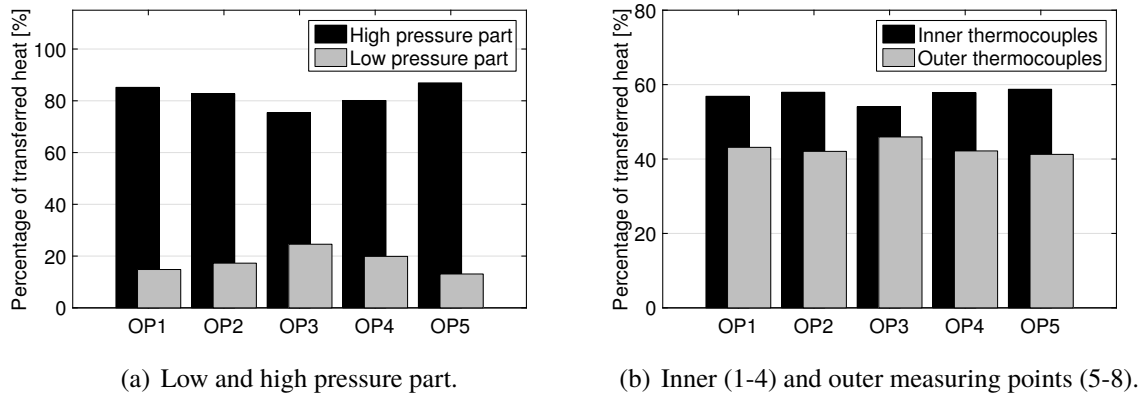
(a) Low and high pressure part.

(b) Inner (1-4) and outer measuring points (5-8).

Figure 4.5: Comparison of the mean transferred heat (mean value of all measuring points).

and flow motion with regard to the wall heat flux can be further examined by analysing single cycles.

4.2.2 Analysis of single cycle and quenching wall heat fluxes

A modern SI engine typically possesses a highly turbulent combustion process which leads to enhanced cycle-to-cycle fluctuations of the flame propagation and consequently of the wall heat flux. Ensemble-averaging leads to a smearing of the individual wall heat flux traces and thus to a substantial loss of information. The analysis of high frequency phenomena such as the quenching wall heat flux $\dot{Q}_{W,Q}$ thus necessitates the analysis of single cycles.

This circumstance can be illustrated by Fig. 4.6 where the wall heat fluxes of 50 successive cycles and their overall ensemble average at OP1 are shown. The single cycle wall heat flux histories are subject to significant cycle-to-cycle fluctuations and exhibit details which are not present in the rather smooth ensemble-average. Despite their seemingly volatile behaviour, a few characteristics can already be recognized. Almost any of the recorded wall heat flux traces exhibits a steep increase around TDC which can again be associated to flame arrival. The corresponding gradient is steeper than the gradient of the ensemble-averaged wall heat fluxes. The steep gradient is commonly followed by a distinctive peak which corresponds to the quenching wall heat flux $\dot{Q}_{W,Q}$. In the highlighted cycle 705, these peaks occur at the measuring points 1,2,4,5,6,8. After flame quenching, the heat transfer can be assumed to be mainly governed by convection which in turn is determined by the large scale fluid motion (Boust et al. [25]). As already indicated before, the charge motion strongly decays around TDC (cf. Fig. 4.3). As a consequence, the convective heat transfer can be expected to be more pronounced for an early flame arrival. This can be illustrated by comparing measuring points with early and late flame arrival, e.g., MP2 vs. MP6. At MP2, the wall heat flux is sustained at a high level for a longer time than at MP6 due to an earlier flame arrival and a higher local fluid motion. The latter may also lead to additional wall heat flux peaks, which can even be higher than the corresponding quenching wall heat flux. At MP6, in contrast, the wall heat flux traces exhibit only one distinct peak associated to flame quenching as the

(a) Measuring point 1,

(b) Measuring point 2.

(c) Measuring point 3.

(d) Measuring point 4.

(e) Measuring point 5.

(f) Measuring point 6.
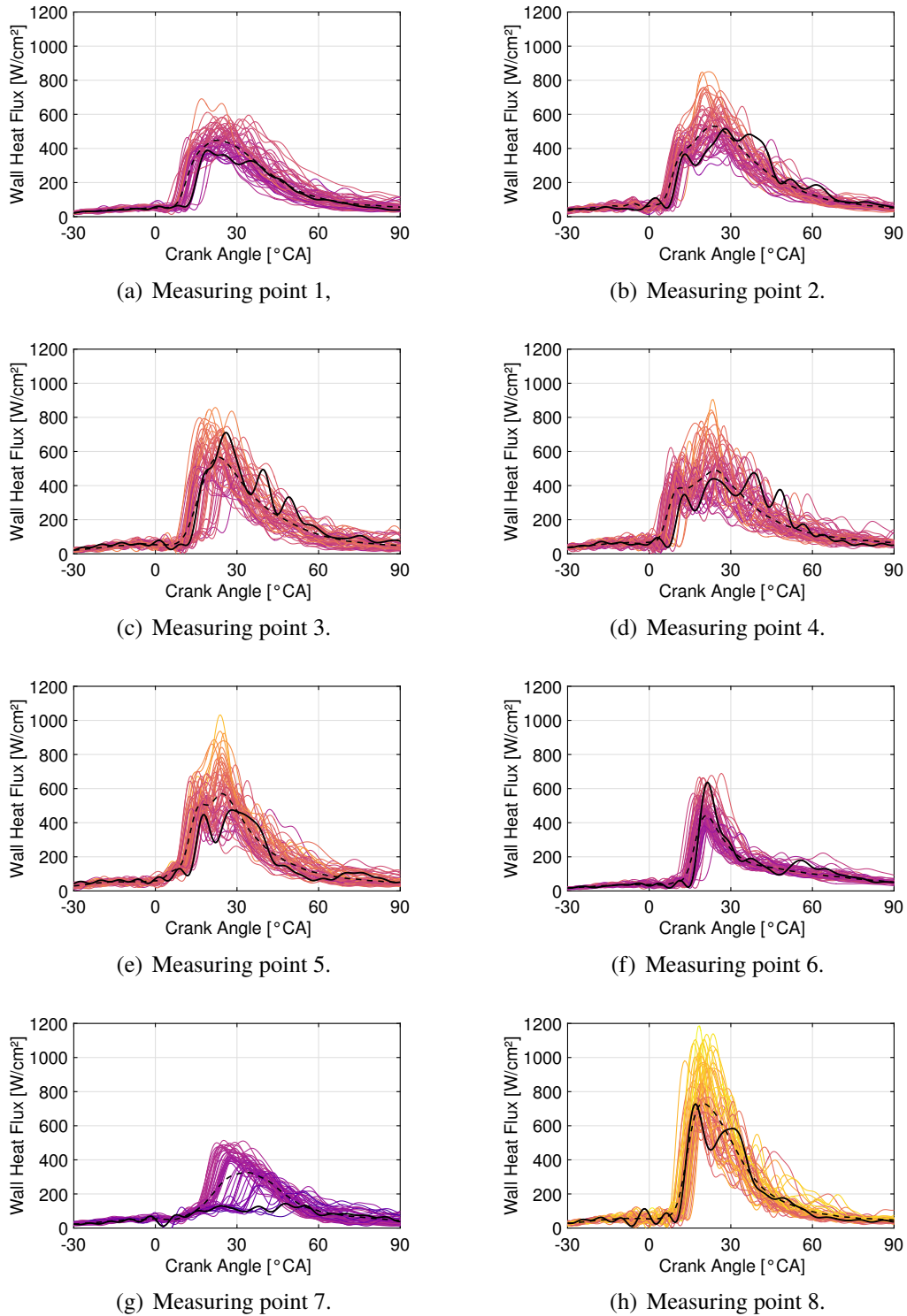
(g) Measuring point 7.

(h) Measuring point 8.

Figure 4.6: Successive wall heat flux traces of the cycles 680-730 at OP1. Cycle 705 is highlighted by a black line whereas the ensemble-averages are indicated by a dashed line.

convective heat transfer is less pronounced due to a lower level of fluid motion.

For a further analysis, it is helpful to discern between three different basic types of wall heat flux histories. All of them are present in cycle 705 shown in Fig. 4.6. Around 60%-80% of all wall heat flux traces can be classified as so-called 'quenching types' (measuring points 1,2,4,5,6,8 in cycle 705). The characteristics of this type have already been described. These are a steep increase of the wall heat flux followed by a distinctive peak associated to flame quenching. The second type is called 'superposition type' and occurs at MP3 in cycle 705. The steep initial gradient flattens succeeded by a delayed peak. It can be speculated that this is the result of flame-wall interaction being superimposed by a high convective wall heat transfer. The third type is the so-called 'convective type' and is characterized by a shallow gradient. In this case, no flame quenching occurs at the measuring location and the wall heat flux can be assumed to be purely convective. The wall heat flux may even remain close to its maximum value before combustion indicating that no burned gases touched the wall at the respective measuring location (cf. MP7 in cycle 705). The convective types are clearly correlated to slow and late combustion, as shown in Fig. 4.7.
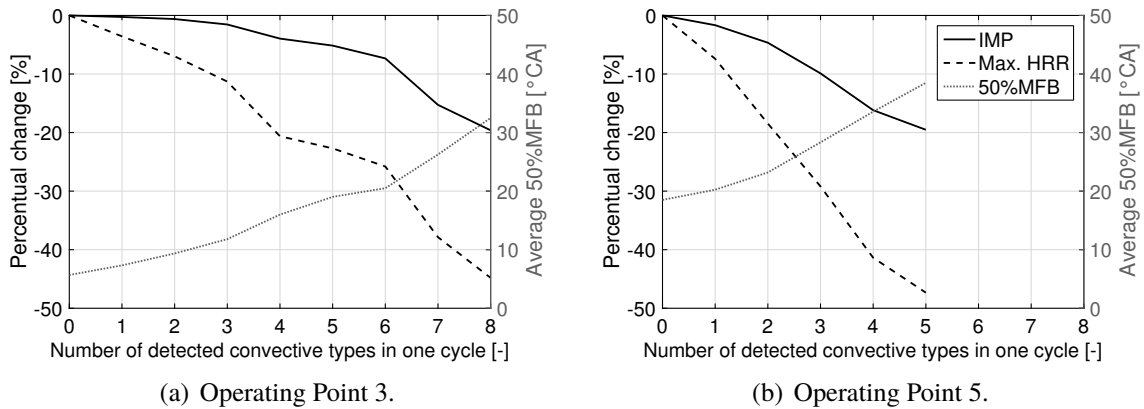

(a) Operating Point 3.

(b) Operating Point 5.

Figure 4.7: Averaged indicated mean pressure, heat release rate and position of 50%MFB depending on the number of identified convection types within one cycle.

To examine the quenching process in a SI engine, all wall heat flux histories were individually analysed using an algorithm described in appendix B. The goal was to uniquely identify the quenching wall heat flux $\dot{Q}_{W,Q}$, its corresponding crank angle α_Q and the location of the highest gradient $\alpha_{\partial Q}$ defining the start of flame-wall interaction. For this reason, only the 'quenching types' were included. An exemplary result of this analysis is shown for MP2 and MP6 at OP1 in Fig. 4.8. Since MP2 is located closer to the spark plug, flame quenching occurs earlier and at lower pressures than at MP6 resulting in slightly smaller quenching wall heat fluxes. The scatter of the data can be attributed to spatial and cycle-to-cycle fluctuations of the local flame orientation (HOQ vs. SWQ, cf. chapter 3) and the mixture properties, in particular of the equivalence ratio and the temperature.

An interesting observation highlighting the impact of convection and flame quenching on the wall heat flux can be made when examining the peak wall heat fluxes at a given location within single cycles. For this purpose, the 'quenching types' are again analysed to
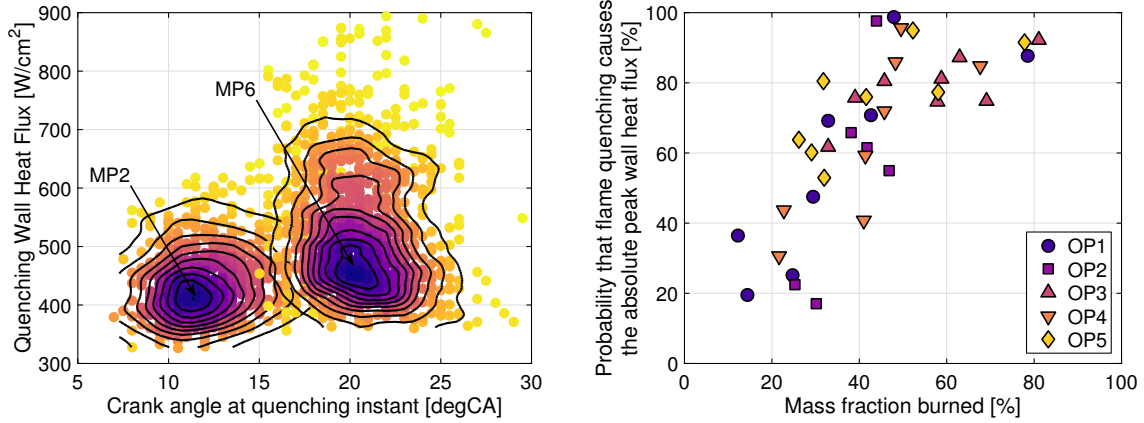
(a) Scatter plot of the quenching wall heat flux $\dot{Q}_{W,Q}$ vs. α_Q at OP1. The probability density is highlighted by a contour plot as well as a density-based colouring.

(b) Probability that flame quenching causes the absolute peak wall heat flux within a single cycle at a given measuring location.

Figure 4.8: Analysis of quenching wall heat fluxes.

identify the (probable) cause of the peak wall heat flux. It is assumed that the first peak of the wall heat flux is induced by flame quenching whereas the succeeding peaks are caused by convection. The result of this analysis (Fig. 4.8b) suggests that the cause of the highest wall heat flux is related to the combustion progress. During early stages of combustion, the pressure and temperature of the unburned gas is relatively low resulting in a low flame power and a low quenching wall heat flux. The flow motion, in contrast, is still high resulting in a high convective wall heat flux. Hence, the maximum wall heat flux is more likely to be caused by convection. This situation reverses for the late stages of combustion: the pressure and the temperature of the fresh gases are relatively high yielding a high quenching wall heat flux whereas the flow motion is much less pronounced than during early stages (cf. Fig. 4.3). The maximum wall heat fluxes are thus mainly caused by flame-wall interaction.

The increase of the quenching wall heat fluxes during combustion is further detailed in Fig. 4.9. The compression of the fresh gases by the progressing combustion leads to a successive increase of the flame power and consequently the quenching wall heat fluxes. Expansion, on the other hand, may significantly decrease the quenching wall heat flux (Fig. 4.9a). The data shown in Fig. 4.9 suggests an approximate linear scaling of the quenching wall heat flux with pressure. It was shown in chapter 3 that the quenching wall heat flux $\dot{Q}_{W,Q}$ is proportional to the flame power $\dot{Q}_F$ for laminar flame-wall interactions. An analysis of the pressure scaling of $\dot{Q}_F$ yields

$$\dot{Q}_{W,Q} \sim \dot{Q}_F = \underbrace{\rho_u}_{pT_u^{-1}} \underbrace{s_L^0}_{T_u^\alpha p^\beta} \underbrace{c_p(T_b - T_u)}_{\approx\text{const.}} \sim p^{1+\beta}T_u^{\alpha-1} \sim p^{1.05}. \tag{4.2}$$

Thereby, the unburned temperature T_u was related to the pressure p by assuming a polytropic compression / expansion of the fresh gases, $T_u \sim p^{(n-1)/n}$ with $n \approx 1.3$ (Heywood [90]). Moreover, a stoichiometric gasoline-air mixture with $\alpha = 2.62$ and $\beta = -0.32$ was assumed
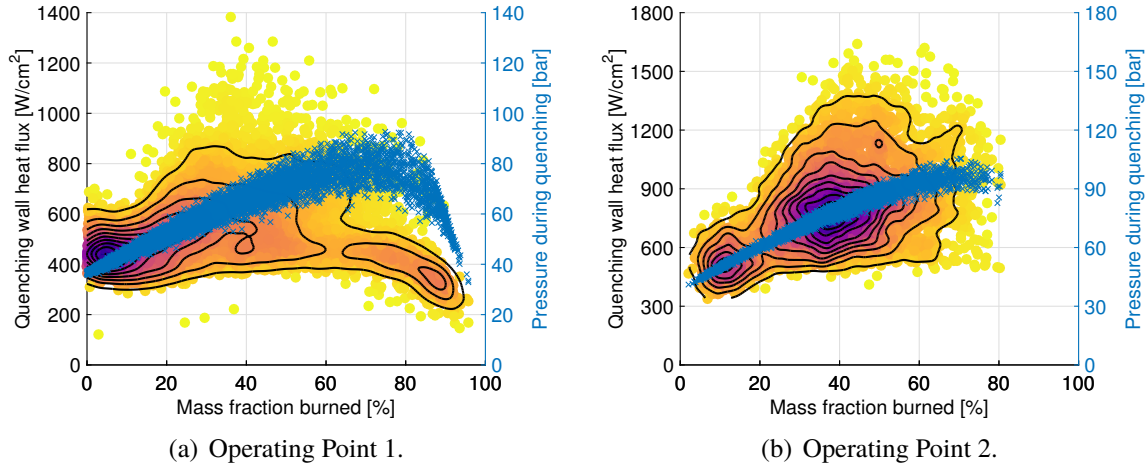
(a) Operating Point 1. (b) Operating Point 2.

Figure 4.9: Scatter plot of the quenching wall heat fluxes $\dot{Q}_{W,Q}$ and pressures p_Q at all measuring locations during quenching vs. combustion progress. The probability density of the quenching wall heat fluxes is highlighted by a contour plot as well as a density-based colouring.

(cf. appendix C). The theoretical scaling $\dot{Q}_{W,Q} \sim p^{1.05}$ is in good agreement with the experimental data indicating that the wall heat fluxes during quenching in a SI engine scale similar as for laminar flame-wall interactions. A more detailed evaluation of the nature of flame-wall interactions in SI engines can be carried out by analysing the quenching distances y_Q, normalized wall heat fluxes φ_Q and Peclet numbers Pe_Q.

4.3 Simulative methodology for analysing the quenching wall heat fluxes

The significance of the quenching wall heat flux $\dot{Q}_{W,Q}$ as a characteristic quantity of flame-wall interactions has already been stressed in chapter 3. This section introduces a methodology to calculate the quenching distance y_Q, the normalized wall heat flux φ_Q and the Peclet number Pe_Q based on $\dot{Q}_{W,Q}$. Two different correlations for calculating the quenching distance are introduced and discussed. To use these correlations, additional input quantities such as the laminar flame velocity are required. Since these quantities are normally not known from experiment, a simulative methodology using 1D, 3D-CFD and 3D-FE simulations is subsequently introduced for their estimation.

4.3.1 Estimation of the quenching distance

The quenching distance y_Q is not uniquely defined in literature. The differences trace back to the definition of the flame position (cf. Table 3.1). In experiments, the flame is often identified optically by its luminosity whereas in simulations, a temperature iso-level or the

position of the maximum heat release is utilized. Hence, the definition of the flame position has to be correctly accounted for in the calculation of the quenching distance. An approach using the inner layer temperature T_0 is introduced in the following and compared to the one developed by Boust et al. [24, 26].

Formulation using the inner layer temperature

A direct way to estimate the quenching distance is using the Fourier's law of heat conduction

$$\dot{Q}_{W,Q} = \lambda \frac{\partial T}{\partial x}\bigg|_W \approx \lambda \frac{T_{F,Q} - T_W}{y_Q}. \tag{4.3}$$

Thereby, it is assumed that the heat flux across a chemically inert unburned gas layer of thickness y_Q is constant in the moment of quenching (Boust et al. [26]). The main difficulty is the estimation of the flame temperature $T_{F,Q}$ during quenching. The use of the adiabatic flame temperature T_b leads to an over-estimation of the quenching distance as T_b is first attained in the oxidation layer, long after the reaction zone (Fig. 2.2). A physically sound definition of the flame temperature in this respect is the inner layer temperature T_0, mainly due to the following reasons:

1. The flame and the position of its main reaction zone can be uniquely identified by tracking the inner layer temperature T_0. This also facilitates the comparison to simulations and the development of a flame-wall interaction model in the *G*-equation framework (see chapter 5).

2. The inner layer temperature plays a decisive role for flame extinction, as already detailed in chapter 2.3.1. When the temperature of the flame falls below T_0 due to an insufficient fuel mass fraction or heat losses, the flame is extinguished as the chain branching reactions come to a halt.

3. The thickness of the inner layer is of order $O(\delta)$ and very small compared to the oxidation layer ($O(\epsilon)$) or the preheat zone ($O(1)$). Thus the zone ahead of it can be considered chemically inert which is a prerequisite for the applicability of Eq. (4.3).

Using the inner layer temperature T_0, the quenching distance can be estimated by

$$y_Q = \lambda_0 \frac{T_0 - T_w}{\dot{Q}_{W,Q}} \tag{4.4}$$

where T_W is the wall temperature in the moment of quenching and λ_0 the thermal conductivity evaluated at $T_{ref,0} = 1/2\,(T_0 + T_W)$. This approach is subsequently called inner layer formulation. By inserting the definition of the normalized wall heat flux φ_Q (Eq. (3.1)) in Eq. (4.4), a relation between φ_Q and the Peclet number can be obtained,

$$Pe_Q = \frac{T_0 - T_W}{T_b - T_u} \frac{1}{\varphi_Q} \qquad \text{where} \qquad Pe_Q = \frac{y_{Q,0}}{l_F|_{T_{ref,0}}} = \frac{\rho_u c_p s_l^0 \, y_Q}{\lambda_0}. \tag{4.5}$$

For consistency, the reference temperature to calculate the Peclet number according to Eq. (3.2) has to be chosen as $T_{ref,0} = 1/2\,(T_0 + T_W)$.

Formulation by Boust et al.

The relations suggested by Boust et al. [24, 26] can also be used to calculate the quenching distance. The authors used an optical criterion (CH^* and C_2^* chemiluminescence) to define the position of the flame which complicates the comparability to simulations. The relations have already been validated numerous times (e.g., Karrer et al. [99], Labuda et al. [105]) and are thus used as a reference for the inner layer formulation (Eq. (4.4)) developed previously. According to Boust et al. [24], the relation between y_Q, Pe_Q and φ_Q is given by

$$y_Q = Pe_Q \times l_F|_{T_{ref,B}} = \frac{T_F - T_W}{T_F - T_u} \frac{1 - \varphi_Q}{\varphi_Q} \times l_F|_{T_{ref,B}} \tag{4.6}$$

where $T_{F,Q}$ was assumed to be approximately equal to T_b and the reference temperature was defined as $T_{ref,B} = 1/2\,(T_b + T_W)$ (Boust et al. [24]).

A brief comparison

Since both approaches are based on Fourier's heat conduction law in essence, it can be expected that their results coincide within certain bounds. However, Eq. (4.4) depends on lesser variables and utilizes a stricter definition of the flame position. The unknown quantities in Eq. (4.4) and Eq. (4.6) , for example T_0 and s_L^0, can be calculated if the local thermodynamic state (i.e., p_Q, $T_{u,Q}$, ϕ_Q, $Y_{EGR,Q}$) during quenching is known. In this regard, the inner layer formulation is less sensitive towards small errors concerning the estimation of these variables. This is particularly important as $T_{u,Q}$, ϕ_Q and $Y_{EGR,Q}$ cannot be directly determined from the experimental data. The sensitivities towards these quantities can be estimated by calculating the first-order taylor series of y_Q around a pre-defined 'operating point', which was chosen as $p_Q = 60\,bar$, $T_{u,Q} = 800K$, $\phi_Q = 1.0$ and $Y_{EGR,Q} = 0$ as well as $T_W = 450K$ and $\dot{Q}_{W,Q} = 600W/cm^2$. All relevant properties were calculated using a 1D flame calculation, which is introduced in the next subsection. The results are presented in Table 4.3. The inner layer formulation is less sensitive towards small changes in $T_{u,Q}$, ϕ_Q and $Y_{EGR,Q}$ and is thus expected to be more robust to errors in the estimate of these values.

Table 4.3: Comparison of the sensitivities of the calculation of y_Q to changes in T_u, ϕ and Y_{EGR}.

	Inner layer formulation	Boust et al. [24]
$\partial y_Q / \partial T_u$	$5.88 \times 10^{-3} \frac{\mu m}{K}$	$2.12 \times 10^{-2} \frac{\mu m}{K}$
$\partial y_Q / \partial \phi$	$0.117 \frac{\mu m}{1/100}$	$0.125 \frac{\mu m}{1/100}$
$\partial y_Q / \partial Y_{EGR}$	$-0.102 \frac{\mu m}{1/100}$	$-0.263 \frac{\mu m}{1/100}$

4.3.2 Simulative methodology

As already indicated, the thermodynamic state of the mixture near the wall is needed to calculate the flame and mixture properties. However, they cannot directly be estimated from

the experimental data, except for the pressure p_Q and the wall temperature T_W. Hence, a comprehensive simulation workflow shown in Fig. 4.10 was developed.

The flow in a direct-injected SI engine is highly unsteady and exhibits considerable spatial gradients as well as cycle-to-cycle fluctuations, in particular of the temperature and the equivalence ratio. For this reason, a zero dimensional modelling of the combustion chamber is insufficient and a three-dimensional simulation method has to be utilized. A 3D URANS-CFD simulation can resolve the spatial gradients but not the cycle-to-cycle fluctuations since the underlying equations are implicitly averaged. Even if a method capable of resolving single cycles such as LES is employed, an unambiguous assignment of simulation and experiment is still not possible. Cycle 25 from LES simulation, for example, does not necessarily represent cycle 25 from experiment. As a consequence, an accurate calculation of the quenching distance in single cycles is not possible. However, the evaluation of the mean quenching distances and therefore the mean mode of flame-wall interactions is feasible by using the suggested methodology.
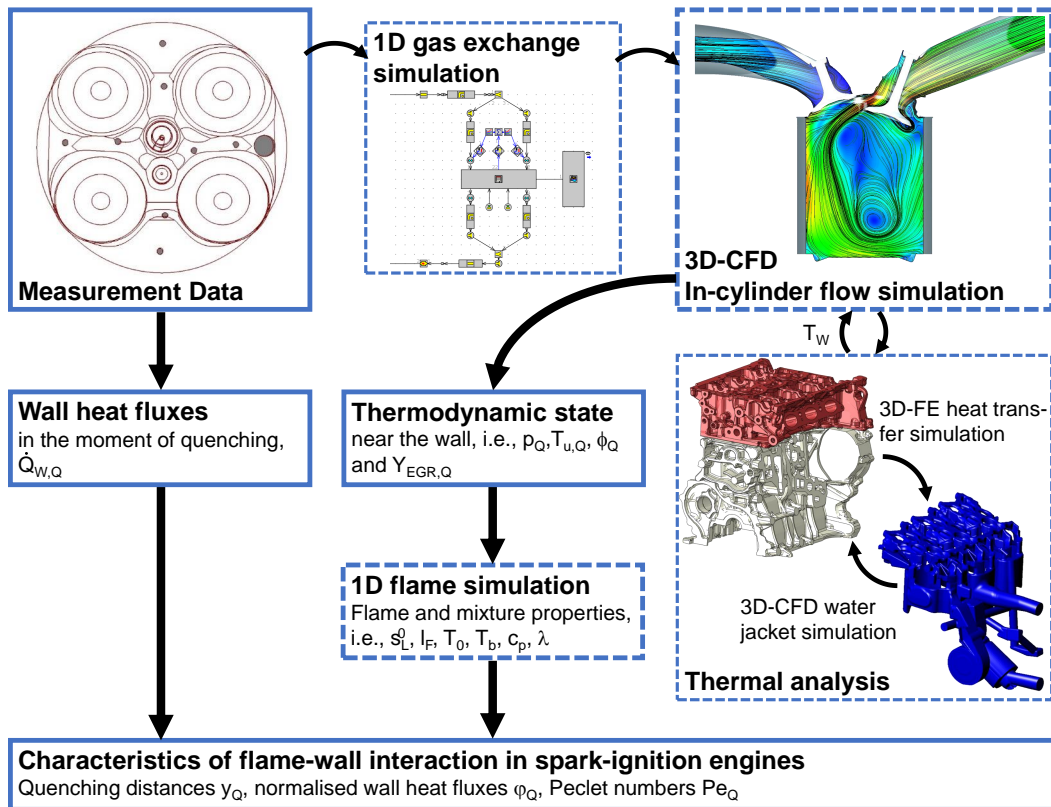

1D gas exchange simulation

Measurement Data

3D-CFD In-cylinder flow simulation

T_W

Wall heat fluxes
in the moment of quenching, $\dot{Q}_{W,Q}$

Thermodynamic state
near the wall, i.e., p_Q, $T_{u,Q}$, ϕ_Q and $Y_{EGR,Q}$

3D-FE heat transfer simulation

1D flame simulation
Flame and mixture properties, i.e., s_L^0, l_F, T_0, T_b, c_p, λ

3D-CFD water jacket simulation

Thermal analysis

Characteristics of flame-wall interaction in spark-ignition engines
Quenching distances y_Q, normalised wall heat fluxes φ_Q, Peclet numbers Pe_Q

Figure 4.10: Overview of the workflow. Simulative tasks are highlighted by dashed lines.

As a starting point, 1D gas exchange simulations were conducted to provide the necessary boundary and initial conditions for the 3D-CFD in-cylinder flow simulations. The latter were subsequently combined with 3D-FE heat conduction and 3D-CFD coolant flow simulations to accurately estimate the wall temperature and the near-wall flow. The local thermodynamic state for each measuring and operating point was determined from the final 3D-CFD calcu-

lations. In contrast to the majority of flame-wall interaction studies in literature, it cannot be assumed that this state is constant during quenching as there are considerable flow gradients (regarding pressure, for example). Unfortunately, there are no studies detailing the effects of such gradients on quenching. To account for this problem at least in a minimal way, all state variables were averaged in the time period defined by the ensemble-averages of α_Q and $\alpha_{\partial Q}$ ($\overline{\alpha}_Q$ and $\overline{\alpha}_{\partial Q}$). Using this information, a 1D flame calculation with detailed chemical kinetics was used to estimate the required flame and mixture properties to assess the quenching process based on the ensemble-average of the quenching wall heat fluxes $\overline{\dot{Q}}_{W,Q}$. Some details of the numerical models and programs employed are presented in the following.

1D gas exchange simulation

The 1D gas exchange simulations were conducted using the commercial software GT-Power. The simulation model comprised the engine itself and the complete test bench periphery. The heat release rates were obtained by a three pressure analysis using the recorded intake, cylinder and exhaust pressures. The computational model was validated by the available measurement data detailed in Fig. 4.1. A particular focus was hereby laid on the reproduction of the measured pressure oscillations in the intake and exhaust manifold, as they are crucial for a correct estimation of the boundary conditions for the 3D-CFD simulation.

3D-CFD simulation of the in-cylinder flow

The 3D-CFD simulations were carried out using the commercial software AVL FIRE™. The simulation setup was also utilized to examine the performance of the GFWI model (see chapter 6) and is thus described in detail. The geometry of the cylinder including parts of the intake and exhaust-ports can be seen in Fig. 4.11a. Specific attention was given to a detailed reconstruction of the real engine geometry, in particular of the measuring positions. The meshes for each operating point mainly consist of hexagonal elements, which were locally refined in order to correctly resolve the geometry and especially the flow in areas with flow separations or high flow gradients. During combustion, for example, the highest cell size is $0.6mm$ and the mesh consists of approximately 2.5 million cells and vertices. The state variables for each measuring point were obtained by averaging over the first cell layer near the wall at the corresponding locations highlighted in Fig. 4.11a. The local cell size of around $60\mu m$ was of order of the quenching distance. Hence, the state variables are expected to be approximated with sufficient accuracy.

To accurately predict the flow within the engine, various submodels were used. The k-ζ-f model was chosen as a turbulence model. The fuel spray was modelled with a discrete droplet method using the Wave break-up model (Liu et al. [114]) and an evaporation model by Dukowicz [56]. Spray-wall interaction was accounted for by a model from Kuhnke [104]. As a surrogate fuel, iso-octane was used. The evaporated fuel mass was reinitialized shortly before ignition to yield the correct equivalence ratio as well as lower heating value. Combustion was calculated employing the ECFM-3Z model (Colin and Benkenida [41]), which was adapted in order to fit the experimental heat release at each operating point. The wall treatment was done utilising the generalized wall functions developed by Popovac and
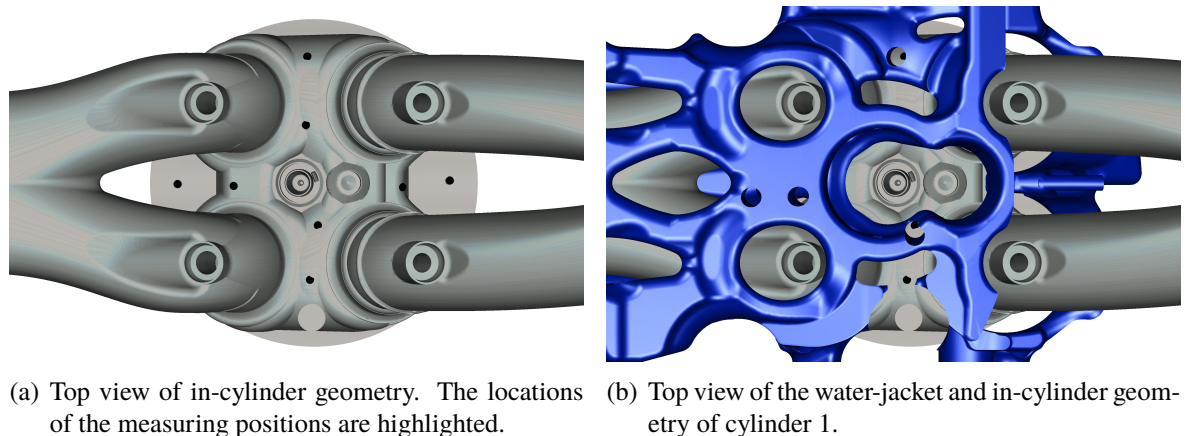
(a) Top view of in-cylinder geometry. The locations of the measuring positions are highlighted.

(b) Top view of the water-jacket and in-cylinder geometry of cylinder 1.

Figure 4.11: Geometry details of the 3D-CFD models.

Hanjalić [156]. The wall heat fluxes were calculated correspondingly by using a hybrid approach developed by Saric and Basara [170] which is equivalent to the Han-Reitz model [84] for large y^+.

The inlet and outlet boundary conditions as well as the initial conditions in the combustion chamber, intake and exhaust ports were taken from the 1D gas exchange simulations. The wall temperatures were prescribed using the results of the thermal analysis described in the following paragraph. The base time step was chosen as $\triangle \alpha = 0.25°CA$ and $\triangle \alpha = 0.5°CA$ for $2000rpm$ and $4000rpm$, respectively. A shorter time-step was applied during the opening and closing of the valves. During combustion, the time step was also shortened and specified as $\triangle \alpha = 0.0625°CA$ and $\triangle \alpha = 0.125°CA$ for $2000rpm$ and $4000rpm$, respectively. The 3D-CFD simulations were validated using the in-cylinder pressure traces and heat release rates as well as the available data from the 1D gas exchange simulations. A satisfactory agreement was found.

3D-CFD coolant flow and 3D-FE solid simulation

The temperature distribution at the walls of the combustion chamber has a great impact on the thermodynamic conditions of the fluid near the wall. A reasonable approximation can be obtained by employing a thermal analysis which is based on several iterative simulations of the coolant / in-cylinder flow (3D-CFD) as well as of the heat conduction in the engine (FE). The FE simulations were carried out with DSS Simulia Abaqus, whereas the coolant flow was calculated with AVL FIRE™. Particular attention was again laid on the reconstruction of geometrical details such as the sleeves carrying the thermocouples (Fig. 4.11).

To calculate the wall temperatures, the heat transfer coefficients and near-wall fluid temperatures estimated by the in-cylinder and coolant flow CFD simulations were mapped onto the FE model. After the temperature distribution within the solid was estimated, the wall temperatures were in turn mapped back. Thereby, two 'outer' loops (in-cylinder flow) were calculated comprising three 'inner' iteration loops (solid and coolant flow) to provide the wall temperature distribution for the final in-cylinder CFD simulation. The approach was
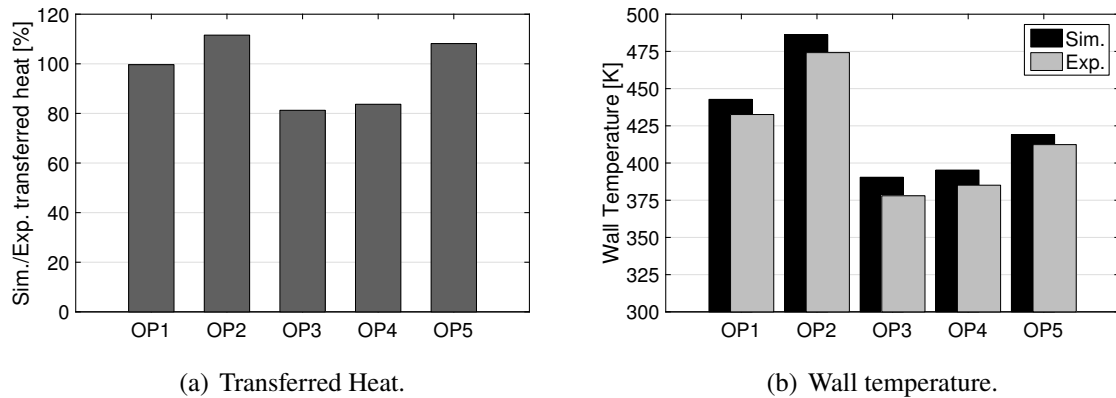
(a) Transferred Heat.　　　　　　　　(b) Wall temperature.

Figure 4.12: Validation of the thermal analysis using the experimentally determined wall heat fluxes and wall temperatures.

validated by comparing the wall temperatures and the transferred heat to the measurements. The total transferred heat at the measuring points is captured within an accuracy of -18% to $+10\%$ (Fig. 4.12a). The mean temperature level of the simulations is slightly above the measured one (Fig. 4.12b). In this context, it has to be noted that the heat conduction between the thermocouple, the sleeve and the surrounding walls cannot be accounted for in the simulation. However, the temperature and its spatial distribution are reproduced with sufficient accuracy.

1D flame simulation

The estimation of the flame properties needed to calculate the quenching distance and normalized scales has to be as accurate as possible to obtain meaningful results. For this reason, they were calculated by a 1D simulation of a freely propagating laminar flame with detailed chemistry. The open-source software Cantera was used for this purpose. The reaction mechanism employed was developed by Cai et al. [32], consists of $N = 339$ chemical species and $M = 2791$ reactions and is tailored to accurately describe the reaction of n-heptane, iso-octane, toluene and ethanol blends with an optimized set of species and reactions.

Table 4.4: Comparison of fuel characteristics.

	Fuel	Surrogate	Iso–Octane
Ethanol volume fraction	10.5%	10.5%	-
H/C-ratio	1.86	1.83	2.25
Air requirement	13.93 kg/kg	13.86 kg/kg	15.06 kg/kg
Lower heating value	41.87 MJ/kg	41.21 MJ/kg	44.31 MJ/kg
RON	98.9	97.5	100
MON	87.0	87.8	100

A crucial aspect for the accuracy of the simulations is the choice of the fuel. Unfortunately,

the exact composition of the gasoline fuel used in the experiments is unknown and has to be approximated by a surrogate. The surrogate was defined as a blend of *n*-heptane, iso-octane, toluene and ethanol. Their individual volume fractions were estimated by analytical relations proposed by Cai et al. [32] which are based on RON, MON and H/C-ratio . The required input values are the RON, the MON and the H/C-ratio of the original fuel, which were obtained by a fuel analysis. As the relations can only be used to calculate the *n*-heptane, iso-octane and toluene volume fraction, the following three steps were performed to approximate the surrogate fuel: first, the gasoline characteristics without ethanol were estimated knowing the ethanol volume fraction. Second, a preliminary surrogate was calculated using the analytical relations and third, the volume fraction of ethanol was added again yielding the final surrogate. It is composed of 43.07vol.-% iso-octane, 13.91vol.-% *n*-heptane, 32.52vol.-% toluene and 10.5vol.-% ethanol. The properties of the original and surrogate fuel as well as iso-octane, which is commonly used as a gasoline surrogate, are compared in Table 4.4.

The RON and MON numbers of the surrogate fuel were approximated using a model for ternary mixtures of *n*-heptane, iso-octane and toluene by Morgan et al. [124]. Ethanol was accounted for by a simple Linear-by-Volume model, i.e., RON and MON are interpolated according to the volume fractions of the mixture. The surrogate fuel and the gasoline show an excellent agreement considering their overall characteristics. Thus it can be expected that the surrogate fuel is able to replicate the behaviour of the real fuel with sufficient accuracy.

4.4 Characteristics of flame-wall interaction in spark-ignition engines

In section 3.4, it was concluded that the quenching process in an engine is very likely to be laminar as the turbulent fluctuations in the vicinity of the wall are expected to be too weak to substantially influence the interaction of flame and wall. To verify this hypothesis and shed light on the nature of flame-wall interactions in SI engines, the results of the previously described analysis are shown and critically reviewed based on the findings of chapter 3. The general duration of the observed flame wall-interactions is between 0.15 and 0.4ms, which is in good accordance with duration of the laminar quenching process of stochiometric methane flames at elevated pressures reported by Sotton et al. [180], Boust et al. [25] and Labuda et al. [105]. In the following, specific attention is given to the quenching distances as well as to the normalized wall heat fluxes and Peclet numbers.

4.4.1 Quenching distance

The quenching distances calculated with the inner layer formulation (Eq. (4.4)) at each operating point are shown in Fig. 4.13a. The average of all measuring points at a specific operating point is represented by the large crosses. The typical quenching distances found in a SI engine are of order $15 - 100\mu m$. The same order of magnitude was already found by Daniel [48] as well as by Ferguson and Keck [71].

It is evident that the quenching distance is influenced less by a variation of speed (OP1 vs.
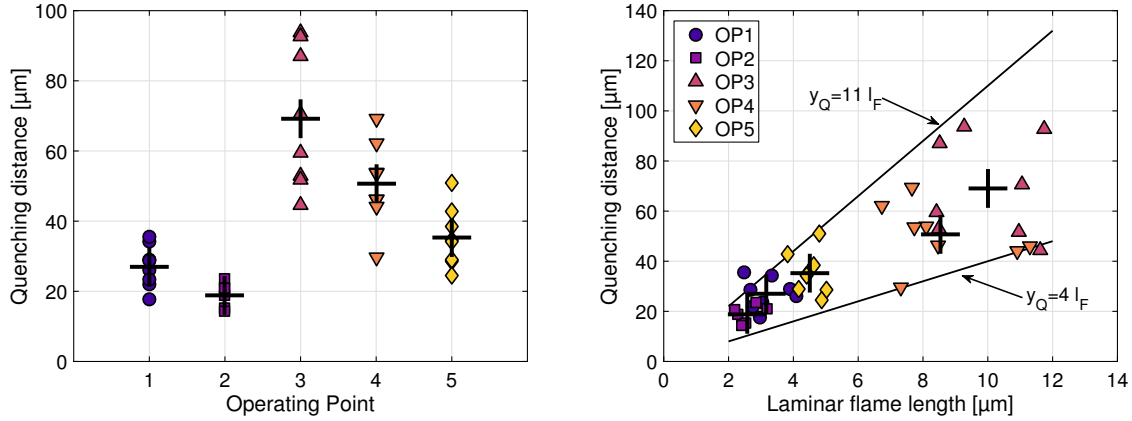
(a) Quenching distances y_Q evaluated with the inner layer formulation (Eq. (4.4)) at each operating point.

(b) Dependence of the quenching distance on the laminar flame thickness l_F. The latter was calculated solely by simulation using Eq. (2.57) with $T_{ref} = 1/2(T_0 + T_W)$.

Figure 4.13: Quenching distances y_Q evaluated with the inner layer formulation. The large crosses represent the average of all MPs at a specific operating point.

OP2) than by a variation of load (OP1 vs. OP4). Lean combustion leads to higher quenching distances than stoichiometric combustion (OP1 vs. OP5). Interestingly, OP3 and OP4 exhibit considerable differences despite the same overall load and speed. A general pattern with respect to the operating conditions detailed in Table 4.2 cannot be identified. Appropriate explanations for these phenomena can only be found by including the flame properties and in particular the laminar flame thickness l_F. This can be illustrated as follows: as detailed in chapter 3, the Peclet number Pe_Q for laminar flame-wall interaction is approximately constant for a given quenching configuration (HOQ or SWQ). The quenching distance is thus proportional to the laminar flame thickness at first order. A thin laminar flame can propagate closer to the wall without being influenced whereas a thick flame starts to interact at a greater distance from the wall resulting in a low respectively high quenching distance. This also applies to the present results as shown in Fig. 4.13b. The obtained quenching distances are proportional to the corresponding laminar flame thicknesses l_F evaluated by simulation and bounded between $4l_F$ and $11l_F$. These limits can be associated to HOQ and SWQ, respectively.

Hence, the impact of the engine operating parameters on the quenching distances can be examined by scrutinizing their impact on the laminar flame thickness. A higher engine load, for example, results in an increased in-cylinder pressure p, which in turn lowers the flame thickness l_F and thereby the quenching distance. Lean flames, on the other hand, possess a higher laminar flame thickness than stoichiometric flames resulting in a higher quenching distance. In this respect, the impact of the engine speed as well as the charge motion is only secondary as they only influence the mixture homogenisation and thus the local equivalence ratio. For a given engine design, the dominant operating parameter concerning the quenching distance is thus the engine load which directly affects the in-cylinder pressure p. The unburned

temperature T_u as well as the equivalence ratio ϕ, in contrast, are mainly defined by the engine design and usually range within certain limits. The former is predominantly determined by the compression ratio whereas the latter is kept within a small operating window specified by the exhaust gas aftertreatment system or the emission regulations. In the present work, the unburned temperature T_u and the equivalence ratio ranged between $800 - 880K$ respectively $0.85 - 1.15$ (apart from OP5) whereas the in-cylinder pressure varied between 15 to 90 bar. Consequently, a discussion of the quenching distances in relation to the pressure during quenching is sensible.
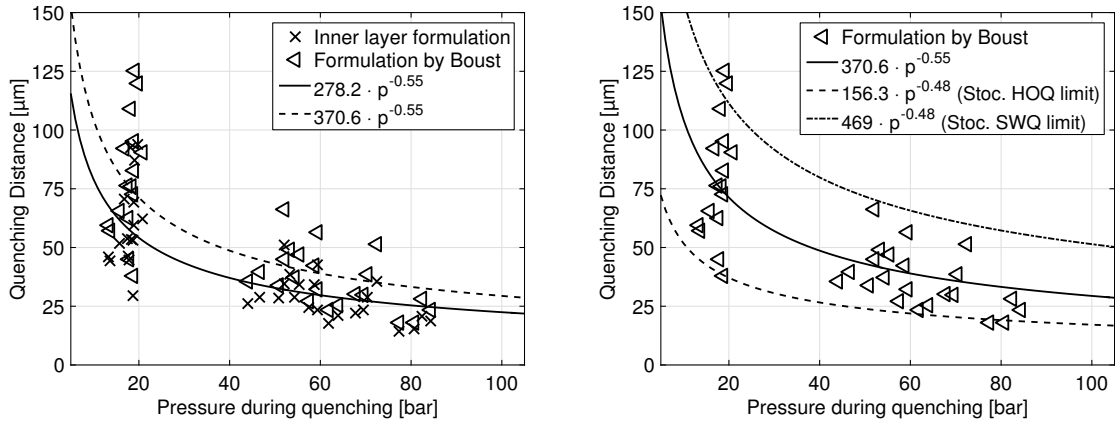
(a) Comparison between the quenching distances obtained by Eqs. (4.4) and (4.6) at all operating and measuring points.

(b) Comparison between the quenching distances obtained by Eq. (4.6) and the predicted limits for the laminar HOQ/SWQ distance of stoichiometric gasoline-air flames.

Figure 4.14: Comparison and pressure dependency of the quenching distances.

The quenching distances for all measuring and operating points estimated by the inner layer formulation (Eq. (4.4)) and the relation by Boust (Eq. (4.6)) are depicted in relation to the pressure during quenching in Fig. 4.14a. To illustrate the trends, least-square fits of the commonly chosen scaling law $a \times p^b$ are shown for each formulation. The magnitude and pressure dependency of the quenching distance is the same for both formulations. However, the distances calculated using the relations of Boust are higher than those estimated by the inner layer formulation. The main reason for this is the different definition of the flame position. The inner layer formulation uniquely identifies the flame by the location of its inner layer whereas the formulation by Boust is based upon an optical the chemiluminescence in the visible light spectrum (mainly CH^* and C_2^*). Both formulations are thus not directly comparable since position of the inner layer does not necessarily coincide with the emission peak of CH^* and C_2^* in general. Based on the inner layer formulation, a first order approximation for the quenching distance in SI engines operated with gasoline fuels reads

$$y_Q \approx 280\mu m \times (p/1bar)^{-0.55}. \tag{4.7}$$

The pressure scaling of $y_Q \sim p^{-0.55}$ is close to the scaling of the laminar flame thickness $l_F \sim p^{-0.65}T^{-1.55}$ obtained by 1D flame simulations of the surrogate fuel. Again, this

highlights the dependency of the quenching distance on the flame thickness. The scaling of l_F was calculated for a stoichiometric flame without residual gas and may differ when the mixture properties deviate significantly from these conditions. When the lean operating point OP5 is excluded for this reason, a scaling $y_Q \sim p^{-0.6}$ is obtained, which is in excellent agreement to the theoretical prediction considering the neglected variation of T_u, ϕ and Y_{EGR}. Moreover, the pressure exponent is in good accordance with the reported values in literature, which range from -0.48 (Labuda et al. [105]), -0.51 (Sotton et al. [180]), -0.56 (Westbrook et al. [208]) for stoichiometric methane-air mixtures to -0.88 (Westbrook et al. [208]) for stoichiometric methanol-air mixtures.

To further analyse the nature of flame-wall interactions in SI engines, it is expedient to compare the quenching distances to the ones found in literature. However, data on laminar flame quenching at conditions similar to the present work is scarce and to the best of the author's knowledge, the only suitable study is the one by Labuda et al. [105]. The authors investigated the HOQ of a stoichiometric methane-air flame at pressures between $8 - 160bar$ and unburned temperatures of $800 - 850K$. These conditions are almost identical to the ones encountered in the present investigation. Moreover, the quenching distances were also estimated using the relation of Boust et al. (Eq. (4.6)) in combination with a highly-resolved wall heat flux measurement. Consequently, the definition of the flame position was identical to the present investigation and the quenching distances can thus be directly compared after compensating the influence of the different fuels. It can be approximated by 1D flame calculations that the flame thickness l_F of stoichiometric methane-air mixtures at $20 - 80bar$ and $T_u = 800K$ is larger by a factor of $l_{F,CH4}/l_{F,g} = 1.7$ compared to gasoline-air flames. As the quenching distance can be assumed to be proportional to the laminar flame thickness, the HOQ limit of stoichiometric gasoline-air flames can be found by scaling the results of Labuda et al. by $l_{F,g}/l_{F,CH4}$. An upper estimate for the SWQ limit can be found by multiplying the HOQ limit with a factor of 3. As shown in Fig. 4.14b, the obtained quenching distances lie between these limits suggesting that the quenching process in a SI engine is essentially laminar despite the varying operating conditions.

4.4.2 Normalized scales of flame-wall interaction in spark-ignition engines

A more detailed analysis can be made using the normalized wall heat flux φ_Q and the Peclet number Pe_Q. As discussed in chapter 3, these are characteristic quantities of the quenching process and expected to remain within certain bounds for premixed hydrocarbon-air flames, irrespective of the fuel. In order to correctly evaluate flame-wall interactions in SI engines, the choice of the characteristic bounds of the normalized scales is decisive. The study of Labuda et al. [105] revealed that the normalized wall heat flux during HOQ at conditions similar to the present study decreases to $\varphi_{Q,HOQ} \approx 0.2$. The corresponding Peclet number can be found by utilising relation (4.6) by Boust et al. and by assuming $T_b \approx 2500K$: $Pe_Q \approx \frac{2500K-415K}{2500K-850K} \frac{1-0.2}{0.2} \approx 5$. It was approximated by Labuda et al. [105] that the error concerning the estimate of φ_Q lies between $15 - 20\%$. Consequently, it can be expected that the typical scales of laminar HOQ at engine-like conditions read $\varphi_{Q,HOQ} \approx 0.17 - 0.23$ and $Pe_{Q,HOQ} \approx 4 - 6$.

During SWQ, the quenching distance is higher whereas the corresponding wall heat flux is lower compared to HOQ by a factor of around 2.5. Reasonable estimates for the typical scales of laminar SWQ at engine-like conditions are thus given by $\varphi_{Q,SWQ} \approx 0.08 - 0.12$ and $Pe_Q \approx 10 - 14$.

Normalized wall heat flux

The normalized wall heat fluxes φ_Q sorted by either the operating or measuring point are shown in Fig. 4.15. The corresponding limits for laminar HOQ and SWQ are highlighted. It is evident that the characteristic scales of quenching lie within the laminar bounds solidifying the hypothesis that flame-wall interactions in SI engines are laminar. The outliers at OP1/MP7 and OP3/MP8 result from a late flame arrival at the measuring point respectively a rich local mixture near the burning limit. In the former case, the flame is already influenced by the expansion process (cf. Fig. 4.9a) whereas in the latter, small errors concerning the estimate of the equivalence ratio lead to large differences in the flame power.
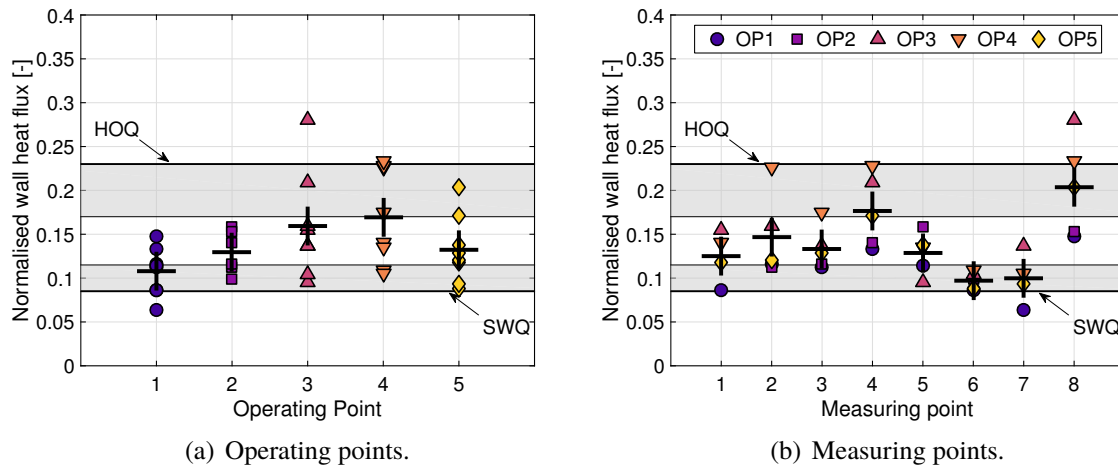

Figure 4.15: Normalized wall heat flux φ_Q sorted by operating and measuring points.

Despite the differences between the operating points regarding quenching distance, charge motion and mixture properties, the normalized wall heat fluxes during quenching are comparable. This indicates that the underlying quenching process at each operating point is similar. Combined with the fact that the normalized scales lie within the bounds of laminar flame-wall interactions, the quenching process in a SI engine can be assumed to be thermally controlled. A flame in a SI engine is quenched when it looses between 10% (SWQ) to 20% (HOQ) of its total power to the wall. The average normalized wall heat flux is

$$\varphi_Q = 0.14 \tag{4.8}$$

highlighting that the mean mode of quenching in a SI engine is a superposition of HOQ and SWQ.

The spatial variation of φ_Q can best be seen in Fig. 4.15b. At MP4 and MP8, HOQ is the predominant mode of quenching whereas SWQ is prevailing at MP6 and MP7. The remaining measuring points exhibit an intermediate quenching regime. At this point, it shall again be pointed out that the normalized wall heat fluxes φ_Q are based on averaged values as a cycle-resolved analysis was not possible in a meaningful way. Hence, they indicate the mean mode of quenching at a specific location. In this context, turbulence does play an important role as it significantly influences the degree of wrinkling and thereby the local structure and orientation of the flame before it is quenched. If the overall turbulence level is high, the flame wrinkling is more pronounced and the flame orientation is expected to exhibit a large cycle-to-cycle variation resulting in an average flame-wall interaction mode between HOQ and SWQ. If it is low in contrast, these effects are less pronounced and it is more likely that the mean quenching mode at a specific location converges to either HOQ and SWQ. This relation can be illustrated by comparing the scatter of φ_Q at OP2 and OP3. The highest degree of scattering can be seen at OP3, which has the lowest overall turbulence level, whereas OP2 having the highest turbulence level exhibits the lowest degree.

These effects can also explain the differences in the degree of scatter of the quenching distances between the different operating points (cf. Fig. 4.13a). In this regard, turbulence also has a secondary effect as it endorses the homogenisation of the mixture thereby reducing the spatial differences of temperature and equivalence ratio between the measuring locations.

Peclet numbers

The Peclet numbers were estimated by normalising the quenching distances calculated with the inner layer formulation according to Eq. (4.5). The results are shown sorted by operating or measuring point in Fig. 4.16. The highlighted areas again correspond to the anticipated scales of laminar HOQ and SWQ, respectively. Similar to the normalized wall heat flux φ_Q, all values of Pe_Q lie within the limits of laminar flame-wall interactions. Since Pe_Q and φ_Q are inversely correlated (cf. Eq. (4.5)), this finding was to be expected and the previous discussion of the normalized wall heat flux φ_Q also applies to the Peclet numbers. The average Peclet number equals

$$Pe_Q \approx 7.7. \tag{4.9}$$

Based on the Peclet number, a more elaborate approach of approximating the quenching distance including the variation of mixture properties can be proposed:

$$y_Q = Pe_Q \times l_F|_{T_{ref,0}} = \frac{\lambda_0}{\rho_u c_p s_L^0} Pe_Q \tag{4.10}$$

In this context, the local flame orientation can also be taken into account by choosing $Pe_{Q,HOQ} = 5$ and $Pe_{Q,SWQ} = 10$ for HOQ and SWQ, respectively.

Dependence on mixture properties

As detailed in chapter 3, the normalized wall heat flux φ_Q and thus the Peclet number Pe_Q do not show any evident dependency on mixture properties despite a slight pressure
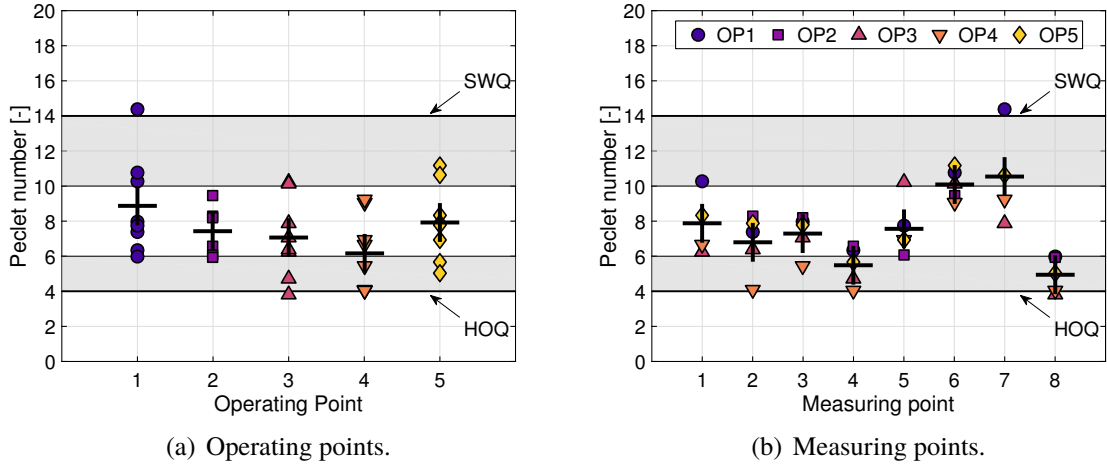
(a) Operating points.

(b) Measuring points.

Figure 4.16: Peclet number Pe_Q sorted by operating and measuring points.

dependence. For this reason, a similar result can be expected for the present results. In Fig. 4.17, the normalized wall heat flux φ_Q is plotted against p, T_u, ϕ, Y_{EGR}, Ze and T_0.

A small pressure dependency, which can be seen in Fig. 4.17a, is also evident in the present results. At higher pressures, the flame can be extinguished by a smaller heat loss increasing the normalized quenching distance in turn. A possible explanation for this phenomenon can be found by investigating the Zeldovich number Ze in combination with the temperature ratio T_0/T_u. The higher the Zeldovich number, the more sensitive the flame becomes towards fluctuations of the temperature T_b (cf. section 2.3.1). According to Peters [139] and Müller et al. [126], it can be approximated by

$$Ze = 4\frac{T_b - T_u}{T_b - T_0}.$$ (4.11)

The Zeldovich number for all measuring and operating points in the moment of quenching is shown in Fig. 4.17e. At OP1, OP2 and OP5, the value of Ze is larger than at OP3 and OP4. Hence, the propagation velocity of the flame and thereby the flame power is more sensitive towards heat losses. In combination with a high inner layer temperature T_0 compared to T_u (Fig. 4.17f), the flame can be extinguished by smaller heat losses. This can best be seen when comparing OP1 and OP2 to OP5. Although the Zeldovich numbers are in the same range, the inner layer temperatures T_0, which have to be exceeded for a sustainable reaction, are smaller relative to the unburned temperatures T_u making the flame more robust towards heat losses. Similar dependencies of the quenching wall heat fluxes on the thermochemical parameters of the flame were also found by Poinsot et al. [149] by numerical simulation. However, more data is needed to substantiate these explanations.

No obvious correlation of the normalized wall heat flux φ_Q on the remaining quantities ϕ, T_u and Y_{EGR} exists. This finding is in good agreement with the general phenomenology of laminar flame-wall interactions discussed in section 3.1.

(a) Pressure p.

(b) Unburned temperature T_u.

(c) Equivalence ratio ϕ.

(d) Residual gas mass fraction Y_{EGR}.

(e) Zeldovich number Ze.

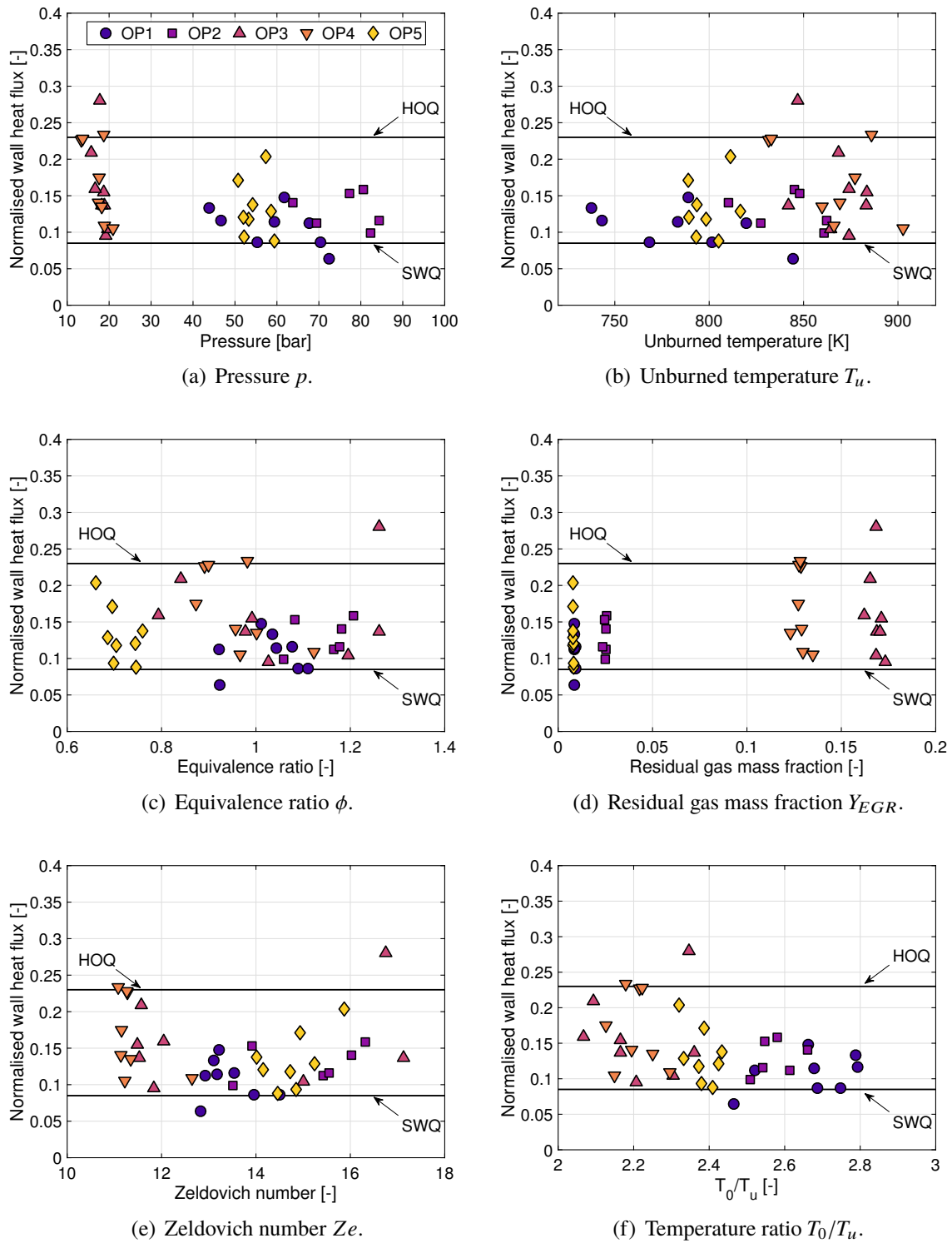(f) Temperature ratio T_0/T_u.

Figure 4.17: Dependency of φ_Q on the state variables during quenching as well as on the Zeldovich number Ze and the temperature ratio T_0/T_u.

4.4.3 Remarks and limitations

At this point, some limitations of the present investigation shall be remarked. Although the surface thermocouples are very small in diameter (0.8mm), they do not provide a strict one-point measurement, especially during sidewall quenching. This may lead to an underestimation of the wall heat flux in this case. Moreover, flame stretch effects have not been accounted for. These may increase the quenching distance, particularly during SWQ (cf. chapter 3.1.3). Another issue is that flame-wall interactions have only been examined for isobaric conditions in literature. In SI engines, however, there is a considerable pressure change during quenching. Due to the lack of studies on this topic, the role of this pressure gradient during quenching remains unclear. To account for this effect in a minimal way, an average between the beginning and the end of the interaction was used. Lastly, the RANS simulation of the in-cylinder flow can only be seen as a good approximation of reality. Charge motion, mixture formation and combustion are all affected by the models and numerics employed. Furthermore, the exact geometry of the engine is unknown due to inevitable manufacturing tolerances. All of the mentioned issues above are expected to have a minor influence on the outcome, as the order of magnitude of the respective results is not influenced by them.

4.5 Conclusion

The aim of this chapter was to gain insight in the flame-wall interaction process of a SI engine and to verify the hypothesis that it is locally laminar. For this purpose, the wall heat flux was measured in the cylinder head of a modern, direct-injected SI engine by using a total of eight highly responsive surface thermocouples. Five operating points with vastly differing operating conditions were examined to clarify the influence of engine speed, load, charge motion and equivalence ratio on the quenching process.

Based on the measurement data, the phenomenology of wall heat fluxes in SI engines was discussed and the differences between ensemble-averaged and single cycle wall heat flux traces were shortly highlighted. To uniquely identify the quenching wall heat flux $\dot{Q}_{W,Q}$, single cycles were analysed. It was revealed that three types of wall heat flux traces can be distinguished, namely a quenching, a superposition and a convective type. The most common type among them was found to be the quenching type which exhibits a steep gradient assigned to the arrival of the flame and a distinct wall heat flux peak associated to quenching afterwards. Hence, only the quenching types were included for the subsequent analysis. The impact of quenching and convection on the peak wall heat flux was discussed and a correlation dependent on the flame arrival was found. The increase of the quenching wall heat flux towards higher pressures was found to be in accordance with the anticipated pressure scaling of laminar flame-wall interactions.

A more thorough analysis was conducted by evaluating the quenching distances y_Q, the normalized wall heat fluxes φ_Q and the Peclet numbers Pe_Q. For this purpose, a new relation for estimating the quenching distance, based on the inner layer temperature T_0, was introduced and compared to the one proposed by Boust et al. [24]. Both formulations require the knowledge of flame properties such as T_0 or s_L^0 in the moment of quenching.

To estimate these values, a simulative methodology comprising 3D-CFD, 3D-FE and 1D simulations was introduced. The main objective was to accurately determine the necessary values using a 1D free flame calculation with detailed chemical kinetics, whose input values (p,T_u,ϕ and Y_{EGR}) were provided by a detailed 3D-CFD simulation of the in-cylinder flow. The boundary conditions for the 3D-CFD simulations were thereby calculated by a 1D gas exchange simulation as well as by a complete thermal analysis of the engine. All simulation models were validated against the available measurement data.

The analysis of the quenching distances revealed that they are proportional to the laminar flame thickness l_F. Hence, the impact of the engine operating parameters on the quenching distance was discussed by questioning their influence on the flame thickness l_F. In this context, the in-cylinder pressure, which is mainly determined by the engine load, was found to be dominant. For this reason, a first order approximation of the quenching distance of gasoline-air mixtures is given by

$$y_Q \approx 280\mu m \times (p/1bar)^{-0.55}. \tag{4.12}$$

Furthermore, it was found that the quenching distances are comparable to the laminar quenching distances published in literature. Moreover, they were also found to be bounded between the laminar HOQ and SWQ limit. Further insight was gained by analysing the normalized wall heat flux φ_Q and the Peclet number Pe_Q. Both quantities were also found to be within the limits of laminar flame-wall interactions. Their respective average was estimated as

$$\varphi_Q \approx 0.14 \tag{4.13}$$
$$Pe_Q \approx 7.7. \tag{4.14}$$

In this context, it was noted that knowing the Peclet number allows a more detailed estimation of the quenching distance

$$y_Q = \frac{\lambda}{\rho_u c_p s_L^0} Pe_Q, \tag{4.15}$$

where Pe_Q can either be assumed to be constant ($Pe_Q = 7.7$) or vary between $Pe_{Q,HOQ} \approx 5$ and $Pe_{Q,SWQ} \approx 10$. This relation can be used for all types of fuels and engines with a premixed combustion process. The dependence of the characteristic scales φ_Q and Pe_Q on the quantities p, T_u, ϕ and Y_{EGR} was discussed. A slight pressure dependency was evident, which was explained by differences of the corresponding Zeldovich numbers and the inner layer temperatures.

The experimental evidence provided in this chapter suggests that flame-wall interactions in SI engines are laminar. This essentially confirms the hypothesis of the a priori analysis in section 3.4. In combination with the explanations in chapter 3, a coherent picture of quenching in a SI engine can be drawn. Although the main combustion phase is highly turbulent, the turbulence and thereby the wrinkling of the flame strongly decays towards the wall. As a consequence, the turbulence is too weak to influence the local thermo-diffusive processes and the final phase of flame propagation and in particular the quenching process is essentially laminar. For this reason, the processes leading to flame extinction, i.e., radical recombination and the decay of chain-branching and radical-fuel reactions due to heat losses, can also be

assumed to be similar to laminar flame-wall interactions. It is expected that this finding is the same for all types of internal combustion engines with a premixed combustion process. The presented results can thus be used to adapt and develop combustion and hydrocarbon emission models aiding the design process of efficient engines. The present approach to model flame-wall interactions, for example, relies strongly on the quenching distance y_Q. It will be presented in detail in the next chapter.

5 Modelling premixed flame-wall interactions using a level-set flamelet approach

The *G*-equation model has been successfully applied to many turbulent combustion problems, especially SI engines (Ewald [66], Dahms [46] and Linse [111]). However, it is not adapted to near-wall combustion. The importance of an accurate representation of flame-wall interactions has already been stressed in section 3.5 and is underlined by the fact that more than two thirds of the in-cylinder charge may be burned in a decelerating flame interacting with the cylinder walls (Heywood [90], Liu et al. [115]). Moreover, it was revealed by Foucher et al. [72, 75] that the burning velocity of a turbulent flame in the vicinity of the a SI engine piston is already reduced at a wall distance of order 1mm, which is much larger than the quenching distance itself. The reason for this is that the leading flamelets are already quenched whereas the trailing flamelets are still burning.

For these reasons, an accurate representation of combustion in a SI engine has to include the effects of flame-wall interaction. As already indicated in Fig. 3.1 and section 3.5, the main effects which have to be considered for this purpose are the effects of quenching and near-wall turbulence (cf. Bruneaux et al. [31], Alshaalan and Rutland [11]). Both of these issues have already been examined from a phenomenological point of view in chapter 3. Near the wall, wall heat loses induce the recombination of radicals and eventually the extinction of the flame. Near-wall turbulence, in contrast, may lead to a combustion regime change and to a decrease of the quenching distance. However, the basic interaction between the turbulence and the flame remains the same as for freely propagating flames (Poinsot and Veynante [150]). Hence, a comprehensive flame-wall interaction model should be integrable into an existing combustion model describing the interaction between the flame and the turbulent flow field.

In this context, a physically sound theoretical approach for the modelling of flame-wall interactions is still missing. For example, the validity of the modelling assumptions of the combustion model such as the flamelet hypothesis have not yet been discussed in the presence of quenching. Moreover, there is no flame-wall interaction model for combustion models based on a turbulent flame speed such as the *G*-equation. In this chapter, these issues are addressed by systematically deriving a flame-wall interaction model based on a level-set approach. For this purpose, this chapter is divided into four main parts. First the original *G*-equation is introduced. The second part focuses on the modelling of quenching effects using a physical description of the post-flame oxidation process. A unified *G*-equation for laminar premixed quenched and unquenched flames is derived using the respective characteristic flame structures. The concept is subsequently transferred to turbulent flames by assuming

that flamelets can be found in either an unquenched or a quenched state. The probability of finding quenched flamelets is introduced yielding the unquenched factor Q as a measure for the unquenched fraction of the turbulent flame brush. It is shown that Q can be used as a proper scaling factor for the turbulent burning velocity in the presence of flame quenching. Based on these findings, a unified level-set approach for modelling turbulent premixed quenched and unquenched flames is proposed. The third part is devoted to the modelling of the effects of near-wall turbulence and to a lesser extent, flame development. Improved modelling closures for the G-equation as well as a correlation for the turbulent burning velocity are proposed based on either the k-ε and k-ζ-f turbulence model. In the last part, the G-equation Flame-Wall Interaction (GFWI) model is analysed and used to simulate combustion in a turbulent channel flow as well as a simple SI engine. The results are compared to experimental as well as simulative data.

5.1 The G-equation model for turbulent combustion

This section briefly summarizes the derivation as well as the main aspects of the G-equation combustion model. First, the level-set approach for laminar flame propagation is introduced before the averaging procedure and the level-set approach for turbulent flames are discussed.

5.1.1 The level-set approach for laminar flames

The motion of a point $\mathbf{x}$ on a flame surface can be described by the kinematic equation

$$\frac{\mathrm{d}\mathbf{x}_f}{\mathrm{d}t} = \mathbf{v} + s_L \mathbf{n} \tag{5.1}$$

where $\mathbf{v}$ is the local convection velocity and s_L the laminar flame velocity parallel to the normal vector $\mathbf{n}$. A convenient way to compute and analyze the motion of interfaces in two or three dimensions are level-set methods. Originally developed by Osher and Sethian [131], level-set methods have become popular in a huge variety of applications such as graphics, image processing and computational fluid dynamics due to their robustness and ability to handle topological changes (cf. Sethian [177], Osher and Fedkiw [129, 130]). Within the level-set approach, the flame front is associated to the iso-scalar surface G_0, i.e.

$$G(\mathbf{x}, t) = G_0, \tag{5.2}$$

whereby $G > 0$ represents burned and $G < 0$ unburned gases, respectively (Fig. 5.1). The physical location of G_0 can be defined anywhere within the flame structure. A common choice is the location of the inner layer, which is defined by either the inner layer temperature T_0 or the corresponding deficient fuel (lean flame) or oxygen (rich flame) mass fraction Y_0 (Peters [141, 142]). To derive a transport equation for the position of the flame front, the total derivative of Eq. (5.2) is used,

$$\frac{\mathrm{D}G}{\mathrm{D}t} = \frac{\partial G}{\partial t} + \nabla G \cdot \frac{\mathrm{d}\mathbf{x}_f}{\mathrm{d}t} = 0. \tag{5.3}$$

After introducing the displacement velocity of the flame front (Eq. (5.1)) and the definition of the normal vector $\mathbf{n} = -\nabla G / |\nabla G|$, the original G-equation introduced by Williams [212] is obtained,

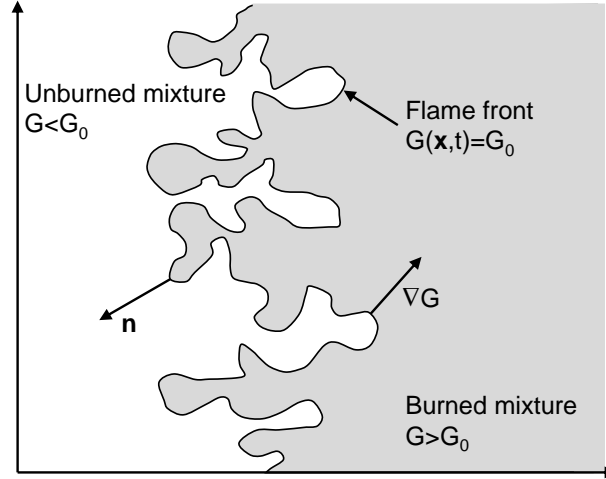$$\frac{\partial G}{\partial t} + \mathbf{v} \cdot \nabla G = s_L |\nabla G|. \tag{5.4}$$

Figure 5.1: Schematic representation of the flame front as the iso-scalar surface $G(\mathbf{x}, t) = G_0$.

To obtain leading order expressions for s_L in the thin reaction zones and corrugated flamelets regime, Peters [141, 142] conducted an order of magnitude analysis. It was revealed that in the corrugated flamelets regime, the influence of flame strain and curvature on the laminar burning velocity can be neglected due to the purely kinematic interaction between turbulence and flame. In the thin reaction zones regime, however, the smallest eddies penetrate the preheat layer of the flame altering the transport processes therein. In this case, the curvature term was found to be dominant. The leading order expression valid in both regimes reads

$$s_L = s_L^0 - D\kappa, \tag{5.5}$$

whereby $\kappa = \nabla \cdot \mathbf{n} = \nabla \cdot (-\nabla G / |\nabla G|)$ is the curvature. The level set equation for the corrugated flamelets and the thin reaction zones regime is thus given by

$$\rho \frac{\partial G}{\partial t} + \rho \mathbf{v} \cdot \nabla G = \left(\rho s_L^0 \right) \sigma - (\rho D) \kappa \sigma \qquad \text{with} \qquad \sigma = |\nabla G|. \tag{5.6}$$

The equation was additionally multiplied with the density in order to be consistent with other field equations and allow for Favre averaging. The mass flow rate (ρs_L^0) through a steady planar flame is constant (cf. Eq. (2.56)). For the present work, the definition $(\rho s_L^0) = (\rho s_L^0)_u$ is used. Similarly, (ρD) is assumed to be constant. The thermal diffusivity is evaluated at the location of the inner layer and can be estimated using Eq. (2.62), $(\rho D) = (\lambda / c_P)|_{T_{ref} = T_0}$.

A drawback of the G-equation approach is that the G-scalar is only valid on the flame front and therefore not uniquely defined outside of $G = G_0$ (Peters [142], Oberlack et al. [128]). A common and reasonable way to extend of the validity of the scalar G is the use of the constraint

$$|\nabla G| = 1 \tag{5.7}$$

outside of $G = G_0$. Hence, the scalar G becomes a signed distance function describing the (normal) distance to the flame front. This approach is permitted as the G-equation fulfills the generalized scaling symmetry (Oberlack et al. [128]). The generalized scaling symmetry states that the transformation $G^* = f(G)$ with an arbitrary, monotonically increasing function $f(G)$ changes neither the functional form of the evolution Eq. (5.6) nor its physical property (i.e., the flame front position). This has two important consequences: on the one hand, the value of G at a given flame front is completely arbitrary and on the other hand, the evolution of the iso-surface $G = G_0$ is not governed by the surrounding G-field.

5.1.2 The level-set approach for turbulent flames

The instantaneous G-equation has to be averaged before it can be used for modelling combustion in turbulent flows. In contrast to other transported scalars, G is not per se defined outside of $G(\mathbf{x}, t) = G_0$. As a result, conventional Reynolds or Favre averaging cannot be used as pointed out by Peters [142] and Oberlack et al. [128]. A suitable averaging procedure for the position of the mean flame front was derived by Oberlack et al. [128] and reads

$$\widehat{\mathbf{x}}_f(\lambda, \mu, t) = \iiint\limits_{-\infty}^{\infty} \mathbf{x} P(G_0; \mathbf{x}(\lambda, \mu, t)) \, dx_1 dx_2 dx_3 \tag{5.8}$$

where (λ, μ) are a set of curvilinear coordinates describing the instantaneous realisation of the flame front. The probability density function $P(G_0; \mathbf{x}(\lambda, \mu, t))$ describes the probability of finding an instantaneous flame front whose mean position is $\widehat{\mathbf{x}}_f$ at the spatial coordinate $\mathbf{x}$. In order to relate this averaging procedure to the G-equation, it is convenient to ignore the nonunique definition of G outside of $G(\mathbf{x}, t) = G_0$ in a first step. This allows to define a probability density function $P(G; \mathbf{x}, t)$ at point $\mathbf{x}$ and time t within the flow field. Using this probability density function, the unconditional mean and the variance of the G-field can be estimated as

$$\overline{G}(\mathbf{x}, t) = \int_{-\infty}^{\infty} G P(G; \mathbf{x}, t) dG, \tag{5.9}$$

$$\overline{G'^2}(\mathbf{x}, t) = \int_{-\infty}^{\infty} (G - \overline{G})^2 P(G; \mathbf{x}, t) dG. \tag{5.10}$$

Although $P(G; \mathbf{x}, t)$ is not uniquely defined, it contains a well-defined quantity, namely the probability of finding an instantaneous flame surface $G(\mathbf{x}, t) = G_0$ at the point $\mathbf{x}$ and time t (Peters [142])

$$P(G_0; \mathbf{x}, t) = \int_{-\infty}^{\infty} \delta(G - G_0) P(G; \mathbf{x}, t) dG. \tag{5.11}$$

A possibility for measuring this quantity is counting the number of flame crossings in a small volume ΔV located at $\mathbf{x}$ over a small time interval Δt. Measurements of $P(G_0; \mathbf{x}, t)$ have been made for a stabilized weak swirl burner by Plessing et al. [148] as well as in an optically accessible SI engine by Wirth [214]. In both cases, it was shown that $P(G_0; \mathbf{x}, t)$ has a gaussian shape which is slightly skewed towards the unburned side due to heat release effects.

For simplicity, a statistically one-dimensional steady turbulent flame propagating in the flame-normal direction x is considered in the following. Consequently, all quantities become a function of x only and $P(G_0; \mathbf{x}(\lambda, \mu, t))$ as well as $P(G_0; \mathbf{x}, t)$ are both reduced to the same probability density function $P(G_0; x)$. By normalizing $P(G_0; x)$, i.e., $\int_{-\infty}^{\infty} P(G_0; x)\mathrm{d}x = 1$, the mean flame position $\widehat{x}_f$ can be determined using Eq. (5.8) as

$$\widehat{x}_f = \int_{-\infty}^{\infty} x P(G_0; x)\mathrm{d}x. \tag{5.12}$$

For the variance, one obtains

$$\widehat{(x - \widehat{x}_f)^2} = \int_{-\infty}^{\infty} (x - \widehat{x}_f)^2 P(G_0; x)\mathrm{d}x \tag{5.13}$$

which, according to Peters [142], can be used to obtain a plausible definition of the turbulent flame brush thickness

$$\ell_{F,t} = \left(\widehat{(x - \widehat{x}_f)^2} \right)^{1/2}. \tag{5.14}$$

Obviously, the averaging procedure described above only includes the position of the instantaneous flame fronts. The main question, which arises at this point, is how these quantities can be related to to the mean $\overline{G}(x)$ and the variance $\overline{G'^2}(x)$ of the G-field. In the present example, this can be done as follows. The level-set of the mean flame front can be defined as

$$\overline{G}(\widehat{x}_f) = G_0. \tag{5.15}$$

By enforcing the constraint $|\nabla \overline{G}| = 1$, the G-scalar outside of G_0 describes the signed distance to the flame front, i.e.,

$$\overline{G}(x) - G_0 = x - \widehat{x}_f \tag{5.16}$$

The spatial fluctuation of the flame front $x - x_f$ can then be related to the scalar fluctuation $G' = G - \overline{G}$ by

$$G' = G - \overline{G} = G - G_0 - (x - \widehat{x}_f) \tag{5.17}$$

Since the scalar G only has a meaning on the instantaneous flame front G_0, G' has to be conditioned and becomes

$$G'|_{G=G_0} = -(x - \widehat{x}_f). \tag{5.18}$$

This shows that the fluctuations of the scalar G are directly related to the spatial fluctuations of the flame front for statistically one-dimensional flames under the premise of using the reinitialization $|\nabla \overline{G}| = 1$. In this case, the conditional variance $\widehat{(x - \widehat{x}_f)^2}$ can be calculated by evaluating the unconditional variance $\overline{G'^2}$ at the position of the mean flame front $\overline{G}(x) = G_0$.

However, the conditional variance is constant along the normal direction of the flame brush whereas in general, $\overline{G'^2}(\mathbf{x}, t)$ is not. If the gradient of $\overline{G'^2}$ in the flame normal direction is high, Peters [142] suggested the use of a reinitialization technique to ensure that the variance is constant along the normal direction.

At this point, it has to be stressed that the previously discussed approach of averaging the G-equation is only valid for statistically one-dimensional flames (i.e., all quantities depend on the flame-normal coordinate x) and only when using a renormalization procedure to enforce $|\nabla \overline{G}| = 1$. In this case, a possible way to derive transport equations for $\overline{G}$ and $\overline{G'^2}$ is to estimate their unconditional averages based upon the instantaneous G-equation (Eq. (5.6)) and viewing them as conditional averages only. Thereby, it has to be ensured thereby that fundamental characteristics of the G-equation such as the previously discussed generalized scaling symmetry are not violated. The averaging procedure should be consistent to the one used for the fluid equations. For variable density flows, the Favre average is commonly utilized. Consequently, the scalar G as well as the velocity $\mathbf{v}$ are split into their respective Favre averages and fluctuations,

$$G = \widetilde{G} + G'' \qquad \text{and} \qquad \mathbf{v} = \widetilde{\mathbf{v}} + \mathbf{v}''. \tag{5.19}$$

The Favre- and Reynolds-average of G are approximately the same, i.e., $\overline{G} \approx \widetilde{G}$, as the density fluctuations along G_0 are expected to be small (Peters [142], Herrmann [89]). The unclosed, Favre-averaged G-equation then reads:

$$\overline{\rho} \frac{\partial \widetilde{G}}{\partial t} + \overline{\rho} \, \widetilde{\mathbf{v}} \cdot \nabla \widetilde{G} + \nabla \cdot \left(\overline{\rho} \, \widetilde{\mathbf{v}'' G''} \right) = \left(\rho s_L^0 \right) \overline{\sigma} - (\rho D) \, \overline{\kappa \sigma} \tag{5.20}$$

The variance equation can be derived by subtracting Eq. (5.20) from Eq. (5.6), multiplying the result with $2G''$ and finally calculating the average. It reads:

$$\overline{\rho} \frac{\partial \widetilde{G''^2}}{\partial t} + \overline{\rho} \, \widetilde{\mathbf{v}} \cdot \nabla \widetilde{G''^2} + \nabla \cdot \left(\overline{\rho} \, \widetilde{\mathbf{v}'' G''^2} \right) = -2 \overline{\rho} \, \widetilde{\mathbf{v}'' G''} \cdot \nabla \widetilde{G} - \overline{\rho} \widetilde{\omega} - \overline{\rho} \widetilde{\chi} - (\rho D) \, \overline{\mathcal{K} \sigma}. \tag{5.21}$$

In this equation, $\widetilde{\omega} = -2 s_L^0 \overline{G'' \sigma}$ denotes the kinematic restoration whereas $\widetilde{\chi} = 2D \left(\widetilde{\nabla G''} \right)^2$ represents the scalar dissipation rate. Both play a similar role in reducing the fluctuations of the flame front due to reaction, however, the former is dominant in the corrugated flamelets regime whereas the latter prevails in the thin reaction zones regime. The term $\overline{\mathcal{K} \sigma}$ is a curvature term.

The Eqs. (5.20) and (5.21) contain unclosed terms such as $(\rho s_L^0) \overline{\sigma}$, $\widetilde{\omega}$ or $\widetilde{\chi}$, which have to be appropriately modelled (see section 5.3). Once $\widetilde{G}$ and $\widetilde{G''^2}$ are known, the unconditional pdf $P(G; \mathbf{x}, t)$ as well as the conditional pdf $P(G_0; \mathbf{x}, t)$ of finding an instantaneous flame front can be estimated by a presumed pdf approach. This information can subsequently be used to link the G-equation model to the chemical reactions and the underlying transport equations of species and enthalpy. Several different possibilities such as the coupling with flamelet equations or tabulated chemistry are available for this purpose. For further details, the reader is referred to Peters [142], Herrmann [89], Ewald [66], Dahms [46] and Linse [111].

5.2 Modelling of flame quenching

The *G*-equation, as introduced in the section before, was derived based on the physics of a freely propagating premixed flame. When the flame is quenched, the underlying physics change and the modelling approaches have to be reviewed and altered accordingly. In this section, a consistent level-set approach for quenched and unquenched flames is developed based on established concepts of combustion modelling. First, the structure and kinematic behaviour of a laminar quenched flame is studied and the applicability of the flamelet hypothesis for quenched flames is discussed. Bases on these findings, a level-set equation valid for laminar quenched and unquenched flames is proposed. The second part deals with the extension of the modelling concept to turbulent flames. Due to the kinematic nature of turbulent flame-wall interactions, the focus lies on the probability of finding quenched flamelets rather than describing the effect of wall heat loss on individual flamelets. The unquenched factor *Q* being a measure for the fraction of unquenched flamelets is introduced and its impact on the turbulent burning velocity is shown. Finally, a level-set approach for turbulent quenched and unquenched flames is proposed.

5.2.1 The level-set approach for laminar quenched and unquenched flames

The level-set approach as well as the flame surface density approach are based on a geometrical description of the flame front. A fundamental cornerstone of these models is the flamelet hypothesis, which states that the flame is thin compared to all flow scales. As a consequence, the main heat release of a freely propagating flame occurs in a spatially thin layer separating the fresh and burned gases. This layer may be wrinkled and distorted by the surrounding flow field, however, the local structure of the flame itself remains similar to the structure of a laminar premixed flame (Fig. 2.2 in section 2.3.1). The reaction zone (inner layer) of the flame in which the fuel/oxygen is consumed can be characterized by either the inner layer temperature T_0 or by the corresponding deficient fuel (lean flame) or oxygen (rich flame) mass fraction $Y_0 = Y|_{T=T_0}$. The analysis of these iso-scalar surfaces results in some well-known modelling concepts of turbulent combustion such as the *G*-equation.

At this point, the question arises whether these approaches can still be used in the presence of flame quenching. To clarify this question and to systematically derive a physically sound level-set approach that is valid for laminar quenched and unquenched flames, the following steps are carried out in the following:

- derivation of the structure of a quenched flame based on the physics of quenching and hydrocarbon post-flame oxidation

- identification of a characteristic layer within the quenched flame

- derivation of the level-set transport equation for laminar quenched flames

- unification of the level-set equations for laminar quenched and unquenched flames

In general, the flame-wall interaction process is divided in three stages (cf. section 3.1): in the initial phase, the flame is already influenced by the wall but retains its inner structure. Hence, T_0 or Y_0 can still be used to define of the position of the reaction zone. The ensuing rapidly proceeding quenching phase can be interpreted as a short transition stage to the final post-flame oxidation stage. The structure of a (quenched) flame in this final phase can be analysed by utilizing the study on hydrocarbon post-flame oxidation by Wu and Hochgreb [215, 216]. After the flame is extinguished, the remaining fuel diffuses from the wall towards the hot burned gases where it reacts with the present radicals and forms intermediate hydrocarbons. This diffusive-reactive process is either limited by diffusion or reaction depending on the core temperature T_c of the burned gases. If T_c is below a certain transition temperature of around 1400-1700K (depending on the fuel), the process and the reaction rate of the fuel are controlled and limited by reaction. On the other hand, if T_c is above this temperature, diffusion controls the process and becomes the limiting factor (Wu et al. [215]). During and shortly after quenching, the core gas temperature can be assumed to be of order of the adiabatic flame temperature, i.e., $T_c \approx T_b$, and thus above the transition temperature. For this reason, the post-flame oxidation process is essentially limited by diffusion after the flame is quenched by the wall. The structure of this diffusion-limited quenched flame can be abstracted from the results of Wu et al. [215]. The result is shown in Fig. 5.2.
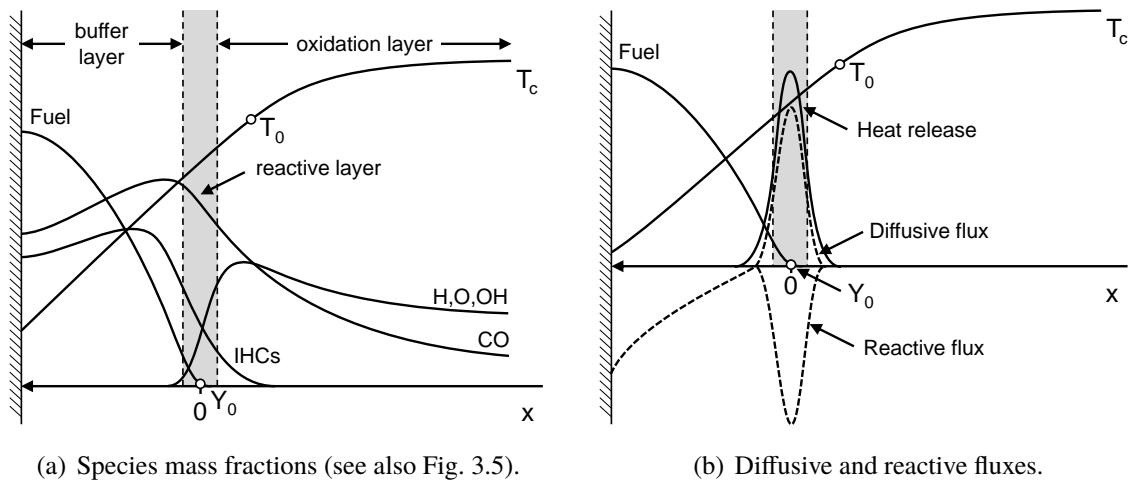

(a) Species mass fractions (see also Fig. 3.5).   (b) Diffusive and reactive fluxes.

Figure 5.2: Schematic illustration of the inner structure of a laminar quenched premixed flame at high core gas temperatures derived from the results of Wu et al. [215, 216].

Similar to an unquenched laminar flame, three characteristic layers can be identified. The buffer layer can be assumed to be chemically inert due to a low temperature level. The more stable species such as intermediate hydrocarbons (IHCs) or CO diffuse from the reaction zone towards the wall and accumulate within the buffer layer. The fuel, on the other hand, diffuses away from the wall towards the reactive layer where it is consumed by radicals. Within this layer, the reactive and diffusive fluxes are in balance (Wu et al. [215]). Furthermore, the fuel is completely consumed and intermediate hydrocarbons as well as CO and radicals

are formed. The peak of the heat release is located where, firstly, the diffusive flux of the fuel mass fraction is large and secondly, the temperature and thus the radical level is high. Consequently, the reaction zone remains spatially thin and can still be identified by the deficient fuel mass fraction Y_0. The inner layer temperature T_0 does no longer coincide with Y_0, since it is affected by the wall heat flux and retreats from the wall. The reactive layer is followed by an oxidation zone in which intermediate species are oxidized to CO_2 and H_2O and the radical concentration decreases to its equilibrium value in the burned gases.

The previous discussion shows that a level-set transport equation for a quenched flame has to be derived by using the species mass fraction Y_0 as it is a sound tracer for the position of the reaction zone. The usage of an iso-scalar species surface is also required for a consistent coupling of the combustion model to the energy equation. The temperature and species field during quenching are no longer aligned as in adiabatic conditions due to the wall heat losses. As a consequence, the temperature field can no longer be used to define the G-equation as the coupling to the species field and thereby to the energy equation would become ambiguous. For these reasons, the quenched flame is represented by the iso-scalar surface

$$Y\left(\mathbf{x}, t\right) = Y_0. \tag{5.22}$$

In combination with the species transport Eq. (2.4), a kinematic equation for the iso-scalar surface $Y\left(\mathbf{x}, t\right) = Y_0$ can be derived (cf. Peters [141]). The resulting equation can be rewritten in terms of the non-reacting scalar G by requesting that $G\left(\mathbf{x}, t\right) = G_0$ coincides with $Y\left(\mathbf{x}, t\right) = Y_0$. This approach yields (Peters [141], Echekki and Chen [60])

$$\rho \frac{\partial G}{\partial t} + \rho \mathbf{v} \cdot \nabla G = \rho\left(s_n + s_r\right)\sigma - \rho D \kappa \sigma, \tag{5.23}$$

where

$$s_n = -\frac{\mathbf{n} \cdot \nabla\left(\rho D \mathbf{n} \cdot \nabla Y\right)}{\rho \left|\nabla Y\right|} \qquad \text{and} \qquad s_r = -\frac{\dot{\omega}}{\rho \left|\nabla Y\right|} \tag{5.24}$$

are the normal diffusion and the reaction velocity which are based on the (normal) diffusive and the reactive flux, respectively. In these equations, D is the diffusion coefficient of the tracked species at Y_0 and $\dot{\omega}$ its chemical source term. The scalar G divides the flow field into an unburned $G < G_0$ and a burned $G > G_0$ region.

Eq. (5.23) is universally valid for any surface defined by an iso-scalar species mass fraction, since no specific assumptions were introduced. Hence, it can be used to describe laminar quenched as well as unquenched flames. However, as already indicated in the previous discussion, the physics of a freely propagating and a quenched flame are quite different. It was previously argued that a quenched flame is dominated by a diffusive-reactive oxidation process limited by the diffusion speed of the fuel mass fraction. In this case, Wu and Hochgreb [215] have shown that the diffusive and the reactive fluxes balance each other in the reaction zone (see also Fig. 5.2b). At first order, the magnitude of the normal diffusion and reaction velocity can thus be assumed to be equal and counteracting, i.e.

$$s_n + s_r = 0. \tag{5.25}$$

Therefore, the leading-order level-set equation for a laminar quenched flame is given by

$$\rho \frac{\partial G}{\partial t} + \rho \mathbf{v} \cdot \nabla G = -\rho D \kappa \sigma. \tag{5.26}$$

Strictly speaking, it has to be remarked that this equation only remains valid as long as T_c is above the transition temperature of $1400 - 1700K$. If T_c falls below this temperature, the post-flame oxidation process becomes limited by the reaction speed, which can no longer fully compensate the diffusive flux. Consequently, the iso-surface $Y(\mathbf{x}, t) = Y_0$ starts to move away from the wall. However, the fuel mass fraction at the wall has already considerably decreased at this point and the sum of the reactive and diffusive speed can be estimated to be very small, i.e., $s_n + s_r \ll s_L^0$. The error made by assuming that $s_n + s_r = 0$ is thus expected to be small. The physical behaviour implied by this equation can be interpreted by considering two limiting cases. For a planar quenched flame ($\kappa = 0$) in a quiescent flow ($\mathbf{v} = 0$), the location of the species mass fraction Y_0 and thereby the reaction zone of remains in place. This result is backed by the study of Kiehne et al. [101], who studied the head-on quenching and the subsequent oxidation of various laminar premixed flames. They state that the position of the maximum heat release remains almost unchanged after quenching although the magnitude of the heat release decreases. In case that the quenched flame is not planar ($\kappa \neq 0$), the curvature tends to smooth out perturbations and cusps leading to a gradual flattening of the flame surface due to diffusion. This prediction is supported by the DNS results obtained by Lai et al. [106]. The published time-sequences of a turbulent flame during HOQ reveal that the initially wrinkled flame profiles gradually flatten after quenching.

It is interesting to note that Eq. (5.26) describing a quenched flame has also been identified by Peters as the leading order equation for an unquenched flame in the thin reaction zones regime. Although it was derived based on different physical arguments, the mathematical character of the present equation and the original G-equation (Eq. (5.6)) is the same. Moreover, the reaction zone of unquenched and quenched flames can be uniquely identified by the same iso-scalar surface $Y(\mathbf{x}, t) = Y_0$. For these reasons, the Eqs. (5.26) and (5.6) can be unified in a coherent way. By comparing these equations to each other, it becomes apparent that the propagation term $\left(\rho s_L^0\right) \sigma$ vanishes once the flame is quenched. This is consistent with the theoretical study of Wichman and Bruneaux [210] in which it was shown that the mass consumption speed of a laminar flame decreases and ultimately drops to zero during quenching. Hence, flame quenching in the context of the G-equation model can be addressed by properly modelling the laminar burning velocity. As indicated in section 3.1, the transient phase of quenching proceeds rapidly (around two flame times) and as a consequence, the impact of the wall heat losses on the laminar flame speed is limited to a small spatial region adjacent to the quenching zone. A simple model for the laminar burning velocity can thus be defined by assuming that the transient phase of quenching is negligible compared to the fully quenched or unquenched stage. This assumption yields

$$s_L = H\left(x_Q\right) s_L^0, \tag{5.27}$$

where H is the Heaviside function and x_Q represents the distance of the flame front $G(\mathbf{x}, t) = G_0$ to the quenching distance. For $x_Q > 0$, the flame is outside of the quenching zone

and is not influenced by the wall. Once it enters the quenching zone, the burning velocity and thereby the mass consumption speed drops to zero. The unified G-equation valid for quenched and unquenched flames is thus given by

$$\rho \frac{\partial G}{\partial t} + \rho \mathbf{v} \cdot \nabla G = (\rho s_L)\, \sigma - (\rho D)\, \kappa \sigma. \tag{5.28}$$

The present model for the laminar burning velocity s_L simplifies the effect of wall heat losses by assuming that flamelets can only be found in two distinct states, i.e., quenched or unquenched. This approach is thus not suited for studying laminar flame-wall interactions as the thermodynamic effects are decisive in this case. For turbulent flame-wall interactions, however, the kinematic effects of turbulence are dominant and the main focus of modelling then lies on determining the probability of finding quenched and unquenched flamelets within a turbulent flame brush rather than describing the spatially limited effects of wall heat losses.

5.2.2 Probability of finding quenched and unquenched flamelets within a turbulent flame brush

For laminar flames, the determination whether the flame front is quenched or not is straightforward: the flame extinguishes once it reaches the quenching distance. However, turbulent flames are an inherently stochastic phenomenon, since the wrinkling of the flame surface is controlled by the erratic turbulent flow motions. For this reason, some parts of the turbulent flame brush may already be quenched whereas others are not as they are still far away from the wall. As shown previously, only the unquenched flamelets can contribute to the overall consumption speed. To tackle the modelling of turbulent flame quenching, it is thus necessary to find an expression for the unquenched fraction of the turbulent flame brush which takes the kinematic and stochastic nature of a turbulent flame into account. For this purpose, the probability that a single realization of the turbulent flame front is quenched has to be determined. Without loss of generality, a statistically one-dimensional flame is considered in the following.

In analogy to laminar flames, it can be assumed that all realizations within a certain distance from the wall are extinguished (Fig. 5.3a). Hence, the main task is estimating the probability of finding an instantaneous flame surface $G = G_0$ within this quenching distance. This is illustrated in Fig. 5.3b. Therein, x is the flame normal coordinate pointing towards the unburned gases. Its origin is assumed to be attached to the position of the mean flame front. The quantities x_Q and x_W represent the average distances between the position of the mean flame front and the quenching zone respectively the wall. They are connected via the mean quenching distance y_Q, which is a cornerstone of the present modelling approach. The probability density function $P(G_0; x, t)$ describes the probability of finding an instantaneous flame surface $G(x, t) = G_0$ at x and time t.

Using these definitions, the fraction of unquenched flames within a turbulent flame brush can be estimated by integration along the normal direction x

$$Q = \int_{-\infty}^{x_Q} P(G_0; x, t)\, \mathrm{d}x. \tag{5.29}$$
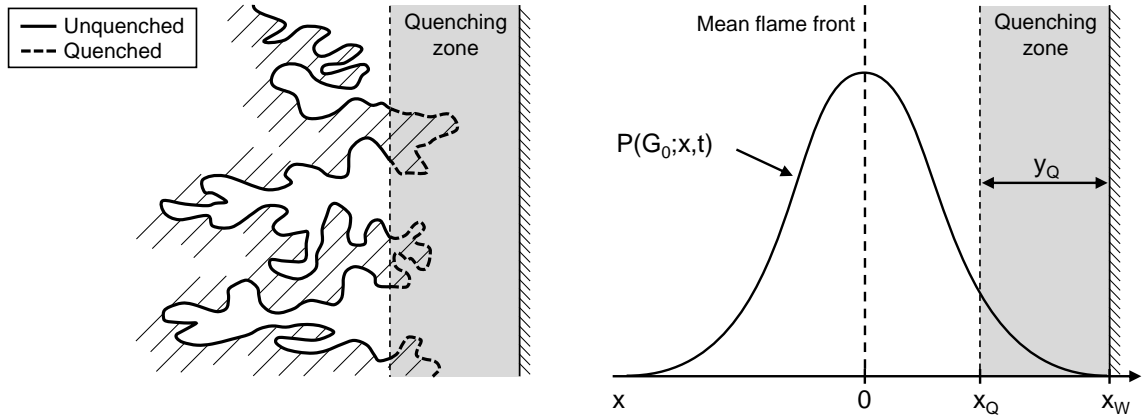
(a) Illustration of the concept of turbulent flame quench- (b) Probability density function $P(G_0; x, t)$ of a statistiing. cally one-dimensional flame interacting with a wall.

Figure 5.3: Visualisation of the interaction of a statistically one-dimensional turbulent flame with a wall.

This formulation implicates that quenched flamelets can only be found in the quenching zone. However, quenched flamelets may also appear outside of the quenching zone due to several reasons: firstly, although the turbulent flow motion is strongly decaying due to the enhanced viscosity in the burned gases, the remaining flow may force the quenched flamelets away from the wall. In this regard, it was shown by Foucher et al. [74] that even the quenching process itself may induce a fresh gas flow pushing the flame from the wall and amplifying small perturbations of the flame front. Secondly, the orientation of the flamelet in relation to the wall influences the quenching distance. Poinsot et al. [149] found that the flamelets within a turbulent flame brush may extinguish in a head-on as well as a sidewall configuration, whereby the quenching distance in the latter case is more than twice as high as in the former one. Thirdly, flamelets may be subject to flame stretch leading to an increased sensitivity towards heat losses and therefore to higher quenching distances (cf. section 2.3.1 and 3.1.3). Lastly, the local thermodynamic state of the turbulent flow can fluctuate which in turn directly affects the quenching distance.

To include these effects, the previous definition of the unquenched factor Q (Eq. (5.29)) has to be generalized. This can be done by only accounting for flamelets whose burning velocity is larger than zero, since the propagation velocity of quenched flamelets drops to zero (cf. section 5.2.1). A generalized definition of the unquenched factor Q is thus given by

$$Q = \int\limits_{-\infty}^{x_Q} \int\limits_{s_L > 0}^{\infty} P\left(s_L \mid G = G_0; x, t\right) P\left(G_0; x, t\right) \mathrm{d}s_L \mathrm{d}x. \qquad (5.30)$$

Therein, the conditional pdf $P\left(s_L \mid G = G_0; x, t\right)$ describes the distribution of the laminar burning velocity among the iso-surfaces that represent the turbulent flame brush at the location x. As one can see, the unquenched factor Q only takes flamelets into account which,

on the one hand, contribute to the overall propagation rate of the flame and on the other hand, can be found outside of the quenching zone. For a further assessment of Q, it is necessary to determine the conditional pdf of s_L. In accordance with the findings of the previous section, it can be assumed that a laminar flamelet can only be found in three distinct states along the normal direction x of the turbulent flame:

1. laminar unquenched flame, i.e., $s_L = s_L^0$.

2. laminar quenched flame, i.e., $s_L = 0$.

3. laminar flame during the transient phase of the quenching process, i.e., $0 < s_L < s_L^0$.

The conditional pdf of s_L along x can thus be described as a BML-type pdf,

$$P(s_L | G = G_0; x, t) = \alpha(x, t)\,\delta(s_L) + \beta(x, t)\,\delta(s_L^0 - s_L) + \gamma(x, t)\,f(s_L, x, t)\,, \quad (5.31)$$

where $\alpha(x, t)$, $\beta(x, t)$ and $\gamma(x, t)$ are the conditional probabilities of finding a flame in a quenched, unquenched or transient state among the instantaneous flame surfaces $G(x, t) = G_0$. For turbulent flame-wall interactions, the effect of wall heat losses on the laminar burning velocity is insignificant compared to the kinematic effects of turbulence. The reason for this is that the characteristic length and time scales of the local quenching process are much smaller than the turbulent ones. Based on the discussion of turbulent flame-wall interactions in chapter 3, it can be assumed that individual flamelets are quenched within a short time $O(t_F)$ in a small spatial region $O(l_F)$ adjacent to the quenching zone. Consequently, the impact of the wall heat losses on the laminar burning velocity is also expected to be confined to this small area. This is confirmed by the DNS simulations of Poinsot et al. [149] showing that the flame speed of individual flamelets starts to drop significantly at $x_Q/l_F \approx 1 - 2$. The characteristic length scale of the turbulent flame brush, in contrast, strongly depends on the turbulent length scale. For many turbulent combustion processes, for example in SI engines, the order of the ratio l_t/l_F is between $O(10) - O(100)$ (e.g., Linse et al. [112]) and thereby much larger than the influence region of the wall heat losses. This finding has two major implications: firstly, the conditional probability of finding quenched flamelets $\gamma(x, t)$ is only important in a small spatial area adjacent to the quenching zone and secondly, its contribution to the integral (Eq. (5.30)) is thus very small. This underlines the kinematic notion of turbulent flame-wall interactions in contrast to the thermodynamic notion of laminar flame-wall interactions. Based on this discussion, $\gamma(x, t)$ can be set to zero and the pdf for s_L simplifies to a bimodal distribution,

$$P(s_L | G = G_0; x, t) = \alpha(x, t)\,\delta(s_L) + \beta(x, t)\,\delta(s_L^0 - s_L). \quad (5.32)$$

This pdf does not account for the effect of wall heat losses, however, the present framework allows for their integration. The normalization of the pdf (Eq. (5.32)) leads to

$$\alpha(x, t) + \beta(x, t) = 1. \quad (5.33)$$

Combining this result with Eq. (5.32) and inserting in Eq. (5.30) yields

$$Q = \int_{-\infty}^{x_Q} P(G_0; x, t)\,\mathrm{d}x - \int_{-\infty}^{x_Q} \alpha(x, t) P(G_0; x, t)\,\mathrm{d}x. \quad (5.34)$$

If this equation is compared to Eq. (5.29), a second term on the r.h.s. appears which decreases the unquenched factor Q by taking flamelets that appear outside of the quenching zone into account. To further evaluate Eq. (5.34), an estimate for $\alpha(x,t)$ has to be made. Unfortunately, no comprehensive set of statistical data which details the effects described above (such as the impact of the flamelet orientation or flame stretch) is available to model $\alpha(x,t)$ without further assumptions.

It can be postulated that any model for $\alpha(x,t)$ has to meet the following two requirements: being a physical quantity, the pdf of finding quenched flamelets $\alpha(x,t)P(G_0;x,t)$ has to be at least a C^0-function. Furthermore, the unquenched factor Q has to drop to zero once the mean flame front reaches the quenching distance and the flame brush is completely quenched. A simple and feasible model which meets this requirements can be defined by assuming that the quenched flamelets are distributed symmetrically around the beginning of the quenching zone at x_Q. This approach is depicted in Fig. 5.4.
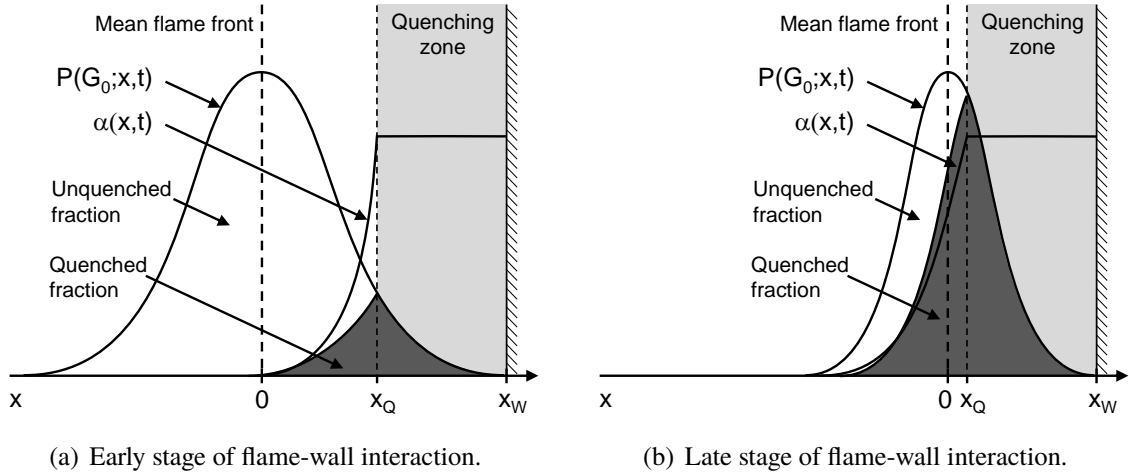

Figure 5.4: Illustration of the model for the probability of finding quenched flamelets within a turbulent flame brush.

The quenched fraction for $x < x_Q$, i.e., outside of the reaction zone, is assumed to be equal to the one for $x > x_Q$ and it follows that

$$\int_{-\infty}^{x_Q} \alpha(x,t)P(G_0;x,t)\,\mathrm{d}x = \int_{x_Q}^{\infty} P(G_0;x,t)\,\mathrm{d}x \tag{5.35}$$

with $\alpha(x < x_Q) = P(G_0; 2x_Q - x, t)/P(G_0; x, t)$ and $\alpha(x \geq x_Q, t) = 1$. In this way, it is ensured that $\alpha(x,t)$ is C^0-continuous and increases towards the wall. This means that flamelets closer to the wall are more likely to be extinguished than the ones located further away (see Fig. 5.4). It has to be remarked that this model constitutes a simplification and that in reality, the pdf of finding quenched flamelets $\alpha(x,t)P(G_0;x,t)$ is expected to be unsymmetrical and skewed towards the wall due to the strong flow anisotropy near the wall caused by temperature and velocity gradients. The error made by the simplification that

the quenched flamelets are distributed symmetrically around the beginning of the quenching zone is analysed in section 5.5.1. Inserting Eq. (5.35) and the normalization condition

$$\int_{-\infty}^{\infty} P(G_0; x, t)\mathrm{d}x = \int_{-\infty}^{x_Q} P(G_0; x, t)\mathrm{d}x + \int_{x_Q}^{\infty} P(G_0; x, t)\mathrm{d}x = 1 \qquad (5.36)$$

into Eq. (5.34) finally yields

$$Q = 1 - 2 \int_{x_Q}^{\infty} P(G_0; x, t)\mathrm{d}x. \qquad (5.37)$$

To evaluate Q according to Eq. (5.37), the pdf $P(G_0; x, t)$ has to be properly estimated. Within the G-equation model, the probability of finding an instantaneous realization of the flame front at $\mathbf{x}$ and time t is given by Eq. (5.11). According to Peters [142], the unconditional probability density function of finding a certain G-level at $\mathbf{x}$ and time t can be modelled as a Gaussian distribution defined by the mean $\widetilde{G}$ and the variance $\widetilde{G''^2}$. By performing the integration according to Eq. (5.11), only the instantaneous flame surfaces are taken into account and it follows that

$$P(G_0; \mathbf{x}, t) = \frac{1}{(2\pi \widetilde{G''^2}|_{\widetilde{G}=G_0})^{1/2}} \exp\left(-\frac{G_0 - \widetilde{G}(\mathbf{x}, t)}{2\widetilde{G''^2}|_{\widetilde{G}=G_0}} \right). \qquad (5.38)$$

An important property of the level-set approach now comes into effect. By enforcing the constraint $|\nabla \widetilde{G}| = 1$, the G-field becomes the signed distance function outside of the mean flame front $\widetilde{G} = G_0$. As a consequence, $G_0 - \widetilde{G}$ coincides with the previous definition of x along the flame normal direction and $P(G_0; \mathbf{x}, t)$ can be rewritten by replacing $G_0 - \widetilde{G}$ with x (cf. section 5.1.2). The unquenched factor Q can now be evaluated for each point on an arbitrarily shaped turbulent flame front by inserting Eq. (5.38) in Eq. (5.37). After integration, the unquenched factor reads

$$Q = \mathrm{erf}\left(\frac{x_Q}{\sqrt{2 l_{F,t}^2}} \right) \qquad (5.39)$$

where $l_{F,t}$ is the turbulent flame brush thickness defined by (Peters [142])

$$l_{F,t} = \left. \frac{\sqrt{\widetilde{G''^2}}}{|\nabla \widetilde{G}|} \right|_{\widetilde{G}=G_0}. \qquad (5.40)$$

Eq. (5.39) implies that a turbulent flame with a larger flame thickness $l_{F,t}$ will be influenced at a greater distance to the quenching zone than a flame with a small turbulent flame brush. The flame is ultimately completely quenched when x_Q decreases to zero, i.e., when the distance of the mean flame front to the wall equals the quenching distance. It is interesting to note that Eq. (5.39) recovers the blending function used in the unified level-set equation for laminar

quenched and unquenched flames, since the cumulative normal distribution converges to the Heaviside function for a disappearing standard derivation, $l_{F,t} \to 0$. Although the unquenched factor Q was derived using a level-set formalism, it can also be used in combination with other combustion models by specifying an appropriate turbulent flame thickness. For example, Peters [142] stated that the turbulent flame brush thickness is proportional to the integral length scale l_t for fully developed turbulent flames. Therefore, an algebraic definition of Q reads

$$Q_{alg} = \mathrm{erf}\left(\frac{x_Q}{\sqrt{2b_2^2 l_t^2}}\right) \tag{5.41}$$

where $b_2 = 1.78$ is the constant relating the turbulent length scale to the turbulent flame thickness. Having discussed the probability of finding quenched flamelets within a turbulent flame brush, the impact of flame quenching on turbulent flames and the turbulent burning velocity in particular can be examined.

5.2.3 Effect of quenching on the turbulent burning velocity

The previous discussion highlighted that the fraction of unquenched flamelets is continuously reduced once a turbulent flame brush interacts with a wall. Consequently, the turbulent burning velocity decreases, since only the unquenched flamelets are able to contribute to the total mass consumption speed of the turbulent flame brush. Finally, the mean flame front comes to a halt at the beginning of the quenching zone when all flamelets are extinguished. This behaviour has also been observed in the experiments by Foucher et al. [72, 75] who investigated the flame propagation near the piston of a SI engine. To derive a formulation for the turbulent burning velocity when parts of the turbulent flame brush are quenched, the flame surface density Σ is chosen as a starting point as it allows for a general geometrical description of the turbulent flame brush. The turbulent burning velocity s_T^0 is related to the flame surface density Σ by

$$\overline{\sigma} = \frac{A_T}{A} = \frac{s_T^0}{s_L^0} = \frac{\int_V \Sigma dV}{A_0} \tag{5.42}$$

where A_0 is the area perpendicular to the direction of flame propagation (e.g., Guelder et al. [78]. However, the relation is only valid if a constant propagation velocity s_L^0 of all flamelets is assumed. This assumption clearly fails in the presence of flame-wall interactions. A generalized relation accounting for spatial variations of the local flame speed is given by

$$s_T = \frac{\int_V \langle s_L \rangle_S \Sigma dV}{A_0}, \tag{5.43}$$

where $\langle s_L \rangle_S$ is the surface average of s_L. In this context, Σ has to be regarded as an interface surface density, since its definition, which is based on an iso-scalar surface of temperature or species mass fraction, does not allow a differentiation between a quenched or an active flame. This notion was already introduced by Bruneaux et al. [30, 31]. The surface average

of s_L is defined according to Pope [153] as

$$\langle s_L \rangle_S = \frac{\overline{s_L \Sigma'}}{\overline{\Sigma'}} = \frac{\overline{s_L \Sigma'}}{\Sigma}, \tag{5.44}$$

where Σ' is the local instantaneous or the fine-grained surface to volume ratio [153]. According to Peters [142], it can be expressed in terms of the G-equation framework as

$$\Sigma' = \sigma \delta \left(G - G_0 \right). \tag{5.45}$$

Inserting Eqs. (5.44) and (5.45) into Eq. (5.43) leads to

$$s_T = \frac{\int_V \overline{s_L \Sigma'} \mathrm{d}V}{A_0} = \frac{\int_V \overline{s_L \sigma \delta \left(G - G_0 \right)} \mathrm{d}V}{A_0}. \tag{5.46}$$

The average $\overline{s_L \Sigma'}$ can be evaluated by introducing the joint pdf $P \left(s_L, \sigma, G; \mathbf{x}, t \right)$ for G, s_L and σ, where G accounts for fluctuations of the instantaneous flame front normal to the mean flame front, σ for fluctuations of its angle and s_L for fluctuations of its propagation speed. This pdf can be decomposed by using the Bayes' theorem into the marginal pdf of G and the conditional pdfs of σ and s_L

$$P \left(s_L, \sigma, G; \mathbf{x}, t \right) = P \left(s_L | \sigma, G; \mathbf{x}, t \right) P \left(\sigma | G; \mathbf{x}, t \right) P \left(G; \mathbf{x}, t \right). \tag{5.47}$$

If the quantities s_L and σ are assumed to be statistically independent, the average $\overline{s_L \Sigma'}$ can be written as

$$\overline{s_L \Sigma'} \left(\mathbf{x}, t \right) = \int_{-\infty}^{\infty} \int_{0}^{\infty} \int_{0}^{\infty} \delta \left(G - G_0 \right) s_L P \left(s_L | G; \mathbf{x}, t \right) \sigma P \left(\sigma | G; \mathbf{x}, t \right) P \left(G; \mathbf{x}, t \right) \mathrm{d}s_L \mathrm{d}\sigma \mathrm{d}G. \tag{5.48}$$

Integration of this equation by applying the delta function yields

$$\overline{s_L \Sigma'} \left(\mathbf{x}, t \right) = \langle \sigma | G = G_0 \rangle \langle s_L | G = G_0 \rangle P \left(G_0; \mathbf{x}, t \right) \tag{5.49}$$

where $\langle \sigma | G = G_0 \rangle$ is the conditional mean gradient of σ at $G \left(\mathbf{x}, t \right) = G_0$,

$$\langle \sigma | G = G_0 \rangle = \int_0^{\infty} \sigma P \left(\sigma | G = G_0; \mathbf{x}, t \right) \mathrm{d}\sigma \tag{5.50}$$

and $\langle s_L | G = G_0 \rangle$ represents the conditional mean laminar burning velocity at $G \left(\mathbf{x}, t \right) = G_0$,

$$\langle s_L | G = G_0 \rangle = \int_0^{\infty} s_L P \left(s_L | G = G_0; \mathbf{x}, t \right) \mathrm{d}s_L. \tag{5.51}$$

When $s_L = s_L^0 = const.$ is assumed, i.e., flame-wall interactions are absent, the classic relationship for the flame surface density is obtained

$$\Sigma \left(\mathbf{x}, t \right) = \langle \sigma | G = G_0 \rangle P \left(\mathbf{x}, t \right). \tag{5.52}$$

To further analyse Eq. (5.49), a statistically one-dimensional flame propagating propagating towards a wall in x-direction is considered again (cf. Fig. 5.3 and Fig. 5.4). Consequently, $P(\mathbf{x}, t)$, $\langle \sigma | G = G_0 \rangle$ and $\langle s_L | G = G_0 \rangle$ become a function of x only. Hence, Eq. (5.46) can be simplified and reads

$$s_T = \frac{A_0 \int_{-\infty}^{x_Q} \overline{s_L \Sigma'} \mathrm{d}x}{A_0} = \int_{-\infty}^{x_Q} \langle \sigma | G = G_0 \rangle \langle s_L | G = G_0 \rangle P(x, t) \, \mathrm{d}x \qquad (5.53)$$

after introducing Eq. (5.49).

In accordance with the previous section, the integration is only performed up to the beginning of the quenching zone at x_Q. For $x > x_Q$, all flamelets are assumed to be quenched and $\langle s_L | G = G_0 \rangle$ consequently equals zero. To further assess (5.53), the conditional mean burning velocity $\langle s_L | G = G_0 \rangle$ as well as the conditional mean gradient $\langle s_L | G = G_0 \rangle$ have to be estimated. The former can be calculated using the results of the previous section,

$$\langle s_L | G = G_0 \rangle = \beta(x, t) s_L^0 = (1 - \alpha(x, t)) s_L^0. \qquad (5.54)$$

To estimate the latter, a study on flamelet statistics by Chang et al. [37] can be utilized. The authors have shown that the mean cosine of the flamelet crossing angles σ_y is only weakly dependent on x for small v'/s_L^0 and becomes independent of x for large v'/s_L. The mean cosine of the flamelet crossing angles is related to the conditional mean gradient of G by $\langle \sigma | G = G_0 \rangle = 1/\sigma_y$ (cf. Wirth [214]). Thus it can be assumed that the conditional mean gradient is independent of x at first order, i.e.

$$\langle \sigma | G = G_0 \rangle \approx \overline{\sigma}. \qquad (5.55)$$

According to Kerstein et al. [100] as well as Peters [141, 142], $\overline{\sigma}$ can be interpreted as a surface area ratio relating the turbulent to the laminar burning velocity. Thus, $\overline{\sigma}$ is related to the classic definition of the turbulent burning velocity (cf. section 2.3.2),

$$\overline{\sigma} = \frac{A_T}{A} = \frac{s_T^0}{s_L^0}. \qquad (5.56)$$

Inserting this result as well as the Eqs. (5.54) and (5.55) in Eq. (5.53) results in

$$\frac{s_T}{s_L^0} = \int_{-\infty}^{x_Q} (1 - \alpha(x, t)) P(G_0; x, t) \, \mathrm{d}x \times \overline{\sigma} = Q \times \frac{s_T^0}{s_L^0}. \qquad (5.57)$$

The integral in this equation is equal to the definition (5.34) of the unquenched factor Q. Consequently, the effects of quenching on the turbulent burning velocity can be taken into account by scaling s_T^0 with the unquenched factor Q. Hence, the present approach can be used in combination with any combustion model that is based on the turbulent flame speed by employing Eqs. (5.39) or (5.41) for the unquenched factor Q. It is also possible to propose different models for $P(s_L | G = G_0; x, t)$ using the presented framework yielding different

expressions for Q. In analogy to the definition of the flame surface area ratio (Eq. 5.56), the reactive flame surface area ratio $\overline{\sigma}_R$ can be introduced and defined as

$$\overline{\sigma}_R = \frac{s_T}{s_L^0} = \frac{A_{T,R}}{A} = \overline{\sigma}\frac{A_{T,R}}{A_T} = \overline{\sigma}Q. \tag{5.58}$$

In this equation, σ now represents the total surface area ratio A_T/A and is related to $\sigma_R = A_{T,R}/A$ by the unquenched factor $Q = A_{T,R}/A_T$. The present approach therefore generalizes and extends the definition of the turbulent burning velocity by clearly differentiating between a total and a reactive surface area ratio. Only the latter is able to contribute to the turbulent flame speed. Flame quenching decreases the reactive flame surface and leads to a diminished burning velocity of the mean flame front. For a freely propagating flame, Q equals 1 and Eq. (5.56) is recovered.

Comparison to the model of Bruneaux et al.

The present approach bears similiarities to the flame-wall interaction model of Bruneaux et al. [31], who distinguished between a total interface density Σ and a reactive interface density Σ_R. An expression for the reactive surface density using the present model can be found by inserting Eq. (5.54) into Eq. (5.49) and substituting the definition of the flame surface density (Eq. (5.52)),

$$
\begin{aligned}
\Sigma_R = \overline{s_L \Sigma'}/s_L^0 &= 1/s_L^0 \langle s_L | G = G_0 \rangle \langle \sigma | G = G_0 \rangle P(\mathbf{x}, t) = \\
&= (1 - \alpha(x, t)) \langle \sigma | G = G_0 \rangle P(\mathbf{x}, t) = (1 - \alpha(x, t)) \Sigma.
\end{aligned}
\tag{5.59}
$$

The ratio between Σ_R and Σ of the present model is thus given by

$$\frac{\Sigma_R}{\Sigma} = 1 - \alpha(x, t) \tag{5.60}$$

and depends on the geometrical properties such as x_Q detailed in section 5.2.2. Consequently, the unquenched factor Q is an integral value that results from an integration of Σ_R/Σ across the flame brush. The model by Bruneaux et al. [31], in contrast, depends on enthalpy losses rather than geometrical properties. Their model for the ratio Σ_R/Σ reads

$$\frac{\Sigma_R}{\Sigma} = e^{-\beta L_H/2}, \tag{5.61}$$

where L_H is the enthalpy loss parameter and β the reduced activation energy.

5.3 The level-set approach for turbulent quenched and unquenched flames

Having examined the effect of quenching on laminar and turbulent flames, a consistent unified level-set approach for turbulent quenched and unquenched flames can be deduced. For this purpose, transport equations for the Favre mean $\widetilde{G}$ and variance $\widetilde{G''^2}$ are derived based on the

previous findings. Furthermore, closures for the unclosed terms appearing in these equations are proposed. The closed equations describe the evolution of the location of the mean flame front $\widetilde{G} = G_0$ as well as the turbulent flame brush thickness $l_{F,t}$ and are used to determine the unquenched factor Q.

5.3.1 Transport equation for the mean flame front position

In analogy to the derivation of the level-set equation for laminar quenched and unquenched flames, the starting point is a comparison between the level-set equations for an unquenched and a quenched flame. To comply with the averaging procedure of the G-equation (cf. section 5.1.2), the level-set equation for a quenched flame (Eq. (5.26)) is Favre-averaged resulting in

$$\overline{\rho}\frac{\partial \widetilde{G}}{\partial t} + \overline{\rho}\,\widetilde{\mathbf{v}} \cdot \nabla \widetilde{G} + \nabla \cdot \left(\overline{\rho\,\widetilde{\mathbf{v}''G''}}\right) = -\,(\rho D)\,\overline{\kappa\sigma}. \tag{5.62}$$

The comparison to the transport equation for unquenched flames (Eq. (5.20)) reveals that the turbulent propagation term $(\rho s_L^0)\overline{\sigma}$ vanishes similar as in the instantaneous equations. A consistent unified equation valid for quenched and unquenched flames can therefore be derived by scaling σ with the unquenched factor Q yielding

$$\overline{\rho}\frac{\partial \widetilde{G}}{\partial t} + \overline{\rho}\,\widetilde{\mathbf{v}} \cdot \nabla \widetilde{G} + \nabla \cdot \left(\overline{\rho\,\widetilde{\mathbf{v}''G''}}\right) = \left(\rho s_L^0\right)\overline{\sigma}_R - (\rho D)\,\overline{\kappa\sigma}. \tag{5.63}$$

In this equation, the identity $\overline{\sigma}_R = Q\overline{\sigma}$ was used. The appearance of the reactive flame surface area ratio $\overline{\sigma}_R$ again highlights that only unquenched flamelets are able to contribute to the propagation velocity of the mean flame front.

Before Eq. (5.63) can be used in a RANS context, the unclosed terms have to be suitably closed. Since Eq. (5.63) is very similar to the original G-equation (Eq. (5.20)), the closures presented in the following are largely based on the ones proposed by Peters [142] and Herrmann [89]. The turbulent transport term $-\nabla \cdot (\overline{\rho}\,\widetilde{\mathbf{v}''G''})$ is modelled in analogy to the curvature term appearing in the instantaneous G-equation (Eq. (5.28)),

$$-\nabla \cdot (\overline{\rho\mathbf{v}''G''}) \equiv -\overline{\rho}D_t\overline{\kappa}|\nabla\widetilde{G}|. \tag{5.64}$$

The curvature term $(\rho D)\overline{\kappa\sigma}$ is commonly neglected as the molecular diffusivity D is expected to be of minor importance in the large Reynolds number limit (cf. Peters [142]). The closure of the turbulent propagation term $(\overline{\rho}s_L^0)\overline{\sigma}_R$ is the only one which is affected by quenching. To model this term, a steady, one-dimensional turbulent flame is considered. Consequently, the G-equation simplifies to (Peters [142], Herrmann [89])

$$(\overline{\rho}\,\widetilde{u})\frac{\mathrm{d}\widetilde{G}}{\mathrm{d}x} = \left(\rho s_L^0\right)\overline{\sigma}_R. \tag{5.65}$$

Similar to the definition of the laminar flame velocity s_L^0, the mass flow rate $(\overline{\rho}\,\widetilde{u})$ is assumed to be equal to $(\overline{\rho}s_T)$. Using the results from the previous section, this approach yields

$$\left(\rho s_L^0\right)\widetilde{\sigma}_R = (\overline{\rho}s_T)\,|\nabla\widetilde{G}| = Q\left(\overline{\rho}s_T^0\right)|\nabla\widetilde{G}| \qquad \text{with} \qquad \mathrm{d}x = \frac{\mathrm{d}\widetilde{G}}{|\nabla\widetilde{G}|}. \tag{5.66}$$

All terms are now closed and the closed equation for the mean flame front position valid for unquenched and quenched flame reads

$$\overline{\rho}\frac{\partial \widetilde{G}}{\partial t} + \overline{\rho}\,\widetilde{\mathbf{v}}\cdot\nabla\widetilde{G} = Q\left(\overline{\rho}s_T^0\right)|\nabla\widetilde{G}| - \overline{\rho}D_t\widetilde{\kappa}|\nabla\widetilde{G}|. \tag{5.67}$$

Expressions for the turbulent burning velocity s_T^0 as well as the turbulent diffusivity D_t which take near-wall turbulence and flame development into account are presented in section 5.4.

5.3.2 Transport equation for the variance of G

To find a unified variance equation, the transport equations for the variance $\widetilde{G''^2}$ for an unquenched and a quenched flame are derived separately and subsequently compared. Both equations can be derived by substracting the averaged from the instantaneous transport equation, i.e., $\widetilde{G''^2} = G - \widetilde{G}$, and multiplying the result with $2\widetilde{G''}$. After Favre-averaging, the unclosed transport equations for the variance are obtained. The variance equation valid for an unquenched flame is given by Eq. (5.21) whereas the one for a fully quenched flame reads

$$\rho\frac{\partial \widetilde{G''^2}}{\partial t} + \rho\widetilde{\mathbf{v}}\cdot\nabla\widetilde{G''^2} + \nabla\cdot\left(\overline{\rho\,\widetilde{\mathbf{v}''G''^2}}\right) = -2\overline{\rho}\,\widetilde{\mathbf{v}''G''}\cdot\nabla\widetilde{G} - \overline{\rho}\widetilde{\chi} - (\rho D)\overline{\mathcal{K}\sigma}. \tag{5.68}$$

Both equations are quite similar, however, the sink terms differ as the kinematic restoration term $\widetilde{\omega}$ is missing in the latter. This is due to the zero propagation velocity of a quenched flame. As a consequence, the fluctuations of the flame front caused by turbulence cannot be countered as much as by an unquenched flame. A unified variance equation can be obtained by scaling the kinematic restoration $\widetilde{\omega}$ with the unquenched factor Q,

$$\rho\frac{\partial \widetilde{G''^2}}{\partial t} + \rho\widetilde{\mathbf{v}}\cdot\nabla\widetilde{G''^2} + \nabla\cdot\left(\overline{\rho\,\widetilde{\mathbf{v}''G''^2}}\right) = -2\overline{\rho}\,\widetilde{\mathbf{v}''G''}\cdot\nabla\widetilde{G} - -\overline{\rho}Q\widetilde{\omega} - \overline{\rho}\widetilde{\chi} - (\rho D)\overline{\mathcal{K}\sigma}. \tag{5.69}$$

Most of the unclosed terms can again be modelled by employing the closures proposed by Peters [142]. Consequently, the turbulent transport term $-\nabla(\overline{\rho}\,\widetilde{\mathbf{v}''G''^2})$ appearing on the right-hand side of Eq. (5.69) is closed by

$$-\nabla(\overline{\rho}\,\widetilde{\mathbf{v}''G''^2}) = \nabla_\parallel\cdot(\overline{\rho}D_t\nabla_\parallel\widetilde{G''^2}) \tag{5.70}$$

where $\nabla_\parallel$ is a tangential diffusion operator permitting only diffusive transport tangential to the flame front surface $\widetilde{G} = G_0$ (Peters [142]). The turbulent production term $-\widetilde{\mathbf{v}''G''}\cdot\nabla\widetilde{G}$ can be closed by employing the gradient-diffusion hypothesis,

$$-\widetilde{\mathbf{v}''G''}\cdot\nabla\widetilde{G} = D_t(\nabla\widetilde{G})^2, \tag{5.71}$$

since it does not contain any second-order derivatives (Peters [142]). Similar to the averaged G-equation, the term $\overline{\mathcal{K}\sigma}$ is neglected as it is proportional to the molecular diffusivity D.

Finally, the sink terms $\widetilde{\omega}$ and $\widetilde{\chi}$ have to be closed. As already indicated, these are the only ones affected by quenching. For unquenched flames, a unified closure of $\widetilde{\omega}$ and $\widetilde{\chi}$ was

derived by Peters [141] based on the observation that the kinematic restoration $\widetilde{\omega}$ acts similar as the scalar dissipation $\widetilde{\chi}$ in reducing scalar fluctuations of the flame front. The combined model for both sink terms reads

$$\widetilde{\omega} + \widetilde{\chi} = c_s \frac{\varepsilon}{k} \widetilde{G''^2}, \tag{5.72}$$

which coincides with the standard closure of the scalar dissipation rate $\widetilde{\chi} = c_\chi \varepsilon/k\widetilde{G''^2}$. Hence, a consistent model can be proposed by blending the proportionality factors c_χ and c_s with the unquenched factor Q leading to

$$Q\widetilde{\omega} + \widetilde{\chi} = c(Q) \frac{\varepsilon}{k} \widetilde{G''^2} \qquad \text{with} \qquad c(Q) = Qc_s + (1 - Q)c_\chi. \tag{5.73}$$

As suggested by Peters [141], the constant c_s is chosen as $c_s = 2.0$. The constant c_χ is used to scale the scalar dissipation rate for fully quenched flames and is selected as $c_\chi = 1.0$. According to Jones [97], this is a standard value which yields satisfactory results for many thin shear layer flows.

With these closures, the unified closed transport equations for the variance of G reads

$$\overline{\rho} \frac{\partial \widetilde{G''^2}}{\partial t} + \overline{\rho}\,\widetilde{\mathbf{v}} \cdot \nabla\widetilde{G''^2} = \nabla_\parallel \cdot \left(\overline{\rho}D_t\nabla_\parallel\widetilde{G''^2}\right) + 2\overline{\rho}D_t(\nabla\widetilde{G})^2 - \overline{\rho}c(Q)\frac{\varepsilon}{k}\widetilde{G''^2} \tag{5.74}$$

and the turbulent flame brush thickness $l_{F,t}$ as defined in Eq. (5.40) can be estimated.

5.4 Modelling of near-wall turbulence and flame development

In addition to flame quenching, the second important feature of flame-wall interactions is the impact of the wall on turbulence. As highlighted in the sections 3.2 and 3.3, the presence of the wall changes the structure of turbulence and thereby the near-wall flame propagation. Consequently, near-wall turbulence has to be properly taken into account in a comprehensive flame-wall interaction model. In a RANS context, the majority of turbulence closures relies on the turbulent diffusivity D_t. With respect to the G-equation model, the curvature term in Eq. (5.67) as well as the turbulent production and transport term in Eq. (5.74) scale with D_t. Moreover, it was argued in section 3.3 that the near-wall flame propagation is likely to take place in the thin reaction zones regime in which the turbulent burning velocity is also dependent on D_t (cf. section 2.3.2). For these reasons, the turbulent diffusivity D_t plays a pivotal role concerning the modelling of near-wall turbulence within the G-equation combustion model. In this context, it is also important to include the effects of flame development, in particular with regard to SI engines in which a transition from a laminar to a fully turbulent flame takes place. The present section therefore focuses on the modelling of D_t including the effects of near-wall turbulence and flame development. On this basis, correlations for the turbulent burning velocity s_T^0 using different turbulence closures are proposed.

5.4.1 Correlations for the turbulent diffusivity

Within the G-equation model, the turbulent diffusivity D_t is defined as

$$D_t = \frac{\nu_t}{Sc_t} \qquad (5.75)$$

where $Sc_t = 0.7$ is the turbulent Schmidt number (Peters [141, 142]). Different expressions for the kinematic viscosity ν_t have already been shortly discussed in section 2.2.3 and three different models were introduced. These were the original k-ε model (Eq. (2.44)), the k-ε-f_μ model (Eq. (2.47)) and the k-ζ-f-model (Eq. (2.49)). The original closures of the G-equation model including the turbulent burning velocity correlation by Peters [141] or Ewald [66, 67] are based on the k-ε turbulence model. Consequently, the diffusivity D_t as well as the turbulent burning velocity are overestimated near the wall. To derive appropriate correlations for these terms, it is beneficial to rewrite D_t in terms of a velocity and a mixing length scale,

$$D_t = c_t v' l_t. \qquad (5.76)$$

The modelling constant c_t and its derivation is detailed in Table 5.1. If the k-ε-f_μ- or the k-ζ-f-closure is used, near-wall effects are accounted for by a damping of D_t as f_μ or ζ decrease towards the wall. Therefore, these formulations already account for the effects of near-wall turbulence.

Table 5.1: Summary of the model constants and their origin. For clarity, the notation by Peters [142] is adopted.

Symbol	Equation	k-ε	k-ε-f_μ	k-ζ-f	Reference/Annotation
c_t	$D_t = c_t v' l_t$	a_4	$a_4 f_\mu$	$a_4 \zeta$	$D_t = \nu_t/Sc_t$
a_1	$\varepsilon = a_1 v'^3/l_t$	0.37	0.37	0.37	Bray [27]
a_2	$k = a_2 v'^2$	1.5	1.5	1.5	Eq. (2.25)
a_4	c_t	0.78	0.78	1.91	$a_4 = (c_\mu a_2^2)/(Sc_t a_1)$
Sc_t	$D_t = \nu_t/Sc_t$	0.7	0.7	0.7	Peters [141]
c_s	$c(Q) = Qc_s + (1-Q)c_\chi$	2.0	2.0	2.0	Peters [141]
c_χ	$c(Q) = Qc_s + (1-Q)c_\chi$	1.0	1.0	1.0	Jones [97]
c'_μ	$\overline{\sigma}_t$	c_μ	$c_\mu f_\mu$	$c_\mu \zeta$	Section 2.2.3
b_1	$\overline{\sigma}_t s_L^0 = b_1 v'$	2.0	2.0	2.0	Abdel-Gayed and Bradley [1]
b_3	$\overline{\sigma}_t = b_3 (D_t/D)^{1/2}$	1.0	1.0	1.0	Damköhler [47]

The definition (5.76) is only valid for a steady-state, fully developed turbulent flame and has to be suitably extended to include the effects of flame development. For this purpose, the algebraic turbulent flame brush thickness $l_{F,t,alg}$ is introduced. It is defined as the steady-state solution of the variance equation for a planar turbulent flame,

$$l_{F,t,alg} = \frac{\sqrt{\widetilde{G''^2_{alg}}}}{|\nabla G|} = \sqrt{\frac{2D_t}{c(Q)}\frac{k}{\varepsilon}} = \sqrt{\frac{2a_2 c_t}{a_1 c(Q)}} l_t. \qquad (5.77)$$

For isotropic turbulence ($f_\mu = 1$, $\zeta = 2/3$) and a fully reactive flame ($Q = 1$), the present approach yields a turbulent flame brush thickness of 1.78 (k-ε and k-ε-f_μ-model) or 2.27 (k-ζ-f-model) times the integral length scale l_t. This compares well to DNS simulations in which the factors range from 1.38 (Wenzel and Peters [207]) to 2.5 (Knudsen et al. [102]). Towards the wall, the algebraic flame brush thickness reduces as ν_t and thereby D_t are dampened. Since the steady-state turbulent flame brush thickness is proportional to l_t, Eq. (5.76) can be rewritten in terms of $l_{F,t,alg}$

$$D_t \sim v' l_t \sim v' l_{F,t,alg}. \tag{5.78}$$

Consequently, it is admissible to use either the turbulent flame brush thickness or the integral length scale as a characteristic mixing length. If the turbulent flame brush is not yet fully developed, an appropriate mixing length scale has to be defined. In this context, Ewald and Peters [67] suggested to scale the mixing length l_t with the scaling factor l^* defined as

$$l^* = \frac{l_{F,t}}{l_{F,t,alg}}. \tag{5.79}$$

The value $l^* = 0$ consequently corresponds to a laminar flame whereas $l^* = 1$ describes a fully turbulent flame. The multiplication of the integral length scale l_t with l^* in Eq. (5.76) results in a mixing length that depends on the actual turbulent flame brush thickness $l_{F,t}$ rather than l_t

$$D_t = c_t v' l_t l^* \sim v' l_{F,t}. \tag{5.80}$$

This scaled diffusivity was originally only applied to the curvature term in the closed $\widetilde{G}$-equation (Eq. (5.67)). The closures in the variance equation remained unaffected. However, it was shown by Lipatnikov and Chomiak [113] that the original closure of the production term in the variance equation (Eq. (5.74)) overestimates the growth of the turbulent flame brush thickness. Hence, it is suggested that the modified turbulent diffusivity (Eq. (5.80)) is also applied for the variance equation. Consequently, the production term is then proportional to $D_t \sim v' l_{F,t}$ instead of $D_t \sim v' l_t$. A similar modelling has also been proposed by Knudsen et al. [102] based on DNS data. A minor drawback of this approach is that an initial value $\widetilde{G''^2} > 0$ has to be provided. In this regard, sound lower estimates are the laminar flame thickness l_F^2 or the thickness of the inner layer l_δ^2.

5.4.2 Correlations for the turbulent burning velocity

The only remaining quantity which has yet to be defined is the turbulent burning velocity without quenching effects s_T^0. In section 2.3.2, it was defined as

$$\frac{s_T^0}{s_L^0} = \frac{A_T}{A} = \overline{\sigma} = 1 + \overline{\sigma}_t. \tag{5.81}$$

The turbulent diffusivity D_t again plays an important role since it defines the turbulent burning velocity in the thin reaction zones regime in which combustion near the wall is likely to take

place (cf. section 3.3). In the following, a correlation for the turbulent burning velocity is derived which takes near-wall turbulence into account. The derivation is largely based on the work of Ewald [66, 67]. To model flame development effects, Ewald and Peters [67] proposed to scale the limits of the turbulent burning velocity in the corrugated flamelets respectively thin reaction zones regime (cf. section 2.3.2) based on the parameter l^*,

$$\overline{\sigma}_t = b_1 \frac{v'}{s_L^0} l^{*1/3} \quad \text{respectively} \quad \overline{\sigma}_t = b_3 \left(\frac{D_t}{D} \right)^{1/2} l^*. \tag{5.82}$$

The diffusivities D and D_t can be expressed by Eqs. (2.61) and (5.76), respectively. This yields after rearranging

$$\frac{s_L^0 \overline{\sigma}_t}{b_1 l^{*1/3}} = v' \quad \text{and} \quad \frac{\overline{\sigma}_t^2}{c_t b_3^2} \frac{s_L^0 l_F}{l_t l^{*2}} = v'. \tag{5.83}$$

The turbulence intensity v' is found to be the driving force of flame surface production in both limits. According to Ewald [66], both equations can be combined by assuming that the production of flame surface is balanced by the kinematic restoration and scalar dissipation, respectively,

$$\underbrace{\frac{s_L^0 \overline{\sigma}_t}{b_1 l^{*1/3}}}_{\text{kinematic restoration}} + \underbrace{\frac{\overline{\sigma}_t^2}{c_t b_3^2} \frac{s_L^0 l_F}{l_t l^{*2}}}_{\text{scalar dissipation}} = \underbrace{v'}_{\text{production}}. \tag{5.84}$$

This quadratic equation can now be solved for $\widetilde{\sigma}_t$. The only physically meaningful solution of this equation is

$$\overline{\sigma}_t = -\frac{c_t b_3^2}{2 b_1} \frac{l_t}{l_F} l^{*5/3} + \sqrt{\left(\frac{c_t b_3^2}{2 b_1} \frac{l_t}{l_F} l^{*5/3} \right)^2 + c_t b_3^2 l^{*2} \frac{v' l_t}{s_L^0 l_F}}. \tag{5.85}$$

This result extends the turbulent burning velocity correlation derived by Ewald and Peters [67] by the use of appropriate near-wall closures. If the k-ε closure is used, the turbulent burning velocity near the wall is overestimated due to the incorrect estimation of D_t. If, in contrast, the k-ε-f_μ or the k-ζ-f closures are utilized, the turbulent burning velocity near the wall decreases since the factor c_t is damped.

It has to be noted that the correlation (5.85) also includes the turbulent burning velocitiy correlations derived by Ewald [67] (k-ε closure) and Peters [141] (k-ε closure, $l^* = 1$). By multiplying with the identity $1 = (l_{F,t}/l_{F,t,alg})/l^*$, Eq. (5.85) can also be rewritten to correspond to the burning velocity correlation given by Ewald [66],

$$\overline{\sigma}_t = -\frac{b_3^2}{4 b_1} \sqrt{\frac{3 c_\mu' c(Q)}{Sc_t}} \frac{l_{F,t}}{l_F} l^{*2/3} + \sqrt{\left(\frac{b_3^2}{4 b_1} \sqrt{\frac{3 c_\mu' c(Q)}{Sc_t}} \frac{l_{F,t}}{l_F} l^{*2/3} \right)^2 + \frac{b_3^2 c(Q)}{2 s_L^0 l_F} l_{F,t}^2 \frac{\varepsilon}{k}}. \tag{5.86}$$

If the k-ε-f_μ or the k-ζ-f closures are used, the constant c_μ' as well as the turbulent flame thickness $l_{F,t}$ decrease towards the wall due to the damping of v_t or D_t, respectively. Eq.

(5.86) differs from Eq. (5.85) by the definition of the turbulent burning velocity in the thin reaction zones limit which was defined by Ewald [66] as

$$D\overline{\sigma}_t^2 = b_3^2 \frac{c(Q)}{2} l_{F,t}^2 \frac{\epsilon}{k} \qquad \text{in contrast to} \qquad D\overline{\sigma}_t^2 = b_3^2 D_t l^{*2}. \qquad (5.87)$$

Note that the constant c_s of the original definition was replaced by $c(Q)$ to comply with the present model. All model constants of the current combustion model are summarized in Table 5.1.

5.5 Model analysis and validation

To study and validate the behaviour of the GFWI model, it is first analysed in an a priori fashion and subsequently used to simulate combustion in appropriate test cases. To begin with, the unquenched factor Q is examined with regard to its underlying modelling assumptions. The present combustion model is then applied to simulate the flame propagation in a turbulent channel flow. The results are compared to DNS data and discussed with a particular focus on the impact of flame quenching and near-wall turbulence on the turbulent burning velocity. Finally, the GFWI model is qualitatively analysed using a simple SI engine with a pancake-shaped combustion chamber.
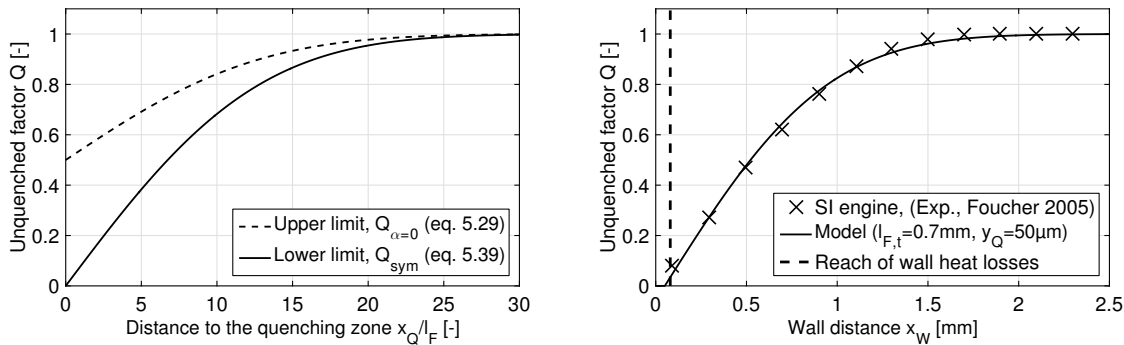
5.5.1 A priori analysis of the unquenched factor Q

The unquenched factor Q was derived using the following two assumptions: firstly, the pdf of finding quenched flamelets was presumed to be symmetrical to the beginning of the quenching zone ($x_Q = 0$) and secondly, the impact of the wall heat losses on the laminar burning velocity was assumed to be negligible.

The error of the symmetry assumption cannot be exactly quantified due to the lack of suitable reference data. However, the feasibility of this assumption for modelling purposes can be assessed by considering two limiting cases as shown in Fig. 5.5a. An estimate for the upper limit of the unquenched factor, $Q_{\alpha=0}$, can be obtained by assuming that no quenched flamelets appear outside of the quenching zone, i.e., $\alpha(x,t) = 0$ for $x > x_Q$. The unquenched factor is then defined by Eq. (5.29). The lower limit Q_{sym}, in contrast, is given by the present model (Eq. (5.37)) as the quenched flamelets are assumed to be distributed symmetrically around the quenching distance. If the pdf of finding quenched flamelets were to be skewed towards the wall by using an appropriate definition of $\alpha(x,t)$, the resulting unquenched factor Q_{skewed} would range between these two limits. As long as the flame is far away from the wall, the differences between $Q_{\alpha=0}$ and Q_{sym} remain small (Fig. 5.5a) and the error due to the symmetry assumption is thus limited. At the beginning of the quenching zone at $x_Q = 0$, the upper limit $Q_{\alpha=0}$ still amounts 0.5 whereas Q_{sym} equals zero. Consequently, $Q_{\alpha=0}$ violates the requirement that the unquenched factor has to drop to zero once the mean flame front reaches the average quenching distance at $x_Q = 0$. As any model for $\alpha(x,t)$ has to meet this requirement, the progression of Q_{skewed} is expected to eventually converge to $Q_{skewed} \to 0$ for $x_Q \to 0$. To put it all in a nutshell, it can be argued that the difference between Q_{sym}

and Q_{skewed} reduces to zero for $x_Q \to 0$ as well as for $x_Q \to \infty$. The error in between these limits cannot exactly be quantified due to the lack of reference data and further research on this topic is thus required in the future.

Nonetheless, the unquenched factor Q and its underlying modelling assumptions can further be qualitatively assessed by comparing the present model to experimental values provided by Foucher et al. [75], who evaluated the burning rate of a turbulent flame near the piston of a SI engine. Fig. 5.5b shows a comparison between the present model for Q (Eq. (5.39)) and the experimental results for a stoichiometric premixed flame. The turbulent flame thickness and the quenching distance needed to calculate Q were estimated as $l_{F,t} = 0.7mm$ and $y_Q = 50\mu m$, respectively. Both values are within their typical range in SI engines. The final model for Q, Eq. (5.39), is capable of correctly reproduce the progression of Q towards the wall. Although this does not constitute evidence for the validity of the symmetry assumption, it shows that the simplifications made to model Q are feasible from a modelling perspective. In fact, the symmetry assumption should be critically reviewed as soon as additional reference and validation data becomes available.

(a) Upper $Q_{\alpha=0}$ and lower limit Q_{sym} of Q for $l_{F,t}/l_F = 10$.

(b) Comparison between experimentally obtained values for Q (Foucher et al. [75]) and the present model (Eq. (5.39)).

Figure 5.5: Analysis of the unquenched factor Q.

To evaluate the error made by neglecting the impact of the wall heat losses on the laminar burning velocity, the characteristic scales of flame quenching and turbulence can be compared using Fig. 5.5b. In the experiments of Foucher et al. [75], the stoichiometric laminar flame thickness was $16.4\mu m$. Assuming that the thickness of the influence zone of wall heat losses equals $2 \times l_F$, the decrease of the laminar burning velocity is expected to start around $80\mu m$ from the wall. This distance is much smaller than the distance at which Q starts to drop (Fig. 5.5b). This can be attributed to the wrinkling of the turbulent flame front causing individual flamelets to enter the quenching zone earlier than other ones. Although the individual flamelets are still quenched due to wall heat losses, turbulent flame-wall interactions are thus dominated by the kinematics of turbulence.

This can be further highlighted by examining the influence of $l_{F,t}$ and y_Q on Q. The resulting curves for three different turbulent flame thicknesses and quenching distances are
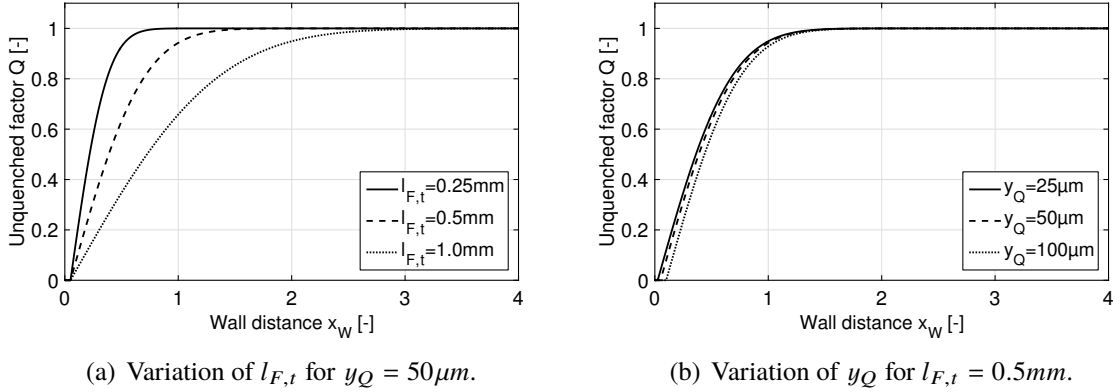
(a) Variation of $l_{F,t}$ for $y_Q = 50\mu m$. (b) Variation of y_Q for $l_{F,t} = 0.5mm$.

Figure 5.6: Dependency of Q on the turbulent flame thickness $l_{F,t}$ and the quenching distance y_Q.

shown in Figs. 5.6a and 5.6b, respectively. The turbulent flame thickness $l_{F,t}$ has a large impact on Q whereas the variation of the quenching distance only has a minor effect. The former is governed by the underlying turbulent flow field whereas the latter is a function of the local thermodynamic properties of the mixture. This further supports the hypothesis that thermodynamic effects only play a secondary role during turbulent flame-wall interactions. It can thus be expected that the error made by assuming that the impact of the wall heat losses on the laminar burning velocity is negligible remains small. This is particularly valid for practical applications such as SI engines in which the ratio between the turbulent length scale and the laminar flame thickness is of order O(100).

5.5.2 Analysis and validation using a turbulent channel flow

The DNS study of Bruneaux et al. [29–31] is an ideal starting point for assessing and validating the performance of the GFWI model due to its simplicity and well-known boundary and initial conditions. The authors investigated the flame propagation and flame-wall interaction process in a turbulent channel flow at $Re_\tau = 180$. An overview is given in Fig. 5.7. Initially, the flame front is laminar and parallel to the wall. It subsequently accelerates as it is wrinkled by turbulence before it is finally extinguished at the wall.

To obtain statistically averaged data, the DNS simulations were repeated 30 times and the results were averaged in wall-parallel planes. As a consequence, the averaged data only depends on time and the wall-normal coordinate y^+ and can be directly compared to a RANS model. Furthermore, Bruneaux et al. conducted simulations with constant density [30] or constant density and viscosity [29, 31]. In the latter case, the flow is not influenced by combustion and the underlying flow-field is identical to a non-reacting turbulent flow. For the present study, density and viscosity are thus also assumed to be constant. The evolution of the system is therefore described by

$$\frac{\partial \overline{G}}{\partial t} = Q s_t^0 |\nabla \overline{G}|$$

(5.88)

(a) Channel geometry and initialisation of the flame front.

(b) Mean streamwise velocity and root-mean squared (RMS) fluctuation velocities in wall units (data from Moser et al. [125]).
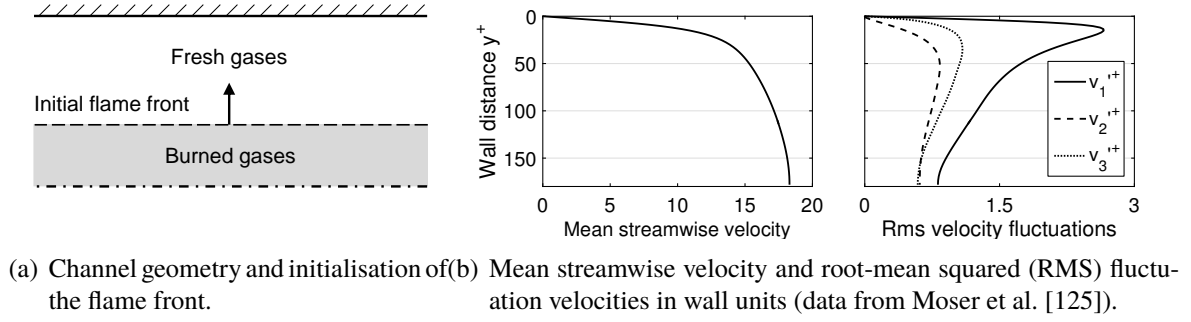
Figure 5.7: Overview and setup of the turbulent channel flow case.

$$\frac{\partial \overline{G''^2}}{\partial t} = 2D_t \left(\nabla \overline{G}\right)^2 - c(Q)\frac{\varepsilon}{k}\overline{G''^2}. \tag{5.89}$$

This set of equations is only time-dependent and can be solved by integration since $|\nabla \overline{G}| = 1$. The flow in a turbulent channel is well known and comprehensive flow statistics are readily available (Moser et al. [125]). The required flame properties such as the laminar flame velocity can be taken from the papers of Bruneaux et al. [29–31]. A summary can be found in Table 5.2.

Table 5.2: Parameters of the channel flow simulation.

Quantity	Value	Origin
$h^+ = Re_\tau$	180	Bruneaux et al. [31]
s_L^{0+}	0.363	Bruneaux et al. [31]
l_F^+	$0.15h^+$	Bruneaux et al. [30]
y_Q^+	10	Bruneaux et al. [31]

The initial zero level-set $\overline{G} = G_0$ at $t = 0$, i.e., the initial position of the flame front, is set at $y^+ = 108$. The system is subsequently free to evolve. For a better comparability of the results, the time was normalized using the same definition of the flame time as Bruneaux et al. The turbulent diffusivity D_t and the turbulent burning velocity s_T^0 were estimated by Eqs. (5.80) and (5.85), respectively. The calculation was carried out for each turbulence closure, i.e., for the k-ε-, k-ε-f_μ- and k-ζ-f-model. In this way, the impact of near-wall turbulence on the flame propagation can be discussed.

Effects of near-wall turbulence

Before discussing the simulation results, the stationary turbulent burning velocity s_T^0 as well as the algebraic turbulent flame thickness $l_{F,t,alg}$ are examined first. For this purpose, the Eqs. (5.85) and (5.77) were estimated for $l^* = 1$ and $Q = 1$. In this way, the effects of the different turbulence closures can be highlighted. The result is shown in Fig. 5.8.

The damping of D_t towards the wall leads to a significant reduction of s_T^0 as well as $l_{F,t}$ for $y^+ < 50$ compared to the unmodified k-ε closure. The k-ε-f_μ-closure behaves similar

(a) Steady-state turbulent burning velocity s_T^0/s_L^0.

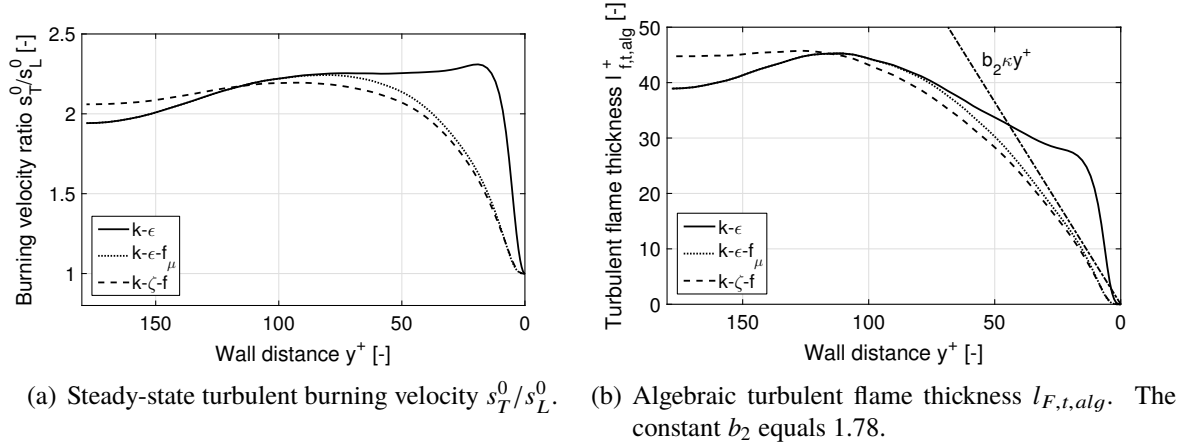(b) Algebraic turbulent flame thickness $l_{F,t,alg}$. The constant b_2 equals 1.78.

Figure 5.8: Steady-state turbulent burning velocity ($l^* = 1$, $Q = 1$) and algebraic turbulent flame thickness for a turbulent channel flow at $Re_\tau = 180$ and the parameters specified in Table 5.2.

to the k-ζ-f-closure apart from the free-stream region $y^+ > 150$, in which the k-ζ-f variant predicts a slightly larger turbulent burning velocity as well as turbulent flame brush thickness. A reason for the good agreement between the k-ζ-f and k-ε-f_μ model is the fact that the near-wall correction f_μ (Eq. (2.48)) was specifically developed using DNS data of fully developed turbulent channel flows. Near the wall, the turbulent length scale and thereby the algebraic turbulent flame brush thickness scales with the mixing length $l_m = \kappa y^+$, which is a classic scaling law for wall-bounded turbulent flows. The k-ε-closure predicts a turbulent flame thickness that is larger than the mixing length limit. Similarly, the turbulent burning velocity is overestimated. For a realistic approximation of these values, the damping of D_t has to be included.

Combined effects of quenching and near-wall turbulence

To discuss the effects of quenching, the transient simulation results have to be examined. These were obtained by solving the Eqs. (5.88) and (5.89) for the aforementioned boundary and initial conditions. The results for the turbulent burning velocity ratio, the turbulent flame thickness as well as the unquenched factor Q with respect to their temporal and spatial evolution are shown in Fig. 5.9. In the initial phase, a transition from a laminar to a fully turbulent flame takes place. The necessity to account for the effects of flame development can be highlighted by a comparison between the steady-state burning velocity ratio (Fig. 5.8a) and the base turbulent burning velocity without quenching s_T^0/s_L^0 (Figs. 5.9a and b). In the present case, the flame attains its fully developed state not until $y^+ \approx 40$ and $t/t_F \approx 8$. As previously discussed, the effects of near-wall turbulence can already be seen for $y^+ < 50$ and become pronounced for $y^+ < 30$ and $t/t_F > 10$. The turbulent flame brush thickness as well as the base turbulent burning velocity s_T^0/s_L^0 are strongly reduced indicating a re-laminarisation of the flame.
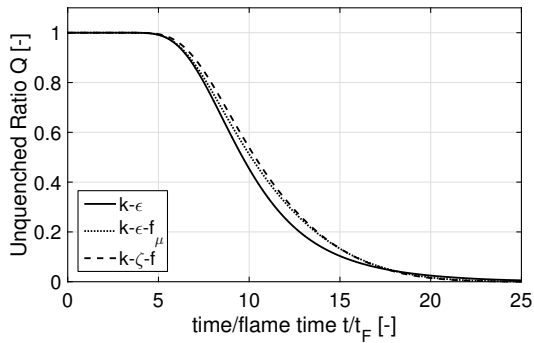
In the present example, the flame is already affected by quenching before it enters the
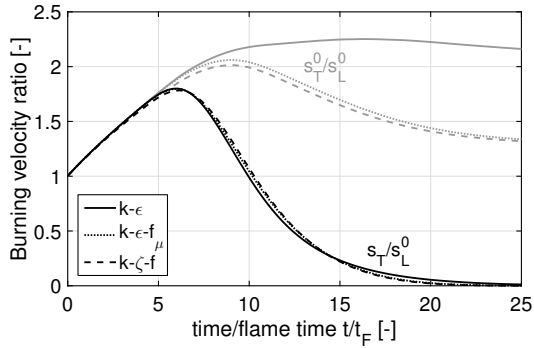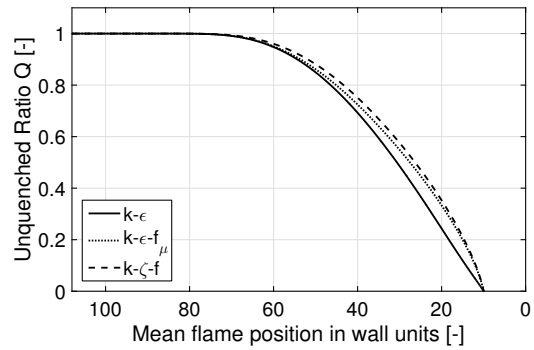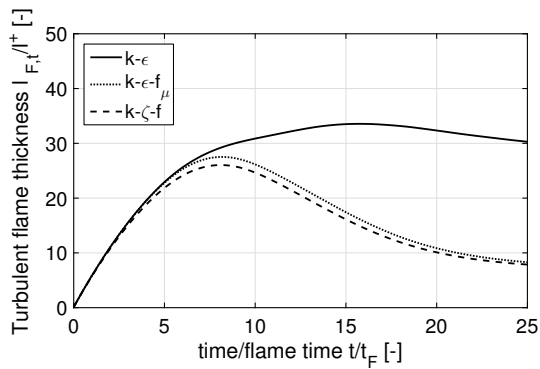
(a) Time evolution of the burning velocity ratio.
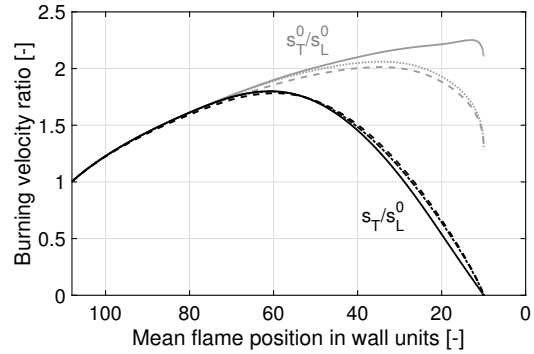
(b) Evolution of the burning velocity ratio with respect to the mean flame position.

(c) Time evolution of the unquenched factor Q.
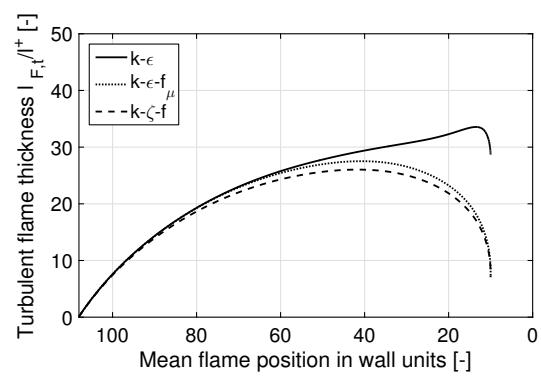
(d) Evolution of the unquenched factor Q with respect to the mean flame position.

(e) Time evolution of the turbulent flame thickness.

(f) Evolution of the turbulent flame thickness with respect to the mean flame position.

Figure 5.9: Results of the simulation of turbulent HOQ in for a turbulent channel flow at $Re_\tau = 180$ and the parameters specified in Table 5.2.

influence zone of near-wall turbulence. The flame starts to interact with the wall at $y^+ \approx 70$ and $t/t_F \approx 5$ despite the fact that the position of the mean flame front is still far away from the quenching region located at $y^+ = 10$. At this point, the leading flamelets of the turbulent flame brush are already quenched in the vicinity of the wall resulting in a decrease of the unquenched factor and thereby of the burning velocity. The maximum burning velocity of $s_T/s_L^0 \approx 1.8$ is reached at $y^+ \approx 60$ and $t/t_F \approx 7$. The increase of s_T^0/s_L^0 can no longer compensate the effect of quenching and the unquenched factor Q continuously decreases until the mean flame front eventually stops at the beginning of the quenching zone $y^+ = 10$ for $t/t_F > 25$.

The choice of the turbulence closure has a surprisingly small effect on the effective burning velocity s_T/s_L^0 and it can thus be suggested that the effect of quenching is dominant compared to the effect of near-wall turbulence in the present example. However, the turbulence closure becomes vital for a proper prediction of the turbulent flame brush thickness. If near-wall turbulence is not taken into account, the flame brush thickness is overestimated. As a consequence, more flamelets are assumed to be in the vicinity of the wall yielding a slightly smaller unquenched factor Q. In case of the k-ε-closure, this overestimation of the turbulent flame brush thickness can compensate the improper calculation of s_T^0/s_L^0 near the wall.

Comparison to DNS data

The validity of the GFWI model and its modelling assumptions can be assessed by comparing the present results to the simulations of Bruneaux et al. [29–31]. Fig. 5.10 shows a comparison of the calculated burning velocities s_T/s_L^0 as well as of the reactive flame surface densities Σ_R for two distinct points in time. The reactive flame surface densities have been estimated by utilizing Eq. (5.59).
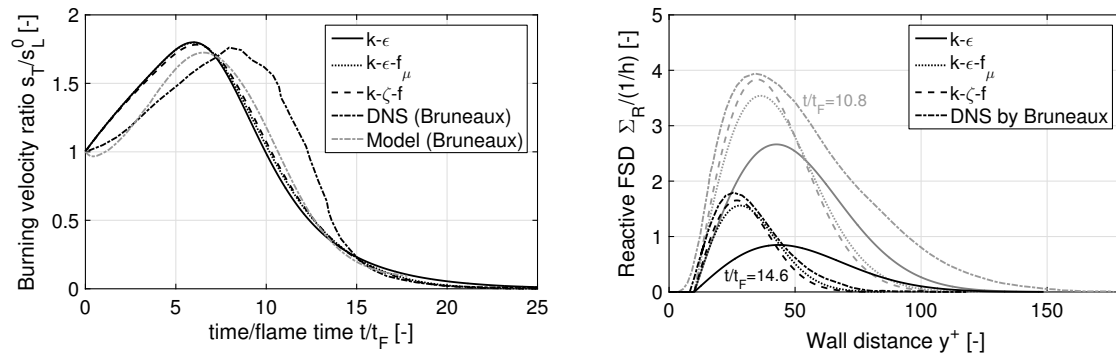
(a) Time evolution of the turbulent burning velocity s_T/s_L^0.

(b) Reactive flame surface densities Σ_R for two distinct points in time.

Figure 5.10: Comparison of the present modelling approaches to the results obtained by Bruneaux et al. [30, 31].

Compared to the DNS simulations, the initial flame development predicted by the present models is faster compared and consequently, the flame is influenced earlier by the wall (Fig.

5.10a). Nevertheless, the overall behaviour is very similar, especially for the late stages $t/t_F > 14$ of flame-wall interaction. The burning velocities estimated by the present models compare favourably to the flame-wall interaction model of Bruneaux et al. [31]. If near-wall turbulence is taken into account (k-ε-f_μ, k-ζ-f), the reactive flame surface densities Σ_R shown in Fig. 5.10b are also found to be in good agreement with the DNS simulations. This applies particularly to the region near the quenching zone and validates the assumptions made to model $\alpha(x,t)$ to a certain extent. The standard k-ε closure is not able to predict the reactive flame surface densities as the turbulent flame thickness is too large. This results in an overestimation of the width of the reaction zone, especially for $t/t_F = 14.6$. The overall agreement between the present results and the data published by Bruneaux et al. [29–31] is very good and it can thus be concluded that the present modelling approach is able to correctly describe the near-wall behaviour of a turbulent flame. Besides the overall combustion parameters such as the turbulent burning velocity, thermal characteristics such as temperature or wall heat flux profiles are important for validating flame-wall interaction models. Unfortunately, a temperature or energy equation cannot be solved in addition to Eqs. (5.88) and (5.89) as required quantities such as the initial fuel mass fraction in the fresh gases Y_F^0 or the average thermal conductivity $\overline{\lambda}$ were not explicitly published by Bruneaux et al. [29–31]. However, a qualitative discussion is feasible by examining the temperature transport equation employed by Bruneaux et al. [31],

$$\frac{\partial \overline{\rho} c_p \overline{T}}{\partial t} = \frac{\partial}{\partial y} \left[\left(\overline{\lambda} + \overline{\rho} c_p \frac{\nu_t}{Pr_t} \right) \frac{\partial \overline{T}}{\partial y} \right] + c_p \left(T_b - T_u \right) \overline{\rho}_u^0 Y_F^0 s_L^0 \Sigma_R. \tag{5.90}$$

Using this equation, Bruneaux et al. [31] have shown that their flame-wall interaction model is able to correctly capture the maximum wall heat flux during flame-wall interaction. The only source term appearing in this equation is the reactive flame surface density Σ_R, which is reasonably well captured by the present model (Fig. 5.10b). Consequently, it can be expected that the maximum wall heat flux would also be predicted correctly by the present modelling approach, if the temperature transport equation (5.90) were to be solved in addition. This discussion underlines the fact that an accurate prediction of the combustion parameters is essential to correctly calculate the wall heat fluxes.

Finally, it has to be remarked that the assumption of constant density and viscosity limits the transferability of these results to actual flows. As combustion does not influence the flow by density and viscosity changes, turbulence and its impact on the flame is likely overestimated in the present case.

5.5.3 Analysis of combustion in a pancake-shaped SI engine

To study the performance of the GFWI model in a more realistic scenario, a simple PFI SI engine with a flat head and piston was used as a test case. For this purpose, the GFWI model was implemented into the CFD code AVL FIRE™ using the existing level-set and flame-tracking framework. The details are provided in appendix D.

The investigated engine was originally used by Alkidas et al. [8, 10] to investigate the wall heat transfer at the combustion chamber walls. For this purpose, the engine was equipped

with pressure and heat-flux transducers. The availability of experimental data in combination with the simple pancake-shaped geometry led to the popularity of the test case in combustion and wall heat transfer literature. It has been frequently used to assess the performance of combustion and wall heat transfer models, e.g., Toninel et al. [191], Tan and Reitz [184], Han and Reitz [84], Angelberger et al. [15].

However, as pointed out by Toninel et al. [191], there is a considerable degree of freedom in the simulation setup as there is no information on velocity and turbulence quantities needed to correctly describe the initial charge motion before combustion. Hence, the example cannot be used as a validation test case. Nevertheless, it remains compelling due to its simple reproducibility and the fact that it can be used to examine the qualitative performance and robustness of combustion models. The technical details of the engine as well as the operating conditions are summarized in Table 5.3.

Table 5.3: Summary of the technical details of the PFI engine and the operating conditions.

Compression ratio	8.56
Displacement volume	$820cm^3$
Bore x Stroke	105.0mm x 95.25mm
Connecting rod length	158mm
TDC clearance	12.6mm
Engine speed	1500rpm
Fuel	C_3H_8
Equivalence ratio	0.87
Volumetric efficiency	40%
Spark timing	$-27°CA$

Toninel et al. [191] proposed to estimate the missing initial conditions based on general guidelines found in literature (e.g., Heywood [90]). The initial fluctuation velocity was assumed to be proportional to 40% of the mean piston speed $\bar{s}_P$

$$k_{ini} = \frac{3}{2}v'_{ini} = 1.5 \times (0.4 \times \bar{s}_P)^2 . \qquad (5.91)$$

The integral length scale was specified by assuming that it increases proportionally with the wall distance y up to a maximum of 30% of the bore diameter in the core region. Moreover, it was clipped to $0.01mm$,

$$l_{t,ini} = \max\left[0.01mm, \min\left(0.3 \times \text{Bore}, \frac{\kappa y}{c_\mu^{3/4}}\right)\right] . \qquad (5.92)$$

Therein, the von Karman constant was assumed to equal $\kappa = 0.419$. The initial dissipation ε_{ini} was subsequently calculated by Eq. (2.24). The initial velocity field in the vertical direction was set to vary linearly from the piston speed at the piston surface to zero at the cylinder head. The velocity components in the peripheral direction of the combustion chamber were assumed to be zero, i.e., there is no initial swirl and tumble motion. The wall temperatures

were assumed to be equal to $420K$ (Han and Reitz [84]). The initial pressure was estimated based on the available experimental data and was set to $5.305bar$. The initial temperature was derived from the equation of state using the volumetric efficiency and pressure. The fuel-air mixture was assumed to be homogeneous.
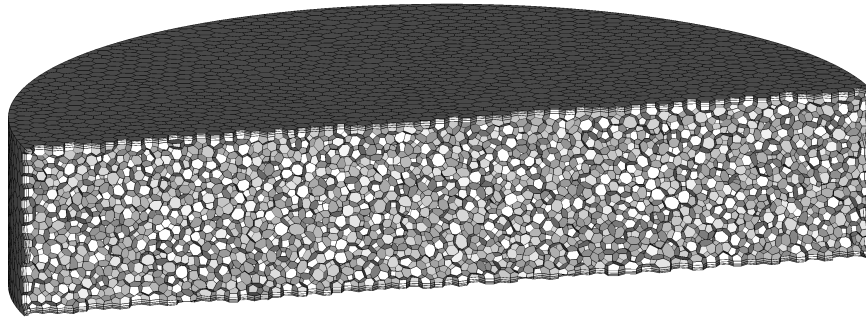

Figure 5.11: Cut through the mesh of the Pancake engine.

The computational mesh is shown in Fig. 5.11 and consists of 372586 nodes and 75503 cells. The times step is $\triangle\alpha = 0.1°CA$. The laminar flame velocity s_L^0 was taken from the FIRE™ database whereas the inner layer temperature T_0 needed to calculate the quenching distance (Eq. (A.18)) was estimated by using a correlation from Müller et al. [126]. The turbulence model which was applied was chosen in accordance with the turbulence closures of the combustion model. The simulation was started at $-30°CA$ and the transition radius of the ignition model was set to $2.5mm$.

(a) Pressure p.

(b) Heat release.
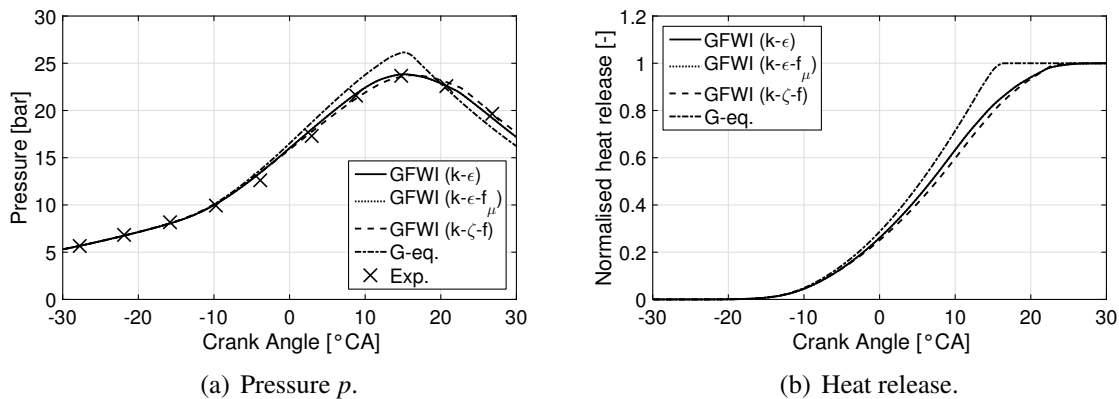
Figure 5.12: Combustion simulation results for the Pancake test case using different closures of the GFWI-model in comparison to the G-equation model without a dedicated flame-wall interaction model.

In addition to three different GFWI model variants, each employing a different turbulence closure, the original G-equation without a flame-wall interaction model (i.e., $Q = 1$ and k-ε-closure) was also used to simulate the combustion process. The results are shown in Fig. 5.12. Initially, the heat release rates calculated by the different variants match closely

and the pressure curve is predicted well up to around $0°CA$. If flame-wall interactions are not considered, combustion proceeds too rapidly in the ensuing phase, particularly when the flame approaches the engine liner. As a consequence, the peak pressure is overestimated and the pressure during the expansion phase is too low compared to the experimental data. If flame-wall interactions are taken into account, the flame slows down towards the combustion chamber walls and a more realistic heat release curve is obtained. All variants of the GFWI model are thus able to predict the pressure curve with a reasonable accuracy. In this context, it has to be stressed that the combustion model constants given in chapter 5 have not been adjusted apart from the ignition timing. Similar to the turbulent channel flow case, the effect of quenching is again found to be dominant compared to the effect of near-wall turbulence. The heat release calculated by the k-ε and k-ε-f_μ-model are almost identical whereas the k-ζ-f variant predicts a slightly slower combustion.

(a) *G*-equation without a flame-wall interaction model (k-ε-closure).
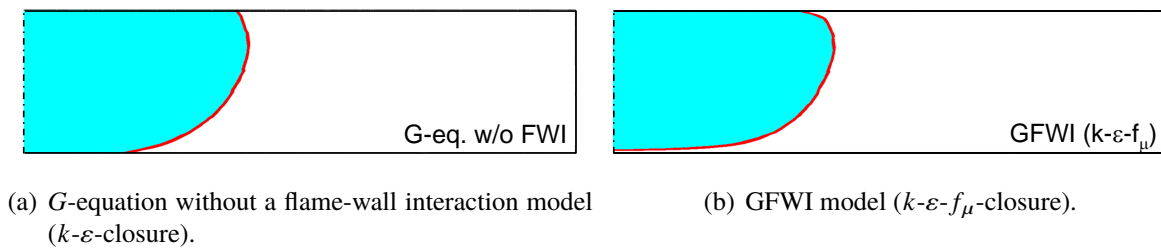
(b) GFWI model (k-ε-f_μ-closure).

Figure 5.13: Comparison of the mean flame front shape at $-10°CA$ calculated with or without a dedicated flame-wall interaction model.

The impact of using the current flame-wall interaction model on the shape of the flame front can be seen in Fig. 5.13. As expected, the flame front is smooth and convex towards the unburned gases in both cases. In the center of the combustion chamber, the differences are only marginal. For example, the tip of the flame front has travelled almost the same distance from the ignition point irrespective of the employed model. The main differences between both cases can be found at the combustion chamber walls. As one can see in Fig. 5.13b, the GFWI model predicts a slower flame propagation near the piston and the cylinder head leading to a higher near-wall curvature of the flame front shape. Although the unknown initial conditions of the Pancake case prevent a more detailed analysis of combustion, the qualitative discussion in this section revealed that combustion can be captured in a more realistic way by employing the GFWI model.

5.6 Conclusion

The near-wall flame propagation is strongly affected by flame quenching and near-wall turbulence. In this chapter, a theoretical approach for modelling flame-wall interactions addressing these effects was presented. The approach is based on established concepts of combustion and turbulence modelling and can thus be transferred to other combustion models, in particular to those based on a turbulent burning velocity.

First, the effect of quenching was studied. As a starting point, the structure of a premixed quenched flame was analysed and it was found that its reaction zone is a diffusive-reactive layer which can be tracked by the iso-scalar species mass fraction Y_0. A transport equation describing its kinematic behaviour was derived. In this equation, the propagation term vanishes in comparison to the original G-equation derived by Peters [142]. Since both equation describe the kinematic behaviour of the iso-scalar species mass fraction Y_0, the respective G-equations for quenched and unquenched flames were subsequently unified by blending the laminar burning velocity.

The effect of turbulence on the flame-wall interaction process was analysed and it was found that its kinematic effect causing a successive quenching of the turbulent flame brush is dominant compared to the effect of wall heat losses. As turbulence is an inherently stochastic phenomenon, a model for the probability of finding quenched flamelets was introduced. The unquenched factor Q, which is a measure for the fraction of unquenched flamelets, was introduced based upon the notion that all flamelets within a certain distance from the wall are quenched. In combination with a Gaussian pdf for the probability of finding instantaneous flamelets, Q depends on the distance to the quenching zone and the turbulent flame brush thickness. Using these results, the turbulent burning velocity of a flame subjected to quenching was analysed. In this context, the definition of the turbulent burning velocity was generalized by distinguishing between the total flame surface ratio $\overline{\sigma}$ and the reactive flame surface ratio $\overline{\sigma}_R$. Only the latter contributes to the overall reaction speed. It was shown that in general, $\overline{\sigma}$ and $\overline{\sigma}_R$ are related by the unquenched factor Q. Hence, the effect of quenching can be taken into account by scaling the turbulent burning velocity with Q.

On this basis, a generalized G-equation for turbulent premixed flames was introduced. It describes the evolution of the mean flame front position and its variance and takes quenched and unquenched flamelets into account. Modelling closures were proposed and suitably extended to incorporate the effects of quenching. To include the effects of near-wall turbulence, the turbulent diffusivity D_t has to be properly defined, since almost any of the employed closures are based on D_t. The common k-ε-closure is known to overestimate D_t near the wall and appropriate definitions are needed. For this purpose, two closures for D_t based on either the k-ζ-f turbulence model or the k-ε model in combination with a damping function f_μ were proposed. Furthermore, the scaling factor l^* was introduced to describe transient flame development effects. Lastly, a generalized turbulent burning velocity correlation based on the limits of small scale and large scale turbulence was introduced. It takes the effects of near-wall turbulence as well as flame development into account and includes the expressions of Ewald and Peters as limiting cases.

The resulting combustion model, called G-equation Flame-Wall Interaction (GFWI) model, is valid far off and near a solid wall as well as for quenched and unquenched flamelets. Particular simplifications of the model, e.g., the symmetry assumption, were examined in an a priori way. While the employed simplifications are feasible from a modelling perspective, it was underlined that further research and validation data is required to conduct a more detailed analysis. The performance of the GFWI model was subsequently analysed using a turbulent channel flow. It was found that the damping of D_t for $y^+ < 50$ leads to a decrease of the turbulent burning velocity as well as of the turbulent flame brush thickness. The effect of quenching was found to be significant at a greater wall distance ($y^+ < 70$)

and dominant compared to the effect of near-wall turbulence in the present example. The comparison of the results to the DNS data of Bruneaux et al. [29–31] revealed that the present modelling approach is able to correctly reproduce the turbulent burning velocity as well as the reactive flame surface density near the wall. The application of the GFWI model to simulate combustion in a simple SI engine revealed that combustion can be captured in a more realistic way by including flame-wall interactions. The simulation of the combustion process of a more complex direct-injection SI engine is investigated in the next chapter.

6 Application to combustion simulation in a direct-injection SI engine

The development and further optimisation of internal combustion engines relies strongly on simulation requiring elaborate computational models. In this chapter, the performance of the previously introduced combustion model is assessed using the available data from the analysis of flame-wall interactions described in chapter 4. First, the performance of the GFWI model concerning the prediction of heat release and pressure is compared to the original G-equation model. Moreover, the influence of the underlying turbulence model is investigated as well. The combustion process is analysed in detail in the subsequent section. The flame structure is discussed and the impact of flame-wall interactions on the flame propagation is highlighted. In the last part, a comprehensive phenomenological picture of flame-wall interactions in SI engines is conceived and the main findings are summarized.

6.1 Comparison of heat release and pressure prediction

To evaluate the performance of the GFWI model for the simulation of combustion in a direct-injection SI engine, the five operating points introduced in chapter 4 were utilized. The simulations were conducted with the CFD software AVL FIRE™ based on the simulative setup described in section 4.3.2. For the present investigations, the k-ε turbulence model, which is still the de facto standard for RANS simulations, is considered in addition to the k-ζ-f-model. Combustion is simulated by the GFWI model with the corresponding turbulence closures as well as by the standard G-equation model in combination with the k-ε model. The thermodynamic properties of the evaporated fuel species are prescribed using the gasoline surrogate introduced in section 4.3.2. Correlations for the laminar flame velocity s_L^0 as well as for the inner layer temperature T_0 are given in appendix C. For the turbulent burning velocity, the modified correlation of Ewald (Eq. (5.86)) was used. The initial spark kernel was initialized between the electrodes of the spark plug and the transition radius was set to 1mm.

Before the results are presented and discussed, a few remarks shall be noted. As stated in appendix D, chemistry had to be represented by a simple one-step reaction. It can thus be expected that the overall heat release is overestimated as there are no intermediate products such as CO. Moreover, it has to be noted that the ignition timing had to be adjusted due to the lack of an elaborate ignition model. However, it has to be stressed that the model constants of the combustion model as stated in chapter 5 were not adapted.

Figs. 6.1, 6.2, 6.3, 6.4 and 6.5 show the predicted in-cylinder pressure and heat release curves for each investigated operating point in comparison to the experimental results. Keep-

Figure 6.1: Combustion simulation results of the GFWI model at OP1 in comparison to the *G*-equation model without a dedicated flame-wall interaction model.

Figure 6.2: Combustion simulation results of the GFWI model for OP2 in comparison to the *G*-equation model without a dedicated flame-wall interaction model.

Figure 6.3: Combustion simulation results of the GFWI model for OP3 in comparison to the *G*-equation model without a dedicated flame-wall interaction model.

(a) Pressure p.

(b) Heat release rate.

(c) Heat release.

Figure 6.4: Combustion simulation results of the GFWI model for OP4 in comparison to the *G*-equation model without a dedicated flame-wall interaction model.

(a) Pressure p.

(b) Heat release rate.
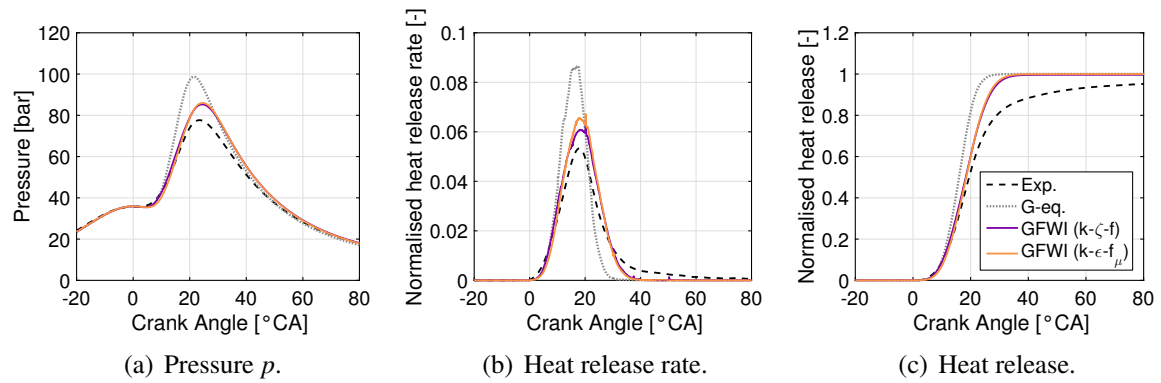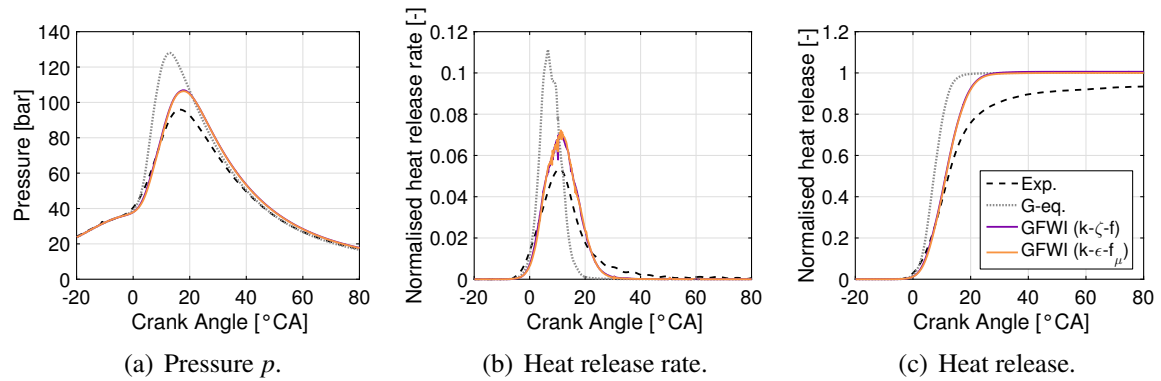
(c) Heat release.
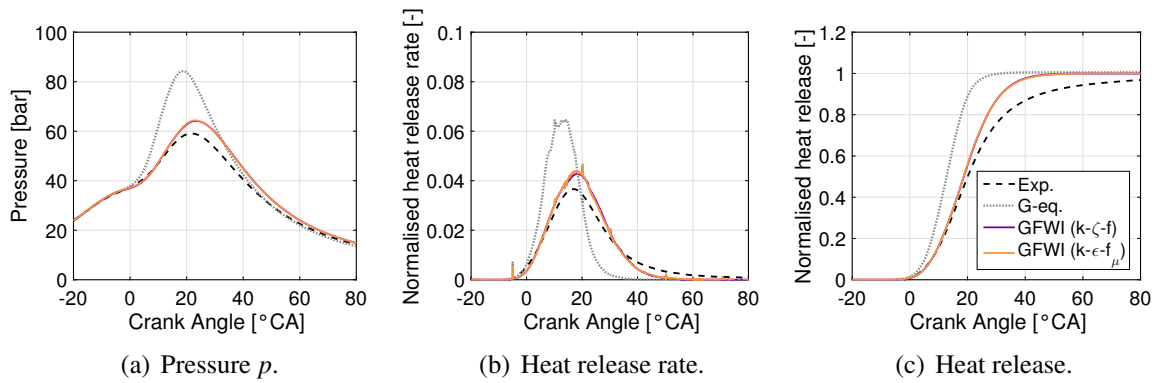
Figure 6.5: Combustion simulation results of the GFWI model for OP5 in comparison to the *G*-equation model without a dedicated flame-wall interaction model.
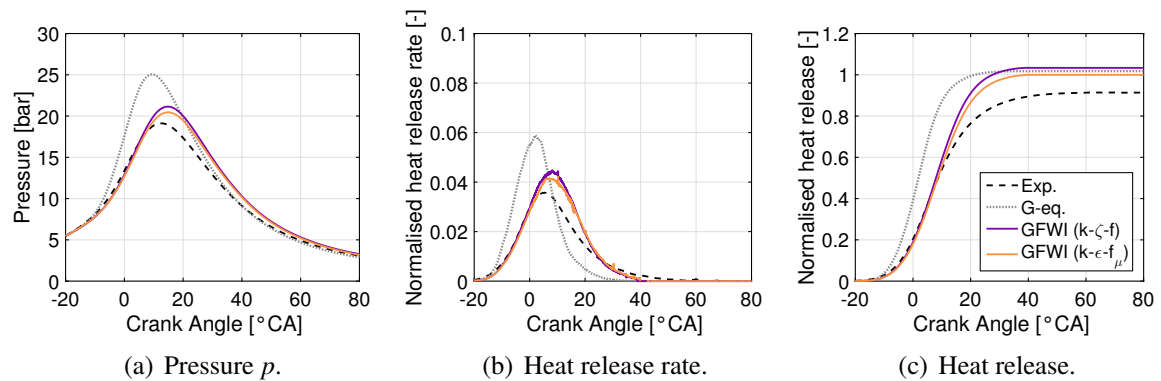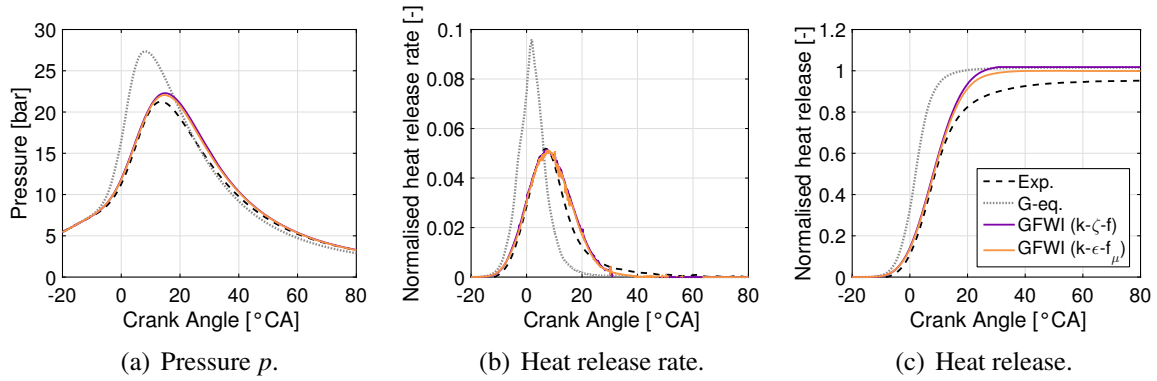
ing in mind the simplified representation of chemistry, the GFWI-model is able to predict the heat release curve and thereby the pressure curve with reasonable accuracy. As expected, both quantities are overestimated at all operating points due to the complete conversion of the reactants. If detailed chemistry were included by solving the flamelet equations or using flamelet libraries, the heat release rate would decrease and the experimental data would be matched more closely. Nonetheless, the GFWI model is able to correctly capture the changes of flame propagation caused by the different operating conditions. This applies for both investigated turbulence models and GFWI model variants, as the respective results are closely matched. The differences can be mainly traced back to the calculation of mixture formation. For example, the use of the k-ζ-f model results in a slightly higher overall heat release at the part load points due to a more homogeneous air-fuel mixture. Nonetheless, the independence of the combustion simulation results from the turbulence model choice underlines the necessity of adapting the closures of a combustion model to the underlying physical models.

When the flame-wall interaction model is turned off without changing any parameters,

combustion proceeds more rapidly and the predicted heat release rate and in-cylinder pressure is much higher. The overall heat release at the end of combustion calculated by the G-equation model is similar to the GFWI model variants. At closer inspection, however, it can be seen that the corresponding GFWI model variant (k-ε-f_μ) predicts a slightly lower overall heat release. This is a result of incomplete combustion and particularly noticeable at the part load operating points OP3 and OP4 (Figs. 6.3c and 6.4c).

If the present results are compared to the previously discussed Pancake case (section 5.5.3), the observed differences between the GFWI model and the standard G-equation model are much larger. The flame propagation is already considerably influenced by the wall at an early stage. This can be attributed to the combustion chamber geometry. The examined direct-injection SI engine has a much more compact design with smaller distances between the cylinder head and the piston. Consequently, the effects of flame-wall interaction are more pronounced, as the turbulent flame brush encounters the wall much earlier. For example, parts of the initial flame kernel are already quenched at the electrodes of the spark plug. This circumstance highlights the necessity of a flame-wall interaction model for simulating combustion in modern downsized engines with high surface-to-volume ratios.

6.2 Analysis of flame structure and flame propagation

To further analyse the combustion process, the characteristic scales of turbulent flame front propagation have to be studied. For this purpose, important quantities such as the turbulent burning velocity, the velocity scales ratio v'/s_L^0 or the length scale ratio l_t/l_F were evaluated on the mean flame front starting from 0.05%MFB up to 99%MFB. In the following, only the results obtained by the k-ε-f_μ-variant of the GFWI model are shown for the sake of clarity. For time-based diagrams, all quantities were area-averaged over the mean flame front. The combustion progress is highlighted by symbols for 10%MFB (symbol ▷), 50%MFB (symbol ◇) and 90%MFB (symbol ○). If a spatial coordinate is used as the abscissa, a spatial average at a distinct point in time was calculated from the entirety of all cells containing a part of the mean flame surface by a local linear regression using a Gaussian kernel.

A qualitative understanding of the turbulent premixed combustion process can be obtained by comparing the scales of turbulence and chemical reactions in a Peters-Borghi diagram, which was introduced in section 2.3.2. Fig. 6.6 shows the trajectories of the combustion process in two separate diagrams for the full and part load operating points, respectively. In both cases, OP1 serves as a reference. As expected, combustion in the present direct-injection SI engine takes place in the thin reaction zones and corrugated flamelets regime. Shortly after a successful ignition, the turbulent flame kernel encounters a high fluctuation velocity whereas the turbulent length scale is still small due to the vicinity of the spark plug walls. As flame starts to expand, the length scale ratio l_t/l_F increases. At around the 10%MFB, the highest values of l_t/l_F and v'/s_L^0 are found. Subsequently, both ratios start to decrease due to the dissipation of turbulence as well as due to the increasing proximity of the flame to the combustion chamber walls. This leads to a combustion regime change, particularly at OP1 and OP4, highlighting the necessity of a proper definition of the turbulent burning velocity s_T^0.
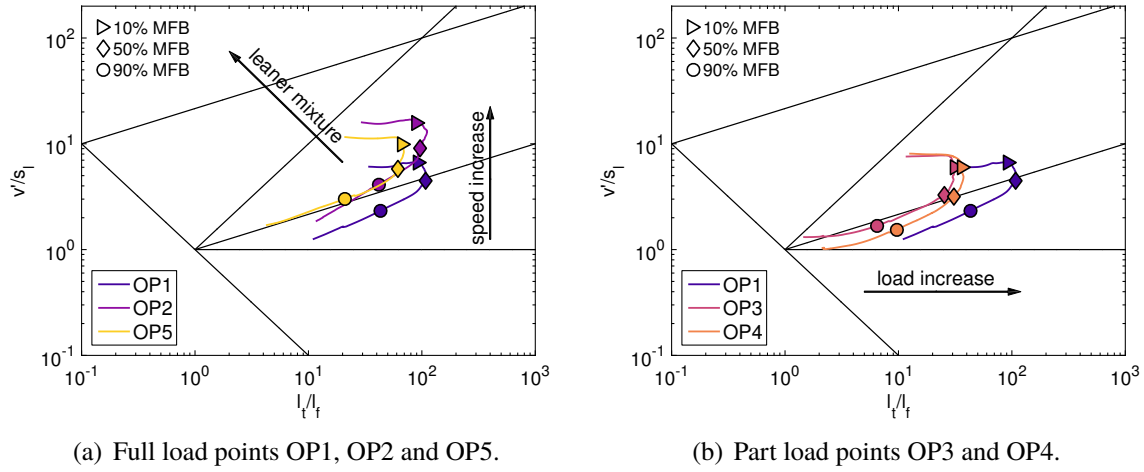
(a) Full load points OP1, OP2 and OP5.

(b) Part load points OP3 and OP4.

Figure 6.6: Trajectories of the combustion process of the present SI engine in the Peters-Borghi diagram.

To understand the shifts between the individual operating points, the impact of the engine operating parameters on the flow and flame scales v', l_t, s_L^0 and l_F has to be examined. According to Heywood [90], the fluctuation velocity v' is proportional to the engine speed whereas the turbulent length scale l_t is mainly dependent on the engine geometry. The laminar flame speed s_L^0 and flame thickness l_F, on the other hand, are defined by the thermodynamic state of the cylinder charge which in turn is mainly controlled by the engine load and the equivalence ratio of the mixture. Consequently, an increase of engine speed leads to a horizontal shift in the combustion regime diagram as v' and thereby v'/s_L^0 increases proportionally (OP1 vs. OP2 in Fig. 6.6a). The transition of the flame structure in this case can thus be attributed to the changes of the turbulence field. An increase of engine load, in contrast, decreases s_L^0 and particularly l_F. The ratio l_t/l_F becomes larger and the combustion trajectory is shifted horizontally (OP1 vs. OP3 and OP4 in Fig. 6.6b). Lean combustion results in a slower laminar flame velocity s_L^0 and a higher laminar flame thickness l_F. This leads to a shift towards the upper left corner of the combustion regime diagram as v'/s_L^0 increases and l_t/l_F decreases (OP1 vs. OP5 in Fig. 6.6a). The transition of the flame structure for a variation of engine load and equivalence ratio can thus be attributed to the changes of the thermo-chemical properties of the mixture.

As discussed in section 4.4, the engine load also strongly impacts the quenching distance. The trajectories of the (average) quenching distances estimated by Eq. (A.18) are shown in Fig. 6.7a. The smallest quenching distances are observed between 50-90%MFB where the cylinder pressure is the highest. The largest quenching distances, in contrast, appear at the beginning of combustion due to the still low in-cylinder pressure. For each operating point, the magnitude of the simulated (average) quenching distance agrees well to the values reported in chapter 4 (Fig. 4.13). In section 3.4, it was speculated that the boundary layer in a SI engine during combustion is similar to a shear-free turbulent boundary layer. It was thus concluded that the local flame-wall interaction process should be similar to laminar flame
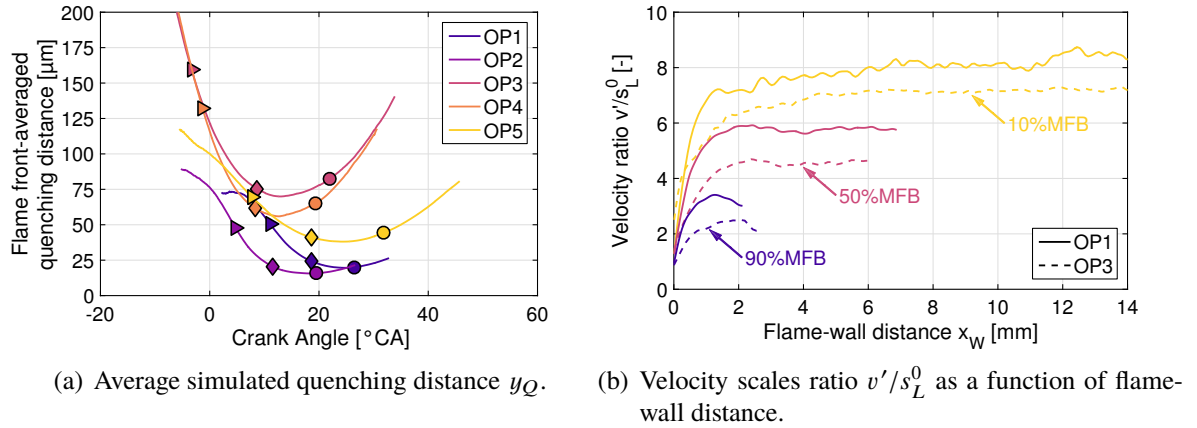
(a) Average simulated quenching distance y_Q.

(b) Velocity scales ratio v'/s_L^0 as a function of flame-wall distance.

Figure 6.7: Analysis of the key characteristics of the quenching process in a SI engine.

quenching, which was later confirmed by a combined experimental and simulative approach (chapter 4). The emerging picture can now be complemented by investigating the velocity ratio v'/s_L^0 as a function of the flame-wall distance. Fig. 6.7b depicts the progression of v'/s_L^0 towards the wall at three different points in time for OP1 and OP3. At any point in time, v'/s_L^0 is almost constant far away from the wall and starts to decrease strongly when the flame-wall distance drops below 2mm. Note that v'/s_L^0 does not decrease to zero in the vicinity of the wall. This is caused by the finite mesh resolution near the wall. The size of the average boundary layer cell was around $0.2 - 0.3mm$. Nonetheless, the profiles of v'/s_L^0 are similar to the ones of a turbulent shear-free boundary layer (cf. Fig. 3.8b). Although this does not prove the validity of the hypothesis that the boundary layer in a SI engine during combustion can be seen as essentially shear-free, it further supports the conclusion drawn in section 4.5 that the turbulent fluctuations near the wall are too weak to substantially influence the local quenching process. Further research, preferably by the means of DNS simulations, is required to clarify the boundary layer structure in an internal combustion engine.

Having discussed the characteristics of the combustion as well as the local flame quenching process, a discussion of the properties of turbulent flame propagation is feasible. Figs. 6.8a and 6.8b show the evolution of the normalized turbulent burning velocity without quenching effects s_T^0/s_L^0 and the turbulent flame thickness $l_{F,t}$, respectively. Similar to the previously discussed velocity (v'/s_L^0) and length scale ratio (l_t/l_F), both quantities attain their maximal value around 10%MFB. Subsequently, s_T^0/s_L^0 as well as $l_{F,t}$ decay due to the increasing proximity of the flame to the combustion chamber walls and the dissipation of turbulence. It is evident from Fig. 6.8a that the normalized turbulent burning velocity s_T^0/s_L^0 is strongly affected by the engine speed (OP1 vs. OP2) as well as by the equivalence ratio (OP1 vs. OP5). The impact of the engine load is less distinct. This can partly be attributed to a higher velocity scale ratio v'/s_L^0 at OP2 and OP5 causing that combustion occurs almost completely within the thin reaction zones regime. Large differences are also found when comparing the turbulent flame thickness $l_{F,t}$ between the different operating points. At first glance, this might seem surprising as the overall turbulent length scale l_t and therefore the steady-state

120

(a) Turbulent burning velocity ratio s_T^0/s_L^0 without quenching effects.

(b) Turbulent flame thickness $l_{F,t}$.

(c) Turbulent burning velocity ratio s_T/s_L^0 with quenching effects.

(d) Unquenched factor Q.
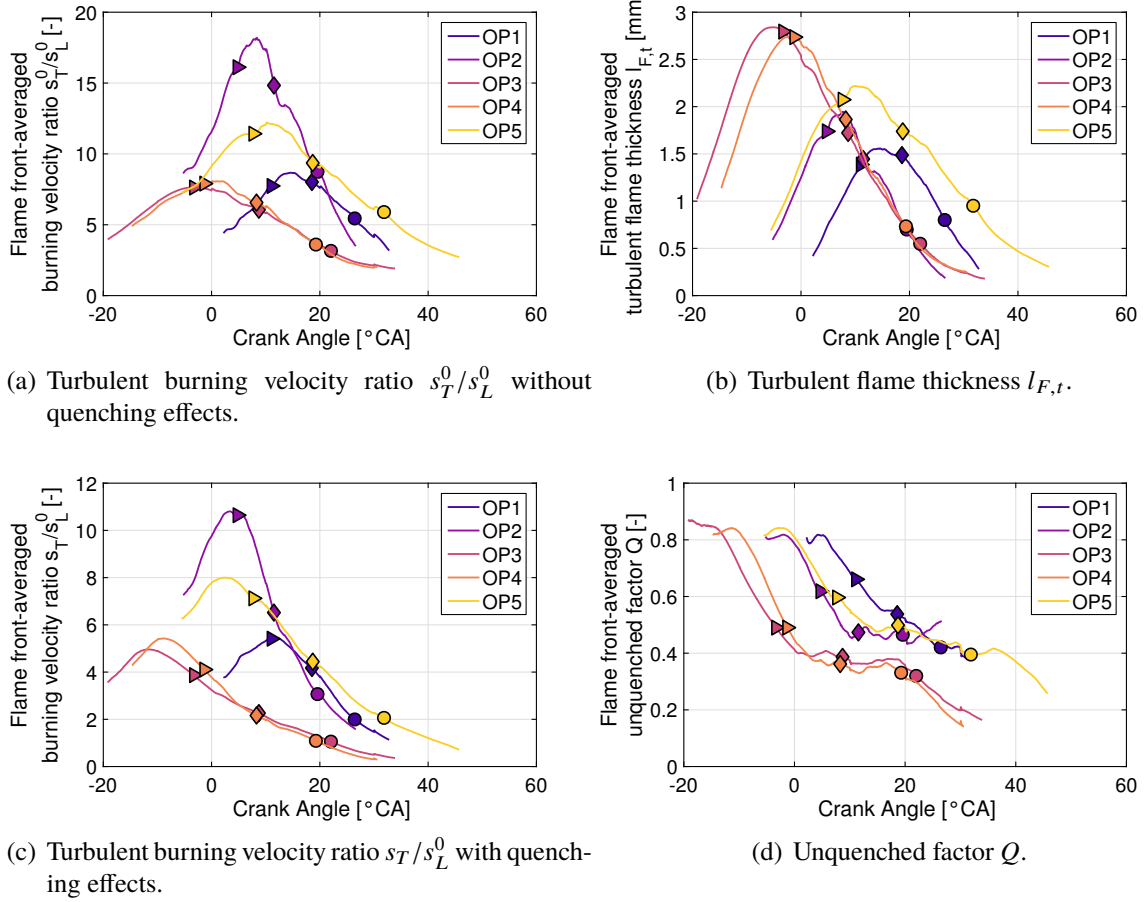
Figure 6.8: Temporal analysis of turbulent flame propagation and turbulent flame-wall interaction in a SI engine.

value of the turbulent flame thickness $l_{F,t}$ is similar at all operating points. However, the development of the turbulent flame brush takes a finite time and is thus strongly influenced by the duration of combustion. Therefore, a fast flame may not be able to reach its steady-state turbulent flame thickness $l_{F,t,alg}$ before interacting with the wall. Consequently, $l_{F,t}$ is the smallest at OP2 and the highest at OP3.

The previously discussed normalized burning velocity s_T^0/s_L^0 is not representative for the actual flame-front averaged burning velocity as the effect of flame quenching is not considered. However, it is an indication of the maximum burning velocity when flame-wall interactions are absent, for example in the middle of the combustion chamber. The trajectories of the normalized turbulent burning velocity including the effect of quenching, s_T/s_L^0, are shown in Fig. 6.8c. The trends of s_T/s_L^0 are similar to the ones of s_T^0/s_L^0, however, the maximum flame speed is attained earlier. This can be attributed to the evolution of the unquenched factor Q, which is depicted in Fig. 6.8d. After ignition, Q quickly starts to decrease until it becomes almost constant at around 50%MFB. As a consequence, the maximum of s_T/s_L^0 is found at an earlier stage of combustion compared to s_T^0/s_L^0. The part load points are

more strongly affected by quenching as the quenching distance as well as the turbulent flame thickness $l_{F,t}$ is larger. It has to be noted that the unquenched factor Q is smaller than unity at all times, as parts of the flame are always in the vicinity of solid walls. Even at the start of combustion, parts of the initial flame kernel are quenched by the electrodes of the spark plug. This highlights the fact that flame-wall interactions are strongly influencing premixed combustion in SI engines and that they cannot be omitted.

It is remarkable that the (flame-front averaged) unquenched factor Q does not drop to zero at the end of combustion, particularly at the full load points. The reason for this is the discrete numerical representation of the otherwise continuous physical processes. At OP2, for example, the quenching distance between 50%MFB and 90%MFB is $y_Q \approx 20\mu m$. To fully resolve the deceleration of the flame, the mesh size has to be at least of order of the quenching distance, preferably smaller. Otherwise, Q remains slightly larger than zero and the flame simply leaves the computational domain as the wall distance computed by the current algorithm cannot be lower than the distance between the cell center and the boundary face within a boundary cell. However, the criterion that the largest cell size adjacent to the wall must be smaller than the quenching distance often cannot be met in practical situations as the computational effort would be too high. Within the current mesh, the size of the boundary layer cells ranges around $0.2 - 0.3mm$ and may drop to around $60\mu m$ in regions with a high mesh refinement (e.g., in the vicinity of the measuring points of the thermocouples). The quenching distances, on the other hand, range approximately between $20 - 200\mu m$. As a consequence, combustion may occur too fast in the final cell at the wall. However, the approach of the flame towards the wall is correctly reproduced and the overall error thus remains limited. In addition to the cell size, the time step also has to be small enough to resolve the quenching process. An upper limit can be estimated by requiring that the distance travelled by the flame is smaller than the local cell size. If the velocity of the flame is close to the laminar burning velocity s_L^0, the maximum time step can be approximated as $\Delta t < y_Q/s_L^0$. At OP2, which is the most critical operating point in this regard, the maximum allowed time step equals $\Delta t \approx 20\mu s = 0.24°CA$, which is larger than the time step of the simulation, $\Delta\alpha = 0.125°CA$. It can thus be concluded that the most critical point for completely resolving the quenching process is the limited mesh resolution near the wall.

To gain insights into the behaviour of the turbulent flame near the wall, the average spatial evolution of the previously discussed quantities has to be investigated. The burning velocity ratios s_T/s_L^0 and s_T^0/s_L^0 at OP1 and OP3 are shown as a function of the flame-wall distance x_W in the Figs. 6.9a and 6.9b, respectively. The normalized turbulent burning velocity without the effects of quenching is almost constant for a given point in time and begins to decrease around $0.5mm$ from the wall. If the spatial discretization of the wall were to be higher, s_T^0/s_L^0 would drop to unity directly at the wall indicating a re-laminarisation of the turbulent flame brush. The normalized burning velocity with the effects of quenching s_T/s_L^0, in contrast, starts to decrease much earlier and eventually becomes zero at the wall. It is interesting to note that the progression of s_T/s_L^0 towards the wall is similar for 10%MFB, 50%MFB and 90%MFB, despite the varying burning velocity ratio s_T^0/s_L^0 and unquenched factor Q (Fig. 6.9d). The turbulent flame brush is influenced by flame quenching at around $5mm$ at OP1 and $8mm$ at OP3. This behaviour can be mainly attributed to the turbulent flame

(a) Turbulent burning velocity ratios s_T/s_L^0 and s_T^0/s_L^0 at OP1.

(b) Turbulent burning velocity ratios s_T/s_L^0 and s_T^0/s_L^0 at OP3.

(c) Turbulent flame thickness $l_{F,t}$.

(d) Unquenched factor Q.

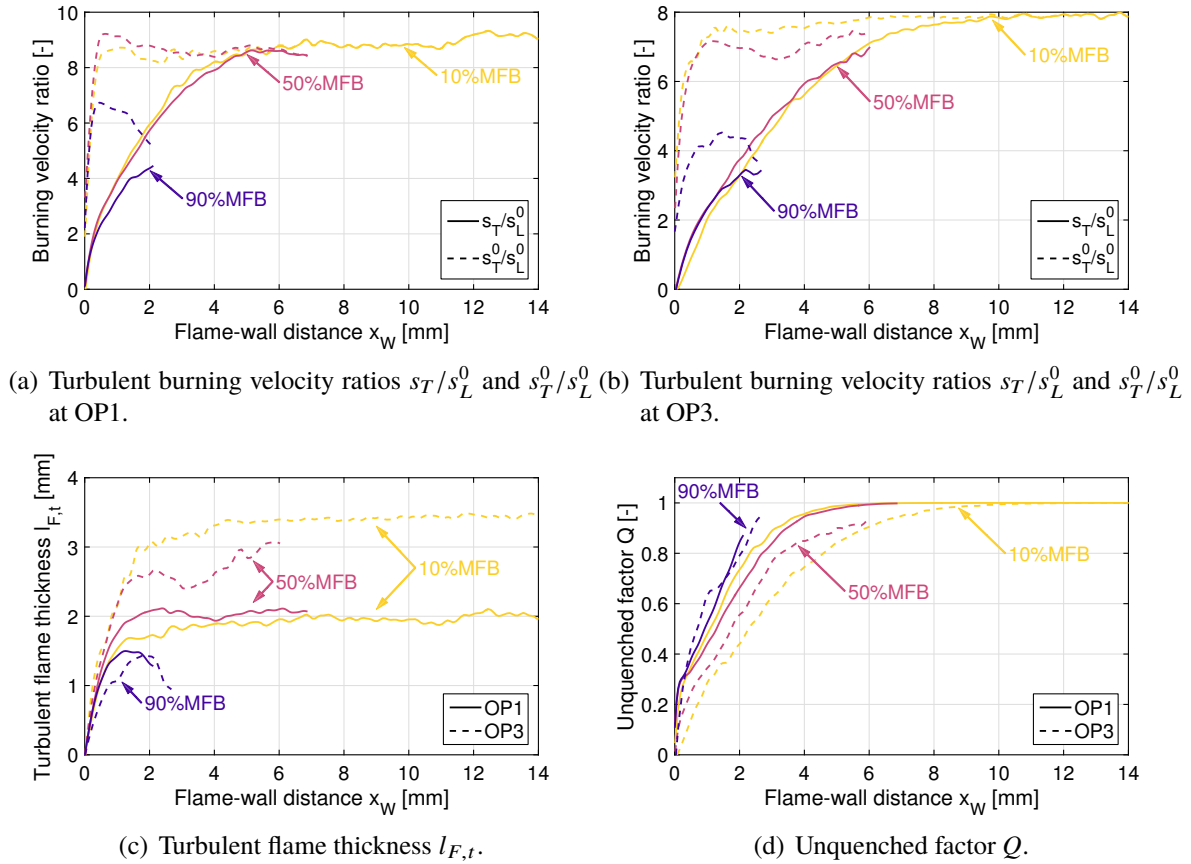**Figure 6.9:** Spatial analysis of turbulent flame propagation and turbulent flame-wall interaction in a SI engine.

thickness. As one can see in Fig. 6.9c, the turbulent flame thickness at OP3 is higher than at OP1 at any point in time causing that the turbulent flame is subject to flame quenching at a higher wall distance. Similar to s_T^0/s_L^0, the turbulent flame thickness is almost constant in the center region for a given point in time. At $x_W \approx 2mm$, it starts to decrease linearly to zero showing that the turbulent flame brush becomes laminar at the wall. The progression of the unquenched factor Q is shown in Fig. 6.9d. The slight discontinuities can be attributed to the limited mesh resolution near the wall. As one can see, the gradient of Q becomes very steep close to the wall. If this gradient cannot be adequately resolved by the mesh, Q remains larger than zero in the boundary layer cell and the flame leaves the computational domain, as previously discussed. The fact that Q still becomes zero at the wall can be attributed to the fact that parts of the computational domain, particularly where fine geometrical details have to be resolved, possess a sufficient mesh resolution.

The evolution of the mean flame front colored with the turbulent burning velocity s_T is shown in Fig. 6.10. The highest burning velocities are found in the center of the combustion chamber. If the flame reaches the vicinity of the wall, the burning velocities start to decrease strongly. The aforementioned effect that Q cannot become zero due to the insufficient mesh

10%MFB

10%MFB

50%MFB

50%MFB

90%MFB

90%MFB

Turbulent burning velocity [m/s]

0   1   2   3   4   5   6   7   8

(a) Operating point 1.

Turbulent burning velocity [m/s]

0   1   2   3   4   5   6   7   8
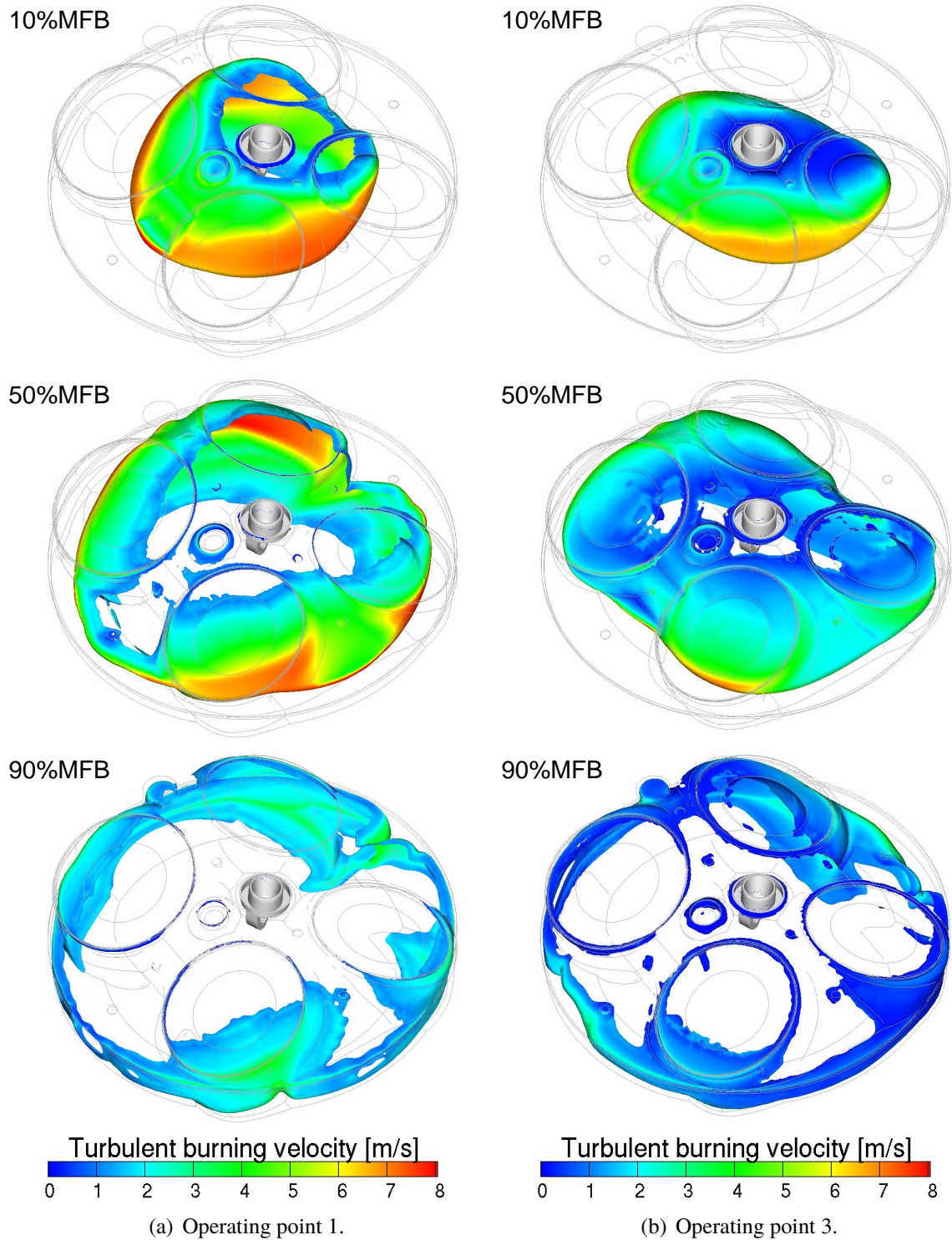
(b) Operating point 3.

Figure 6.10: Mean flame front at OP1 and OP3 at different points in time. The surface is coloured with the turbulent burning velocity including the effects of quenching s_T.

resolution can be seen best at OP1. The burning velocity at the edges of the flame front is still larger than zero and the flame leaves the computational domain. The effect is less pronounced at OP3 as the quenching distance is much higher. The flame propagation at OP1 and OP3 is vastly different as the charge motion is dominated by either tumble (OP1) or swirl (OP3). At OP1, the flame propagates faster towards the intake valves on the left-hand side as turbulence and thereby the turbulent burning velocity is higher in this region. This results in a spherical flame front shape, as the spark plug is located towards the exhaust valves. At OP3, in contrast, the flame propagation is less spherical and the flame mainly spreads along the axis of the crankshaft. This can again be attributed to the charge motion which causes that the turbulence level is the highest along a central axis parallel to the crankshaft. Overall, the shape of the flame front as well as the distribution of the turbulent burning velocity looks realistic.
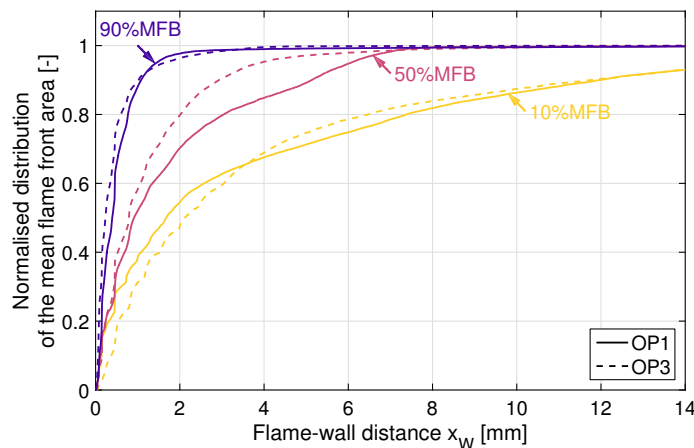
Figure 6.11: Distribution of the mean flame front area with respect to the flame-wall distance x_W at OP1 and OP3.

The importance of flame-wall interactions in SI engines can be stressed by examining the distribution of the mean flame front area with respect to the wall distance (Fig. 6.11). At 10%MFB, the flame-wall distance of more than 50% of the mean flame front area is less than 2mm. For 50%MFB and 90%MFB, this number is even higher. As a consequence, flame-wall interactions are a significant part of combustion in SI engines that have to be taken into account in combustion modelling. It has to be remarked that the impact of flame-wall interactions on the combustion process strongly depends on the geometry of the engine. The present engine has a compact combustion chamber with a high surface-to-volume ratio. The Pancake engine, which was investigated in section 5.5.3, has a higher compression volume and a simpler overall shape which in turn decreases the surface-to-volume ratio. As a result, flame-wall interactions were found to be less pronounced compared to the present direct-injection SI engine. It can thus be concluded that flame-wall interactions are more important for applications such as downsized car engines and less pronounced for industrial engines (e.g., large-bore gas engines).

6.3 Flame-wall interactions in SI engines - a phenomenological summary

Combining the simulation results with the findings of chapter 3 and 4, a comprehensive phenomenological picture of flame-wall interactions in SI engines can be drawn regarding the main quenching mode and the characteristics of the wall heat fluxes. As already suggested by Dreizler et al. [54], the flame-wall interaction process in a SI engine can be divided in three sequenced stages. Each of these stages has its unique characteristics, which are summarized in Fig. 6.12:

- Early combustion phase, central region (highlighted by ▬▬▬):
  During the early combustion phase, the radius of the flame kernel is still small and it can travel almost freely in any direction. As a consequence, it usually hits the wall at normal angles, e.g., within piston bowl leading to HOQ (e.g., OP3, MP4). Although the normalized wall heat fluxes during HOQ are the highest among all quenching modes, the absolute peak of the wall heat flux at a given location within the central region is likely to be caused by convection. This can be attributed to the fact that the charge motion is high whereas the flame power $\dot{Q}_F$ is still low due to the relatively low in-cylinder pressure and temperature. Typically, the progression of the wall heat flux exhibits several maximums (e.g., OP1, MP4). The first can be attributed to flame quenching whereas the succeeding ones are caused by convection. In the central region around the spark plug, the wall heat flux is sustained at a high level for a longer time than in the intermediate or outer region.

- Main combustion phase, intermediate region (highlighted by ▬▬▬):
  In the subsequent main combustion phase, the flame radius increases strongly leading to a mix of HOQ and SWQ depending on the local combustion chamber and flame front geometry (e.g., OP3, MP3). Moreover, the highest (absolute) quenching wall heat fluxes are found in this stage as the in-cylinder pressure and temperature and thereby the flame power $\dot{Q}_F$ peak. The decaying charge motion leads to a decrease of the convective heat transfer and hence, the absolute peak wall heat flux is more likely to be caused by quenching. A high wall heat flux is sustained for a shorter period of time compared to the central region (e.g., OP1, MP3).

- Late combustion phase, outer region (highlighted by ▬▬▬):
  In the late combustion phase, the flame enters crevices such as the squish area and SWQ becomes the dominant form of quenching (e.g., OP1,MP7). Although the quenching wall heat fluxes decrease due to the decreasing in-cylinder pressure and temperature, the peak of the wall heat flux is almost exclusively caused by quenching as the charge motion and thereby the convective heat transfer have already decayed considerably up to this point. The secondary peaks appearing in the wall heat flux trace remain weak and the overall period in which a high wall heat flux is sustained is very short compared to the central region of the combustion chamber (e.g., OP1, MP7).
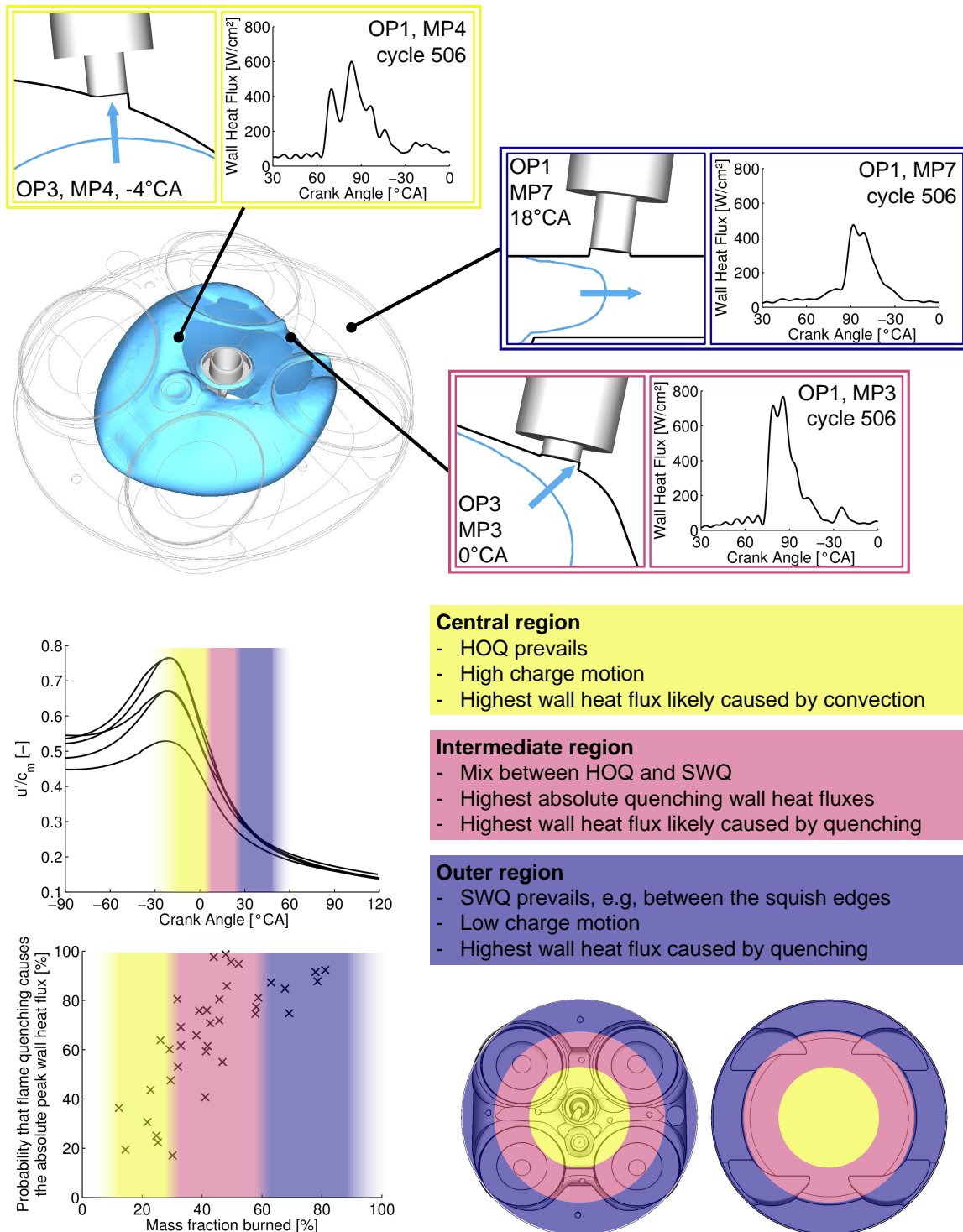
Figure 6.12: Phenomenological characteristics of the flame-wall interaction process in a SI engine.

It has to be noted that the phenomenology described in Fig. 6.12 depends on the engine design and cannot be directly transferred to an arbitrary SI engine. On the one hand, the spatial distribution of the three regions is defined by the propagation of the flame within the combustion chamber. The central region is expected to be located where the flame front first touches the combustion chamber walls. If the spark plug is placed between the exhaust valves, for example, the central region moves accordingly. On the other hand, the wall heat flux characteristics of the individual regions are primarily affected by the flow motion. If the engine is designed to have a low charge motion, the role of flame quenching becomes more dominant concerning the cause of the peak wall heat flux, even in the central region. This situation reverses for a high level of charge motion. Similarly, the appearance of secondary wall heat flux peaks is also controlled by the level of charge motion. By taking these considerations into account, the present classification can also be transferred to other SI engines.

6.4 Conclusion

In this chapter, the performance of the previously derived GFWI model was assessed by investigating the simulation results for a direct-injection SI engine. The predicted heat release and pressure curves were compared to the experimental results. Despite the simple one-step chemical reaction, a satisfactory agreement was found and the trends were correctly captured by the current combustion model irrespective of the underlying turbulence model. Additionally, the turbulent combustion process was analysed in detail. It was found that in the present engine, combustion occurs in the thin reaction zones and corrugated flamelets regime. The impact of the operating parameters on the combustion regime was discussed.

The propagation of the turbulent flame was studied by examining the spatial and temporal evolution of the characteristic scales of combustion such as the turbulent burning velocity. It was shown that the turbulent fluctuations decrease towards the wall and that the turbulent flame brush becomes laminar again. This result partly confirms and complements the findings of chapter 3 and 4 indicating that the local flame-wall interaction process in a SI engine can essentially be seen as laminar. Furthermore, it was found that the mean turbulent flame front is already influenced by flame quenching at a wall distance of several millimeters. This can be attributed to the thickness of the turbulent flame brush which is much larger than the actual quenching distance itself. Fast flames (e.g., at OP2) are not able to attain the equilibrium value of the turbulent flame brush thickness and are thus able to propagate closer to the wall without being influenced by flame quenching. The importance of flame-wall interactions in SI engines was underlined by investigating the distribution of the mean flame front area with respect to the wall distance. In the present case, it was found that a major part of the turbulent flame brush is located in the vicinity of the wall, even at early stages of combustion. It was thus concluded that flame-wall interactions in downsized SI engines have a major impact on the flame propagation and cannot be omitted. In this context, it was argued that the relative importance of flame-wall interactions may depend on the engine geometry.

The calculated shape of the flame front was found to be realistic, however, large parts of the flame did not stop at the quenching distance and left the computational domain. This

was attributed to the limited mesh resolution near the wall causing that the distance to the quenching zone x_Q and thereby unquenched factor Q remains larger than zero in the boundary layer cell. In this context, it was revealed that the time step of the simulation is small enough to resolve the process.

Finally, the insights gained by experiment and simulation were combined in a coherent way to obtain a physically meaningful picture of flame-wall interactions. Three regions with distinct wall heat flux and quenching characteristics were distinguished.

7 Summary and conclusion

In this thesis, the flame-wall interaction process in a spark-ignition engine was studied in detail to improve its understanding and modelling. Starting from a comprehensive literature review, fundamental aspects of flame quenching such as the wall heat flux were investigated in a spark-ignition engine using a combination of highly-resolved wall heat flux measurements and an elaborate simulative methodology. An enhanced combustion model accounting for flame quenching and near-wall turbulence was subsequently derived in the context of a level-set framework using established concepts of combustion and turbulence modelling. The model was implemented into the existing level-set and flame-tracking framework in AVL FIRE™ and tested against the available experimental data.

First, a thorough analysis of flame-wall interactions was conducted based on the existing literature on the topic. The wall influences the propagation of a turbulent flame mainly in two ways - quenching and near-wall turbulence. To discern the characteristics and individual contributions of these effects, the interaction between walls and laminar flames as well as between walls and turbulence was discussed separately. Laminar flame-wall interactions are characterised by the normalized quenching wall heat flux φ_Q and the normalized quenching distance Pe_Q and it was shown that these quantities remain within certain bounds for hydrocarbon-air mixtures. Two limits of near-wall turbulence, a shear-free turbulent boundary layer and a turbulent channel flow, were introduced and their main features were discussed. Based on these fundamentals, turbulent flame-wall interactions were discussed. It was shown that the type of boundary layer significantly affects the characteristics of the interaction process. In shear-free turbulent boundary layers, the flow motions are too weak to substantially influence the local quenching process and as a consequence, the characteristic scales are similar to the ones of laminar flame-wall interactions. In a turbulent channel flow, on the other hand, the vigorous turbulent activity near the wall may lead to smaller quenching distances and higher wall heat fluxes compared to the laminar case. Turbulent flame-wall interaction were thus found to be decisively influenced by near-wall turbulence and its characteristics. Based on this conclusion, the flame-wall interaction process in a spark-ignition engine was characterised in an a priori way by analysing the near-wall flow characteristics. It was argued that the boundary layer in a spark-ignition engine bears strong similarities to a shear-free turbulent boundary layer. Hence, it was suggested that the local quenching process in a spark-ignition engine is laminar.

To prove or disprove this hypothesis, a highly-resolved wall heat flux measurement was combined with comprehensive simulations to analyse the quenching process in a modern spark-ignition engine. Five significantly different operating points were examined to investigate the influence of the engine speed and load, equivalence ratio and charge motion on the quenching process. The ensemble-averaged and single-cycle wall heat flux traces were analysed and a methodology was introduced to estimate the quenching wall heat fluxes $\dot{Q}_{W,Q}$ for

each operating and measuring point. Two approaches for calculating the quenching distance y_Q as well as the normalized scales φ_Q and Pe_Q, namely the inner layer formulation and the formulation by Boust, were introduced. For their application, flame properties such as the laminar flame velocity s_L^0 were necessary. These were determined by a combination of 3D-CFD, 3D-FE and 1D simulations. The flame-wall interaction process in a spark-ignition engine was discussed based on the quenching distance, normalized wall heat flux and Peclet number. Characteristic scales of each quantity were reported. The normalized wall heat flux and the Peclet number were found to be almost independent from the operating conditions. The quenching distance, in contrast, was shown to be mainly influenced by the in-cylinder pressure and thereby the engine load. Each of the characteristic scales remained within the bounds of laminar flame-wall interactions providing strong evidence for the initial hypothesis that the local flame quenching process in a spark-ignition engine is laminar. Finally, two correlations for calculating the quenching distance in spark-ignition engines were given.

Subsequently, the well-known G-equation combustion model was extended to account for flame quenching as well as near-wall turbulence yielding the G-equation Flame-Wall Interaction (GFWI) model. Having employed classic guidelines of combustion and turbulence modelling, the presented approach can also be transferred to other combustion models, particularly to ones using the turbulent burning velocity. Analogously to existing flamelet models, the derivation of the GFWI model was based upon the analysis of the structure of a quenched flame, the definition of its characteristic layer and the subsequent determination of its kinematic behaviour. The resulting G-equation describing the kinematic behaviour of a laminar quenched flame was found to be very similar to the original G-equation. A unified equation was proposed by blending the burning velocity. To transfer this concept to turbulent flames, the probability of finding quenched flamelets was introduced as the kinematic effects of turbulence were found to be dominant compared to the local thermodynamic effects for turbulent flame-wall interactions. The unquenched factor Q was introduced as a measure for the unquenched flamelet fraction within a turbulent flame brush. It was subsequently shown that it is a scaling factor for the turbulent burning velocity in case of flame quenching. Based on these findings, a generalized G-equation accounting for quenched and unquenched flamelets within a turbulent flame brush was proposed and suitable modelling closures were derived. To incorporate the effects of near-wall turbulence, accurate definitions for the turbulent diffusivity D_t were shown to be indispensable. As a consequence, modified correlations for the unclosed terms appearing in the transport equations as well as for the turbulent burning velocity were derived. Some of the modelling assumptions were reviewed in an a priori fashion. The final model was successfully validated against DNS data and shown to enable a more realistic simulation of flame propagation near solid walls.

The applicability of the GFWI model for combustion simulation in a spark-ignition engine was assessed. It was shown that the model is capable of predicting the heat release and pressure curves for a wide range of operating conditions with reasonable accuracy. The analysis of flame propagation revealed that in the present example, the mean turbulent flame is already influenced by the wall at a flame-wall distance of several millimetres. Moreover, a major fraction of the turbulent flame brush was found to be located within this influence region at any time during combustion. It was thus concluded that flame-wall interactions play a major role for the flame propagation in downsized spark-ignition engines. With

increasing cylinder displacement, the effects are expected to become less important. Finally, a comprehensive overview of the phenomenology of flame-wall interactions in spark-ignition engines based upon the aggregated findings of this thesis was presented.

The results of this thesis are very encouraging, however, there are several uncertainties left which should be addressed in future works. First of all, a further validation of the GFWI model and its underlying modelling assumptions is required. In this context, DNS simulations may provide valuable insights into the near-wall behaviour of a turbulent flame, e.g. about the distribution of quenched flamelets within a turbulent flame brush or about the chemical state of partially quenched turbulent flames. Moreover, carefully conducted DNS simulations can be utilized as further validation cases. To further evaluate the GFWI model and its predictive capabilities, a more elaborate coupling to the flow field and representation of chemistry is also necessary, e.g., by flamelet libraries. In this context, the incorporation of the post-flame oxidation process within quenched flamelets or the prediction of wall heat fluxes in combination with a suitable wall heat flux model might be promising directions for future research. The present combustion model should thereby also be applied to a variety of different spark-ignition engines to estimate its ability to predict combustion for a wide range of applications. Aside from the GFWI model and its validation, DNS simulations may also be used to provide new insights into the boundary layer structure of spark-ignition engines and the flame-wall interaction process in general. In this way, the findings of this thesis can be further substantiated or appropriately adapted. Moreover, the resulting data can also be used to further improve the physical models such as turbulent wall functions or wall heat flux models used within spark-ignition engine simulations and thereby the accuracy of the predictions. Eventually, elaborate models such as the presented GFWI model are needed to meet the development challenges for future engines and propulsion systems.

Appendix

A Definition of the tumble and swirl number

The charge motion in an engine can be characterised by the tumble and swirl number. In the present work, these dimensionless quantities were estimated based on the 3D-CFD calculations described in section 4.3.2. For calculating the tumble or swirl number, the respective angular velocity ω_{charge} of the charge motion was calculated by dividing the angular momentum around a predefined rotation axis with the corresponding density-weighted squared average radius

$$\omega_{charge} = \frac{\int_{cyl} \overline{\rho}\, \mathbf{x}_c \times \mathbf{v}\, \mathrm{d}V \cdot \mathbf{n}_{rot}}{\int_{cyl} \overline{\rho} \left(\mathbf{x}_c \cdot \mathbf{x}_c - (\mathbf{x}_c \cdot \mathbf{n}_{rot})^2 \right) \mathrm{d}V}. \tag{A.1}$$

Therein, the vector $\mathbf{x}_c$ can be calculated by subtracting the coordinates of the rotation center $\mathbf{x}_{rot}$ from the spatial coordinate $\mathbf{x}$, i.e., $\mathbf{x}_c = \mathbf{x} - \mathbf{x}_{rot}$. The rotation center $\mathbf{x}_{rot}$ was located in the middle of the combustion chamber and moved in accordance with the piston motion. The rotation axis was defined by the unit vector $\mathbf{n}_{rot}$. For calculating the tumble number, this vector was parallel to the crankshaft whereas it coincided with the vertical axis of the cylinder for estimating the swirl number. Finally, the corresponding angular velocity was normalised with the angular velocity of the crankshaft $\omega_{engine} = 2\pi n$ yielding

$$Tu = \frac{\omega_{charge,tumble}}{2\pi n} \qquad \text{with } \mathbf{n}_{rot} \text{ parallel to the crankshaft} \tag{A.2}$$

and

$$Sw = \frac{\omega_{charge,swirl}}{2\pi n} \qquad \text{with } \mathbf{n}_{rot} \text{ parallel to the vertical axis of the cylinder} \tag{A.3}$$

for the tumble number Tu and swirl number Sw.

B Algorithmic evaluation of single-cycle wall heat flux traces

The single cycle wall heat flux traces for each measuring and operating point have to be analysed in order to extract the quenching wall heat flux $\dot{Q}_{W,Q}$, its corresponding crank angle α_Q and the crank angle $\alpha_{\partial Q}$. The latter is associated to the highest gradient of the wall heat flux which can be attributed to the arrival of the flame.

For this purpose, an algorithm was developed which is shortly explained in the following. Note that all quantities are evaluated at i operating points, j measuring points for k cycles

meaning that $\dot{Q}_W = \dot{Q}_{W,ijk}$. For the sake of simplicity, the subscripts ijk are omitted in the following.

(a) Example for a quenching type (cycle 293). (b) Example for a superposition type (cycle 711).
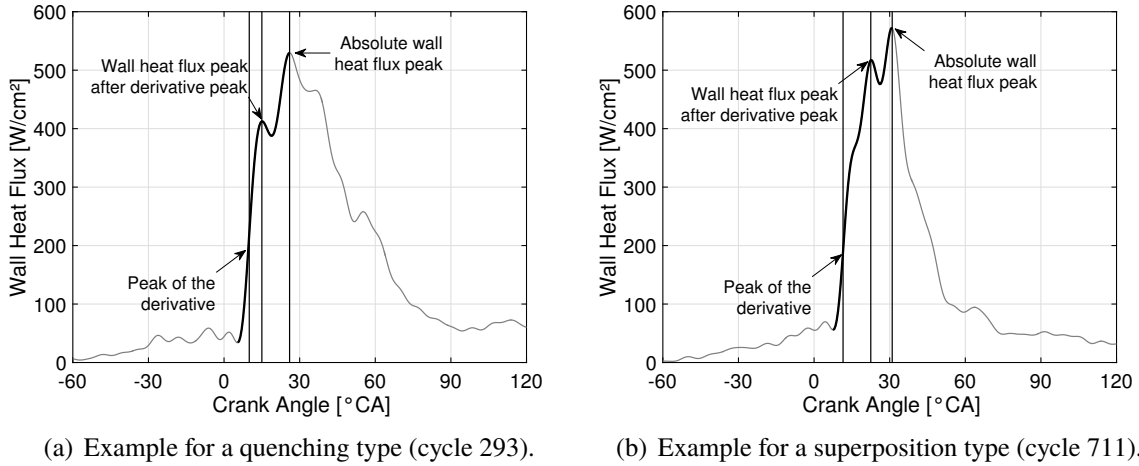
Figure A.1: Example wall heat flux traces and their characteristics at measuring position 1 at operating point 1.

The first step is to extract the relevant part of the wall heat flux in which flame quenching occurs (highlighted in black in Figs. A.1). For this purpose, it is assumed that quenching takes place between the arrival of the flame and the maximum wall heat flux. The procedure to find this part is as follows:

1. Find the absolute peak of the wall heat flux $\dot{Q}_{W,max}$ and its location $\alpha_{Q,max}$ between $-30°CA$ and $90°CA$.

2. Find the position $\alpha_{Q,T}$ of a dynamically estimated threshold: $\dot{Q}_{W,T} = 1/3\dot{Q}_{W,max}$.

3. Find the position $\alpha_{Q,min}$ of the first local minimum of the wall heat flux before $\alpha_{Q,T}$.

Having calculated $\alpha_{Q,min}$ and $\alpha_{Q,max}$, the sought-after part of the wall heat flux is known. Next, the derivative of the wall heat flux $\psi = \frac{\partial}{\partial\alpha}\dot{Q}_W$ is estimated by a central finite difference. The absolute peak of the derivative ψ_{max} and its location $\alpha_{\partial Q}$ is particularly important as it is used to identify the arrival of the flame and the subsequent quenching process. Consequently, the preliminary quenching wall heat flux $\dot{Q}_{W,Q}$ and its position α_Q is determined by searching the first maximum after the derivative peak at $\alpha_{\partial Q}$.

However, as already discussed in section 4.2.2, there is a certain subset of wall heat flux traces which do not exhibit the characteristics of flame quenching. These 'superposition' or 'convective types' have to be properly excluded so that only the 'quenching types' remain. Based on the phenomenology of the single cycle wall heat flux histories described in 4.2.2, the following guidelines were derived to discern between the three types:

- Quenching types: high gradient / short time until the first peak is reached.

- Superposition types: high gradient / long time until the first peak is reached or presence of a turning point between the largest gradient and the first peak.

- Convective types: low gradient.

The quantities ψ_{max} and $\dot{Q}_{W,Q}$ as well as their respective locations $\alpha_{\partial Q}$ and α_Q (Figs. A.1) are subsequently used for the classification of the individual cycles according to the following rules:

1. As flame-wall interactions are characterized by a rapid increase of the wall heat flux, it is assumed that flame quenching occurred if the peak of the derivative ψ_{max} is greater than a predefined threshold. The threshold ψ_T can be determined individually for each measuring position depending on the peak derivative of the corresponding mean wall heat flux, $\psi_T = 1.1\overline{\psi}_{max}$. The peak derivative of the mean wall heat flux $\overline{\psi}_{max}$ was chosen as a lower limit since the averaging procedure leads to a smearing of the individual traces where the characteristics of quenching events are not present anymore as they are filtered due to their inherent cycle-to-cycle variability. The procedure can be summarized as:

$$\psi_{max} \begin{cases} > \psi_T : \text{quenching or superposition type} \\ \leq \psi_T : \text{convective type} \end{cases} \tag{A.4}$$

2. If flame quenching occurred according to the prior rule, quenching and superposition types can be distinguished by either the presence of an turning point between $\alpha_{\partial Q}$ and α_Q or by the absolute duration between $\alpha_{\partial Q}$ and α_Q. In the latter case, the threshold is dynamically estimated by $\Delta\alpha = \dot{Q}_{W,Q}/\psi_{max}$. If the absolute time $\alpha_Q - \alpha_{\partial Q}$ is larger than $\Delta\alpha$, a superposition type is assumed. Superposition types exhibit a longer duration between the peak gradient and the ensuing maximum of the wall heat flux as shown in Figs. A.1a and A.1b. The rules can be summarized as

$$\frac{\partial \psi}{\partial \alpha} \begin{cases} > 0 \text{ in } [\alpha_{\partial Q}, \alpha_Q] : \text{superposition type} \\ \leq 0 \text{ in } [\alpha_{\partial Q}, \alpha_Q] : \alpha_Q - \alpha_{\partial Q} \begin{cases} < \Delta\alpha : \text{quenching type} \\ \geq \Delta\alpha : \text{superposition type} \end{cases} \end{cases} \tag{A.5}$$

The algorithm was applied for all measuring locations j and all cycles k resulting in a total of 8000 classified wall heat flux traces per operating point i. Around 60%-80% of the analysed wall heat flux traces were identified as a quenching type and subsequently included in the analysis of flame-wall interactions described in chapter 4.

C Correlations for the laminar burning velocity and the inner layer temperature of gasoline-air flames

To obtain correlations for the laminar burning velocity and inner layer temperature of gasoline, 1D flame calculations were conducted as described in section 4.3.2. A total of 216 different

thermodynamic states ($p \in [20bar, 40bar, 60bar, 80bar]$; $T_u \in [700K, 800K, 900K]$; $\phi \in [0.8, 0.9, 1.0, 1.1, 1.2, 1.3]$; $Y_{EGR} \in [0\%, 10\%, 20\%]$) were calculated using the gasoline surrogate as a fuel. The laminar burning velocity s_L^0 was approximated by

$$s_L^0(p, T_u, \phi, Y_{EGR}) = s_{L,ref}^0(\phi, Y_{EGR}) \left(\frac{T_u}{T_{u,ref}}\right)^{\alpha(\phi, Y_{EGR})} \left(\frac{p}{p_{ref}}\right)^{\beta(\phi, Y_{EGR})} \tag{A.6}$$

where $s_{L,ref}^0$ is a polynomial fit of the laminar burning velocity as a function of the equivalence ratio ϕ and the residual gas mass fraction Y_{EGR} at the reference conditions, $p_{ref} = 40bar$ and $T_{u,ref} = 800K$,

$$\begin{aligned} s_{L,ref}^0(\phi, Y_{EGR}) = {} & a_{00} + a_{10}(\phi - 1) + a_{01}Y_{EGR} + a_{20}(\phi - 1)^2 + a_{11}(\phi - 1)Y_{EGR} + \\ & + a_{02}Y_{EGR}^2 + a_{30}(\phi - 1)^3 + a_{21}(\phi - 1)^2 Y_{EGR} + a_{12}(\phi - 1)Y_{EGR}^2 \,. \end{aligned} \tag{A.7}$$

The exponential factors α and β are given by the approximations

$$\begin{aligned} \alpha(\phi, Y_{EGR}) = {} & b_{00} + b_{10}(\phi - 1) + b_{01}Y_{EGR} + b_{20}(\phi - 1)^2 + b_{11}(\phi - 1)Y_{EGR} + \\ & + b_{02}Y_{EGR}^2 + b_{30}(\phi - 1)^3 + b_{21}(\phi - 1)^2 Y_{EGR} + b_{12}(\phi - 1)Y_{EGR}^2 \end{aligned} \tag{A.8}$$

and

$$\begin{aligned} \beta(\phi, Y_{EGR}) = {} & c_{00} + c_{10}(\phi - 1) + c_{01}Y_{EGR} + c_{20}(\phi - 1)^2 + c_{11}(\phi - 1)Y_{EGR} + \\ & + c_{02}Y_{EGR}^2 + c_{30}(\phi - 1)^3 + c_{21}(\phi - 1)^2 Y_{EGR} + c_{12}(\phi - 1)Y_{EGR}^2 \,. \end{aligned} \tag{A.9}$$

Table A.1: Model constants of the correlation for the laminar burning velocity of gasoline-air flames.

Constant	Value	Constant	Value	Constant	Value
a_{00}	0.9965	b_{00}	2.6188	c_{00}	-0.3173
a_{10}	0.3416	b_{10}	-0.0563	c_{10}	-0.1163
a_{01}	-3.0783	b_{01}	2.3888	c_{01}	-0.3078
a_{20}	-3.3428	b_{20}	5.6223	c_{20}	-0.5165
a_{11}	-1.5696	b_{11}	2.6289	c_{11}	-0.1921
a_{02}	2.4583	b_{02}	2.1395	c_{02}	0.3014
a_{30}	0.2084	b_{30}	-2.7763	c_{30}	2.2358
a_{21}	7.2018	b_{21}	-1.0402	c_{21}	2.8479
a_{12}	2.3398	b_{12}	-15.0068	c_{12}	3.3951

Similarly, the inner layer temperature T_0 is approximated by

$$T_0(p, T_u, \phi, Y_{EGR}) = T_{0,ref}(\phi, Y_{EGR}) \left(\frac{T_u}{T_{u,ref}}\right)^{\alpha'(\phi, Y_{EGR})} \left(\frac{p}{p_{ref}}\right)^{\beta'(\phi, Y_{EGR})} \tag{A.10}$$

where $T_{0,ref}$ is a polynomial fit of the inner layer temperature as a function of the equivalence ratio ϕ and the residual gas mass fraction Y_{EGR} at the reference conditions, $p_{ref} = 40bar$ and

$T_{u,ref} = 800K,$

$$T_{0,ref}(\phi, Y_{EGR}) = a'_{00} + a'_{10}(\phi - 1) + a'_{01}Y_{EGR} + a'_{20}(\phi - 1)^2 + a'_{11}(\phi - 1)Y_{EGR} + \\ + a'_{02}Y_{EGR}^2 + a'_{30}(\phi - 1)^3 + a'_{21}(\phi - 1)^2 Y_{EGR} + a'_{12}(\phi - 1)Y_{EGR}^2 \,.$$

(A.11)

Here, the exponential factors α and β are given by the approximations

$$\alpha(\phi, Y_{EGR}) = b'_{00} + b'_{10}(\phi - 1) + b'_{01}Y_{EGR} + b'_{20}(\phi - 1)^2 + b'_{11}(\phi - 1)Y_{EGR} + \\ + b'_{02}Y_{EGR}^2 + b'_{30}(\phi - 1)^3 + b'_{21}(\phi - 1)^2 Y_{EGR} + b'_{12}(\phi - 1)Y_{EGR}^2$$

(A.12)

and

$$\beta(\phi, Y_{EGR}) = c'_{00} + c'_{10}(\phi - 1) + c'_{01}Y_{EGR} + c'_{20}(\phi - 1)^2 + c'_{11}(\phi - 1)Y_{EGR} + \\ + c'_{02}Y_{EGR}^2 + c'_{30}(\phi - 1)^3 + c'_{21}(\phi - 1)^2 Y_{EGR} + c'_{12}(\phi - 1)Y_{EGR}^2 \,.$$

(A.13)

The 27 model constants for each correlation were fitted with the Levenberg-Marquardt algorithm using the available simulation data. The constants are summarized in Tables A.1 and A.2. Example results for the burning velocity and inner layer temperature at $T_u = 900K$ and $Y_{EGR} = 0$ are shown in Fig. A.2. The quality of the approximation is shown in Fig. A.3. The correspondence between the simulated values and the ones calculated using the correlations is satisfactory. The error of the approximation is within 10% for the laminar burning velocity and 2% for the inner layer temperature, respectively. It has to be noted that this error may be significantly higher if the thermodynamic state of the mixture differs strongly from the initially mentioned conditions.

Table A.2: Model constants of the correlation for the inner layer temperature of gasoline-air flames.

Constant	Value	Constant	Value	Constant	Value
a'_{00}	2053.6557	b'_{00}	0.1125	c'_{00}	0.0489
a'_{10}	532.2486	b'_{10}	-0.0366	c'_{10}	-0.0188
a'_{01}	-450.4712	b'_{01}	-0.1482	c'_{01}	0.0336
a'_{20}	-422.3795	b'_{20}	0.0906	c'_{20}	-0.0949
a'_{11}	-157.2877	b'_{11}	-0.2395	c'_{11}	-0.0284
a'_{02}	-398.0337	b'_{02}	0.9935	c'_{02}	-0.2200
a'_{30}	-1619.8139	b'_{30}	1.3937	c'_{30}	-0.2886
a'_{21}	-1800.7295	b'_{21}	4.7932	c'_{21}	-1.0299
a'_{12}	-1304.2270	b'_{12}	1.3428	c'_{12}	-0.3508

D Implementation of the GFWI model

To implement the GFWI model, the existing level-set and flame-tracking framework in the CFD code AVL FIRE™ was used. The numerical scheme used to solve the level set equations was a semi-implicit, cell-centered finite volume method with an inflow-based gradient and linearly extended boundary conditions. It has a second order accuracy in time and space and
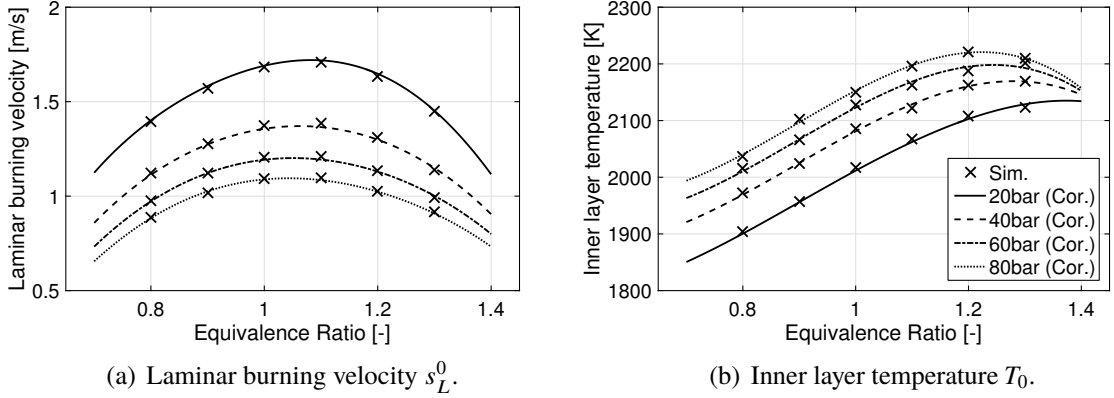
(a) Laminar burning velocity s_L^0.

(b) Inner layer temperature T_0.

Figure A.2: Example results for $T_u = 900K$ and $Y_{EGR} = 0$.

(a) Quality of the s_L^0-fit.
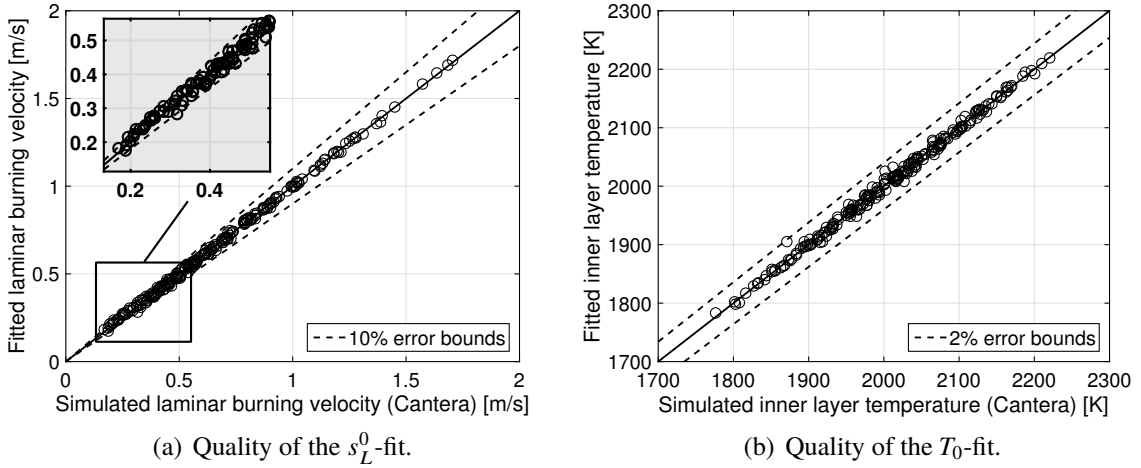
(b) Quality of the T_0-fit.

Figure A.3: Comparison between correlation and simulation.

can be used in combination with polyhedral meshes in contrast to classic level-set schemes such as the Rouy-Tourin [166] or the Osher-Sethian scheme [131]. Further details on the solution method of the level-set equations can be found in the papers of Hahn et al. [82, 83]. To maintain the G-field as a signed distance function, the constraint $|\nabla \widetilde{G}| = 1$ was enforced by solving the partial differential equation

$$\frac{\partial \widetilde{G}}{\partial t} = \text{sign}(\widetilde{G}^0)(1 - |\nabla \widetilde{G}|), \tag{A.14}$$

where $\widetilde{G}^0$ is the initial solution of the level-set equation. The function sign returns the sign of $\widetilde{G}^0$. This reinitialization approach was originally proposed by Sussman et al. [182, 183] and has the advantage that the contour of the zero-level set does not have to be reconstructed to reinitialize the G-field. Hence, errors associated to the reconstruction of the zero-contour are avoided (Sussman and Fatemi [182]). Eq. (A.14) and the transport equation for the variance

of G (5.74) were discretized using the same numerical schemes as for the level-set Eq. (5.67). The tangential diffusion term appearing in the variance equation was approximated by (Peters [142])

$$\nabla_\| \cdot (\overline{\rho} D_t \nabla_\| \widetilde{G''^2}) \equiv \nabla \cdot (\overline{\rho} D_t \nabla \widetilde{G''^2}) - \widetilde{\mathbf{n}} \cdot \nabla(\overline{\rho} \, \widetilde{\mathbf{n}} \cdot D_t \nabla \widetilde{G''^2}). \tag{A.15}$$

The turbulent burning velocity and the turbulent diffusivity were defined according to Eq. (5.86) and (5.80), respectively. The scaling factor l^* was clipped to 1.

The combustion model was coupled to the flow solver by a local progress variable which is based on the burned volume within the computational cell. The level-set and flame-tracking framework used for the present investigations only allowed to use a simple one-step reaction to calculate the heat release as well as the species composition. In the simplest case, i.e., stoichiometric combustion, this one-step reaction reads

$$C_x H_y O_z + \left(x + \frac{y}{4} - \frac{z}{2}\right) O_2 \longrightarrow x CO_2 + \frac{y}{2} H_2 O. \tag{A.16}$$
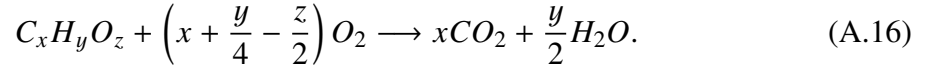
Excess fuel or oxygen remains in fuel rich or lean conditions, respectively. Time integration was split into two major substeps. The solution to the level set equations was calculated first before the coupled system of conservation equations was solved by a combination of the PISO (Pressure-Implicit Split Operator; Issa [94]) and SIMPLE (Semi-Implicit Method for Pressure Linked Equations; Patankar [134]) algorithm. For the spatial discretization of the conservation equations second-order (momentum and continuity equation) and first-order order schemes (enthalpy, turbulence, dissipation and species equations) were used. The discretization in time was performed by using the implicit Euler method. Further informations regarding the CFD code can be found in detail in the software documentation of FIRE™.

D.1 Quenching and wall distance estimation

The unquenched ratio Q has to be determined at the position of the mean flame front $\widetilde{G} = G_0$. It is thus convenient to switch to a moving reference frame attached to the mean flame front. For arbitrarily shaped flame fronts and boundaries, the distance to the quenching zone x_Q can be calculated by

$$x_Q = x_W - y_Q / \sin(\theta), \tag{A.17}$$

where x_W is the flame-normal wall distance and y_Q the quenching distance (cf. Fig. 5.3b). The quantity θ represents the angle between the normal direction of the flame front x and the boundary layer face at the corresponding impact point of the flame. In a HOQ situation, the flame is parallel to the wall, i.e., $\theta = \pi/2$, whereas during SWQ, the flame is perpendicular to the wall, i.e., $\theta = 0$. To achieve a computationally stable calculation for arbitrary geometries, the flame-normal wall distance was estimated for each computational cell containing a part of the mean flame front by calculating the distance between its center and the boundary face which is located along the normal direction of the local flame surface. The minimum wall distance thus depends on the local size of the boundary layer cells. Based on the results presented in chapter 4, the quenching distance y_Q can be specified by a quenching Peclet

number Pe_Q. For the present simulations, the quenching distance was thus calculated by

$$y_Q = Pe_Q l_F = Pe_Q \frac{(\lambda/c_p)_{T_{ref}}}{\rho_u s_L^0} \qquad \text{(A.18)}$$

where $T_{ref} = 1/2(T_0 + T_W)$ (cf. section 4.3.1). By including the laminar flame length l_F, mixture properties can be accounted for. The characteristic Peclet number can be specified based on the geometrical orientation of the flame front, i.e.,

$$Pe_Q = \sqrt{(5\sin(\theta))^2 + (10\cos(\theta)^2)}. \qquad \text{(A.19)}$$

At this point, it should be noted that a pure SWQ configuration cannot be covered by the current model, since the flame-normal wall distance x_W becomes infinite in this case. However, this is in accordance with the derivation and mathematical character of the G-equation combustion model being valid for statistically one-dimensional flames. It has to be noted that other implementations, for example based on a wall-normal (rather than a flame-normal) wall distance, can also be used.

D.2 Spark ignition modelling

Although the GFWI model is able to describe the transition from a laminar flame kernel to a fully turbulent flame, a dedicated spark ignition model is needed. This is mainly due to two reasons: firstly, the finite resolution of the mesh is normally too coarse to resolve the initial flame kernel and secondly, the physics of spark ignition differ from the physics of combustion. Elaborate approaches such as the Spark-Channel Ignition Monitoring Model (SparkCIMM) by Dahms [46] or the Curved Arc Diffusion Ignition Model (CADIM) by Schäfer [171] are available to describe ignition phenomena in combination with the G-equation combustion model.

In the present work, however, a simple spark ignition model, which is consistent to the combustion model, was used. To describe the initial flame kernel growth, an ordinary differential equation for the spark kernel radius r_K

$$\frac{\mathrm{d}r_K}{\mathrm{d}t} = \frac{\rho_u}{\rho_b} s_{T,\kappa} \qquad \text{(A.20)}$$

is solved in combination with the closed variance Eq. (5.74). During the ignition stage, the unquenched factor is set to $Q = 1$. The growth rate $s_{T,k}$ includes curvature effects and can be derived from the closed $\overline{G}$-Eq. (5.67) by substituting $\widetilde{\kappa} = 2/r_K$ (Ewald [66])

$$s_{T,k} = \max\left(s_L^0, s_T^0 - \frac{2}{r_K}D_t\right). \qquad \text{(A.21)}$$

Therein, s_T^0 and D_t are defined according to Eq. (5.85) and (5.80), respectively. The spherical ignition kernel is centered at the user-defined ignition location. All quantities needed to evaluate Eq. (A.20) are averaged over this spherical domain. During the ignition stage, the

$\widetilde{G}$-field is given by a spherical distribution of $\widetilde{G}$ whereby the zero-level set surface $\widetilde{G} = G_0$ coincides with the sphere of radius r_K around the user-defined ignition location. Once the kernel radius r_K exceeds a user-defined transition radius, the ignition model is turned off and the level-set Eq. (5.67) is solved instead.

Bibliography

[1] Abdel-Gayed, R.G., Bradley, D. A two-eddy theory of premixed turbulent flame propagation. *Philosophical Transactions of the Royal Society of London A*, 301:1–25, 1981.

[2] Abdel-Gayed, R.G., Bradley, D. Combustion regimes and the straining of turbulent premixed flames. *Combustion and Flame*, 76:213–218, 1989.

[3] Abe, K., Suga, K. Towards the development of a Reynolds-averaged algebraic turbulent scalar-flux model. *International Journal of Heat and Fluid Flow*, 22:19–29, 2001.

[4] Abu-Orf, G.M., Cant, R.S. A Turbulent Reaction Rate Model for Premixed Turbulent Combustion in Spark-Ignition Engines. *Combustion and Flame*, 122:233–252, 2000.

[5] Adrian, R.J. Hairpin vortex organization in wall turbulence. *Physics of fluids*, 19, 2007.

[6] Adrian, R.J., Meinhart, C.D., Tomkins, C.D. Vortex organization in the outer region of the turbulent boundary layer. *Journal of Fluid Mechanics*, 422:1–54, 2000.

[7] Alharbi, A.Y., Sick, V. Investigation of boundary layers in internal combustion engines using a hybrid algorithm of high speed micro-PIV and PTV. *Experiments in Fluids*, 49:949–959, 2010.

[8] Alkidas, A.C. Heat Transfer Characteristics of a Spark-Ignition Engine. *Journal of Heat Transfer*, 102:189–193, 1980.

[9] Alkidas, A.C. Combustion and Heat Transfer Studies in a Spark-Ignited Multivalve Optical Engine. *Journal of Heat Transfer*, 102:189–193, 1980.

[10] Alkidas, A.C. Thermal Loading of the Cylinder Head of a Spark-Ignition Engine. *Heat Transfer Engineering*, 3:66–75, 1982.

[11] Alshaalan, T.M., Rutland, C.J. Turbulence, scalar transport, and reaction rates in flame-wall interaction. *Symposium (International) on Combustion*, 27:793–799, 1998.

[12] Alshaalan, T.M., Rutland, C.J. Wall heat flux in turbulent premixed reacting flow. *Combustion Science and Technology*, 174:135–165, 2002.

[13] Andrae, J., Björnbom, P., Edsberg, L. Numerical Studies of Wall Effects with Laminar Methane Flames. *Combustion and Flame*, 128:165–180, 2002.

[14] Andrae, J., Björnbom, P., Edsberg, L., Eriksson, L.-E. A numerical study of side wall quenching with propane/air flames. *Proceedings of the Combustion Institute*, 29: 789–795, 2002.

[15] Angelberger, C., Poinsot, T., Delhay, B. Improving Near-Wall Combustion and Wall Heat Transfer Modeling in SI Engine Computations. *SAE Paper 972881*, 1997.

[16] Bai, B., Chen. Z., Zhang, H., Chen, S. Flame propagation in a tube with wall quenching of radicals. *Combustion and Flame*, 160:2810–2819, 2013.

[17] Bellenoue, M., Kageyama, T., Labuda, S.A., Sotton, J. Direct measurement of laminar flame quenching distance in a closed vessel. *Experimental Thermal and Fluid Science*, 27:323–331, 2003.

[18] Benkhaldoun, F., Larrouturou, B., Denet, B. Numerical Investigation of the Extinction Limit of Curved Flames. *Combustion Science and Technology*, 64:187–198, 1989.

[19] Bilger, R.W., Pope, S.B., Bray, K.N.C. und Driscoll, J.F. Paradigms in turbulent combustion research. *Proceedings of the Combustion Institute*, 30:21–42, 2005.

[20] Bird, R.B., Steward, W.E., Lightfoot, E.N. *Transport Phenomena*. Cambridge University Press, 1960.

[21] Biringen, S., Reynolds, W.C. Large-eddy simulation of the shear-free turbulent boundary layer. *Journal of Fluid Mechanics*, 103:53–63, 1981.

[22] Blint, R., Bechtel, J. Flame/Wall Interface: Theory and Experiment. *Combustion Science and Technology*, 27:87–95, 1982.

[23] Borghi, R. On the structure of turbulent premixed flames. In Casci, C., Bruno, C., editor, *Recent Advances in Aerospace Sciences*, pages 117–138. Springer, 1985.

[24] Boust, B., Bernard, L., Sotton, J., Labuda, S.A., Bellenoue, M. A Model of Flame Quenching in Non-Isothermal Initial Conditions. *Proceedings of the European Combustion Meeting*, 2009.

[25] Boust, B., Sotton, J., Bellenoue, M. Unsteady heat transfer during the turbulent combustion of a lean premixed methane-air flame: Effect of pressure and gas dynamics. *Proceedings of the Combustion Institute*, 31, 2007.

[26] Boust, B., Sotton, J., Labuda, S.A., Bellenoue, M. A thermal formulation for single-wall quenching of transient laminar flames. *Combustion and Flame*, 149:286–294, 2007.

[27] Bray, K.N.C. Studies of the Turbulent Burning Velocity. *Proceedings of the Royal Society A*, 431:315–335, 1990.

[28] Bray, K.N.C., Moss, J.B. A unified statistical model of the premixed turbulent flame. *Acta Astronautica*, 4:291–319, 1977.

[29] Bruneaux, G., Akselvoll, K., Poinsot, T., Ferziger, J.H. Simulation of a turbulent flame in a channel. *Proceedings of the 1994 Summer Program*, Center for Turbulence Research, NASA Ames/Stanford Univ.:157–174, 1994.

[30] Bruneaux, G., Akselvoll, K., Poinsot, T., Ferziger, J.H. Flame-Wall Interaction Simulation in a Turbulent Channel Flow. *Combustion and Flame*, 107:27–44, 1996.

[31] Bruneaux, G., Poinsot, T., Ferziger, J.H. Premixed flame-wall interaction in a turbulent channel flow: budget for the flame surface density evolution equation and modelling. *Journal of Fluid Mechanics*, 349:191–219, 1997.

[32] Cai, L., Pitsch, H. Optimized chemical mechanism for combustion of gasoline surrogate fuels. *Combustion and Flame*, 162:1623–1637, 2015.

[33] Candel, S., Poinsot, T. Flame Stretch and the Balance Equation for the Flame Area. *Combustion Science and Technology*, 70:1–15, 1990.

[34] Cant, S. RANS and LES Modelling of Premixed Turbulent Combustion. In Echekki, T., Mastorakos, E., editor, *Turbulent Combustion Modeling*, volume 95 of *Fluid Mechanics and Its Applications*, pages 117–138. Springer, 2011.

[35] Carrier, G., Fendell, F., Feldman, P. Laminar flame propagation/quench for a parallel-wall duct. *Symposium (International) on Combustion*, 20:67–74, 1985.

[36] Chang, J., Güralp, O., Filipi, Z., Assanis, D., Kua, T.-W., Najt, P., Rask, R. New Heat Transfer Correlation for an HCCI Engine Derived from Measurements of Instantaneous Surface Heat Flux. *SAE Paper 2004-01-2996*, 2004.

[37] Chang, N.W., Shy, S.S., Yang, S.I., Yang, T.S. Spatially Resolved Flamelet Statistics for Reaction Rate Modeling Using Premixed Methane-Air Flames in a Near-Homogeneous Turbulence. *Combustion and Flame*, 127:1880–1894, 2001.

[38] Chao, B.H., Law, C.K. Laminar flame propagation with volumetric heat loss and chain branching-termination reactions. *International Journal of Heat and Mass Transfer*, 37:673–680, 1994.

[39] Chauvy, M., Delhom, B., Reveillon, J., Demoulin, F.-X. Flame/Wall Interactions: Laminar Study of Unburnt HC Formation. *Flow Turbulence Combustion*, 84:369–396, 2010.

[40] Clendening Jr., C., Shackleford, W., Hilyard, R. Raman scattering measurements in a side-wall quench layer. *Symposium (International) on Combustion*, 18:1583–1590, 1981.

[41] Colin, O., Benkenida, A. The 3-Zones Extended Coherent Flame Model (ECFM3Z) for Computing Premixed/Diffusion Combustion. *Oil & Gas Science and Technology*, 59:593–609, 2004.

[42] Colin, O., Benkenida, A., Angelberger, C. 3D Modeling of Mixing, Ignition and Combustion Phenomena in Highly Stratified Gasoline Engines. *Oil & Gas Science and Technology*, 58:47–62, 2003.

[43] Connelly, L., Ogasawara, T., Lee, D., Greif, R., Sawyer, R.F. The effect of wall temperature on stagnation and sidewall flame quenching and resulting heat transfer. *Fall Meeting, The Combustion Institute/Western States Section*, Stanford, CA, Paper No. WSCI 92-109, 1992.

[44] Connelly, L., Ogasawara, T., Lee, D., Greif, R., Sawyer, R.F. Stagnation quenching of laminar, methane-air flames in a constant volume chamber: Wall temperature effects. *Fall Meeting, The Combustion Institute/Western States Section*, Stanford, CA, Paper No. WSCI 93-077, 1993.

[45] Dabireau, F., Cuenot, B., Vermorel, O., Poinsot, T. Interaction of flames of $H_2 + O_2$ with inert walls. *Combustion and Flame*, 135:123–133, 2003.

[46] Dahms, R. *Modeling of Combustion in Spray-Guided Spark-Ignition Engines*. Dissertation, Rheinisch-Westfälisch Technische Hochschule Aachen, 2010.

[47] Damköhler, G. Der Einfluss der Turbulenz auf die Flammengeschwindigkeit in Gasgemischen. *Zeitschrift für Elektrochemie und angewandte physikalische Chemie*, 46: 601–652, 1940.

[48] Daniel, W.A. Flame quenching at the walls of an internal combustion engine. *Symposium (International) on Combustion*, 6:886–894, 1957.

[49] Davidson, P.A. *Turbulence: An Introduction for Scientists and Engineers*. Oxford University Press, 2004.

[50] Davy, H. Some Researches on Flame. *Philosophical Transactions of the Royal Society of London*, 107:45–76, 1817.

[51] De Lataillade, A., Dabireau, F., Cuenot, B., Poinsot, T. Flame/wall interaction and maximum wall heat fluxes in diffusion burners. *Proceedings of the Combustion Institute*, 29:775–779, 2002.

[52] Desoutter, G., Cuenot, B., Habchi, C., Poinsot, T. Interaction of a premixed flame with a liquid fuel film on a wall. *Proceedings of the Combustion Institute*, 30:259–266, 2005.

[53] Drake, M.C., Haworth, D.C. Advanced gasoline engine development using optical diagnostics and numerical modeling. *Proceedings of the Combustion Institute*, 31: 99–124, 2007.

[54] Dreizler, A., Böhm, B. Advanced laser diagnostics for an improved understanding of premixed flame-wall interactions. *Proceedings of the Combustion Institute*, 35:37–64, 2015.

[55] Duclos, J.M., Bruneaux, G., Baritaud, T.A. 3D Modelling of Combustion and Pollutants in a 4-Valve SI Engine; Effect of Fuel and Residuals Distribution and Spark Location. *SAE Paper 961964*, 1996.

[56] Dukowicz, J.K. Quasi-Steady Droplet Phase Change in the Presence of Convection. *Informal Report, Los Alamos Scientific Laboratory*, LA-7997-MS, 1979.

[57] Durbin, P.A. Near-wall turbulence closure modeling without 'damping functions'. *Theoretical and Computational Fluid Dynamics*, 3:1–13, 1991.

[58] Durbin, P.A. Separated Flow Computations with the k-ϵ-v^2 Model. *AIAA Journal*, 33:659–664, 1995.

[59] Durbin, P.A. On the k-ϵ stagnation point anomaly. *International Journal of Heat and Fluid Flow*, 17:89–90, 1996.

[60] Echekki, T., Chen, J.H. Analysis of the Contribution of Curvature to Premixed Flame Propagation. *Combustion and Flame*, 118:308–311, 1999.

[61] Echekki, T., Mastorakos, E. *Turbulent Combustion Modeling*, volume 95 of *Fluid Mechanics and Its Applications*. Springer, 2011.

[62] Egolfopoulos, F.N., Zhang, H., Zhang, Z. Wall Effects on the Propagation and Extinction of Steady, Strained, Laminar Premixed Flames. *Combustion and Flame*, 109: 237–252, 1997.

[63] Eichelberg, G. *Temperaturverlauf und Wärmespannungen in Verbrennungsmotoren*. Doctoral Thesis, Eidgenössische Technische Hochschule Zürich, 1922.

[64] Enomoto, M. Head-on Quenching of a Premixed Flame on the Single Wall Surface. *JSME International Journal, Series B*, 44:624–633, 2001.

[65] Enomoto, M. Sidewall quenching of laminar premixed flames propagating along the single wall surface. *Proceedings of the Combustion Institute*, 29:781–787, 2002.

[66] Ewald, J. *A Level Set Based Flamelet Model for the Prediction of Combustion in Homogeneous Charge and Direct Injection Spark Ignition Engines*. Cuvillier Verlag Göttingen, 2006.

[67] Ewald, J., Peters, N. On unsteady premixed turbulent burning velocity prediction in internal combustion engines. *Proceedings of the Combustion Institute*, 31:3051–3058, 2007.

[68] Ezekoye, O.A., Greif, R. A Comparison of One and Two Dimensional Flame Quenching: Heat Transfer Results. *ASME National Heat Transfer Conference*, Atlanta, GA, 1993.

[69] Ezekoye, O.A., Greif, R., Sawyer, R.F. Increased surface temperature effects on wall heat transfer during unsteady flame quenching. *Symposium (International) on Combustion*, 24:1465–1472, 1992.

[70] Fairchild, P., Fleeter, R., Fendell, F. Raman spectroscopy measurements of flame quenching in a duct-type crevice. *Symposium (International) on Combustion*, 20: 85–90, 1985.

[71] Ferguson, C.R., Keck, J.C. On Laminar Flame Quenching and Its Application to Spark Ignition Engines. *Combustion and Flame*, 28:197–205, 1977.

[72] Foucher, F., Burnel, S., Mounaïm-Rousselle, C. Evaluation of burning rates in the vicinity of the piston in a spark-ignition engine. *Proceedings of the Combustion Institute*, 29:751–757, 2002.

[73] Foucher, F., Burnel, S., Mounaïm-Rousselle, C., Boukhalfa, M., Renou, B., Trinité, M. Laminar Flame - Wall Interaction Study: Stretch Effect Analysis. *Proceedings of the 18th International Colloquium on the Dynamics of Explosion and Reactive Systems (ICDERS)*, Paper 202, 2001.

[74] Foucher, F., Burnel, S., Mounaïm-Rousselle, C., Boukhalfa, M., Renou, B., Trinité, M. Flame wall interaction: effect of stretch. *Experimental Thermal and Fluid Science*, 27:431–437, 2003.

[75] Foucher, F., Mounaïm-Rousselle, C. Fractal approach to the evaluation of burning rates in the vicinity of the piston in a spark-ignition engine. *Combustion and Flame*, 143:323–332, 2005.

[76] Gerlinger, P. *Numerische Verbrennungssimulation*. Springer-Verlag, 2005.

[77] Gilaber, P., Pinchon, P. Measurements and Multidimensional Modeling of Gas-Wall Heat Transfer in a S.I. Engine. *SAE Paper 880516*, 1988.

[78] Gülder, L., Smallwood, G. Flame surface densities in premixed combustion. *Combustion Science and Technology*, 179:191–206, 2007.

[79] Gruber, A. *Direct Numerical Simulation Of Turbulent Combustion Near Solid Surfaces*. Doctoral Thesis, Norwegian University of Science and Technology, 2010.

[80] Gruber, A., Chen, J.H., Valiev, D., Law, C.K. Direct numerical simulation of premixed flame boundary layer flashback in turbulent channel flow. *Journal of Fluid Mechanics*, 709:516–542, 2012.

[81] Gruber, A., Sankaran, R., Hawkes, E.R., Chen, J.H. Turbulent flame-wall interaction: a direct numerical simulation study. *Journal of Fluid Mechanics*, 658:5–32, 2010.

[82] Hahn, J., Mikula, K., Frolkovič, P., Basara, B. Inflow-Based Gradient Finite Volume Method for a Propagation in a Normal Direction in a Polyhedron Mesh. *Journal of Scientific Computing*, 72:442–465, 2017.

[83] Hahn, J., Mikula, K., Frolkovič, P., Basara, B. Semi-implicit Level Set Method with Inflow-Based Gradient in a Polyhedron Mesh. In Cancès, C., Omnes, P., editor, *Finite Volumes for Complex Applications VIII - Hyperbolic, Elliptic and Parabolic Problems, FVCA 8, Lille, France, June 2017*, pages 81–89. Springer, 2017.

[84] Han, Z., Reitz, R. A temperature wall function formulation for variable-density turbulent flows with application to engine convective heat transfer modeling. *International Journal of Heat and Mass Transfer*, 40:613–625, 1997.

[85] Hanjalić, K., Popovac, M., Hadžiabdić, M. A robust near-wall elliptic-relaxation eddy-viscosity turbulence model for CFD. *International Journal of Heat and Fluid Flow*, 25:1048–1051, 2004.

[86] Harigaya, Y., Fujio, T., Shigeharu, O., Hiroshi, T. Surface Temperature and Wall Heat Flux in a Spark-Ignition Engine Under Knocking and Non-Knocking Conditions. *SAE Paper 891795*, 1989.

[87] Hasse, C., Bollig, M., Peters, N. Quenching of Laminar Iso-Octane Flames at Cold Walls. *Combustion and Flame*, 122:117–129, 2000.

[88] Haworth, D.C. Progress in probability density function methods for turbulent reacting flows. *Progress in Energy and Combustion Science*, 36:168–259, 2010.

[89] Herrmann, G. *Numerical Simulation of Premixed Turbulent Combustion Based on a Level Set Flamelet Model*. Doctoral Thesis, RWTH Aachen University, 2001.

[90] Heywood, J.B. *Internal combustion engine fundamentals*. McGraw-Hill, 1988.

[91] Hirschfelder, J.O., Curtiss, C.F., Bird, R.B. *Molecular Theory of Gases and Liquids*. Wiley, New York, 1964.

[92] Huang, W.M., Vosen, S.R., Greif, R. Heat transfer during laminar flame quenching: effect of fuels. *Symposium (International) on Combustion*, 21:1853–1860, 1988.

[93] Hunt, J.C.R., Graham, J.M.R. Free-stream turbulence near plane boundaries. *Journal of Fluid Mechanics*, 84:209–235, 1978.

[94] Issa, R.I. Solution of Implicitly Discretized Fluid Flow Equations by Operator Splitting. *Journal of Computational Physics*, 62:40–65, 1986.

[95] Jainski, C., Lu, L., Dreizler, A., Sick, V. High-speed micro particle image velocimetry studies of boundary-layer flows in a direct-injection engine. *International Journal of Engine Research*, 14:247–259, 2012.

[96] Jennings, M.J. Multi-Dimensional Modeling of Turbulent Premixed Charge Combustion. *SAE Paper 920589*, 1992.

[97] Jones, W.P. Turbulence Modelling and Numerical Solution Methods for Variable Density and Combusting Flows. In Libby, P.A., Williams, F.A., editor, *Turbulent Reacting Flows*, pages 309–374. Academic Press, 1994.

[98] Jones, W.P, Launder, B.E. The prediction of laminarization with a two-equation model of turbulence. *International Journal of Heat and Mass Transfer*, 15:301–314, 1972.

[99] Karrer, M., Bellenoue, M., Labuda, S.A., Sotton, J., Makarov, M. Electrical probe diagnostics for the laminar flame quenching distance. *Experimental Thermal and Fluid Science*, 34:131–141, 2010.

[100] Kerstein, A.R., Ashurst, W.T., Williams, F.A. Field equation for interface propagation in an unsteady homogeneous flow field. *Physical Review A*, 37:2728–2731, 1988.

[101] Kiehne, T., Matthews, R., Wilson, D. The significance of intermediate hydrocarbons during wall quench of propane flames. *Symposium (International) on Combustion*, 21:481–489, 1988.

[102] Knudsen, E., Kurenkov, O., Kim, S., Oberlack, M., Pitsch, H. Modeling flame brush thickness in premixed turbulent combustion. *Center for Turbulence Research, Proceedings of the Summer Program*, pages 299–310, 2006.

[103] Kolmogorov, A.N. The local structure of turbulence in incompressible viscous fluid for very large reynolds numbers. *Doklady Akademii Nauk SSSR*, 30:299–303, 1941.

[104] Kuhnke, D. *Spray wall interaction modelling by dimensionless data analysis*. Shaker-Verlag, Aachen, 2004.

[105] Labuda, S.A., Karrer, M., Sotton, J., Bellenoue, M. Experimental study of single-wall flame quenching at high pressures. *Combustion Science and Technology*, 183: 409–426, 2011.

[106] Lai, J., Chakraborty, N. Effects of Lewis Number on Head on Quenching of Turbulent Premixed Flames: A Direct Numerical Simulation Analysis. *Flow, Turbulence and Combustion*, 96:279–308, 2016.

[107] Lai, J., Chakraborty, N. A Priori Direct Numerical Simulation Modeling of Scalar Dissipation Rate Transport in Head-On Quenching of Turbulent Premixed Flames. *Combustion Science and Technology*, 188:1440–1471, 2016.

[108] Lai, J., Chakraborty, N. Modelling of Progress Variable Variance Transport in Head-On Quenching of Turbulent Premixed Flames: A Direct Numerical Simulation Analysis. *Combustion Science and Technology*, 188:1925–1950, 2016.

[109] Laurence, D.R., Uribe, J.C., Utyuzhnikov, S.V. A Robust Formulation of the v2-f Model. *Flow, Turbulence and Combustion*, 73:169–185, 2004.

[110] Libby, P.A., Bray, K.N.C. Countergradient diffusion in premixed turbulent flames. *AIAA Journal*, 19:205–213, 1981.

[111] Linse, D. *Modeling and Simulation of Knock and Nitric Oxide Emissions in Turbocharged Direct Injection Spark Ignition Engines*. Cuvillier Verlag Göttingen, 2013.

[112] Linse, D., Hasse, C., Durst, B. An experimental and numerical investigation of turbulent flame propagation and flame structure in a turbo-charged direct injection gasoline engine. *Combustion Theory and Modeling*, 13:167–188, 2009.

[113] Lipatnikov A.N., Chomiak, J. Turbulent flame speed and thickness: phenomenology, evaluation, and application in multi-dimensional simulations. *Progress in Energy and Combustion Science*, 28:1–74, 2002.

[114] Liu, A., Mather, D., Reitz, R. Modeling the Effects of Drop Drag and Breakup on Fuel Sprays. *SAE 930072*, 1993.

[115] Liu, K., Burluka, A.A., Sheppard, C.G.W. Turbulent flame and mass burning rate in a spark ignition engine. *Fuel*, 107:202–208, 2013.

[116] Lu, J., Ezekoye, O., Greif, R., Sawyer, R. Unsteady heat transfer during side wall quenching of a laminar flame. *Symposium (International) on Combustion*, 23:441–446, 1991.

[117] Magnussen, B.F., Hjertager, B.H. On mathematical modeling of turbulent combustion with special emphasis on soot formation and combustion. *Symposium (International) on Combustion*, 16:719–729, 1977.

[118] Makhviladze, G., Melikhov, V. Flame propagation in a closed channel with cold side walls. *Combustion, Explosion and Shockwaves*, 27:176–183, 1991.

[119] Mann, M. *Laserbasierte Untersuchung der Flamme-Wand-Interaktion*. Optimus Verlag, 2013.

[120] Mann, M., Jainski, C., Euler, M., Böhm, B., Dreizler, A. Transient flame-wall interactions: Experimental analysis using spectroscopic temperature and *CO* concentration measurements. *Combustion and Flame*, 161:2371–2386, 2014.

[121] Marble, F.E., Broadwell, J.E. The coherent flame model for turbulent chemical reactions. *Technical Report No. TRW-9-PU, Project Squid*, 1977.

[122] Meneveau, C., Poinsot, T. Stretching and Quenching of Flamelets in Premixed Turbulent Combustion. *Combustion and Flame*, 86:311–332, 1991.

[123] Merker, G.P., Schwarz, C. (Ed.). *Grundlagen Verbrennungsmotoren*. Vieweg+Teubner, 2009.

[124] Morgan, N., Smallbone, A., Bhave, A., Kraft, M., Cracknell, R., Kalghatgi, G. Mapping surrogate gasoline compositions into RON/MON space. *Combustion and Flame*, 157:1122–1131, 2010.

[125] Moser, R.D., Kim, J., Mansour, N.N. Direct Numerical Simulation of turbulent channel flow up to $Re_\tau = 590$. *Physics of Fluids*, 11:943–945, 1999.

[126] Müller, U.C., Bollig, M., Peters, N. Approximations for Burning Velocities and Markstein Numbers for Lean Hydrocarbon and Methanol Flames. *Combustion and Flame*, 108:349–356, 1997.

[127] Nishiwaki, K. Modeling Engine Heat Transfer and Flame-Wall Interaction. *Proceedings of the International Symposium on Diagnostics and Modeling of Combustion in Internal Combustion Engines (COMODIA)*, 4:35–44, 1998.

[128] Oberlack, M., Wenzel, H., Peters, N. On symmetries and averaging of the G-equation for premixed conbustion. *Combustion Theory and Modelling*, 5:363–383, 2001.

[129] Osher, S., Fedkiw, R. Level Set Methods: An Overview and Some Recent Results. *Journal of Computational Physics*, 169:463–502, 2001.

[130] Osher, S., Fedkiw, R. *Level Set Methods and Dynamic Implicit Surfaces*. Springer-Verlag, New York, 2003.

[131] Osher, S., Sethian, J.A. Fronts propagating with curvature dependent speed: Algorithms Based on Hamilton-Jacobi formulations. *Journal of Computational Physics*, 79:12–49, 1988.

[132] Owston, R., Magi, V., Abraham, J. A numerical study of thermal and chemical effects in interactions of n-heptane flames with a single surface. *Combustion and Flame*, 148:127–147, 2007.

[133] Owston, R., Magi, V., Abraham, J. Interactions of hydrogen flames with walls: Influence of wall temperature, pressure, equivalence ratio, and diluents. *International Journal of Hydrogen Energy*, 32:2094–2104, 2007.

[134] Patankar, S.V. *Numerical Heat Transfer and Fluid Flow*. Hemisphere Publishing Corporation, 1980.

[135] Perot, B., Moin, P. Shear-free turbulent boundary layers. Part 1. Physical insights into near-wall turbulence. *Journal of Fluid Mechanics*, 295:199–227, 1995.

[136] Peters, N. Laminar flamelet concepts in turbulent combustion. *Symposium (International) on Combustion*, 21:1231–1250, 1988.

[137] Peters, N. Length scales in laminar and turbulent flames. In Oran, E.S., Boris, J.A., editor, *Numerical Approaches to Combustion Modeling*, volume 135 of *Progress in Astronautics and Aeronautics*, pages 155–182. American Institute of Aeronautics and Astronautics, 1991.

[138] Peters, N. A spectral closure for premixed combustion in the flamelet regime. *Journal of Fluid Mechanics*, 242:611–629, 1992.

[139] Peters, N. *Fifteen Lectures on Laminar and Turbulent Combustion*. Ercoftac Summer School, September 14-28, 1992. Institut für Technische Mechanik, RWTH Aachen, 1992.

[140] Peters, N. Kinetic foundation of thermal flame theory. In Sirignano, W.A., Merzhanov, A.G., de Luca, L., editor, *Advances in Combustion Science: in Honor of Ya. B. Zel'dovich*, volume 173 of *Progress in Astronautics and Aeronautics*, pages 73–91. American Institute of Aeronautics and Astronautics, 1997.

[141] Peters, N. The turbulent burning velocity for large-scale and small-scale turbulence. *Journal of Fluid Mechanics*, 384:107–132, 1999.

[142] Peters, N. *Turbulent combustion*. Cambridge University Press, 2000.

[143] Peters, N., Bray, K.N.C. Laminar Flamelets in Turbulent Flames. In Libby, P.A., Williams, F.A., editor, *Turbulent Reacting Flows*, pages 63–113. Academic Press, 1994.

[144] Peters, N., Williams, F.A. The asymptotic structure of stoichiometric methane-air flames. *Combustion and Flame*, 68:185–207, 1987.

[145] Philips, D.A., Rossi, R., Iaccarino, G. The influence of normal stress anisotropy in predicting scalar dispersion with the v^2-f model. *International Journal of Heat and Fluid Flow*, 32:943–963, 2011.

[146] Pitsch, H. Shedding new light on a burning question. *Journal of Fluid Mechanics*, 658:1–4, 2010.

[147] Pitsch, H., Peters, N., Seshadri, K. Numerical and asymptotic studies of the structure of premixed iso-octane flames. *Symposium (International) on Combustion*, 26:763–771, 1996.

[148] Plessing, T., Kortschik, C., Peters, N., Mansour, M.S., Cheng, R.K. Measurements of the turbulent burning velocity and the structure of premixed flames on a low-swirl burner. *Proceedings of the Combustion Institute*, 28:359–366, 2000.

[149] Poinsot, T., Haworth, D.C., Bruneaux, G. Direct Simulation and Modeling of Flame-Wall Interaction for Premixed Turbulent Combustion. *Combustion and Flame*, 95: 118–132, 1993.

[150] Poinsot, T., Veynante, D. *Theoretical and Numerical Combustion*. Third Edition. Thierry Poinsot, Denis Veynante, 2011.

[151] Poinsot, T., Veynante, D., Candel, S. Diagrams of Premixed Turbulent Combustion based on Direct Numerical Simulations. *Symposium (International) on Combustion*, 23:613–619, 1991.

[152] Pope, S.B. PDF methods for turbulent reactive flows. *Progress in Energy and Combustion Science*, 11:119–192, 1985.

[153] Pope, S.B. The evolution of surfaces in turbulence. *International Journal of Engineering Science*, 26:445–469, 1988.

[154] Pope, S.B. *Turbulent Flows*. Cambridge University Press, 2000.

[155] Pope, S.B. Small scales, many species and the manifold challenges of turbulent combustion. *Proceedings of the Combustion Institute*, 34:1–31, 2013.

[156] Popovac, M., Hanjalić, K. Compound Wall Treatment for RANS Computation of Complex Turbulent Flows and Heat Transfer. *Flow, Turbulence and Combustion*, 78: 177–202, 2007.

[157] Popp, P., Baum, M. Analysis of Wall Heat Fluxes, Reaction Mechanisms, and Unburnt Hydrocarbons during the Head-on Quenching of a Laminar Methane Flame. *Combustion and Flame*, 108:327–348, 1997.

[158] Popp, P., Smooke, M., Baum, M. Heterogeneous/homogeneous reaction and transport coupling during flame-wall interaction. *Symposium (International) on Combustion*, 26:2693–2700, 1996.

[159] Potter Jr., A., Berlad, A. The effect of fuel type and pressure on flame quenching. *Symposium (International) on Combustion*, 6:27–36, 1957.

[160] Prandtl, L. Bermerkungen über die Entstehung der Turbulenz. *Zeitschrift für Angewandte Mathematik und Mechanik*, 5:431–436, 1921.

[161] Reynolds, O. On the Dynamical Theory of Incompressible Viscous Fluids and the Determination of the Criterion. *Philosophical Transactions of the Royal Society of London, A*, 186:123–164, 1895.

[162] Richard, G., Escudié, D. Turbulence effect on the flame-wall interaction. *International Symposium on Turbulence and Shear Flow Phenomena*, 1:519–523, 1999.

[163] Robinson, S.K. Coherent Motions in the Turbulent Boundary Layer. *Annual Reviews of Fluid Mechanics*, 23:601–639, 1991.

[164] Robinson, S.K. The Kinematics of Turbulent Boundary Layer Structure. *NASA Report No. TM-103859*, 1991.

[165] Rodi, W., Mansour, N.N. Low Reynolds number k-ϵ modelling with the aid of direct simulation data. *Journal of Fluid Mechanics*, 250:509–529, 1993.

[166] Rouy, E., Tourin, A. A Viscosity Solutions Approach to Shape-From-Shading. *SIAM Journal on Numerical Analysis*, 29:867–884, 1992.

[167] Rutland, C.J., Cant, R.S. Turbulent transport in premixed flames. *Proceedings of the Summer Program*, Center for Turbulence Research:75–94, 1994.

[168] Saffman, M. Parametric Studies of a Side Wall Quench Layer. *Combustion and Flame*, 55:141–159, 1984.

[169] Salzmann, F. *Wärmefluß durch Kolben und Kolbenring im Dieselmotor*. Doctoral Thesis, Eidgenössische Technische Hochschule Zürich, 1932.

[170] Saric, S., Basara, B. A Hybrid Wall Heat Transfer Model for IC Engine Simulations. *SAE International Journal of Engines*, 8:411–418, 2015.

[171] Schaefer, L. *Modeling and Simulation of Spark Ignition in Turbocharged Direct Injection Spark Ignition Engines*. Verlag Dr. Hut, 2016.

[172] Schlichting, H., Gersten, K. *Boundary-Layer Theory*. Springer-Verlag Berlin Heidelberg, 2000.

[173] Schmitt, M. *Direct numerical simulations in engine-like geometries*. PhD thesis, ETH Zürich, 2014.

[174] Schmitt, M., Frouzakis, C.E., Wright, Y.M., Tomboulides, A.G., Boulouchos, K. Direct numerical simulation of the compression stroke under engine-relevant conditions: Evolution of the velocity and thermal boundary layers. *International Journal of Heat and Mass Transfer*, 91:948–960, 2015.

[175] Sellmann, J., Lai, J., Kempf, A.M., Chakraborty, N. Flame surface density based modelling of head-on quenching of turbulent premixed flames. *Proceedings of the Combustion Institute*, 36:1817–1825, 2017.

[176] Seshadri, K., Bollig, M., Peters, N. Numerical and Asymptotic Studies of the Structure of Stoichiometric and Lean Premixed Heptane Flames. *Combustion and Flame*, 108: 518–536, 1997.

[177] Sethian, J.A. *Level Set Methods and Fast Marching Methods*. Cambridge University Press, 1999.

[178] Smooke, M.D. The computation of laminar flames. *Proceedings of the Combustion Institute*, 34:65–98, 2013.

[179] Smooke, M.D., Giovangigli, V. Formulation of the premixed and non-premixed test problems. In Smooke, M.D., editor, *Reduced Kinetic Mechanisms and Asymptotic Approximations for Methane-Air Flames*, volume 384 of *Lecture Notes in Physics*, pages 1–28. Springer, 1991.

[180] Sotton, J., Boust, B., Labuda, S.A., Bellenoue, M. Head-on quenching of transient laminar flame: heat flux and quenching distance measurements. *Combustion Science and Technology*, 177:1305–1322, 2005.

[181] Spalding, D.B. Mixing and chemical reactions in steady confined turbulent flames. *Symposium (International) on Combustion*, 13:649–657, 1971.

[182] Sussman, M., Fatemi, E. An Efficient, Interface-Preserving Level Set Redistancing Algorithm and Its Application to Interfacial Incomprerssible Fluid Flow. *SIAM Journal on Scientific Computing*, 20:1165–1191, 1999.

[183] Sussman, M., Smereka, P., Osher, S. A Level Set Approach for Computing Solutions to Incompressible Two-Phase Flow. *Journal of Computational Physics*, 114:146–159, 1994.

[184] Tan, Z., Reitz, R.D. An ignition and combustion model based on the level-set method for spark ignition engine multidimensional modeling. *Combustion and Flame*, 145: 1–15, 2006.

[185] Tavoularis, S., Corrsin, S. Experiments in nearly homogenous turbulent shear flow with a uniform mean temperature gradient. Part 1. *Journal of Fluid Mechanics*, 104: 311–347, 1981.

[186] Tayebi, B., Galizzi, C., Guo, H., Escudié, D. An experimental study of the flame-wall interaction: temperature analysis near the wall. *The 19th International Symposium on Transport Phenomena*, Reykjavik, Iceland, 17-20 August 2008.

[187] Tayebi, B., Galizzi, C., Leone, J.F., Escudié, D. Experimental study of the Flame-Wall Interaction. *Third European Combustion Meeting*, Chania, Crete, 11-13 April 2007.

[188] Tayebi, B., Galizzi, C., Leone, J.F., Escudié, D. Topology structure and flame surface density in flame-wall interaction. *5th European Thermal-Sciences Conference*, Eindhoven, The Netherlands, 18-22 May 2008.

[189] Theodorsen, T. Mechanism of turbulence. *Proceedings of the Midwestern Conference on Fluid Dynamics*, Ohio State University, Columbus, Ohio, 1952.

[190] Thomas, N.H., Hancock, P.E. Grid turbulence near a moving wall. *Journal of Fluid Mechanics*, 82:481–496, 1977.

[191] Toninel, S., Forkel, H., Frank, T., Durst, B., Hasse, C., Linse, D. Implementation and Validation of the G-equation Model Coupled with Flamelet Libraries for Simulating Premixed Combustion in I.C. Engines. *SAE Paper 2009-01-0709*, 2009.

[192] Trouvé, A., Poinsot, T. The evolution equation for the flame surface density in turbulent premixed combustion. *Journal of Fluid Mechanics*, 278:1–31, 1994.

[193] Uzkan, T., Reynolds, W.C. A shear-free turbulent boundary layer. *Journal of Fluid Mechanics*, 28:803–821, 1967.

[194] Vervisch, L., Bidaux, E., Bray, K.N.C., Kollmann, W. Surface density function in premixed turbulent combustion modeling, similarities between propability density function and flame surface approaches. *Physics of Fluids*, 7:2496–2503, 1995.

[195] Vervisch, L., Veynante, D. Interlinks between approaches for modeling turbulent flames. *Proceedings of the Combustion Institute*, 28:175–183, 2000.

[196] Veynante, D., Trouvé, A. , Bray, K.N.C., Mantel, T. Gradient and counter-gradient scalar transport in turbulent premixed flames. *Journal of Fluid Mechanics*, 332: 263–293, 1997.

[197] Veynante, D., Vervisch, L. Turbulent combustion modeling. *Progress in Energy and Combustion Science*, 28:193–266, 2002.

[198] Vlachos, D.G., Schmidt, L.D., Aris, R. Ignition and Extinction of Flames Near Surfaces: Combustion of CH_4 in Air. *AIChE Journal*, 40:1005–1017, 1994.

[199] von Kármán, T. Mechanische Ähnlichkeit und Turbulenz. *Nachrichten von der Gesellschaft der Wissenschaften zu Göttingen, Fachgruppe 1 (Mathematik)*, 5:58–76, 1930.

[200] von Kármán, T., Millan, G. Thermal theory of a laminar flame front near a cold wall. *Symposium (International) on Combustion*, 4:173–177, 1953.

[201] Vosen, S.R., Greif, R., Westbrook, C.K. Unsteady heat transfer during laminar flame quenching. *Symposium (International) on Combustion*, 20:75–83, 1985.

[202] Wang, Y., Trouvé, A. Direct numerical simulation of nonpremixed flame-wall interactions. *Combustion and Flame*, 144:461–475, 2006.

[203] Warnatz, J., Maas, U., Dibble, R.W. *Combustion*. Springer-Verlag, 2006.

[204] Weil, E. An unpublished letter by Davy on the safety-lamp. *Annals of Science*, 6: 306–307, 1950.

[205] Weller, H.G., Uslu, S., Gosman, A.D., Maly, R.R., Herweg, R., Heel, B. Prediction of Combustion in Homogeneous-Charge Spark-Ignition Engines. *Proceedings of the International Symposium on Diagnostics and Modeling of Combustion in Internal Combustion Engines (COMODIA)*, 3:163–169, 1994.

[206] Wendland, D.W. The effect of periodic pressure and temperature fluctuations on unsteady heat transfer in a closed system. *NASA Report No. CR - 72323*, 1968.

[207] Wenzel, H., Peters, N. Scaling of production, kinematic restoration, and dissipation of the mean flame surface area. *Combustion Science and Technology*, 177:1095–1107, 2005.

[208] Westbrook, C.K., Adamczyk, A.A., Lavoie, G.A. A Numerical Study of Laminar Flame Wall Quenching. *Combustion and Flame*, 40:81–99, 1981.

[209] Westbrook, C.K., Mizobuchi, Y., Poinsot, T.J., Smith, P.J., Warnatz, J. Computational combustion. *Proceedings of the Combustion Institute*, 30:125–157, 2005.

[210] Wichman, I.S., Bruneaux, G. Head-on Quenching of a Premixed Flame by a Cold Wall. *Combustion and Flame*, 103:296–310, 1995.

[211] Wilcox, D.C. *Turbulence Modeling for CFD*. La Cañada, CA: DCW Industries, 1993.

[212] Williams, F.A. *Combustion Theory*. Perseus Books Publishing, 1985.

[213] Wimmer, A., Pivec, R., Sams, T. Heat Transfer to the Combustion Chamber and Port Walls of IC Engines - Measurement and Prediction. *SAE Paper 2000-01-0568*, 2000.

[214] Wirth, M. *Die turbulente Flammenausbreitung im Ottomotor und ihre charakteristischen Längenskalen*. VDI Fortschritt-Berichte, VDI Verlag, Düsseldorf, 1993.

[215] Wu, K., Hochgreb, S. The Roles of Chemistry and Diffusion on Hydrocarbon Post-Flame Oxidation. *Combustion Science and Technology*, 130:365–398, 1997.

[216] Wu, K., Hochgreb, S. Numerical Simulation of Post-Flame Oxidation of Hydrocarbons in Spark Ignition Engines. *SAE Paper 970886*, 1997.

[217] Zeldovich, Ya. B., Frank-Kamenetzki, D.A. A theory of Thermal Propagation of Flame. *Acta Physicochimica*, 9:341–350, 1938.

[218] Zhang, H., Chen, Z. Effects of heat conduction and radical quenching on premixed stagnation flame stabilised by a wall. *Combustion Theory and Modelling*, 17:682–706, 2013.